



**NAVAL
POSTGRADUATE
SCHOOL**

MONTEREY, CALIFORNIA

THESIS

**MODELING OF THERMAL AND MECHANICAL
EFFECTS DURING FRICTION STIR PROCESSING
OF NICKEL-ALUMINUM BRONZE**

by

Jay Dee Jamison

September 2004

Thesis Advisor:

Terry R. McNelley

Approved for Public Release; Distribution is Unlimited

THIS PAGE INTENTIONALLY LEFT BLANK

REPORT DOCUMENTATION PAGE

Form Approved OMB No. 0704-0188

Public reporting burden for this collection of information is estimated to average 1 hour per response, including the time for reviewing instruction, searching existing data sources, gathering and maintaining the data needed, and completing and reviewing the collection of information. Send comments regarding this burden estimate or any other aspect of this collection of information, including suggestions for reducing this burden, to Washington headquarters Services, Directorate for Information Operations and Reports, 1215 Jefferson Davis Highway, Suite 1204, Arlington, VA 22202-4302, and to the Office of Management and Budget, Paperwork Reduction Project (0704-0188) Washington DC 20503.

1. AGENCY USE ONLY (<i>Leave blank</i>)	2. REPORT DATE September 2004	3. REPORT TYPE AND DATES COVERED Master's Thesis
4. TITLE AND SUBTITLE: Modeling of Thermal and Mechanical Effects During Friction Stir Processing of Nickel-Aluminum Bronze		5. FUNDING NUMBERS
6. AUTHOR(S) Jamison, Jay D.		
7. PERFORMING ORGANIZATION NAME(S) AND ADDRESS(ES) Naval Postgraduate School Monterey, CA 93943-5000		8. PERFORMING ORGANIZATION REPORT NUMBER
9. SPONSORING /MONITORING AGENCY NAME(S) AND ADDRESS(ES) N/A		10. SPONSORING/MONITORING AGENCY REPORT NUMBER
11. SUPPLEMENTARY NOTES The views expressed in this thesis are those of the author and do not reflect the official policy or position of the Department of Defense or the U.S. Government.		
12a. DISTRIBUTION / AVAILABILITY STATEMENT Approved for Public Release; Distribution is Unlimited	12b. DISTRIBUTION CODE	
13. ABSTRACT (maximum 200 words) Friction Stir Processing (FSP), although relatively simple in concept, results in an extremely complex thermomechanical treatment to the material being processed. Previous studies of FSP have shown that the process results in extremely high strain, strain rates and temperatures as well as gradients in strain, strain rate and temperature within a small volume of material. This thesis will study the effect of varying FSP parameters during the processing of Nickel-Aluminum-Bronze (NAB) propeller material. The modeling program CTH was used to define the relationship between tool rotation speed, traversing speed and the total power input to the material. The tool's mechanical power and the power generated by deformation of the material has been investigated. The modeling experiments were designed to gain an understanding of the relationship of process parameters, microstructure and mechanical properties, and to enhance our understanding of the flow patterns and thermal histories of the NAB material in the stir zone.		
14. SUBJECT TERMS Friction Stir, Modeling, Simulation, Thermal Power, Heat Input, Welding, NiAl Bronze		15. NUMBER OF PAGES 171
		16. PRICE CODE
17. SECURITY CLASSIFICATION OF REPORT Unclassified	18. SECURITY CLASSIFICATION OF THIS PAGE Unclassified	19. SECURITY CLASSIFICATION OF ABSTRACT Unclassified
		20. LIMITATION OF ABSTRACT UL

NSN 7540-01-280-5500

Standard Form 298 (Rev. 2-89)
Prescribed by ANSI Std. Z39-18

THIS PAGE INTENTIONALLY LEFT BLANK

Approved for Public Release; Distribution is Unlimited

**MODELING OF THERMAL AND MECHANICAL EFFECTS DURING
FRICTION STIR PROCESSING OF NICKEL-ALUMINUM BRONZE**

Jay D. Jamison
Lieutenant, United States Navy
B.S., University of Utah, 1995

Submitted in partial fulfillment of the
requirements for the degree of

**MECHANICAL ENGINEER
and
MASTER OF SCIENCE IN MECHANICAL ENGINEERING**

from the

**NAVAL POSTGRADUATE SCHOOL
September 2004**

Author: Jay Dee Jamison

Approved by: Terry R. McNelley
Thesis Advisor

Anthony J. Healey
Chairman, Department of Mechanical and Astronautical
Engineering

THIS PAGE INTENTIONALLY LEFT BLANK

ABSTRACT

Friction Stir Processing (FSP), although relatively simple in concept, results in an extremely complex thermo-mechanical treatment to the material being processed. Previous studies of FSP have shown that the process results in extremely high strain, strain rates and temperatures as well as gradients in strain, strain rate and temperature within a small volume of material. This thesis will study the effect of parametric variations in process parameters on Nickel-Aluminum Bronze (NAB) propeller material. The modeling program CTH was exercised to define the relationship between tool rotation speed, traversing speed, effective heat input and generated thermal power. The tool's mechanical power and the adiabatic thermal power generated by deformation of the material have been investigated. The relationships between process parameters of conventional fusion welding were studied to determine any parallel relationships might be drawn with FSP. The modeling simulations were designed to gain an understanding of the relationship of process parameters, microstructure and mechanical properties, and to enhance our understanding of the flow patterns and thermal histories of the NAB material in the stir zone and the thermal mechanical affected zone.

THIS PAGE INTENTIONALLY LEFT BLANK

TABLE OF CONTENTS

I.	INTRODUCTION.....	1
A.	OVERVIEW.....	1
B.	FRICTION STIR PROCESSING	2
C.	NICKEL-ALUMINUM-BRONZE AND IT'S MICROSTRUCTURES	6
1.	NAB Phases.....	7
2.	Beta (β) and Retained-Beta (β')Phases.....	8
3.	Alpha (α) Phase	9
4.	Kappa Phases (κ).....	10
C.	FRICTION STIR PROCESSING MODELING EFFORT	11
II.	OBJECTIVES OF THIS RESEARCH.....	15
III.	SIMULATION PROCEDURES AND TESTING	17
A.	MODELING PROGRAM SELECTION	17
B.	TOOL SELECTION AND GRID SETUP.....	21
C.	PARAMETRIC VARIATION OF PROCESS PARAMETERS.....	23
D.	DEFINING THE STIR ZONE VOLUME	24
1.	Temperature Based SZ Volume	24
2.	Strain-Rate Based SZ Volume	24
E.	THE CTH SIMULATION	25
1.	Setup of Unix Machines.....	25
2.	FSW-CTH Suite Input.....	26
3.	FSW-CTH Steady State.....	26
4.	FSW-CTH Output	29
F.	POST-PROCESSING THE DATA	31
IV.	RESULTS AND DISCUSSION	33
A.	ANALYSIS OF THE SZ VOLUME BASED ON TEMPERATURE	33
B.	ANALYSIS OF THE SZ VOLUME BASED ON STRAIN-RATE.....	36
C.	ANALYSIS OF THE GENERATED THERMAL POWER	38
D.	THERMAL CYCLES USING ROSENTHAL'S 3D APPROXIMATION	41
V.	CONCLUSIONS AND RECOMMENDATIONS.....	43
APPENDIX A – CTHPLT OUTPUT	45	
A.	100 RPM 1 IPM.....	46
B.	100 RPM 5 IPM.....	50
C.	100 RPM 10 IPM.....	54
D.	100 RPM 20 IPM.....	58
E.	500 RPM 1 IPM.....	62
F.	500 RPM 5 IPM.....	66
G.	500 RPM 10 IPM.....	70

H.	500 RPM 20 IPM.....	74
I.	1000 RPM 1 IPM.....	78
J.	1000 RPM 5 IPM.....	82
K.	1000 RPM 10 IPM.....	86
L.	1000 RPM 20 IPM.....	90
M.	2000 RPM 1 IPM.....	94
N.	2000 RPM 5 IPM.....	98
O.	2000 RPM 10 IPM.....	102
P.	2000 RPM 20 IPM.....	106
Q.	5000 RPM 1 IPM.....	110
R.	5000 RPM 5 IPM.....	114
S.	5000 RPM 10 IPM.....	118
T.	5000 RPM 20 IPM.....	122
APPENDIX B – MATLAB ANALYSIS PLOTS		127
A.	VOLUME PLOTS BASED ON TEMPERATURE.....	127
B.	VOLUME PLOTS BASED ON STRAIN-RATE	131
C.	POWER GENERATION FRACTIONS.....	140
D.	DERIVATION OF THE POWER LAW RELATIONSHIP	144
E.	ROSENTHAL'S 3-DIMENSIONAL APPROXIMATION	145
LIST OF REFERENCES.....		149
INITIAL DISTRIBUTION LIST		153

LIST OF FIGURES

Figure 1.	Example of FSP Region (courtesy of LCDR R. Williams, NPS).....	3
Figure 2.	Friction Stir Process Illustration (adapted from [Ref. 1]) ;	4
Figure 3.	Friction Stir Terminology (diagram courtesy of Dr. K. Oishi, NPS)	5
Figure 4.	Transformation of NAB Phases during Cooling of NAB Materials (courtesy of Prof. Terry McNelley, NPS).....	8
Figure 5.	NAB Kappa Phase Structures (From Ref. 10).....	10
Figure 6.	Comparison of simulated maximum temperature profiles to the microstructurally-based estimated maximum temperature profiles seen in the SZ, TMAZ and HAZ of the provided materials.....	20
Figure 7.	Standard FSP tool incorporating a threaded, tapered pin.	22
Figure 8.	Configuration of Axes for simulations	22
Figure 9.	CTH grid for NAB material.....	23
Figure 10.	Output of HISPLT showing Tool Torque vs number of cycles.....	27
Figure 11.	Output of HISPLT showing Tool x, y and z Forces vs number of cycles.....	27
Figure 12.	Output of HISPLT showing Tool z Force vs number of cycles.....	28
Figure 13.	Output of HISPLT showing tracer temperatures vs time (cycles).....	28
Figure 14.	Output of CTHPLT showing temperature and max temperature on xz- plane.....	29
Figure 15.	Output of CTHPLT showing strain and strain-rate on xz-plane	29
Figure 16.	Output of CTHPLT showing z-velocity and velocity fields on xz-plane	30
Figure 17.	Output of CTHPLT showing stress on xz-plane.....	30
Figure 18.	Output of CTHPLT showing quality of mixing on xz and yz-planes.....	30
Figure 19.	CTHPLT temperature output for Traversing Rate of 5 inch/min	33
Figure 20.	SZ Volume based on T>800 °C wrt Rotation Speed.....	34
Figure 21.	SZ Volume based on T>900 °C wrt Rotation Speed.....	35
Figure 22.	CTHPLT strain-rate output for Traversing Rate of 5 inch/min	36
Figure 23.	SZ Volume based on $\dot{\epsilon}$ wrt Rotation Speed for Traversing Rate of 5 ipm....	37
Figure 24.	Power Generation Fractions wrt Rotation Rate for Traversing Rate of 5 ipm.	39
Figure 25.	Effective Heat Input wrt Tool Coefficient.....	40
Figure 26.	100 rev/min 1 inch/min – Temperature distribution.....	46
Figure 27.	100 rev/min 1 inch/min – Strain distribution.....	47
Figure 28.	100 rev/min 1 inch/min – Strain-rate distribution.....	48
Figure 29.	100 rev/min 1 inch/min – Stress distribution.....	49
Figure 30.	100 rev/min 5 inch/min – Temperature distribution.....	50
Figure 31.	100 rev/min 5 inch/min – Strain distribution.....	51
Figure 32.	100 rev/min 5 inch/min – Strain-rate distribution.....	52
Figure 33.	100 rev/min 5 inch/min – Stress distribution.....	53
Figure 34.	100 rev/min 10 inch/min – Temperature distribution.....	54
Figure 35.	100 rev/min 10 inch/min – Strain distribution.....	55
Figure 36.	100 rev/min 10 inch/min – Strain-rate distribution.....	56
Figure 37.	100 rev/min 10 inch/min – Stress distribution.....	57

Figure 38.	100 rev/min 20 inch/min – Temperature distribution.....	58
Figure 39.	100 rev/min 20 inch/min – Strain distribution.....	59
Figure 40.	100 rev/min 20 inch/min – Strain-rate distribution.....	60
Figure 41.	100 rev/min 20 inch/min – Stress distribution.....	61
Figure 42.	500 rev/min 1 inch/min – Temperature distribution.....	62
Figure 43.	500 rev/min 1 inch/min – Strain distribution.....	63
Figure 44.	500 rev/min 1 inch/min – Strain-rate distribution.....	64
Figure 45.	500 rev/min 1 inch/min – Stress distribution.....	65
Figure 46.	500 rev/min 5 inch/min – Temperature distribution.....	66
Figure 47.	500 rev/min 5 inch/min – Strain distribution.....	67
Figure 48.	500 rev/min 5 inch/min – Strain-rate distribution.....	68
Figure 49.	500 rev/min 5 inch/min – Stress distribution.....	69
Figure 50.	500 rev/min 10 inch/min – Temperature distribution.....	70
Figure 51.	500 rev/min 10 inch/min – Strain distribution.....	71
Figure 52.	500 rev/min 10 inch/min – Strain-rate distribution.....	72
Figure 53.	500 rev/min 10 inch/min – Stress distribution.....	73
Figure 54.	500 rev/min 20 inch/min – Temperature distribution.....	74
Figure 55.	500 rev/min 20 inch/min – Strain distribution.....	75
Figure 56.	500 rev/min 20 inch/min – Strain-rate distribution.....	76
Figure 57.	500 rev/min 20 inch/min – Stress distribution.....	77
Figure 58.	1000 rev/min 1 inch/min – Temperature distribution.....	78
Figure 59.	1000 rev/min 1 inch/min – Strain distribution.....	79
Figure 60.	1000 rev/min 1 inch/min – Strain-rate distribution.....	80
Figure 61.	1000 rev/min 1 inch/min – Stress distribution.....	81
Figure 62.	1000 rev/min 5 inch/min – Temperature distribution.....	82
Figure 63.	1000 rev/min 5 inch/min – Strain distribution.....	83
Figure 64.	1000 rev/min 5 inch/min – Strain-rate distribution.....	84
Figure 65.	1000 rev/min 5 inch/min – Stress distribution.....	85
Figure 66.	1000 rev/min 10 inch/min – Temperature distribution.....	86
Figure 67.	1000 rev/min 10 inch/min – Strain distribution.....	87
Figure 68.	1000 rev/min 10 inch/min – Strain-rate distribution.....	88
Figure 69.	1000 rev/min 10 inch/min – Stress distribution.....	89
Figure 70.	1000 rev/min 20 inch/min – Temperature distribution.....	90
Figure 71.	1000 rev/min 20 inch/min – Strain distribution.....	91
Figure 72.	1000 rev/min 20 inch/min – Strain-rate distribution.....	92
Figure 73.	1000 rev/min 20 inch/min – Stress distribution.....	93
Figure 74.	2000 rev/min 1 inch/min – Temperature distribution.....	94
Figure 75.	2000 rev/min 1 inch/min – Strain distribution.....	95
Figure 76.	2000 rev/min 1 inch/min – Strain-rate distribution.....	96
Figure 77.	2000 rev/min 1 inch/min – Stress distribution.....	97
Figure 78.	2000 rev/min 5 inch/min – Temperature distribution.....	98
Figure 79.	2000 rev/min 5 inch/min – Strain distribution.....	99
Figure 80.	2000 rev/min 5 inch/min – Strain-rate distribution.....	100
Figure 81.	2000 rev/min 5 inch/min – Stress distribution.....	101
Figure 82.	2000 rev/min 10 inch/min – Temperature distribution.....	102

Figure 83.	2000 rev/min 10 inch/min – Strain distribution.....	103
Figure 84.	2000 rev/min 10 inch/min – Strain-rate distribution.....	104
Figure 85.	2000 rev/min 10 inch/min – Stress distribution.....	105
Figure 86.	2000 rev/min 20 inch/min – Temperature distribution.....	106
Figure 87.	2000 rev/min 20 inch/min – Strain distribution.....	107
Figure 88.	2000 rev/min 20 inch/min – Strain-rate distribution.....	108
Figure 89.	2000 rev/min 20 inch/min – Stress distribution.....	109
Figure 90.	5000 rev/min 1 inch/min – Temperature distribution.....	110
Figure 91.	5000 rev/min 1 inch/min – Strain distribution.....	111
Figure 92.	5000 rev/min 1 inch/min – Strain-rate distribution.....	112
Figure 93.	5000 rev/min 1 inch/min – Stress distribution.....	113
Figure 94.	5000 rev/min 5 inch/min – Temperature distribution.....	114
Figure 95.	5000 rev/min 5 inch/min – Strain distribution.....	115
Figure 96.	5000 rev/min 5 inch/min – Strain-rate distribution.....	116
Figure 97.	5000 rev/min 5 inch/min – Stress distribution.....	117
Figure 98.	5000 rev/min 10 inch/min – Temperature distribution.....	118
Figure 99.	5000 rev/min 10 inch/min – Strain distribution.....	119
Figure 100.	5000 rev/min 10 inch/min – Strain-rate distribution.....	120
Figure 101.	5000 rev/min 10 inch/min – Stress distribution.....	121
Figure 102.	5000 rev/min 20 inch/min – Temperature distribution.....	122
Figure 103.	5000 rev/min 20 inch/min – Strain distribution.....	123
Figure 104.	5000 rev/min 20 inch/min – Strain-rate distribution.....	124
Figure 105.	5000 rev/min 20 inch/min – Stress distribution.....	125
Figure 106.	SZ Volume based on T>800 °C wrt Rotation Speed.....	127
Figure 107.	SZ Volume based on T>900 °C wrt Rotation Speed.....	128
Figure 108.	SZ Volume based on T>800 °C wrt Traversing Speed.....	129
Figure 109.	SZ Volume based on T>900 °C wrt Traversing Speed.....	130
Figure 110.	SZ Volume based on $\dot{\epsilon}$ wrt Rotation Speed for Traversing Rate of 1 ipm.....	131
Figure 111.	SZ Volume based on $\dot{\epsilon}$ wrt Rotation Speed for Traversing Rate of 5 ipm.....	132
Figure 112.	SZ Volume based on $\dot{\epsilon}$ wrt Rotation Speed for Traversing Rate of 10 ipm.....	133
Figure 113.	SZ Volume based on $\dot{\epsilon}$ wrt Rotation Speed for Traversing Rate of 20 ipm.....	134
Figure 114.	SZ Volume based on $\dot{\epsilon}$ wrt Rotation Speed for Rotation Rate of 100 rpm.....	135
Figure 115.	SZ Volume based on $\dot{\epsilon}$ wrt Rotation Speed for Rotation Rate of 500 rpm.....	136
Figure 116.	SZ Volume based on $\dot{\epsilon}$ wrt Rotation Speed for Rotation Rate of 1000 rpm.....	137
Figure 117.	SZ Volume based on $\dot{\epsilon}$ wrt Rotation Speed for Rotation Rate of 2000 rpm.....	138
Figure 118.	SZ Volume based on $\dot{\epsilon}$ wrt Rotation Speed for Rotation Rate of 5000 rpm.....	139
Figure 119.	Power Generation Fractions wrt Traversing Rate for Rotation Speed of 100 rpm.....	140
Figure 120.	Power Generation Fractions wrt Traversing Rate for Rotation Speed of 500 rpm.....	140

Figure 121.	Power Generation Fractions wrt Traversing Rate for Rotation Speed of 1000 rpm	141
Figure 122.	Power Generation Fractions wrt Traversing Rate for Rotation Speed of 2000 rpm	141
Figure 123.	Power Generation Fractions wrt Traversing Rate for Rotation Speed of 5000 rpm	142
Figure 124.	Power Generation Fractions wrt Rotation Speed for Traversing Rate of 1 ipm	142
Figure 125.	Power Generation Fractions wrt Rotation Speed for Traversing Rate of 5 ipm	143
Figure 126.	Power Generation Fractions wrt Rotation Speed for Traversing Rate of 10 ipm	143
Figure 127.	Power Generation Fractions wrt Rotation Speed for Traversing Rate of 20 ipm	144
Figure 128.	Temperature profiles of 1000 rpm 5 ipm simulation at $y=1.5$ cm	145
Figure 129.	Rosenthal's 3D approximation for $Q=1.902$ kW at $y=1.5$ cm	146
Figure 130.	Comparison of modified Rosenthal's 3D solution.....	147

LIST OF TABLES

Table 1.	Average composition (wt.%) of UNS C95800 NAB & Research Material (adapted from [Ref. 11])	6
Table 2.	Chemical Analysis of Phases Present in NAB (adapted from [Ref. 15,16])	9
Table 3.	NAB values for Johnson-Cook formulation	19
Table 4.	Comparison of simulated peak temperatures to the microstructurally based estimated peak temperature seen in the SZ of the provided materials.....	20
Table 5.	CTH output compared to experimental data.....	21
Table 6.	Tool Specifications.	21
Table 7.	Variation of Parameters	23

THIS PAGE INTENTIONALLY LEFT BLANK

ACKNOWLEDGMENTS

The author would like to thank the Defense Advanced Research Projects Agency – Dr. Leo Christodoulou for their support of this research; Mr. Abe Askari, Mr. Alvin Monk and Mr. Chuck Kline at the Boeing – Bellevue Division for the modeling program and additional technical support. Also thanks to Mr. Murray Mahoney and his crew at the Rockwell Scientific Center, Thousand Oaks, CA for experimental data support and the chance to get a glimpse of future with a tour of their facility.

Special thanks to Professor Terry McNelley for sharing his knowledge; while somehow he remained patient and understanding through the entire learning process.

Special thanks to Professor Garth Hobson for his patience and help in interpreting coding and unix machine technical assistance.

Thanks to Ms Donna Burych and Dr. Peter Chu for their help with setup and maintenance of computing capabilities on the NPGS campus.

Thanks to Dr. Chanman Park, Dr. Keiichiro Oishi, and Dr. Alex Zhilyaev for providing technical assistance and keeping me focused on the goal.

Thanks to LCDR Brian Vasquez, LCDR Rob Williams and LT Frank Pierce for their devotion and work to the understanding of FSP.

To Colleen, Bethany, Ethan, Zachary and Hannah with love - Thank you so much your patience, and for handling all of the work that I laid on you during this journey; I couldn't have done it without your love and support.

THIS PAGE INTENTIONALLY LEFT BLANK

I. INTRODUCTION

A. OVERVIEW

The ability to form and improve material properties through thermal cycling and deformation by hotworking has long been recognized. The Japanese Samurai Swordmakers were masters at the art of hotworking and forming of steels into samurai swords. Even today the ‘art’ of manipulating the material properties of different metals is continuously changing and growing in response to a demanding world. The industry wants materials which are lighter and cheaper, as well as stronger and tougher than the predecessors.

Friction Stir Processing (FSP) is a newly developed technology that is gaining considerable attention and momentum in the industrial community. FSP is a fabrication method that significantly increases desirable material properties. FSP produces extreme deformation conditions and gradients in the material while maintaining the temperatures below the melting temperature of the metal. The lower temperature of this process creates less distortion and residual stresses than conventional fusion welding.

The development of FSP has followed largely an Edisonian approach. Today, development of such processes requires predictive models to fully realize process potential. With the advancements in computing capabilities and the increased availability of cheaper computers, a predictive model is necessary to fully understand the process. In turn, understanding is necessary to optimize and choose the processing parameters necessary to gain the desired material properties.

In a program funded by the Defense Advanced Research Projects Agency, research is being conducted at the Naval Postgraduate School in collaboration with other program participants. The aim is to provide key relationships among the processing parameters and the material properties, and to develop the predictive models necessary to help commercialize FSP. In particular, the goal of the present investigation is to develop the technique for use in the post processing of U.S. Navy propeller castings that utilized Nickel-Aluminum Bronze (NAB) material.

B. FRICTION STIR PROCESSING

Friction Stir Processing (FSP) is an extension of the solid-state joining process known as Friction Stir Welding (FSW) that was discovered and patented by The Welding Institute, Ltd., in 1991 [Ref. 1]. Several different alloys were investigated and the microstructural and mechanical characteristics realized in the FSW joints ultimately revealed that the process gave a highly refined and homogenized microstructure [Ref. 2-4]. The wrought condition produced by FSW lead to significant increases in material properties, namely the strength, toughness, ductility and resistance to fatigue and corrosion [Ref. 2,3].

FSP is a hotworking process in which extreme values of strain and strain-rate, as well as steep gradients in strain, strain-rate and temperature, exist within a small volume immediately adjacent to the tool shoulder and pin [Ref. 4]. This process is achieved by using a non-consumable tool that, simply stated, is rotated, plunged into the material and then traversed through it. Conventional fusion welding process parameters and material conditions are also used with FSP. Thus, FSP shares the concept of a “heat affected zone” (HAZ) wherein the material only undergoes a thermal cycle. However, FSP also has a region that undergoes localized hotworking as well as thermal cycling. This region has been termed the thermomechanically affected zone (TMAZ) [Ref. 4]. During FSP, the peak temperatures (T_{peak}) reach $> 0.9 T_{melt}$, though melting is not observed. Since the temperature of material is always less than T_{melt} , there is no fusion zone. In FSP the equivalent zone is termed the Stir Zone (SZ) or the ‘stir nugget’ [Ref. 1-4]. This is the region that incurs very large deformations and the highest temperatures. The FSP zones can be seen in the montage of micrographs in Figure 1. This montage shows a transverse section through unaffected base metal, the HAZ, TMAZ and SZ for material processed with a 13 mm pin tool. The tool axis is vertical and the tool motion is into the plane of the montage. The controlling process parameters and the terminology associated with FSP are illustrated in Figures 2 and 3, respectively.

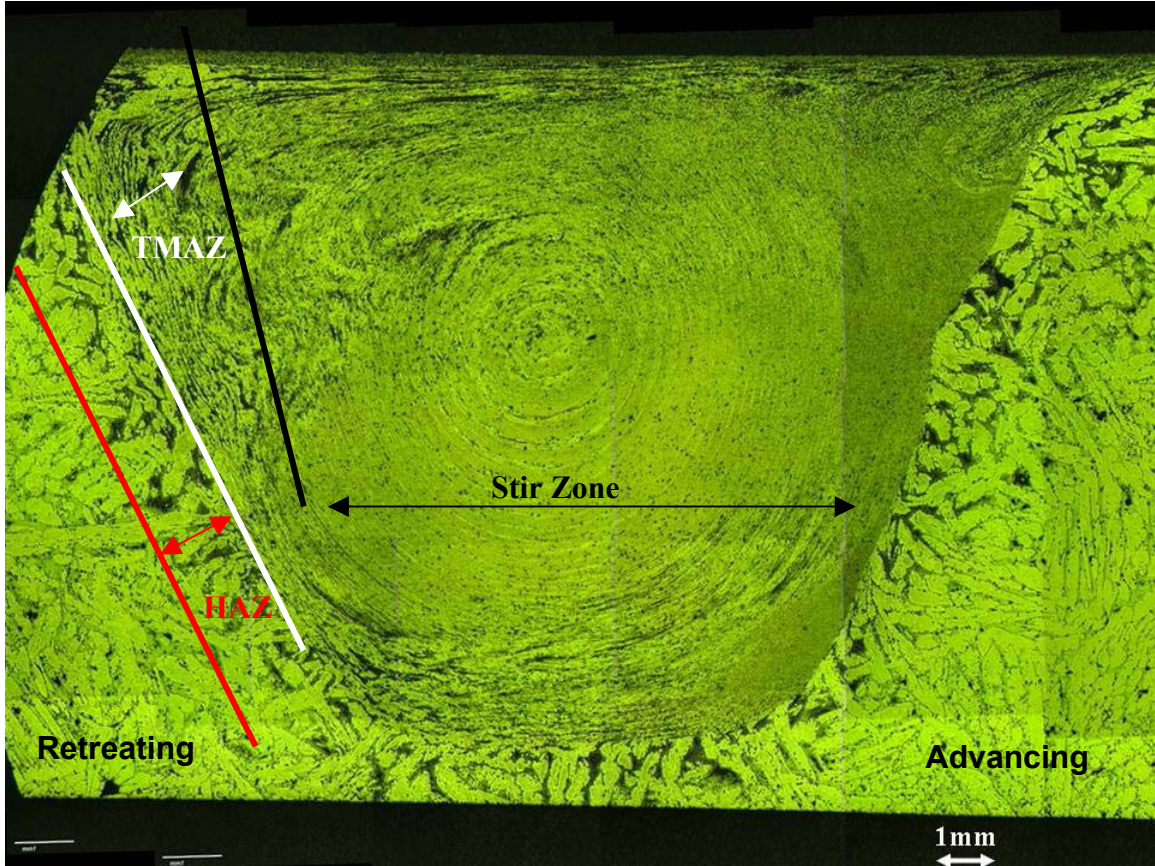


Figure 1. Example of FSP Region (courtesy of LCDR R. Williams, NPS)

The Stir Zone incurs the largest deformation and is at the highest temperatures. The TMAZ incurs a much lower deformation while undergoing a thermal cycle. The HAZ only undergoes thermal cycling due to the heat source traversing past it. The Advancing side is the side where the tool velocity is in the opposite direction of the traversing rate. The Retreating side is the side where the tool velocity is in the same direction as the traversing rate.

Figure 2 illustrates the individual steps in the friction stir process. Figure 2(a) shows that the tool is brought up to speed at a predetermined rotation rate (RPM) prior to penetration. Next, in Figure 2(b), the tool is moved toward the material until the tip of the pin is in contact with the material surface. This initial contact creates frictional heating that is a function of axial force and rotation rate. The axial force is held constant and results in thermal softening of the local material as the local temperature increases. The tool will eventually start to penetrate the material as it softens. The penetration will continue until the shoulder makes contact with the surface, as seen in Figure 2(c). The shoulder contact will provide frictional and adiabatic heating as well as restrict further

penetration of the tool. When the frictional and adiabatic heating has developed a sufficient temperature field, the tool is ready to be traversed, as seen in Figure 2(d), at the predetermined traversing rate (IPM).

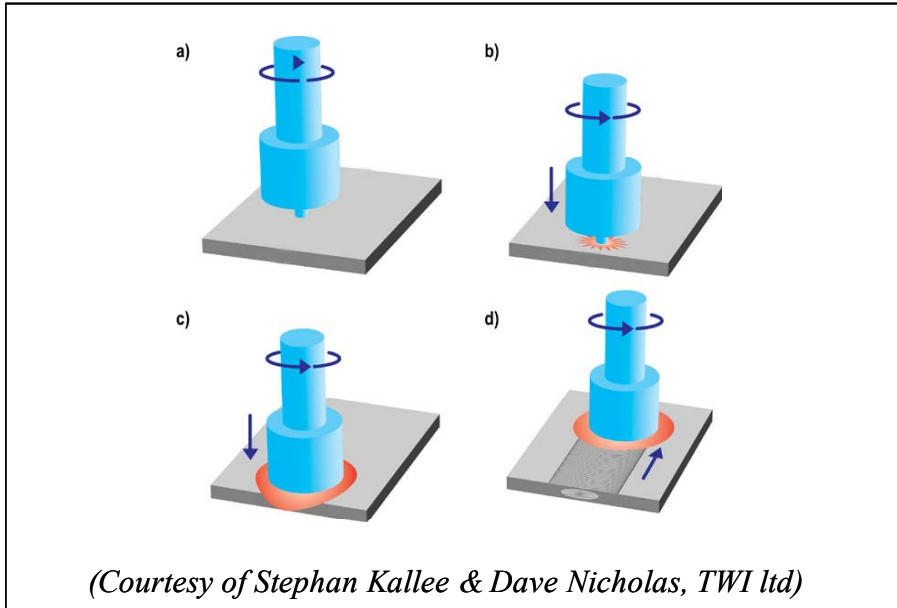


Figure 2. Friction Stir Process Illustration (adapted from [Ref. 1]) ;

(a.) Shows that the tool is brought up to speed at a predetermined rotation rate (RPM) prior to penetration. (b.) shows the tool plunging toward the material until the tip of the pin is in contact with the material surface. The tool will eventually start to penetrate the material as it softens. The penetration will continue until the shoulder makes contact, seen in (c.). When the frictional and adiabatic heating has developed a sufficient temperature field, the tool is ready to be traversed, as seen in (d.), at the predetermined traversing rate (IPM).

Figure 3 depicts FSP terminology used to describe the process. The tool geometry and special features will define the material flow characteristics and quality of the FSP. The primary characteristics of the tool are shoulder and pin diameters, pin depth, pin shape, thread geometry and scroll geometry. Much time and effort is being invested in designing specialized tools for enhancing the material and heat flow characteristics of the material in the SZ [Ref. 5,6]. The rotation direction defines the advancing and retreating sides of the “Stir Zone”. The advancing side is defined when the outer radius tool velocity is in the opposite direction as the travel/traversing speed. This combination results in the greatest relative speed between the tool and the material. The retreating side is defined when the outer radius tool velocity is in the same direction

as the travel/traversing speed. Rotation rate is variable and has units of revolutions per minute (RPM). The travel direction or traversing rate is defined as the direction and speed the rotational axis of the tool travels and is not restricted to straight lines. Rastering and multi-pass processes through a material is possible. The traversing rate of the tool has units of inches per minute (IPM). The axial force is applied uniaxially along the tool's rotational axis and nearly normal to the surface of the material. A tilt in the tool alignment is specified by the user and usually results in the tool being inclined opposite the travel direction. This is to minimize defect formation.

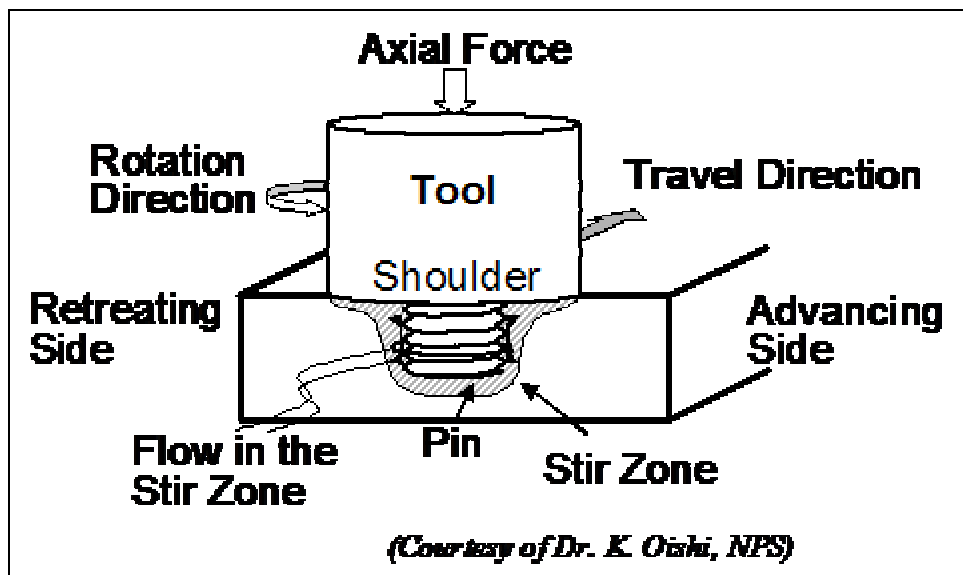


Figure 3. Friction Stir Terminology (diagram courtesy of Dr. K. Oishi, NPS)

This figure shows the relationship of the process parameters to the material. It also illustrates the geometric relationship of the SZ to the tool.

Friction Stir Processing is as unique in its process advantages as the process itself. Contrary to fusion welding, no filler material or shielding gasses are required for FSP or FSW. The design of the non-consumable tools used in the process is as varied as the imagination of the engineers who design them. Material preparation is essentially not required and light to moderate oxide layers are acceptable in most cases [Ref. 7]. FSP advantages include the absence of arc radiation and fume generation. However, the process does require robust mechanical fixturing. Further characterization of the SZ,

TMAZ, and HAZ various materials continue. The complex microstructural, thermomechanical and thermal histories require a systematic approach to understand the key relationships of process parameters and the resulting material microstructures and properties in the processed material. There have been many advances into the understanding of FSP and FSW since 1991; however, on-going research is needed to help refine modeling algorithms and process parameters relationships. These include rotation rate, traversing rate and tool geometry which is the work presented in this thesis.

C. NICKEL-ALUMINUM-BRONZE AND IT'S MICROSTRUCTURES

NAB, commonly termed “propeller bronze”, has become popular for use in the marine industry due to its unique combination of properties including moderate strength and toughness as well as excellent fatigue, corrosion, cavitation and erosion resistance [Ref. 8,9]. Propeller bronzes are Copper (Cu) based alloys with additions of Aluminum (Al), Nickel (Ni), Iron (Fe) and Manganese (Mn). The nominal alloy composition falls under the specification ASTM B 148-78 designation C95800 [Ref. 10]. Table 1 contains the nominal as well as the range of acceptable component composition of C95800 NAB.

Element	Cu	Al	Ni	Fe	Mn	Si	Pb
Min - Max	(min)79.0	8.5 – 9.5	4.0 – 5.0	3.5 – 4.5	0.8 – 1.5	0.10(max)	0.03(max)
Nominal	81	9	5	4	1	-	-

Table 1. Average composition (wt.%) of UNS C95800 NAB & Research Material
(adapted from [Ref. 11])

Due to their immense size and the casting process, the material property values of as-cast NAB differs greatly from wrought NAB. The massively thick sections in sand-cast propellers lead to extremely low cooling rates (10^{-3} C/s) in the thickest sections and somewhat faster cooling rates in the thinner sections [Ref. 12]. Temperature gradients experienced nominally are very shallow. Altogether, an as-cast propeller or propeller component may require more than a week to cool to ambient temperature. Many investigations have attributed grain coarsening due to the slow cooling rates as the main factor in the degradation in properties [Ref. 8,12]. Due to the wide variation in cooling rates and thickness, the NAB microstructure may exhibit segregation and gas evolution

resulting in porosity, leading to many months of post-cast processing to render the propellers fit for sea [Ref. 13]. Post-casting heat treatments have been devised to mitigate the microstructural changes and segregation effects. Heat treatments in general, alter the material's microstructure to gain more desirable properties. The heat treatment generally strengthens the material while lowering the overall ductility [Ref. 8]. The heat treatment process does not have the capability to mitigate any of the physical defects due to casting, such as porosity [Ref. 8,12]. An inspection, fusion weld repair and re-inspection procedure is currently being used for correction of such physical defects of sand-casting. The technique, known as "buttering", is used for correction of the porosity. "Buttering" can further introduce thermal stresses and microstructural changes [Ref. 13]. This repetitive method for cast porosity repair is very costly in time and material and up to 18 months time is required to produce a fit propeller.

In comparison, FSP using a rastering pattern may be used to selectively treat particular regions or the entire cast surface. The advantage of FSP is that the porosity is 'stirred' and completely eliminated while the process increases the material properties. The post-cast processing time has been projected to be reduced significantly.

1. NAB Phases

Review of the transformation products of NAB will prove useful upon investigation of key relationships between process parameters and material properties. Figure 4 illustrates the equilibrium and high-cooling-rate transformation products and temperatures for NAB. Following Figure 4 is a brief description of each phase.

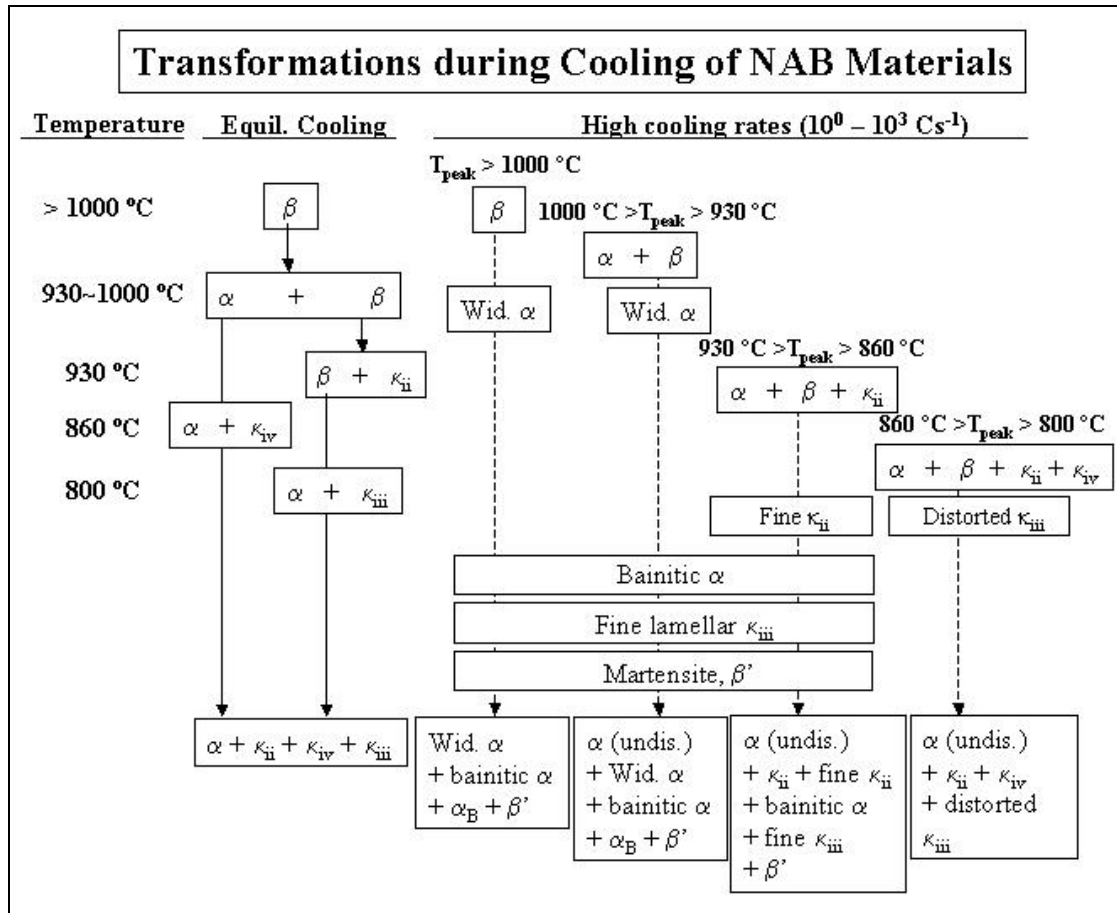


Figure 4. Transformation of NAB Phases during Cooling of NAB Materials
(courtesy of Prof. Terry McNelley, NPS)

2. Beta (β) and Retained-Beta (β')Phases

The β phase is a high-temperature solid-solution phase in NAB. The β has a BCC structure at high temperatures with a lattice parameter equal to 0.3568 nm. However, β is not a stable phase at ambient temperature. Various β -transformation products form as a function of cooling rate. These products of β are summarized in Figure 4. These products are alpha (α) and kappa (κ) phases, which will be explained in the following sections.

The propeller casting results in equilibrium cooling and therefore follows the left hand side of Figure 4. These very slow cooling rates result in virtually all of the β transforming into α and various κ products.

Conventional fusion welding and FSP result in relatively larger cooling rates and these processes therefore follow the right hand side of Figure 4. Dependent upon the T_{peak} attained and the cooling rate, the microstructure will resolve into more complex component mixtures that include primary α and β transformation products; the latter includes α in a Widmanst  tten morphology, β in coarse/fine bainitic structures or β in its martensitic form. High density precipitates throughout the β region form nucleation sites for the formation of alpha [Ref 14]. The β compositions vary dependent on the amount of alloying constituents that are consumed while forming other phases and/or precipitates/particles; in general the composition measured by chemical analyses reported are listed in Table 2.

Phase	Cu	Al	Ni	Fe	Mn
Alpha	85.4	8.3	2.5	2.7	1.4
Beta	85.2	8.7	3.5	1.6	1
Kappa I	8.4	17.5	3	65.6	2.7
Kappa II	9.3	22.2	6.6	53	1.9
Kappa III	12	44.3	31.5	10.2	1.6
Kappa IV	2	18.9	6.1	63.8	2.1

Table 2. Chemical Analysis of Phases Present in NAB (adapted from [Ref. 15,16])

3. Alpha (α) Phase

The α phase is the ambient-temperature terminal solid-solution of NAB. Alpha has an FCC lattice structure with a lattice parameter of 0.364 nm [Ref. 17]. The α phase is generally the first phase to form during cooling of β . This is independent of the cooling rate. The temperature at which the α phase becomes observable is highly dependent on alloy composition [Ref. 14,15,18]. Microstructurally-derived transition temperatures estimated in this laboratory are indicated on Figure 4. The composition of the alpha phase is given in Table 2. Diffusion of elements occurs during the cooling process at the α/β boundaries and within β to form other phases.

4. Kappa Phases (κ)

There are four distinctly different κ phases that are observable in NAB. All of these phases are stable at ambient temperature. The κ phases form as a result of the decreasing solubility of Fe, Al, and Ni resulting from the lower temperatures. These phases are involved in the subsequent transformation sequence of a selected NAB.

The first kappa phase (κ_I) will generally occur in NAB compositions where the Fe content is 5% or greater [Ref. 14] and is usually fully surrounded by alpha when present. The κ_I precipitates are mostly iron-rich compounds (Fe_3Al , FeAl) surrounding smaller Cu-rich particles. Composition is shown in Table 2 and the crystalline structure can vary (BCC or DO_3 or B2; the latter two are shown in Figure 5). The κ_I phase will exhibit a large, rosette shape 20 to 50 microns across and will etch gray in a micrograph [Ref 10].

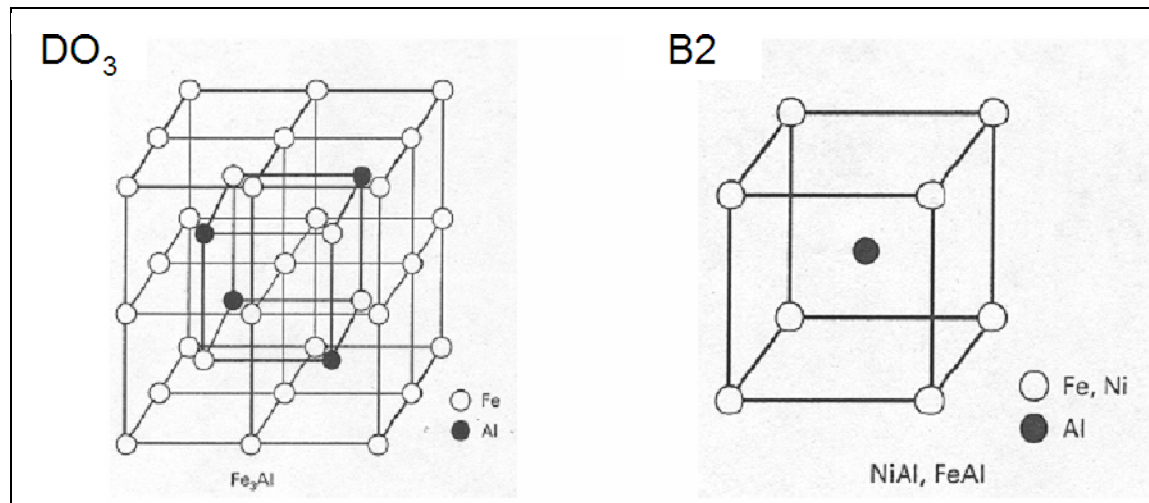


Figure 5. NAB Kappa Phase Structures (From Ref. 10)

The second kappa phase (κ_{II}) precipitate is Fe-rich (Fe_3Al) and has a DO_3 lattice structure shown in Figure 5 [Ref 14]. The α/β grain boundary provides the nucleation sites for the κ_{II} particles. The κ_{II} particles can be found surrounded by α phase at ambient temperature and are usually between 5 and 10 microns in diameter [Ref. 17]. It has been observed that the κ_{II} particles form in the same temperature region as Widmanstätten - α during the transformation of β . The approximate composition for this phase is in Table 2 and will also etch gray in a micrograph.

The third kappa phase (κ_{III}) precipitate is Ni-rich (NiAl) and has a B2 lattice structure seen in figure 5 [Ref. 17]. This phase does form above ~ 800 °C [Ref. 14]. The weight pct. of nickel in the NAB alloy will drive the formation of κ_{III} ; its approximate composition can also be found in Table 2. The κ_{III} phase can be take on a globular or lamellar form. The observation of the κ_{III} phase is difficult since the etching compound readily attacks this phase.

The fourth kappa phase (κ_{IV}) precipitate has an interatom spacing nearly identical to that of the κ_{II} phase and has a similar lattice structure. The κ_{IV} particles are usually found distributed throughout the α grains except in a band near the grain boundary, i.e., a “precipitate free zone” [Ref. 14,17]. The κ_{IV} composition is located in Table 2.

C. FRICTION STIR PROCESSING MODELING EFFORT

Since the inception of FSW, it was known that a predictive model would be required. An extensive modeling effort has been put forth to understand the flow characteristics and the thermal histories associated with friction stir. The FSP is known to generate heat in the workpiece by frictional heating at the tool/workpiece interface and by adiabatic heating due to the deformation of the material. The rotating tool, a 3D object, is plunged into the workpiece to produce the heat necessary for the deformation.

The initial efforts in modeling were developed to characterize the flow patterns developed by the tool [Ref. 19-24]. Even at the early stages in development, it was known that the flow patterns played a very important role in the overall quality of the weld. The understanding of the relationship of the tool design with the flow patterns lead to more emphasis being placed on the optimization of the tool design [Ref. 5,6]. As the tools became more complicated in shape and geometry, the models were still using the simplified flux or point source approach.

Chao and Qi, using a constant heat flux input from the tool shoulder/workpiece interface, developed a 3-dimensional heat transfer model. A trial and error procedure was employed until all of the estimated temperatures matched the experimental temperatures [Ref. 25]. An updated model by the same authors assumed that all heat was

generated by frictional heat at the tool/workpiece interface. The conclusion is drawn that only 5% of the heat generated is conducted away through the tool and the other 95% goes to the workpiece [Ref. 26].

Rosenthal's thin plate solution was employed by Russell and Shercliff to model the heat conduction [Ref. 27]. This model considered the heat source to be a point source on the surface of the workpiece. The question may be asked: What power should be used as an equivalent point source? An updated model was developed by Frigaard, Grong and Midling, which models the heat input as the frictional heat generated at the tool/workpiece interface but added a varying coefficient of friction based on the melting temperature of the material [Ref. 28]. Thermal softening was seen as an important contribution to the effectiveness of the process. Experimental results showed that the mechanical power to the tool is correlated to the frictional heat generated in the workpiece [Ref. 29]. The authors used this corrected power in their model.

A variety of fluid-dynamics-based modeling codes have been applied to further understand FSW [Ref. 30,31]. Fluid dynamic modeling codes are readily available and can show insight into flow, but cannot model the material properties of the material. Finite Element codes employing a moving heat source at the surface of the workpiece, dealt with heat conduction in the tool and workpiece [Ref. 27,30-37]. Finite Element codes are LaGrangian mesh codes such that work well for heat conduction or small deformations. For larger deformations the mesh gets severely distorted.

An analytical model was introduced by Schmidt, Hattel and Wert which developed the fraction of power generated on the shoulder, pin and tip of pin. They showed that the pin could produce as much as 20% of the power [Ref. 38]. The authors also introduced the notion of sticking, sliding or sticking/sliding tool/workpiece contact surface. All of the friction based models use a sliding contact condition. All numerical models thus far have ignored the heat generated by the pin and the adiabatic heating of the material. A recurring question: Is the contact condition really sliding?

The most prominent barrier in the modeling effort has been the modeling of FSW as if it were a conventional welding process. The modeling efforts thus far have considered FSW to involve a point source or a distributed source on the surface of the

workpiece. This approach is similar to Rosenthal's 3D approach. FSW, though also a joining process, is significantly different in that the source of heat is penetrating well into the material and is relatively large in size. Therefore the effective source of heat seen by the material just outside of the SZ is much closer and will therefore create a much more severe thermal cycle than previously expected. How much correlation can be drawn between FSW and conventional fusion welding? Our understanding of fusion welding should enhance our understanding of FSW, but it should not limit our ability to apply new theories.

One of the most recent and novel modeling efforts was undertaken by Askari, Silling, London and Mahoney [Ref. 7]. The model uses a finite volume method coupled with a hydro-code modeling program that employs an Eulerian mesh. This model forces a sticking contact condition and uses the Johnson-Cook plasticity model for thermo-viscoplastic response of ductile metals, therefore, incorporating thermal softening, strain-rate dependence and work hardening. The model allows the tool to be inserted into the workpiece and the deformation of the material around the rotating tool is developed. This model is based on the adiabatic heating due to the deformation of the material.

THIS PAGE INTENTIONALLY LEFT BLANK

II. OBJECTIVES OF THIS RESEARCH

A considerable effort has been directed toward prediction of the peak temperature attained by the material during FSP. This has included microstructure based estimates of the peak temperature in the material. Less effort has been directed toward understanding of the relationship of the tooling parameters and post-processing material properties. To date, a majority of the effort has been to refine simulations to more closely match the nominal variations of process parameters.

The objective of the current effort is to devise a parametric variation of the traversing rate and rotation rate that will include and extend beyond nominal experimental parameters. By such extension, key relationships between material properties and the selected process parameters may be established. The relationship between rotation rate and traversing rate, and thermal generated power and effective heat input will be scrutinized. Matlab (a robust data analysis program) will be used to analyze the raw output data to gain the correlation with the key FSP process parameters.

Conventional arc welding is very well known and is well documented. The process parameters, such as arc voltage, current, efficiency, power, heat input and welding speed have a well-defined relationship to the material properties and thermal cycles of the material near the fusion zone. Can these relationships of fusion welding be correlated to similar parameters in FSP? Can the mechanical power of the tool be correlated to the electrical power of conventional arc welding process? Can the traversing rate be correlated to the welding speed? Again, the CTH model, coordinated with the use of Matlab, will be exercised to evaluate the relationships of key parameters, and thus be able to determine if a correlation between FSP and fusion welding is possible.

THIS PAGE INTENTIONALLY LEFT BLANK

III. SIMULATION PROCEDURES AND TESTING

A. MODELING PROGRAM SELECTION

CTH, a Sandia National Laboratory – Los Alamos developed code, is a general, robust, hydro-code that was written specifically for applications in which the interval of time is on the order of milli- or microseconds. Collisions and explosions are processes that require a hydrocode model.

How does FSP correlate to the very short time processes for which CTH was written? To make CTH a viable model for FSP, Askari (Boeing Corp. – Bellevue) has modified the code to include an operator splitting strategy, that, when implemented, solves the steady-state FSP problem iteratively. In this approach, the model alternatively solves the steady-state continuity and momentum balance equations using CTH as a relaxation method and then solves the steady-state energy balance equation using a finite-difference convection-diffusion solver. This operator-splitting approach results in a great reduction of computing time. An initial prescribed temperature field is used; CTH then quickly converges to a steady-state velocity field. The velocity field is then used to compute the heat production rate due to plastic deformation in each cell. The velocity field plus the heat production rate are then used by the convection-diffusion solver to update the temperature field. This updated temperature field is then used to refine the velocity field and so forth until converging upon a solution [Ref. 7].

A scaling factor is also used in CTH to effectively ‘speed up’ the simulation. This is noted in the values for all of the rates or velocities. All of the parameters used in further calculations must be scaled back. CTH is Eulerian, meaning that the numerical mesh is fixed in space and the material flows through it. If a LaGrangian code were used, the extreme deformation would distort and entangle the mesh. Due to the extreme deformations produced in this process, the Eulerian code has a distinct advantage [Ref. 7].

The modified CTH code is restricted to generating a mesh with a rectangular geometry. The cell spacing of the mesh may vary over the region modeled. The advantage of varying the size of each cell is that a finer mesh may be incorporated to

enhance the model in higher gradient regimes and a coarser mesh may be incorporated where the gradients are more shallow. Since the material is moving through the mesh, the requirement for the mesh to match the measurements of the material is negated. Partially filled, empty cells or cells with multiple materials are handled easily by CTH.

The Eulerian code also allows the requirement for generating a mesh for the tool to be negated. Since the mesh can be filled with multiple materials, the introduction of the rigid tool material requires only that it be inserted into the appropriate cells. The tool is then treated as a rigid object rotating about a fixed axis at a specified rotation rate. The specific tool design parameters can be easily controlled and changed. The motion of the tool is easily calculated by using classical dynamical theory. The backplate, or base, is also modeled as a rigid body, but its velocity is set to zero throughout [Ref. 7].

In the modified CTH code, the J_2 plasticity theory is used to model plastic deformation of the material. The associated flow rule is implemented numerically through radial return methods. CTH contains a collection of versatile constitutive models for the strength (flow stress) of metals and other solids under a wide range of strain, strain-rate and temperature [Ref. 7].

CTH models the full three-dimensional equations of continuity, momentum balance and energy balance. A non-slipping (100% sticking) condition between the material and the tool is used in the model. During steady state FSP, the thermally softened material cannot sustain the frictional forces produced at the tool/material interface and will therefore undergo plastic deformation within its volume [Ref. 7].

CTH invokes adaptive mesh refinement if the cell size specified does not allow the program to accurately simulate the gradients calculated. The adaptive mesh refinement divides the cell into further subcells to break the gradient into more manageable sizes. This allows the simulator to control the variations within each cycle and reach a solution faster.

The material model currently used for NAB is elastic-plastic deformation theory incorporating work hardening, strain rate dependence and thermal softening. The Johnson-Cook plasticity model, utilized by the modified CTH code, contains a good approximation to the thermo-viscoplastic response of NAB [Ref. 7]. The Strain

Hardening Formulation, Thermal Softening Formulation and Strain Rate Sensitivity are given in equations 1, 2 and 3, respectively (courtesy of Askari, Boeing). Relevant Johnson-Cook formulation values for NAB are given in Table 3.

$$g(\varepsilon^p) = \begin{cases} \sigma_o \left(1 + \frac{\varepsilon^p}{\varepsilon_o^p}\right)^{1/n} & \text{if } \varepsilon^p < \varepsilon_{cut}^p \\ \sigma_o \left(1 + \frac{\varepsilon_{cut}^p}{\varepsilon_o^p}\right)^{1/n} & \text{if } \varepsilon^p > \varepsilon_{cut}^p \end{cases} \quad (1)$$

$$\Theta(T) = \begin{cases} c_o + c_1 T + c_2 T^2 + c_3 T^3 + c_4 T^4 + c_5 T^5 & \text{if } T < T_{cut} \\ \Theta(T_{cut}) - \frac{(T - T_{cut})}{(T_{melt} - T_{cut})} & \text{if } T \geq T_{cut} \end{cases} \quad (2)$$

$$\sigma_{eff} = \sigma_o \left(1 + \frac{\varepsilon^p}{\varepsilon_o^p}\right)^{1/n} \left(1 + \frac{\dot{\varepsilon}^p}{\dot{\varepsilon}_o^p}\right)^{1/m} \quad (3)$$

Symbol	Name	NAB value
ε_o^p	Plastic strain reference	0.002
ε_{cut}^p	Plastic strain cutoff	0.46
σ_o	Reference stress	8.44×10^8 dyne/cm ²
n	Sensitivity factor	2.363
c ₀	Temperature coefficient 0	1.0414
c ₁	Temperature coefficient 1	-1.7144×10^{-3}
c ₂	Temperature coefficient 2	1.1361×10^{-5}
c ₃	Temperature coefficient 3	-3.6926×10^{-8}
c ₄	Temperature coefficient 4	4.0437×10^{-11}
c ₅	Temperature coefficient 5	-1.3749×10^{-14}
T _{cut}	Cutoff Temperature	800 °C
T _{melt}	Melting Temperature	1060 °C
$d\varepsilon_o^p/dt$	Reference plastic strain rate	1 s ⁻¹
m	$= \partial\sigma/\partial(\text{d}\varepsilon/\text{dt})$	1/116

Table 3. NAB values for Johnson-Cook formulation

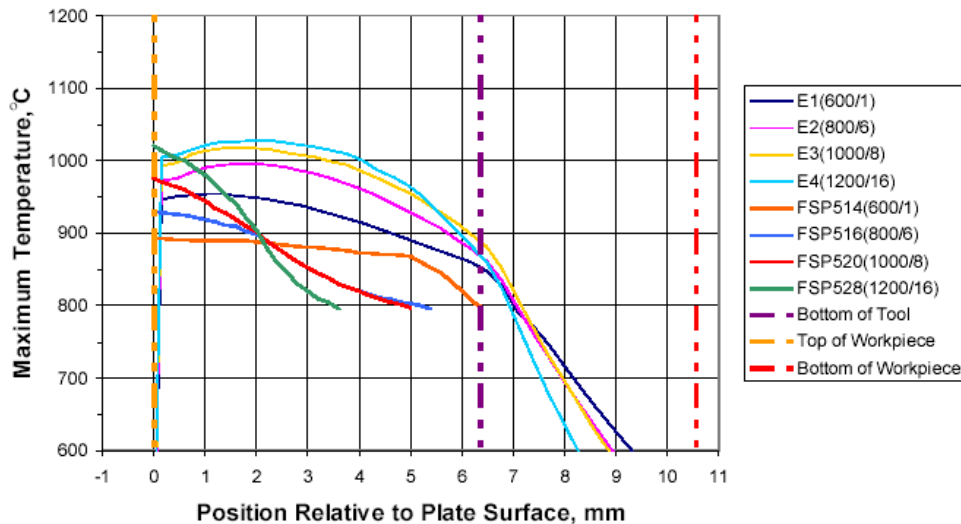
In FSP, it is easy to visualize an imaginary boundary between the material near the tool undergoing permanent plastic deformation and the material further from the tool which is only deforming elastically. The material in the elastic region may sustain a

significant load during the process. Therefore, the elastic region has significant effects on the stress fields as well as other material properties. It is thus easy to see why the material undergoing processing cannot be treated as a fluid [Ref. 7].

CTH is currently being utilized by Askari and the other program participants to model FSP. The simulated temperature profiles have been compared to the microstructurally based estimated temperature profiles derived from the processed material by McNelley and Oishi [Ref. 39]. CTH has proven to be a valid simulator within the normal operating bands of rotation rate, traversing rate and forces applied on the tool as seen in Table 4 and Figure 6.

Processing Condition (RPM / IPM)	T_{peak} , °C Estimated from microstructure	T_{peak} , °C Model
528 (1200/16)	1020	1029
520 (1000/8)	975	1018
516 (800/6)	930	995
514 (600/1)	890	954

Table 4. Comparison of simulated peak temperatures to the microstructurally based estimated peak temperature seen in the SZ of the provided materials.



* A. Askari, Boeing Inc., Seattle, WA

Figure 6. Comparison of simulated maximum temperature profiles to the microstructurally-based estimated maximum temperature profiles seen in the SZ, TMAZ and HAZ of the provided materials.

Table 5 shows the CTH output compared to experimental data (courtesy of Fuller, Rockwell Scientific). Mechanical power is calculated using tool torque and rotation rate.

	Torque (ft lbf) (N m)	Pin Depth (cm)	Rotation Rate (rpm) (rad/s)	Traversing Rate (ipm) (m/s)	Mechanical Power (kW)	Power Deposited (kW)
Rockwell Science	16 (21.69)	0.648	1000 (104.72)	4 (2.625e-4)	2.272	
NPS CTH simulation	(22.66)	0.531	1000 (104.72)	5 (3.281e-4)	2.374	1.902

Table 5. CTH output compared to experimental data

CTH is available for Unix, Linux and PC platforms. In the current investigation, the Unix version was employed to take advantage of available parallel processor capabilities. The FSP model utilizes 5.7 Gbytes of RAM/Swap Memory for each simulation, thereby limiting the available number of machines that could perform the simulation.

B. TOOL SELECTION AND GRID SETUP

The tool design chosen was of a standard size tool having a threaded, tapered pin. No extra scrolls or features were chosen due to the simplicity of this tool. Specifications are listed in Table 6 and the tool is shown in Figure 7.

Material	Shoulder Radius (cm)	Pin Top radius (cm)	Pin Tip radius (cm)	Pin Depth (cm)	Threads	Scrolls	Flats
Densimet	1.43	0.70	0.42	0.53	Yes	No	No

Table 6. Tool Specifications.



Figure 7. Standard FSP tool incorporating a threaded, tapered pin.

The chosen tool was used throughout the variation of process parameters for the sake of continuity so that changes in the dependent variables would be due only to the changes of the independent variables.

A variable grid increment was used due to the realization that majority of the deformation occurs immediately around the tool and therefore a coarser grid can be used away from it. A finer grid was chosen for the material around the pin due to the extreme deformation occurring and the large gradients in material properties and parameters. The axes are defined (Figure 8) according to the grid generated by CTHGEN (Figure 9).

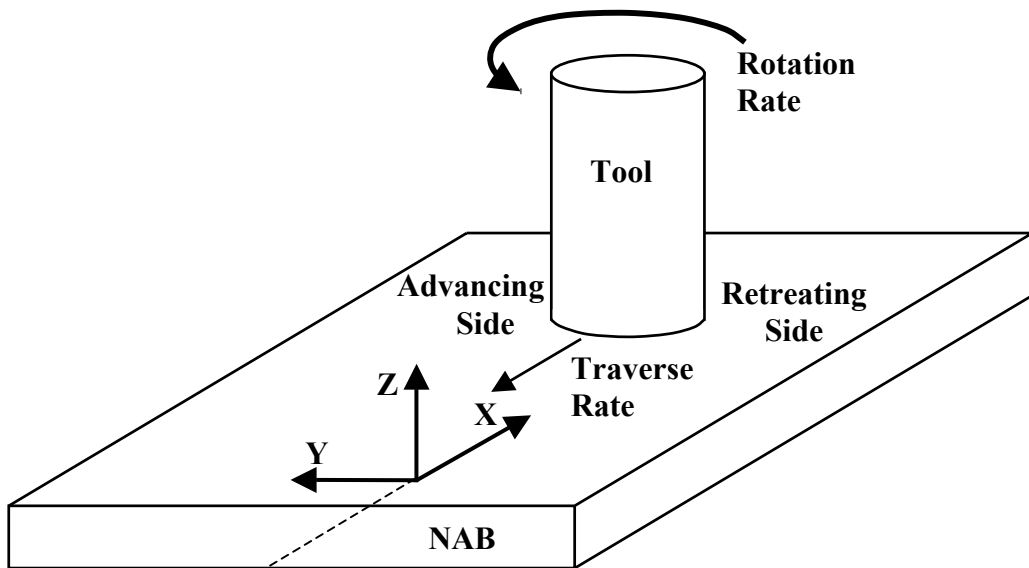


Figure 8. Configuration of Axes for simulations

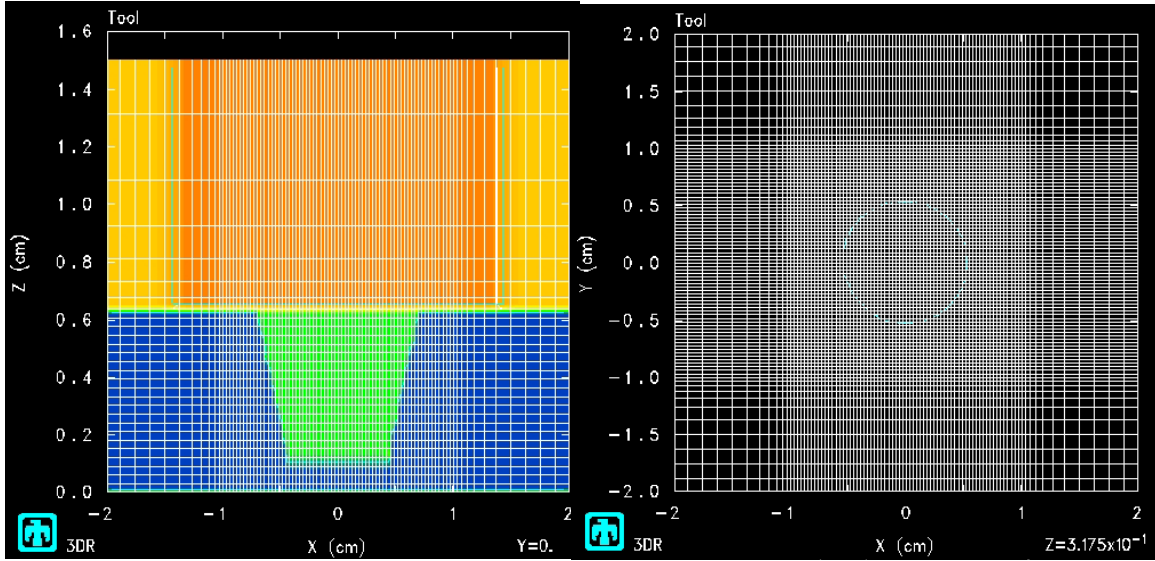


Figure 9. CTH grid for NAB material

C. PARAMETRIC VARIATION OF PROCESS PARAMETERS

Past modeling efforts have been focused on modeling within the nominal range of experimental process parameters. What does CTH tell us about FSP parameters when the variation of the process parameters go beyond the tested values? The values of the sets of parameters given in Table 7 were chosen to exercise CTH and to expand the envelope of parameters to allow for the relationship between the dependent and the independent variables to be realized.

IPM \ RPM	100	500	1000	2000	5000
1	X	X	X	X	X
5	X	X	X	X	X
10	X	X	X	X	X
20	X	X	X	X	X

Table 7. Variation of Parameters

D. DEFINING THE STIR ZONE VOLUME

On the advancing side of the tool, a clear delineation between the severely strained material in the SZ and the stressed, heat-treated material in the HAZ can be easily seen. On the retreating side of and beneath the tool, the delineation of the zones is much more difficult. For NAB, several SZ definitions will be discussed.

1. Temperature Based SZ Volume

From hot-rolling studies, NAB deforms easily above 800 °C without fracture or excessive cracking [Ref. 40,41]. Below 800 °C, the material deformed to only a limited extent prior to severe cracking and/or fracture. At and above 800 °C the κ_{iii} phase reverts to β and 800 °C is the equilibrium temperature for the $\beta \rightarrow \alpha + \kappa_{\text{iii}}$ eutectoid decomposition reaction during cooling. Above 900 °C, the prior κ_{ii} and κ_{iv} have reverted to $\alpha + \beta$. These transformations lead to microstructures that are very easily deformed to large strains without the detrimental effects found at temperatures lower than 800 °C [Ref. 39].

Therefore, limiting temperatures of either 800 °C or 900 °C were used to define the limits of the volume in the SZ. The 800 °C reflects deformation around the tool and sufficient stirring to form the fine equiaxed grain structures observed in the SZ. The limit of 900 °C shows the volume of material that has undergone a significant transformation back to β . If the NAB reaches temperatures of 1000 °C, all of the α and other phases have reverted to β .

2. Strain-Rate Based SZ Volume

The FSP is wholly based on the deformation of the material around the tool. Therefore, if the material exhibits a significant strain-rate then it must be considered part of the SZ. The obvious question would be, what is a significant strain-rate?

The nominal strain rate associated with the 800 °C limit was near 600 1/s. The nominal strain rate associated with the 900 °C limit was near 60,000 1/s. The inability to determine a clear limit of strain-rate led to the variation of limits approach. The limits were varied by factors of 10 starting at 0.1 up to 100,000 1/s.

E. THE CTH SIMULATION

1. Setup of Unix Machines

The generic Sandia National Laboratory's CTH program suite was loaded and built on an SGI Octane R10000 250 MHz single processor machine. CTH could also be built on the SGI Octane II R12000 300 MHz single processor machines. Many difficulties arose; CTH could not be built on the newer SGI Fuel R14000 600 MHz single processor machine. SGI help and the Unix machine administrators at NPS could not resolve this problem with CTH, thus initially limiting the study to the slower machines.

When a new revision of the Boeing-modified CTH program suite (FSW-CTH suite) was completed, Askari loaded and built the FSW-CTH program with help from the NPS administrators. Upon testing of the program using a trial input deck, it was discovered that a majority of the machines at NPS did not have the memory capabilities necessary to run the simulation. With special thanks to the Oceanography Department, one machine had enough RAM and swap memory to allow the testing of the FSW-CTH suite. Upon a successful completion of the trial run, NPS now had the capability to perform our own simulations. This machine was an SGI Octane II, R12000 300MHz four processor machine, but only two simulations could be run due to the memory constraints. The memory limitations (the need for 5.7 GB of memory for each simulation) greatly reduced the ability of NPS to perform simulations.

Upon further investigation in the capabilities of other research departments and with the help and persuasion of Ms. D. Burych, Dr. P. Chu, Oceanography, graciously allowed the author to add his profile to a personal research machine. This was an SGI-based server with 32 R12000, 300 MHz processors with 27 GB of RAM. This generosity by allowed the author to run four more simulations.

The next hurdle was the time for completion of the simulations. Though running six simulations simultaneously, it was taking 8 to 9 days to complete the necessary 3000 iterations. The reason was finally determined to be the time required to read and write the necessary files and data to the storage drive. The files and data were stored on a

server different than the machines running the simulations; therefore, the time necessary to complete each cycle was limited to the transfer rate of the information to and from the files.

2. FSW-CTH Suite Input

The FSW-CTH suite is comprised of four main components. CTHGEN is used to define the computational mesh, insert material into that mesh and define basic material properties. CTH integrates the problem through time. CTHPLT and HISPLT are the postprocessors used to view the output of CTH.

Once the necessary computing capabilities were acquired, the input decks used for each parametric variation needed to be changed to the proper parameters. The input deck for CTHGEN contains the necessary information to generate the desired mesh. The mesh grid dimensions and cell size variations are specified. The tool placement and design geometry is specified. The materials used and associated properties are specified. The placement of the material into the mesh is specified.

Since only the rotation rate and the traversing rate were varied, this lead to approximately 10 changes to the coding in the input deck necessary to ensure the proper alignment of variables.

3. FSW-CTH Steady State

Anytime during the simulation, HISPLT or CTHPLT can be employed to determine if the simulation has reached steady state. Since the temperature attained will determine the amount and ease of deformation, the parameter seen externally is torque on the tool. The x and y forces on the tool also will reach an equilibrium value that will tell of the temperature and deformation around the tool reaching steady state. These are the main parameters monitored in order to determine steady state.

Five tracer elements are placed into the material by specification in the input deck. The tracers record the cyclic history of all parameters of that cell. When the torque and the x force, y force and z force on the tool all reached a steady value, the temperature was then checked at these tracer elements to verify that it had reached a steady value with respect to iterations (shown by HISPLT as time). An example of the HISPLT output

showing torque, x and y forces and z force are shown in Figures 10, 11, and 12, respectively. The temperature histories are shown in Figure 13.

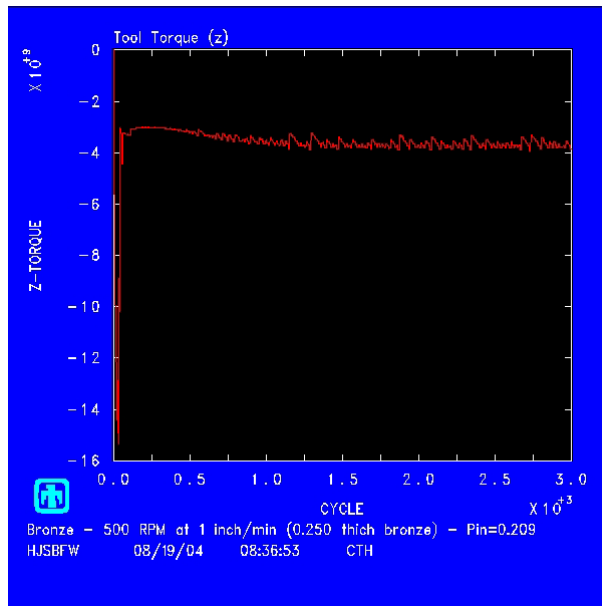


Figure 10. Output of HISPLT showing Tool Torque vs number of cycles.

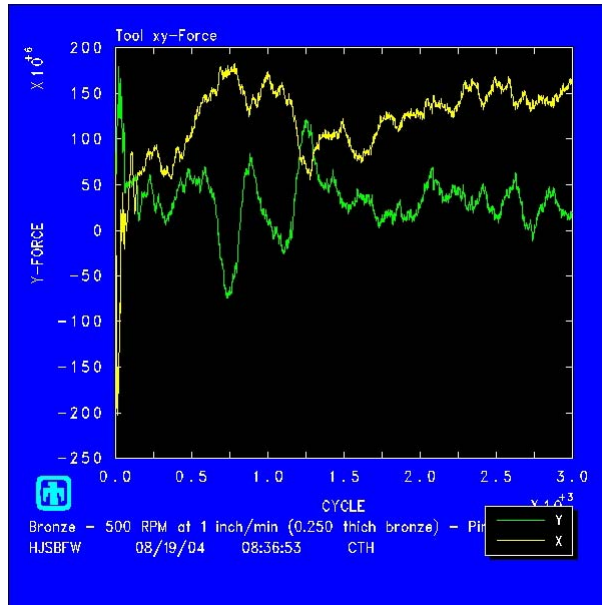


Figure 11. Output of HISPLT showing Tool x, y and z Forces vs number of cycles.

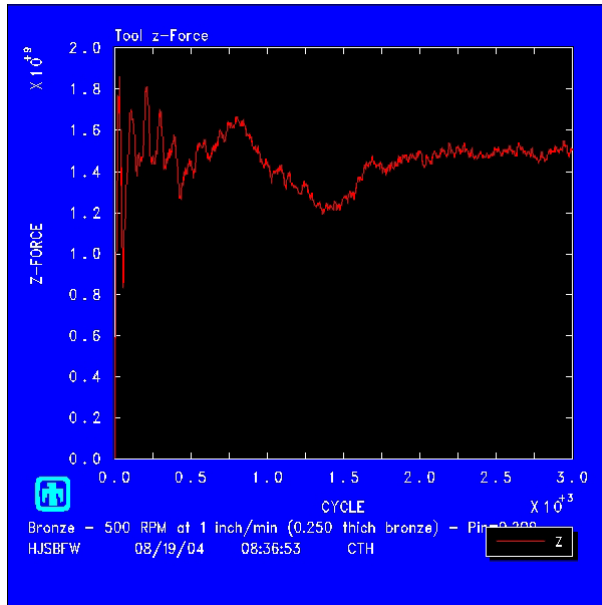


Figure 12. Output of HISPLT showing Tool z Force vs number of cycles.

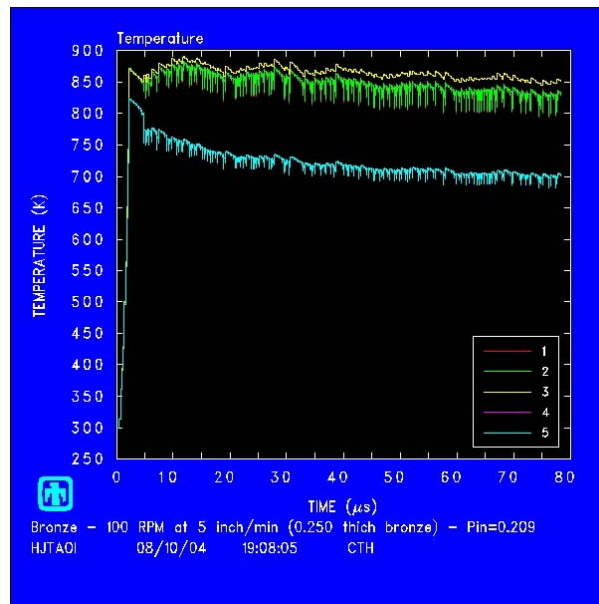


Figure 13. Output of HISPLT showing tracer temperatures vs time (cycles)

It is noteworthy that the torque and tracer temperatures are very nearly the same shape. Both of these parameters seemed to converge quickly while the forces on the tool seemed to take longer.

4. FSW-CTH Output

Once the simulation has converged, or reached 3000 iterations and stopped, the CTHPLT post-processor is engaged to analyze more closely the output data. Some output examples of the process parameters are shown in Figures 14 – 18.

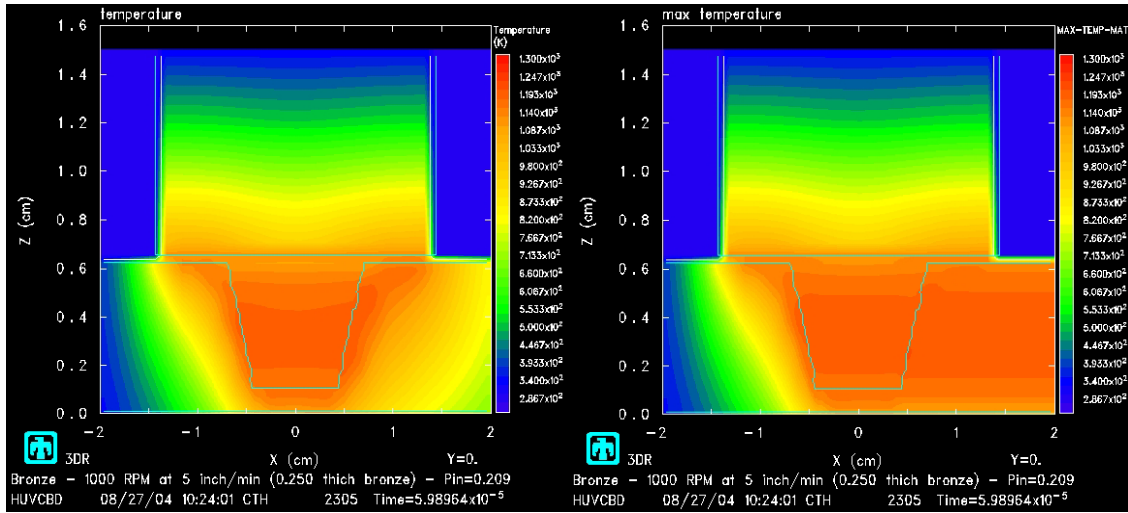


Figure 14. Output of CTHPLT showing temperature and max temperature on xz-plane

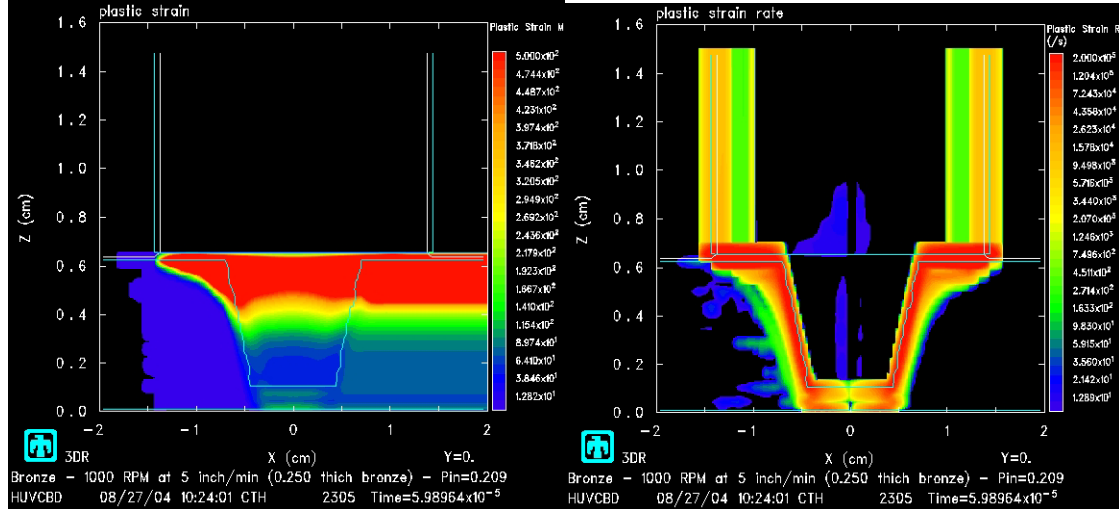


Figure 15. Output of CTHPLT showing strain and strain-rate on xz-plane

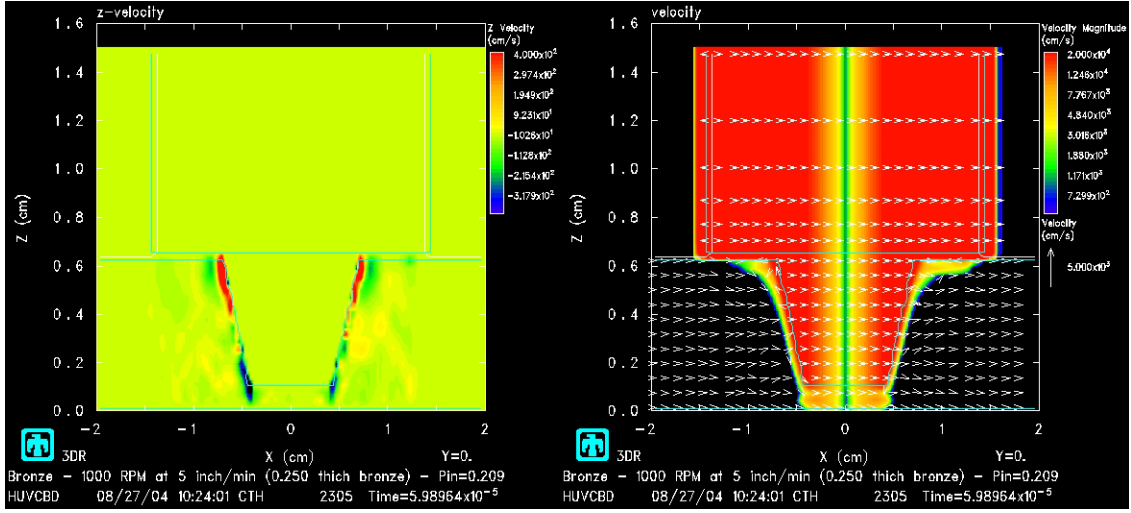


Figure 16. Output of CTHPLT showing z-velocity and velocity fields on xz-plane

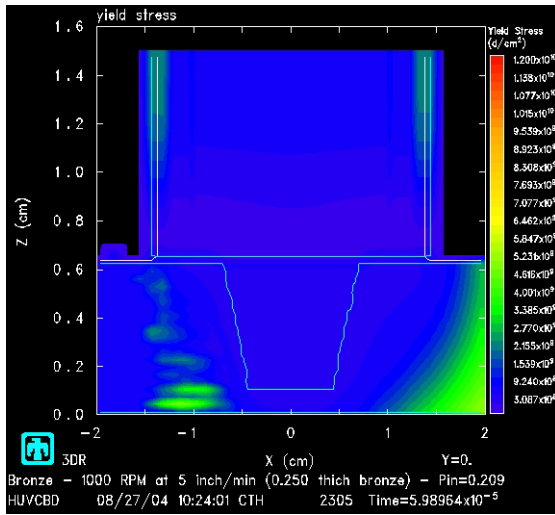


Figure 17. Output of CTHPLT showing stress on xz-plane

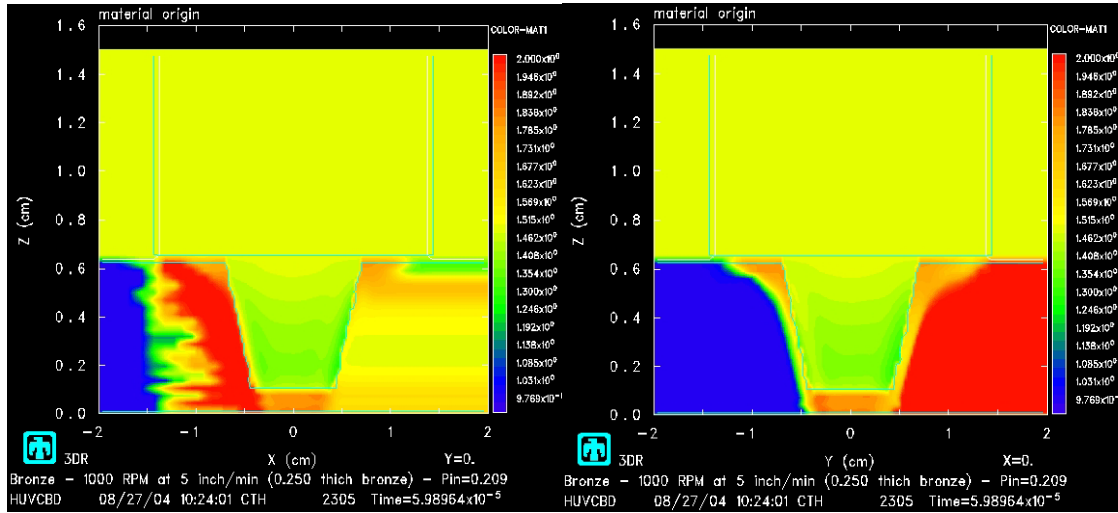


Figure 18. Output of CTHPLT showing quality of mixing on xz and yz-planes

CTHPLT can show any plane from the 3D model, the coordinates need only be specified in the input deck.

F. POST-PROCESSING THE DATA

The raw data from CTH was extracted using the algorithm Extract (courtesy of Askari - Boeing). The extracted file was written in a delimited format, which is easily read into Matlab, “The Language of Technical Computing” by The MathWorks, Inc. The 501622x9 vector of data was converted to a 151x151x22x6 4-dimensional matrix representing the 3-dimensional NAB material in the model. The fourth dimension will hold all of the parametric data. Matlab will then be used to further manipulate, analyze and interpret the data. The volumes, temperatures, strain-rates, generated thermal power, mechanical power, effective heat input and power fractions were analyzed.

Upon extraction from CTH, the grid is changed from a variable cell dimension to a fixed cells dimension by the algorithm Extract. Therefore a new cell size must be chosen to allow the detail of all the variable sized cells to be seen. The dimension chosen for the fixed would be the smallest of the variable cell sizes, namely 0.03 cm. Therefore the number of cells went from 104x94x37 in CTH to 151x151x22 in Matlab. The reduction of the z-direction cells accounts for only extracting the cells with NAB in them. The dimensions in CTH of the NAB was 5.86 cm x 4.56 cm x 0.635 cm, while the extracted dimensions were 4.5 cm x 4.5 cm x 0.635 cm centered on the tool axis. This allows the details of the process to be shown while reducing the storage requirements.

Upon compilation of the 4D matrix for each simulation, the trapezoidal rule will be invoked for integration purposes. The advantage of all cells having the same cell size is that during the integration process, the cell volume can be factored out of the calculation and therefore, the total sum, post-integration, is multiplied by the cell volume. Lastly the temperature profiles in the HAZ region will be compared to Rosenthal’s 3D approximation to determine if it is a good approximation for thermal cycling for FSP.

THIS PAGE INTENTIONALLY LEFT BLANK

IV. RESULTS AND DISCUSSION

What is the correct way to define SZ volume? What are the primary mechanisms that produce the material response delineation between the stressed HAZ and the high deformation SZ? What is the difference between the advancing and retreating sides? Due to the complexity of the process, only strain-rate and temperature dependence will be investigated in this study. Also, what are the relationships of key process parameters and generated thermal power, heat input and thermal cycles? Can these relationships be correlated to fusion welding?

The following discussion will be organized into the evaluation of the data pertaining to SZ volume, then key process parameter relationships and finally the applicability of applying Rosenthal's approach to FSP. For more detailed description of each section see Appendix A for CTHPLT output and Appendix B for Matlab output.

A. ANALYSIS OF THE SZ VOLUME BASED ON TEMPERATURE

NAB does not deform readily unless the material is above 800 °C [Ref. 40,41]. This temperature limit is the eutectoid temperature for the $\beta \rightarrow \alpha + \kappa_{\text{iii}}$ eutectoid decomposition reaction during cooling. As heating takes place to temperatures above this limit, the brittle $\alpha + \kappa_{\text{iii}}$ constituent will revert and form β . The resulting mixture of β and primary α apparently supports severe straining without failure [Ref. 39]. Figure 19 shows the temperature profiles of varying rotation rates for a given traversing rate of 5 inch/min.

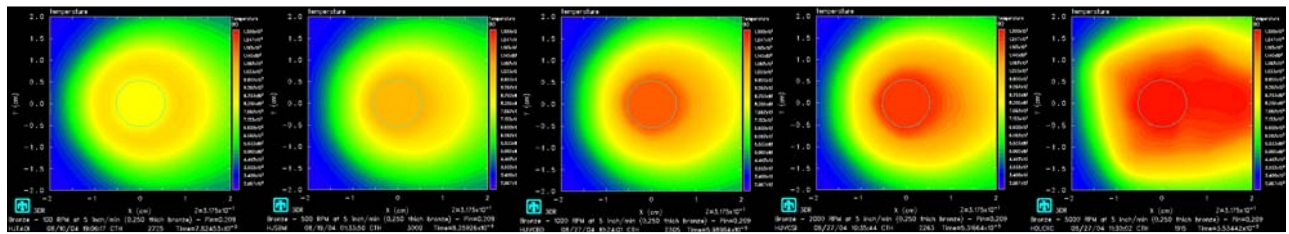


Figure 19. CTHPLT temperature output for Traversing Rate of 5 inch/min

Figure 19 illustrates the changes in magnitude of adiabatic heating in response to varying the rotation rate. The red indicates higher temperatures and thus the more adiabatic heating. It is observed that a temperature greater than 800 °C is not achieved until the rotation rate is at or above 1000 rev/min. It is also observed that a maximum temperature near 1000 °C is attained at 2000 rev/min and is approximately the same as the 5000 rev/min maximum temperature. Furthermore, although the temperatures in the higher rotation rates are nearly the same, the volume of material at those temperatures changes drastically. Figure 20 is a plot of the volume of material at or above 800 °C with respect to a varying rotation rate.

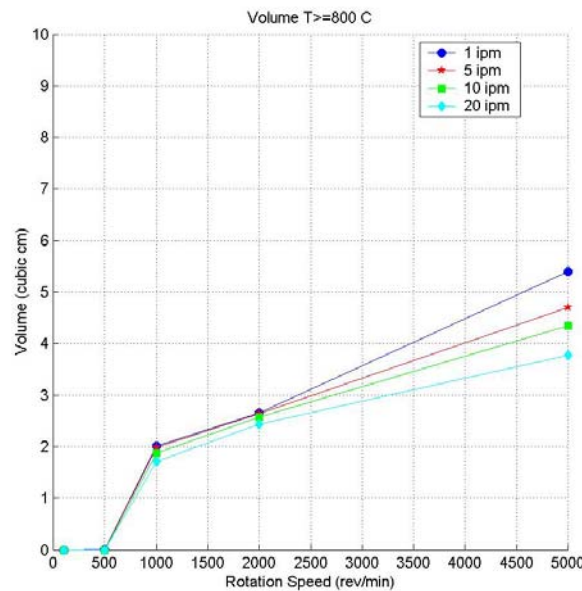


Figure 20. SZ Volume based on $T>800$ °C wrt Rotation Speed.

For all traversing rates, when the rotation rate is below 1000 rev/min, the process does not generate the energy needed to raise the temperature above the eutectoid temperature. Above 1000 rev/min, the volumes increase, as expected. It is interesting to note that for 1000 and 2000 rev/min, the volumes are relatively constant for all traversing rates. For 5000 rev/min, the variation in volume is attributable to the flux of material flowing past the tool. The higher the traversing rate, the higher flux of relatively cooler material passes the tool, thus not allowing the material to heat as much prior to entering

the SZ. This leads to an overall cooler material leading the tool, as seen in Figures 38, 54, 70, 86, and 102 (Appendix A). Figure 21 shows the volume of material at or above 900 °C with respect to a varying rotation rate.

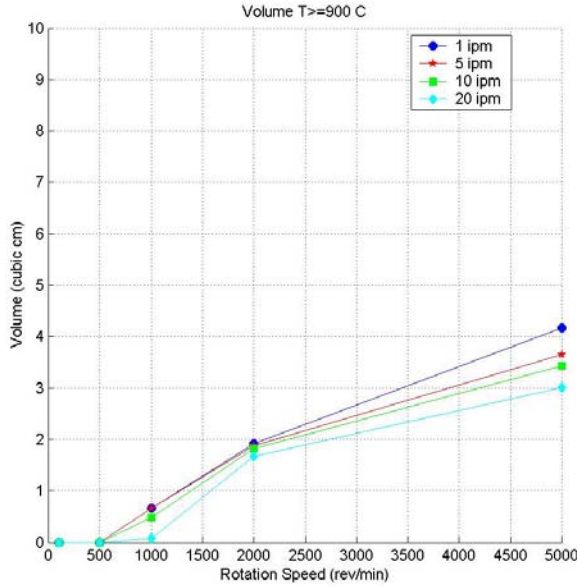


Figure 21. SZ Volume based on $T > 900$ °C wrt Rotation Speed.

The profiles observed are of the same shape as observed for a limit of 800 °C. The volume of material achieving 900 °C has a stronger dependence on rotation rate at 20 inch/min than the lower traversing rates. This is due again to the flux of material around the tool being able to remove the heat faster than the material is adiabatically heated, thus not being able to maintain 900 °C. The small volume that did exceed 900 °C was seen directly trailing the pin. It is also noteworthy that the volume attaining 900 °C is approximately 80% of the volume attaining 800 °C for all cases at or above 2000 rpm.

Is there an optimal set of process parameters? Is there a given TC that must be exceeded to produce a quality product? The observed effects of the traversing and rotation rates on the maximum temperature and the temperature distribution leads to the $TC > 100$ while rotation rate is at or above 1000 rev/min. If these limits are not met, a quality process will not be achieved.

B. ANALYSIS OF THE SZ VOLUME BASED ON STRAIN-RATE

Deformation occurs in the SZ. Strain-rate is a measure of how much deformation is occurring in the material at any given time. Is there a strain-rate limit associated with the higher deformation SZ? Figure 22 shows the strain-rate profiles of varying rotation rates for a given traversing rate of 5 inch/min.

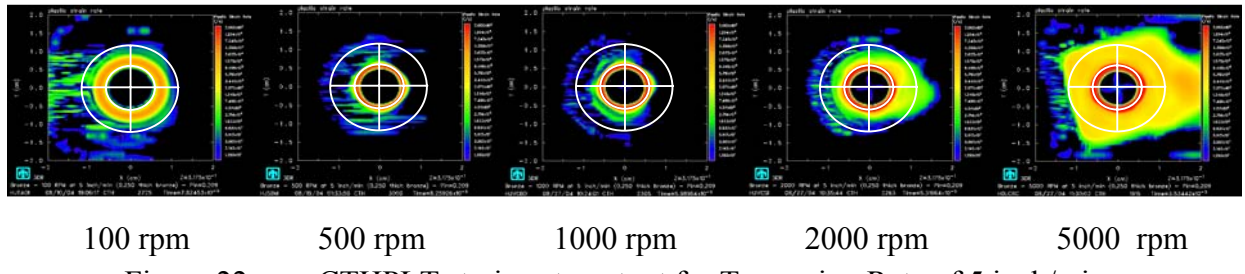


Figure 22. CTHPLT strain-rate output for Traversing Rate of 5 inch/min

For 100 rev/min, the magnitude of strain-rate at it's maximum is low compared to higher rotation rates, as also evidenced by the lower temperatures achieved in Figure 19. A lower temperature, and therefore with less thermal softening, is also seen in the wider volume of material experiences this strain-rate. The material just outside of this region is highly stressed, as seen in Figure 33 (Appendix A), and therefore has more influence on the material being deformed. There is a very large, lower strain-rate field leading and to the sides of the tool. This lower strain-rate is due to the tool not being capable of 'stirring' the material around the tool fast enough prior to the pin 'plowing' through it.

Revisiting the tool forces, the y-direction force was significant on the sets of parameters that were of the slower traversing rates. There seemed to be an optimum ratio of these tooling parameters. This ratio, termed as the 'Tool Coefficient' (TC), is defined as the rotation rate divided by the traversing rate. The physical meaning of the TC is the ability of the process to be able to stir the material as the tool moves through it.

For 500 and 1000 rev/min, the maximum strain-rates are very tight around the tool. The lower strain-rate fields are at a minimum. At and above 1000 rev/min, the strain-rate immediately around the tool shoulder and pin increases. This correlates with the higher temperatures seen in Figure 19. The higher temperatures lower the flow stress of the material and allows a larger volume to deform. Figure 23 shows the volume of material at or above a varying strain rate limit with respect to rotation rate.

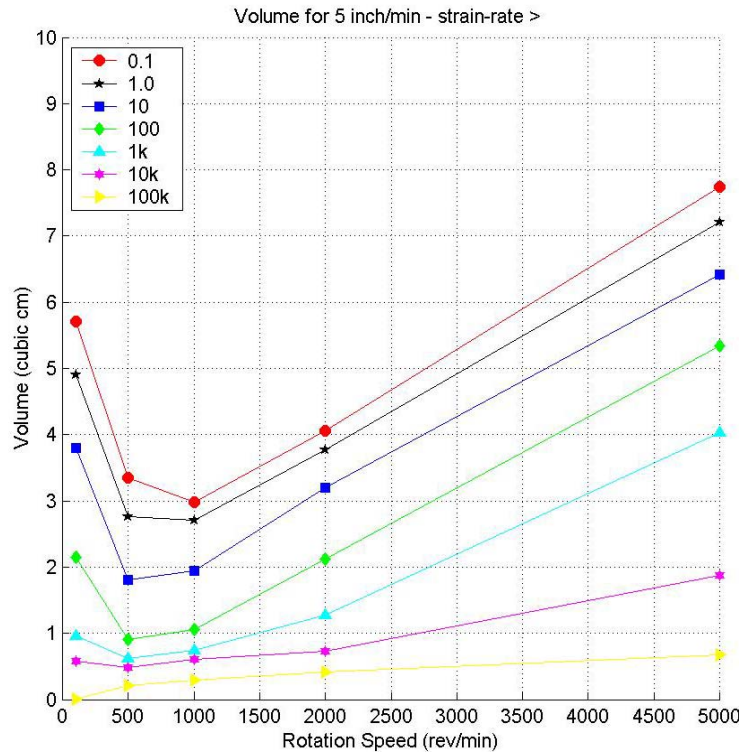


Figure 23. SZ Volume based on $\dot{\varepsilon}$ wrt Rotation Speed for Traversing Rate of 5 ipm.

The lower magnitude strain-rate fields dominate the high volumes at 100 rpm in all variations of traversing rate as seen in Figures 110-118 (Appendix B). The high volumes reflect the ‘plowing’ regime. The process does not have a high enough TC, and therefore does not have the capability to move the material around the tool sufficiently. Instead, excess material is essentially extruded around the stirring material and gets warm-worked in the process.

Around 1000 rpm, in all traversing rates, a minimum volume occurs for the straining material. The high strain-rate volumes immediately around the tool stay

constant, but the lower magnitude strain-rate fields are smaller. The dominance of the lower strain-rate fields due to the extrusion effect gives way to the increased volumes of deforming material due to the higher temperatures attained where it is easier for the material to deform. It appears that 1000 rev/min is the transition from the plowing regime to the heat generation regime. These simulations did not include a fracture criterion. From prior experimental hot rolling studies, NAB will likely fail during deformation at temperatures below 800 °C [Ref. 40,41] and so these lower temperature regimes would not be accessible experimentally. These simulations suggest a broad pattern of behavior in the form of a transition from plowing to stirring that might be expected in other materials as well.

C. ANALYSIS OF THE GENERATED THERMAL POWER

At the start of this investigation, the ability of CTH to produce a variable for the ‘heat generation rate’ was not known. Further studies using this variable should be done to corroborate this author’s results. The method of analyzing Generated Thermal Power used by the author was to calculate a function of stress times the strain-rate. Therefore, the comparison of stresses and strain-rates combined is important in the understanding of the adiabatic heating occurring in FSP. Which part of the tool is most important in the production of power? Does this vary with process parameters? Figure 24 shows the relative fraction of generated thermal power with respect to rotation rate for a given traversing rate of 5 inch/min.

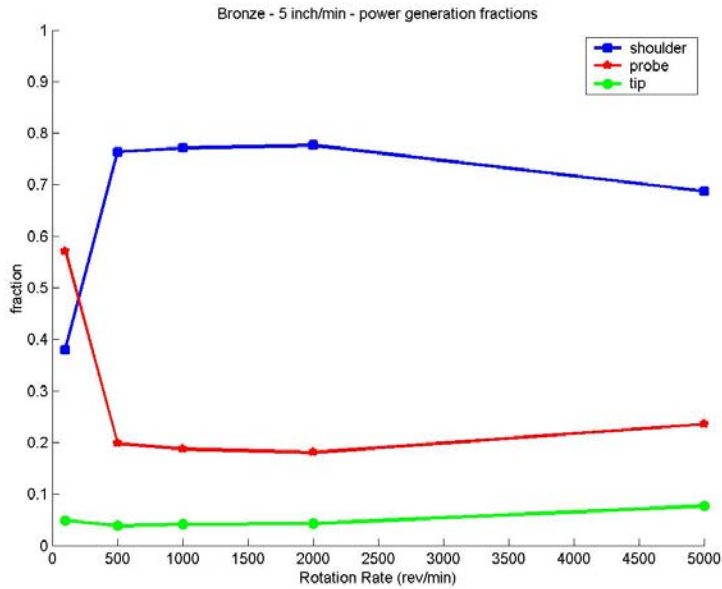


Figure 24. Power Generation Fractions wrt Rotation Rate for Traversing Rate of 5 ipm.

In the nominal range, the tool shoulder generates approximately 75 percent of the power while the pin generates nearly 20 percent. This estimate correlates with the prior work cited in Section I. At 100 rev/min, the plowing regime is dominant; therefore, the pin is the primary part of the tool involved in straining the workpiece and this is reflected in Figure 24.

Effective Heat Input is the ratio of generated power to traversing rate. Plotting the Heat Input and TC allows the effect of both process parameters to be analyzed at the same time. Figure 25 is the Effective Heat Input with respect to the Tool Coefficient.

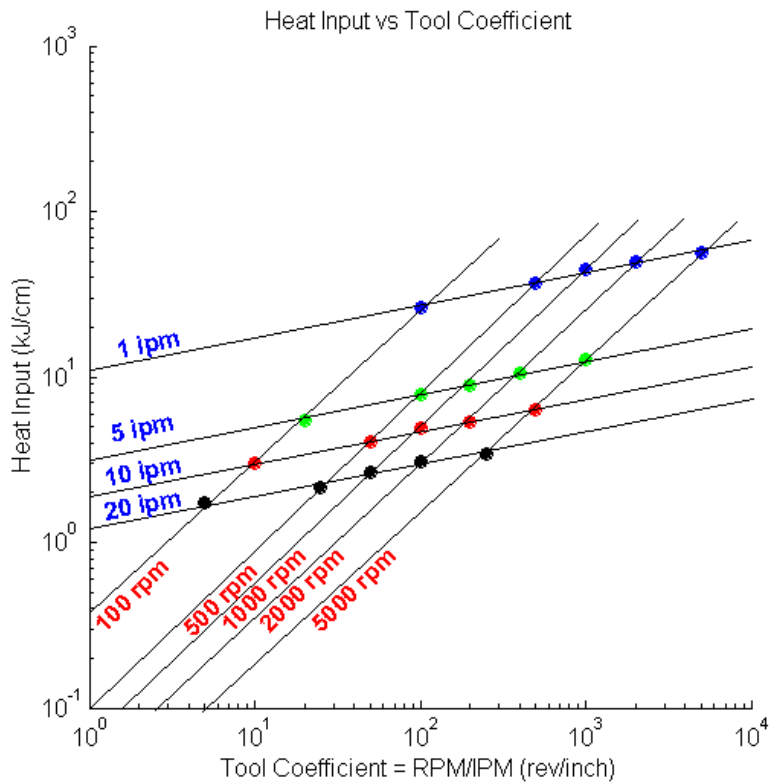


Figure 25. Effective Heat Input wrt Tool Coefficient.

An increase of the heat input with increasing rotation rate was expected although the form of the dependence on rotation rate (or TC) was not. The higher stress fields further from the tool, coupled with the lower strain-rate fields, generate a significant amount of heat. The plowing effect, though not dominant, is relevant in all processes.

Analyzing this data leads to a power law relationship that is intriguing.

$$\log(H) = 0.969 \log(TC) - 0.75 \log(RPM) - 0.8 \quad (4)$$

$$\Rightarrow Q(\text{kW}) = 9.3595 RPM^{0.219} IPM^{0.031} \quad (5)$$

Generalizing equation (5) results in a general form for the power:

$$Q(\text{kW}) = K (RPM)^{n_1} (IPM)^{n_2} \quad (6)$$

where K , n_1 and n_2 are material and process constants. Certainly, K will depend upon the tool and material properties. The coefficients n_1 and n_2 are probably related to

the material's flow characteristics, although neither corresponds directly to the rate sensitivity in the Johnson-Cook formulation used here. The generality of equation (6), and process and material factors involved in K , n_1 and n_2 , require further investigation.

The power in fusion welding is directly proportional to the voltage and the current applied. With exception to the similarity of the power being deposited into the material, a correlation of power and/or heat input of FSP to conventional fusion welding can not be drawn by this author without further testing and analysis.

D. THERMAL CYCLES USING ROSENTHAL'S 3D APPROXIMATION

The Rosenthal's 3D solution is based on several assumptions. The source is a point source moving on the surface of the material. The Rosenthal's approximation is only valid outside of the fusion zone. The power used in Rosenthal's approximation was 1902 W, correlating to the generated thermal power for 1000 rev/min at 5 inch/min. The material properties used were from Ref. 11 for C95800 NAB.

There was only a very poor correlation of Rosenthal's results to FSP simulations. Realizing that the source of the heat was not a point source nor on the surface, this author devised a varying correction that was subtracted from the radial distance to correlate to the distance to the edge of the stir zone. The modified Rosenthal's solution used the same information as previously, only the radial distance to the source was modified. Further work will need to be done on this problem. This will prove to be a difficult challenge due to the complex shape of the SZ.

THIS PAGE INTENTIONALLY LEFT BLANK

V. CONCLUSIONS AND RECOMMENDATIONS

Based on the simulation results the following conclusions are drawn:

1. There exists a Power Law relationship between Thermal Power and the Tool Parameters following the form of $Q = K (RPM)^{n_1} (IPM)^{n_2}$ where K , n_1 and n_2 are functions of material properties, tool design and process parameters.
2. There is an optimal region of process parameters, below which the detrimental effects of the plowing regime dominate. Above this region the higher volumes attaining higher temperatures correlate to lower cooling rates and a much larger TMAZ and HAZ. For this specific tool geometry and material, the TC should be between 200 to 500 rev/inch.
3. There is no direct correlation of power or heat input between FSP and conventional fusion welding due to physical and geometrical differences and complexities of friction stir processing.
4. Rosenthal's 3-dimensional approximation is not accurate in estimating the thermal cycling of the material immediately around the SZ.

The exercising of CTH has proven to be beneficial in understanding the relationship of the process parameters to the thermal power generated in the material. Further testing needs to be completed to determine the relationship of the power law constants to the material properties, tool design and process parameters. The thermal cycles of the material immediately surrounding the SZ is related to the power. Modification of Rosenthal's solution to include a 3D distributed power source is needed for an accurate estimation to the thermal cycles.

THIS PAGE INTENTIONALLY LEFT BLANK

APPENDIX A – CTHPLT OUTPUT

In Appendix A, the reader will find for each parametric variation, sets of pictures representing the temperature distribution, the strain distribution, the strain-rate distribution and the stress distribution within the material. Each set of picture shows the xy-plane in the lower left corner ($z=0.3175$ cm or half way through the material), the xz-plane is shown above the xy-plane ($y=0$ or through the center axis of the tool in the direction of traverse) and the yz-plane is shown to the right of the xy-plane ($x=0$ or perpendicular to the direction of traverse through the center axis of the tool).

The xy-plane picture depicts the tool moving to the left through the material or conversely the material is flowing around the stationary, rotating tool to the right. The tool is rotating counter-clockwise, therefore the advancing side is the top of the tool and the retreating side is the bottom of the tool.

The xz-plane picture shows the tool moving to the left through the material or conversely the material is flowing around the stationary, rotating tool to the right.

The reader must be extremely careful when, the yz-plane picture is as if the reader is looking at the tool going away from them. This gives the advancing side to the right and the retreating side to the left of the picture.

A. 100 RPM 1 IPM

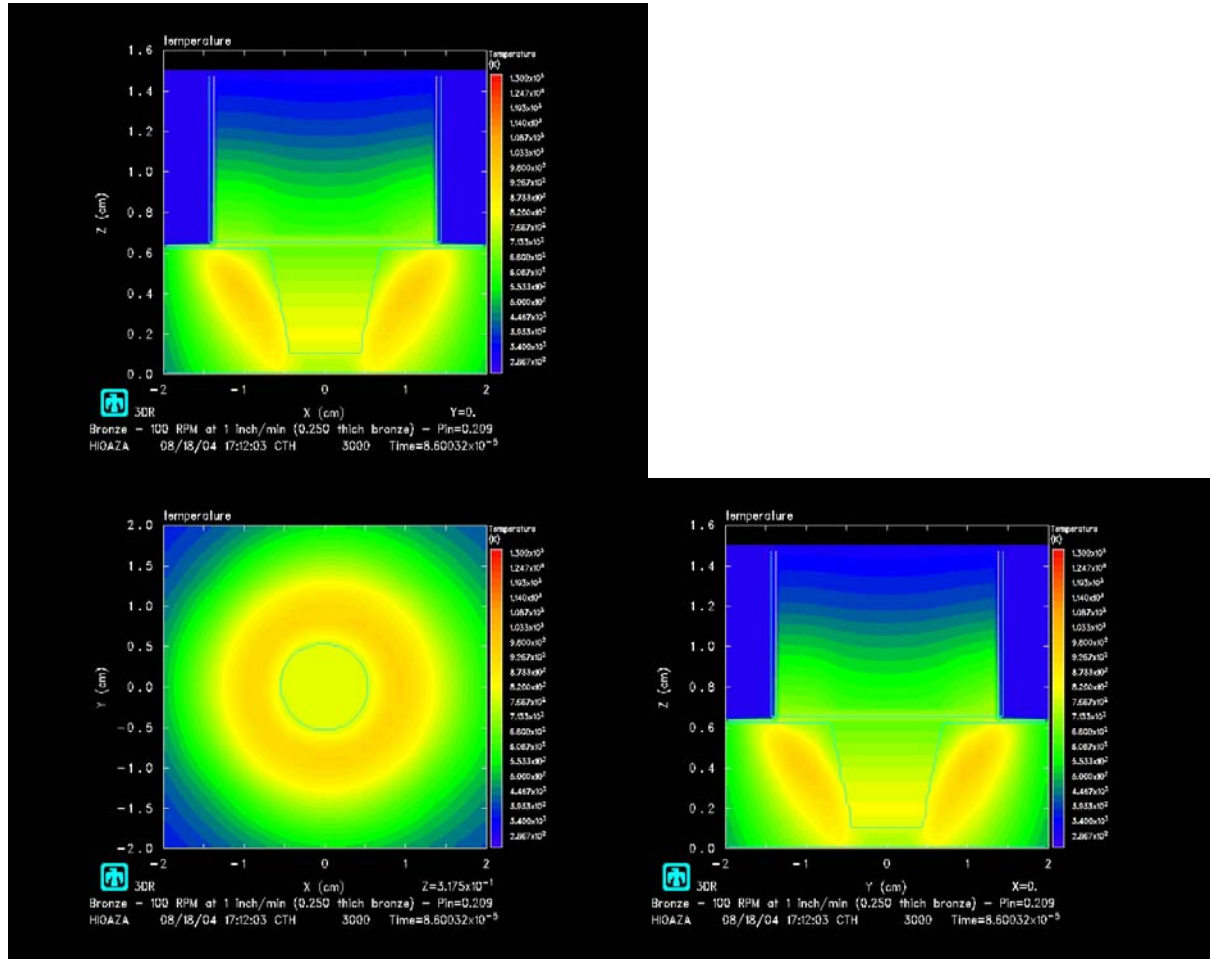


Figure 26. 100 rev/min 1 inch/min – Temperature distribution.

It is easy to see the volume of material in the corner of the tool where the shoulder and pin are connected. This volume is rotating with the tool not generating any heat, therefore this volume of material is only conducting the heat into the tool and up the shoulder. The capacity of the tool to conduct heat away is higher than the flux of the heat transferred into it. Therefore the temperature of the tool is lower than the material in deformation. It is also noteworthy to note that the maximum temperature attained is approximately 650 °C.

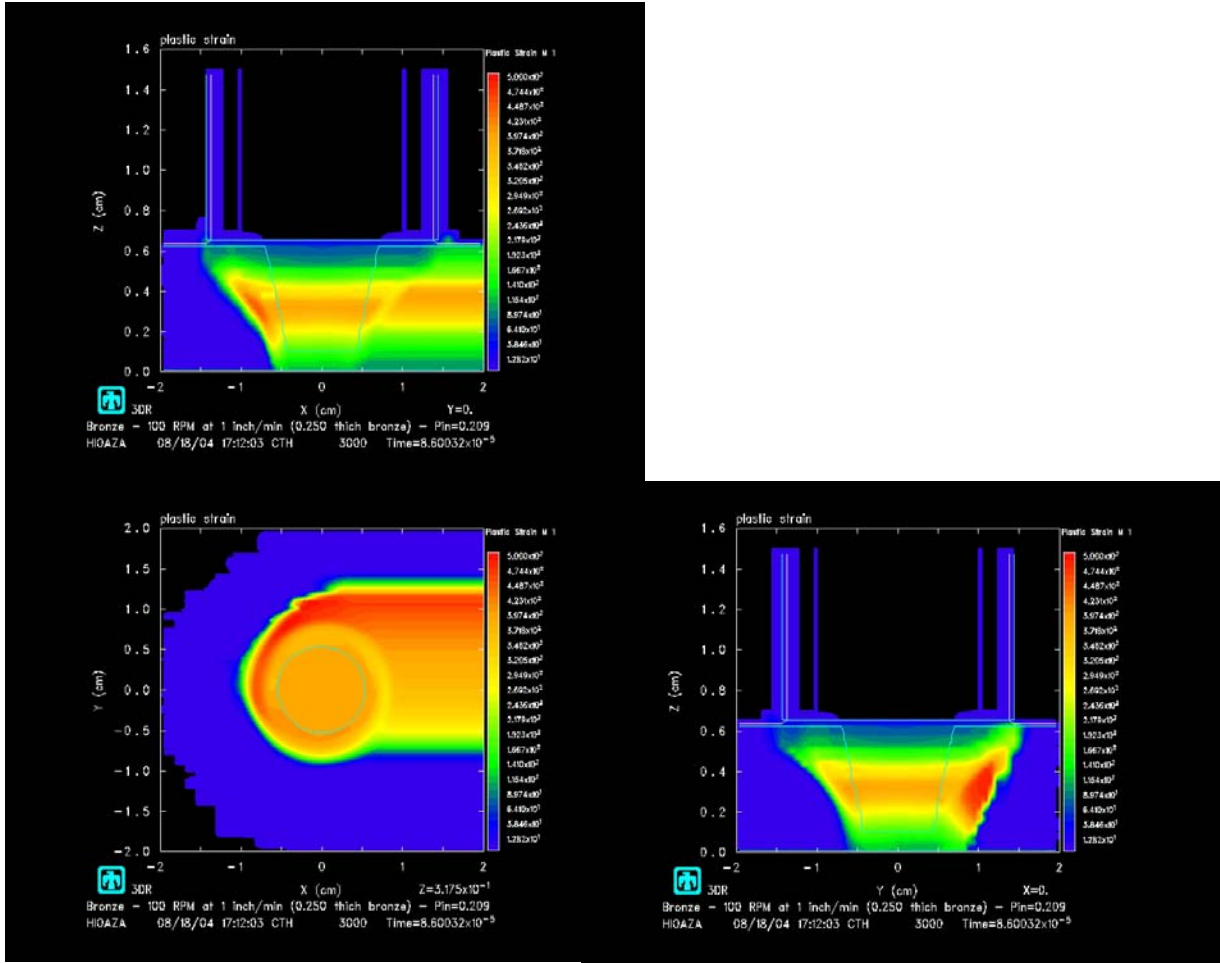


Figure 27. 100 rev/min 1 inch/min – Strain distribution.

It is easy to see that the maximum strains are attained a significant distance away from the tool/material interface. This correlates to the maximum temperature attained further away from the tool. The maximum strains are seen on the advancing side of the tool as expected. It is noteworthy to write that a large volume of low strains are occurring leading and to both sides of the tool.

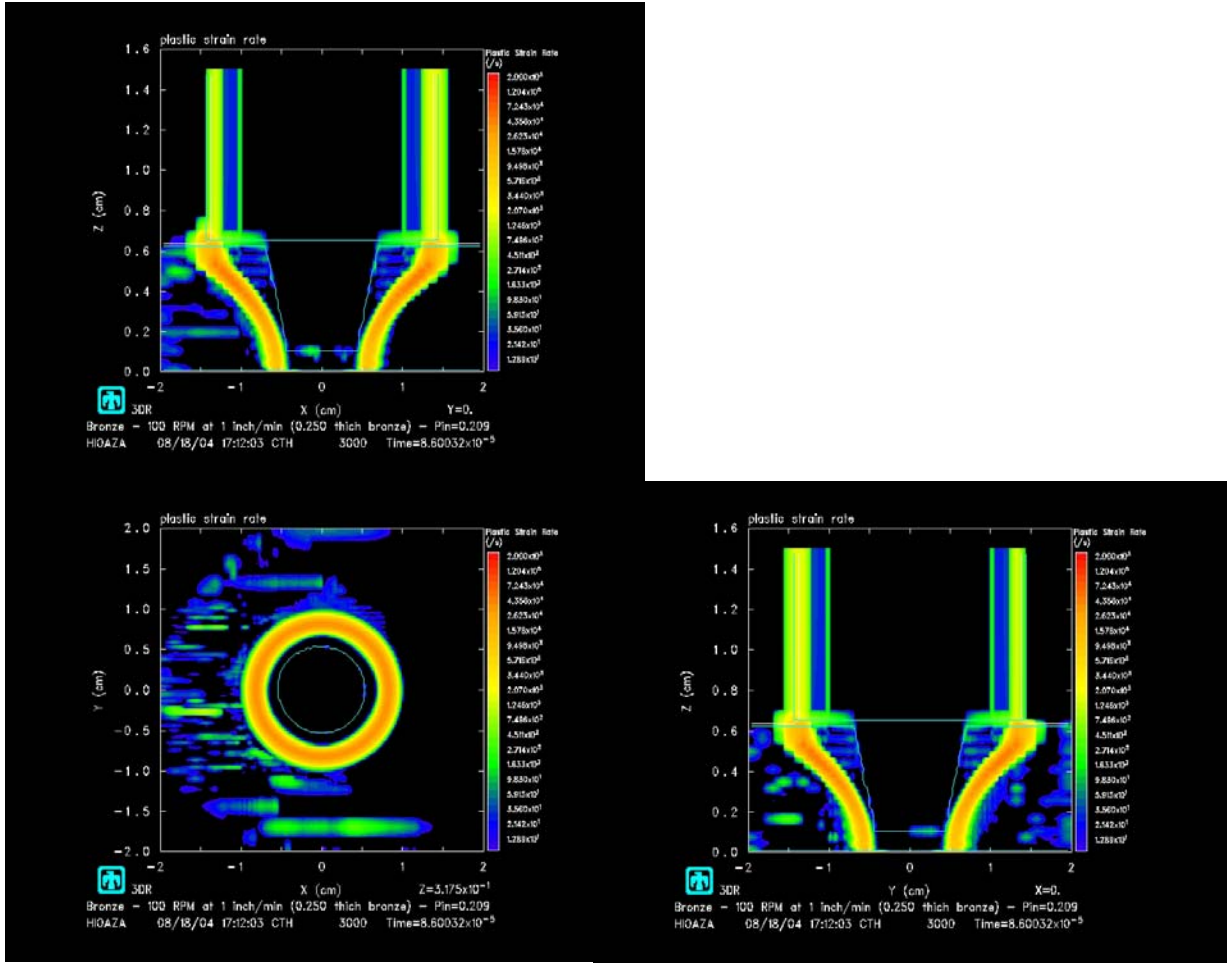


Figure 28. 100 rev/min 1 inch/min – Strain-rate distribution.

It is easy to see that the maximum strain-rates are attained a significant distance away from the tool/material interface. This correlates to the maximum temperature attained further away from the tool. The maximum strain-rates seem to not be affected by the position relative to the tool. It is also noteworthy of the large strain-rate field leading and to the side of the tool.

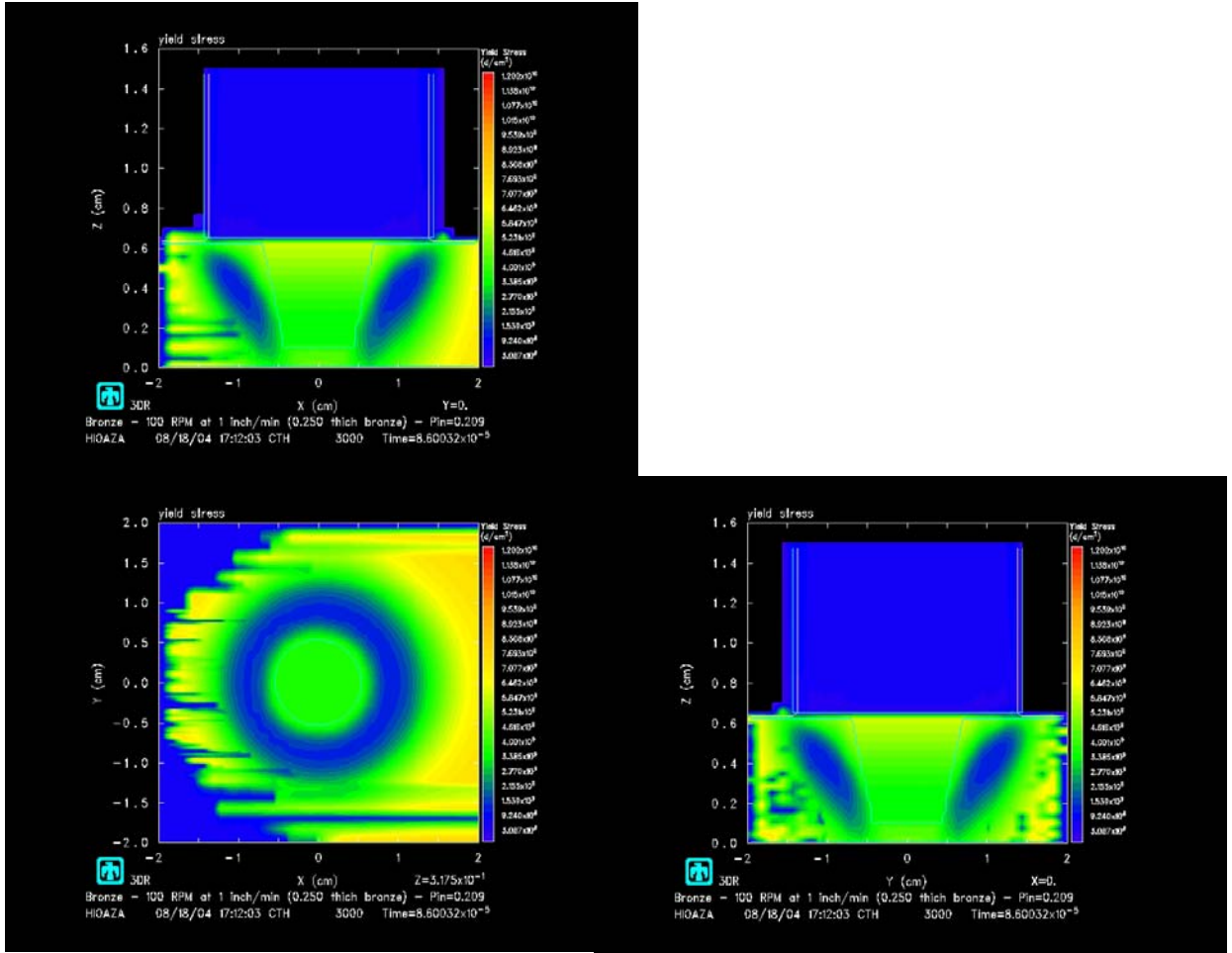


Figure 29. 100 rev/min 1 inch/min – Stress distribution.

It is easy to see that the minimum stress is attained a congruent to the higher temperatures, thus correlating with thermal softening. The maximum stress occurs further from the tool within the previously viewed strain-rate field of Figure 28. This picture also shows the residual stress field post processing.

B. 100 RPM 5 IPM

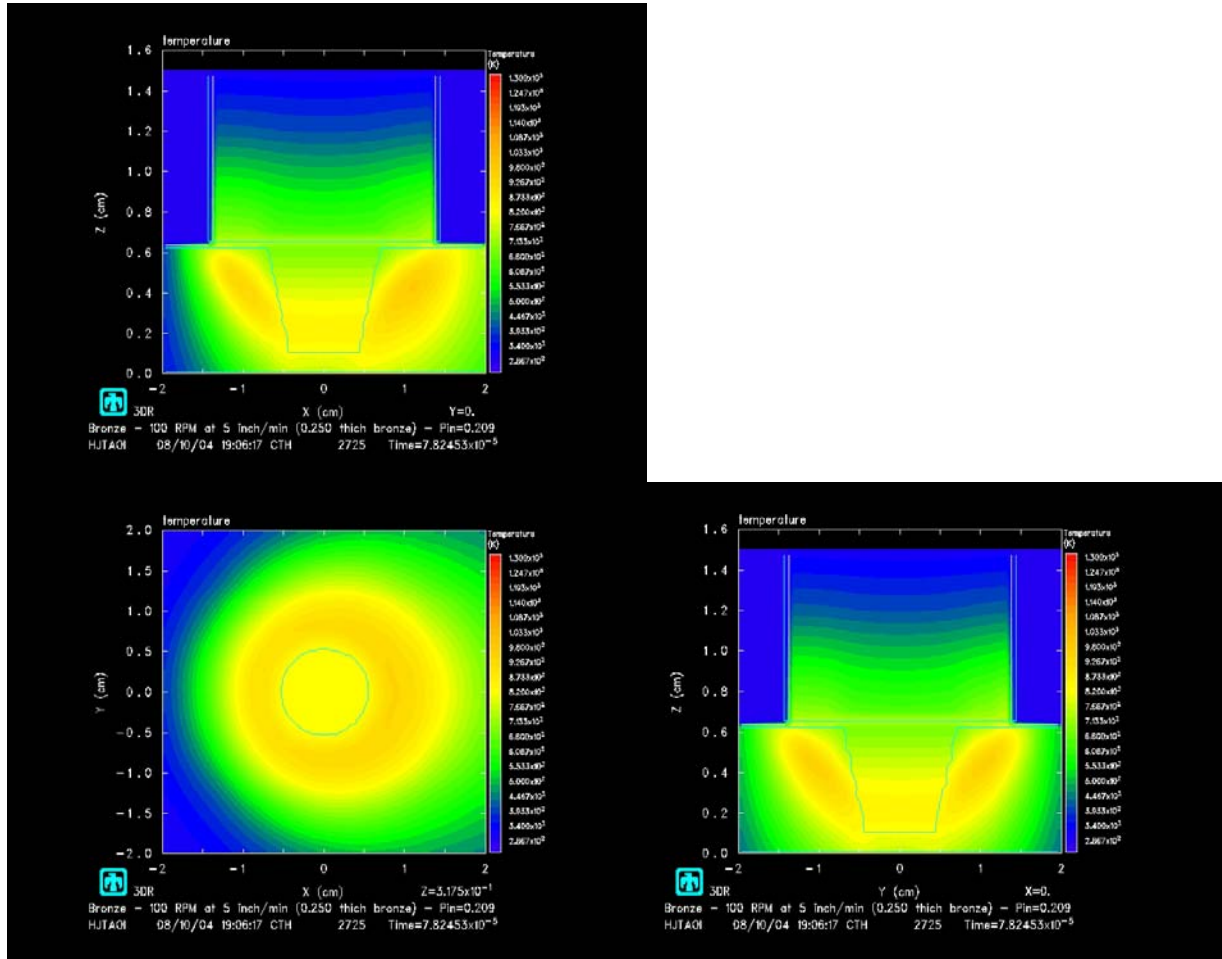


Figure 30. 100 rev/min 5 inch/min – Temperature distribution.

It is easy to see the volume of material in the corner of the tool where the shoulder and pin are connected. This volume is rotating with the tool not generating any heat, therefore this volume of material is only conducting the heat into the tool and up the shoulder. The capacity of the tool to conduct heat away is higher than the flux of the heat transferred into it. Therefore the temperature of the tool is lower than the material in deformation. It is also noteworthy to note that the maximum temperature attained is approximately 700 °C trailing the tool. The shape of the temperature field is elongated with emphasis to the trailing side. The profiles of the transverse sides remain approximately constant.

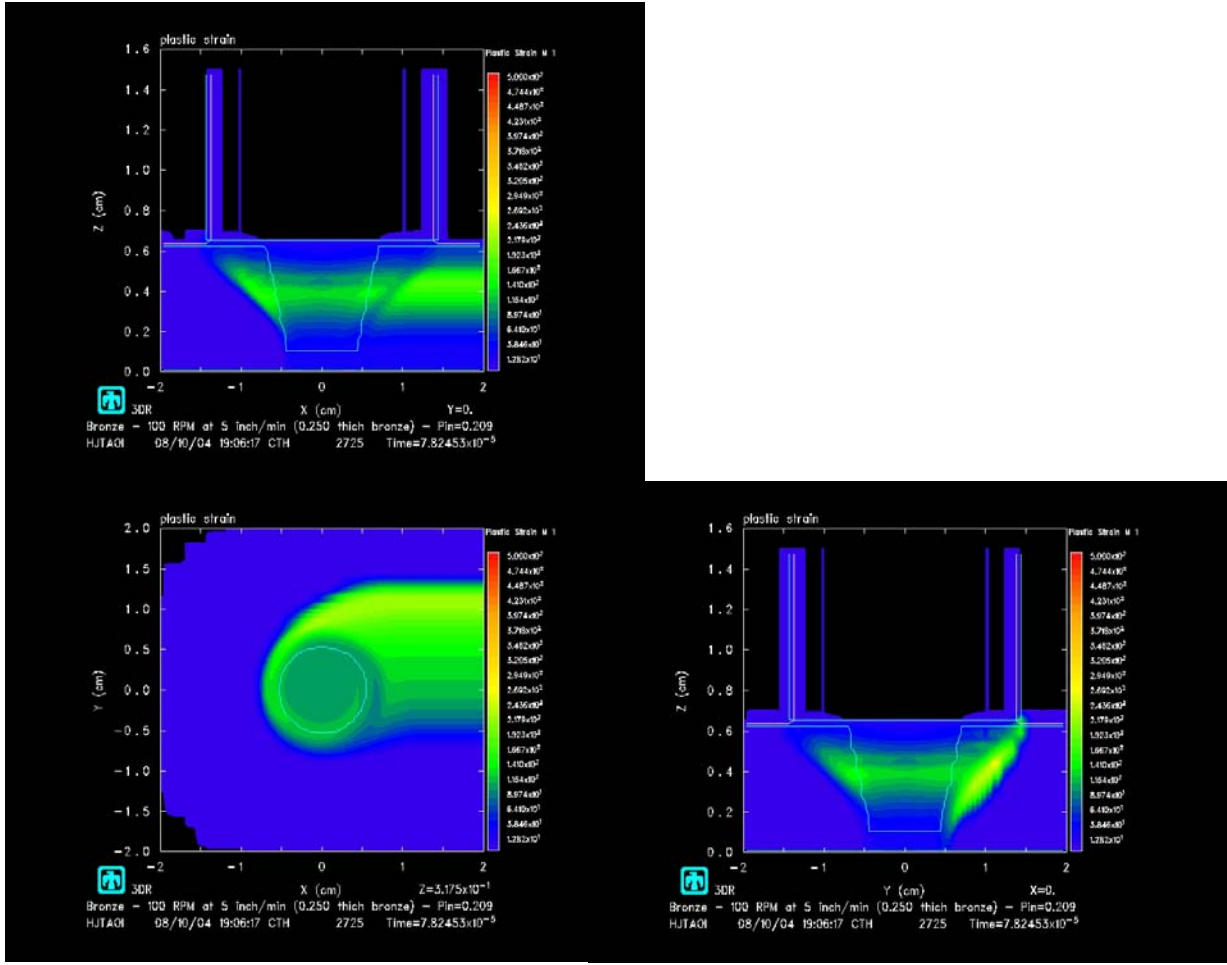


Figure 31. 100 rev/min 5 inch/min – Strain distribution.

It is easy to see that the majority of the strain is accumulated a significant distance away from the tool/material interface. This correlates to the maximum temperature attained further away from the tool. The maximum strains are seen on the advancing side of the tool as expected. It is noteworthy to write that a large volume of low strains are occurring leading and to both sides of the tool. This strain field is extends further from the tool than that seen in figure 27. Also the maximum strains attained are much lower correlating to the logic of less time spent around the tool.

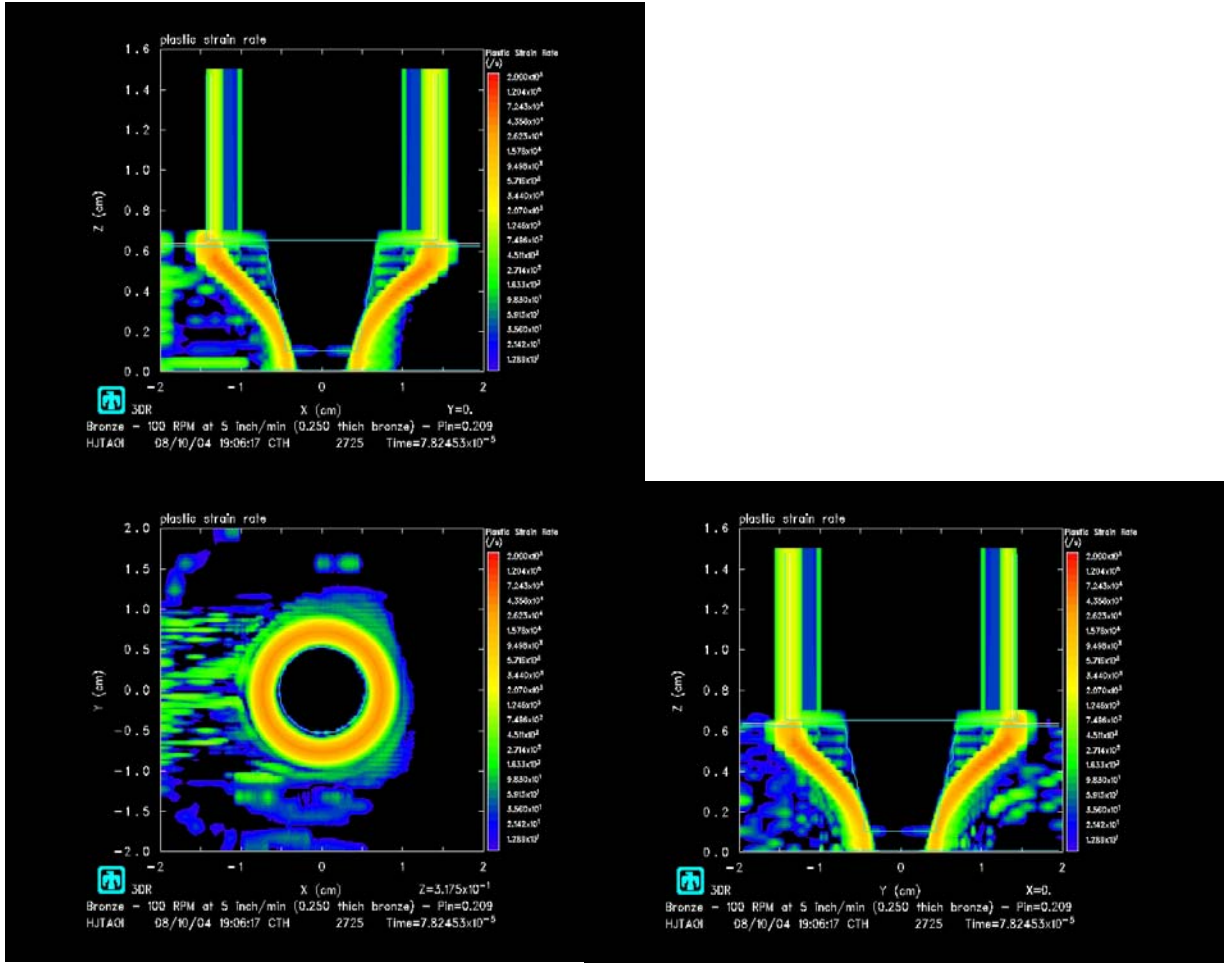


Figure 32. 100 rev/min 5 inch/min – Strain-rate distribution.

It is easy to see that the maximum strain-rates are attained a significant distance away from the tool/material interface. This correlates to the maximum temperature attained further away from the tool. The maximum strain-rates now are leading the tool. The large strain-rate field leading and to the sides extend further from the tool than in Figure 28.

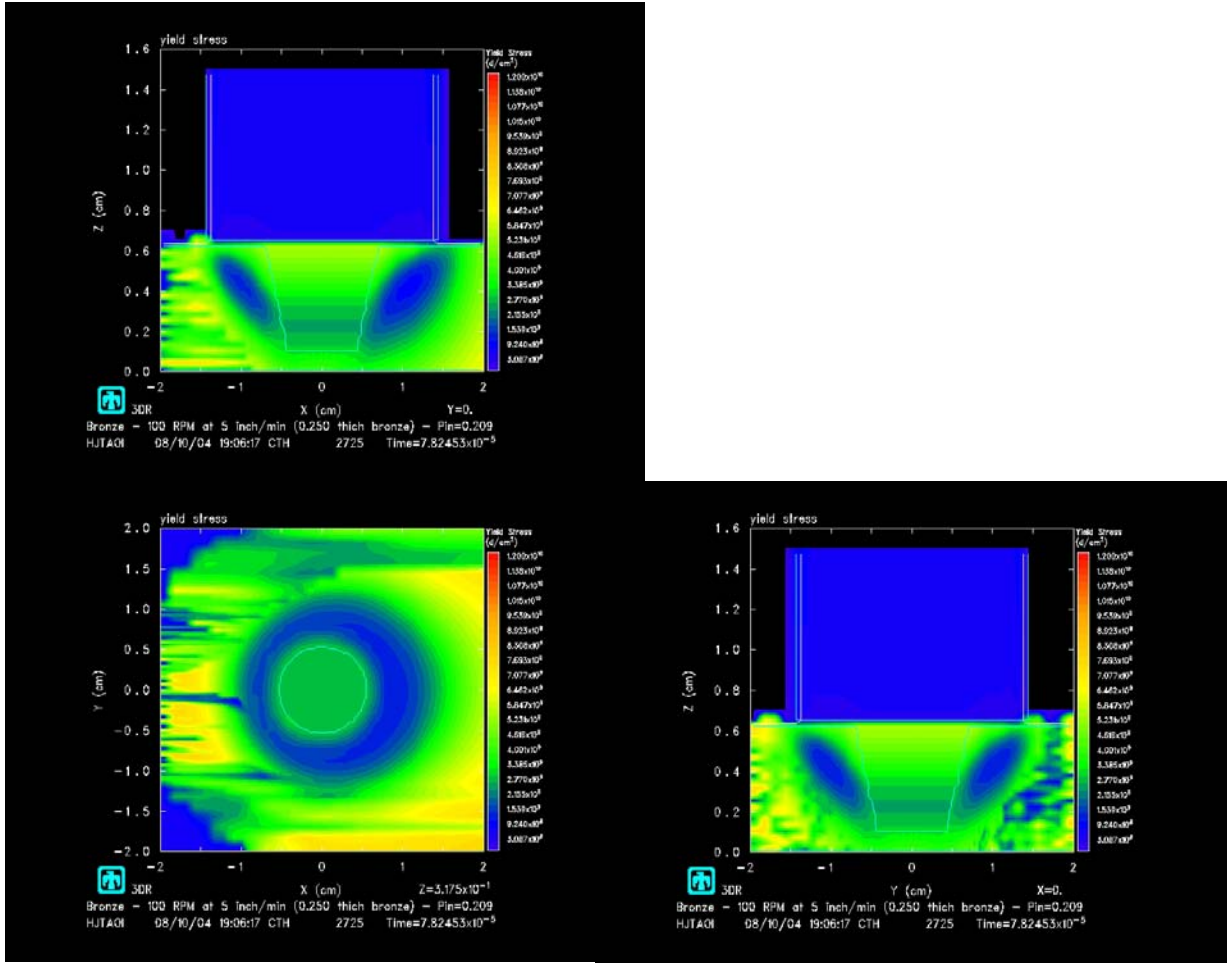


Figure 33. 100 rev/min 5 inch/min – Stress distribution.

It is easy to see that the minimum stress is attained congruent to the higher temperatures, thus correlating with thermal softening. The maximum stress occurs further from the tool within the previously viewed strain-rate field of Figure 32. A larger stress is noted on the retreating side vice the advancing side of the tool. This picture also shows the residual stress field post processing.

C. 100 RPM 10 IPM

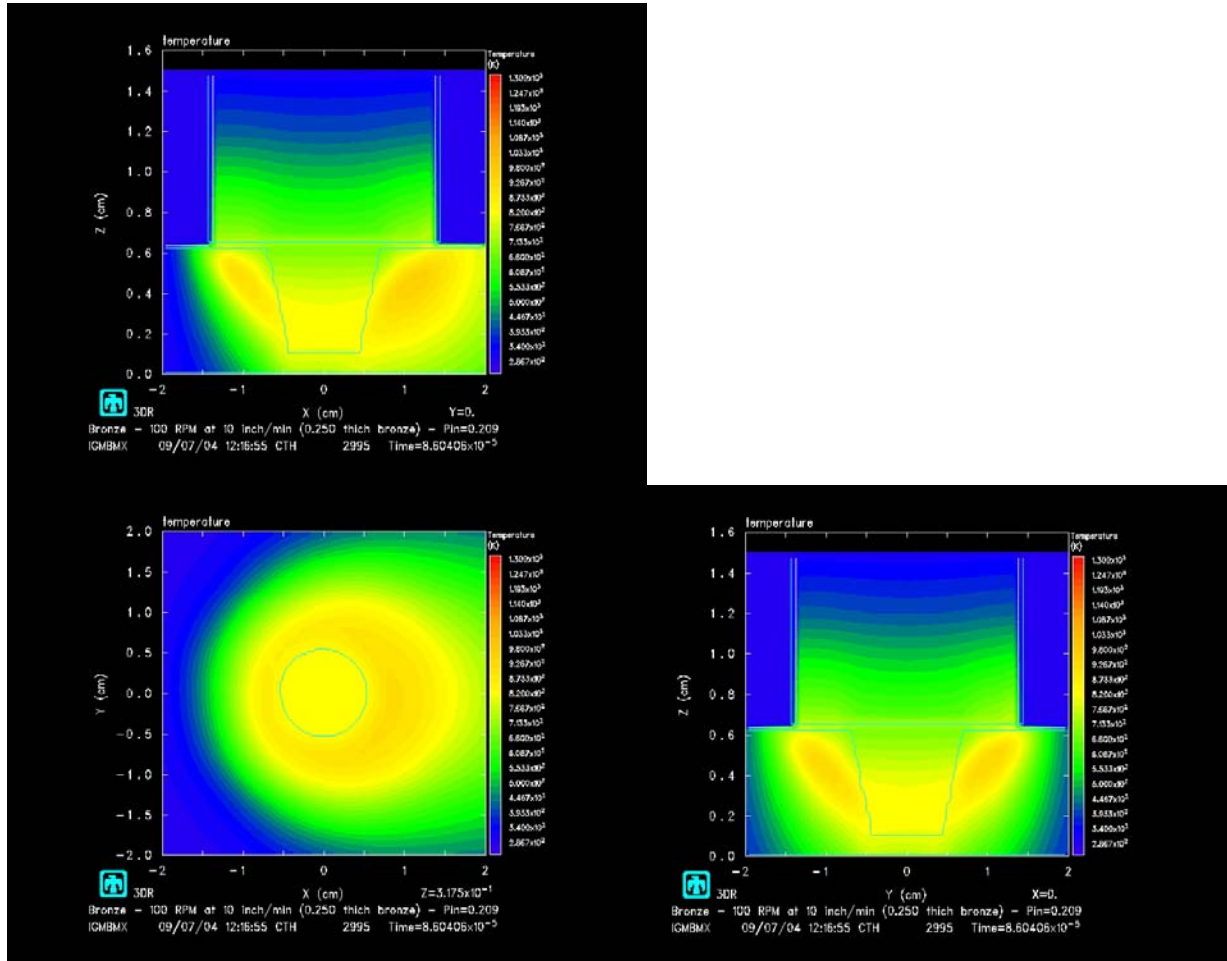


Figure 34. 100 rev/min 10 inch/min – Temperature distribution.

It is easy to see small volume of material in the corner of the tool where the shoulder and pin are connected. This volume is rotating with the tool not generating any heat, therefore this volume of material is only conducting the heat into the tool and up the shoulder. The lower half of the pin is exposed to the higher temperature material, therefore the pin is approximately 550°C . The capacity of the tool to conduct heat away is higher than the flux of the heat transferred into it. Therefore the temperature of the tool is lower than the material in deformation. A relatively large volume of material trailing the tool is maintaining a maximum temperature approximately 700°C . The shape of the temperature field is elongated with emphasis to the trailing side. The profiles of the transverse sides remain approximately proportional, yet when compared to a traversing rate of 5 inch/min, the volume is becoming more compact. It is noteworthy that the maximum temperature in the volume leading the tool is only approximately 625°C .

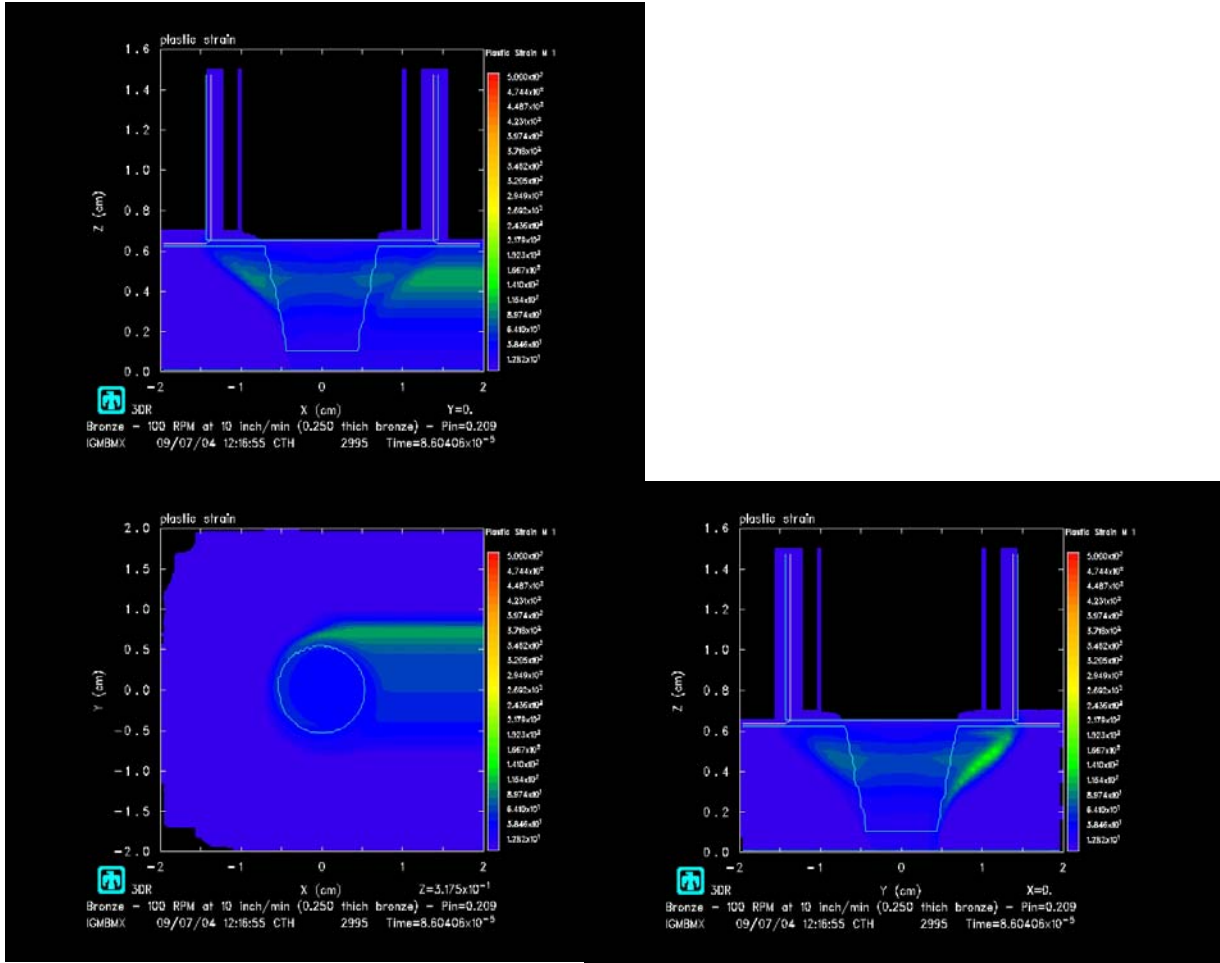


Figure 35. 100 rev/min 10 inch/min – Strain distribution.

It is easy to see that the majority of the strain is accumulated a significant distance away from the tool/material interface. This correlates to the maximum temperature attained further away from the tool. The maximum strains are seen on the advancing side of the tool as expected. It is noteworthy to write that a large volume of low strains are occurring leading and to both sides of the tool. This strain field extends further from the tool than that seen in figure 31. Also the maximum strains attained are much lower correlating to the logic of less time spent around the tool.

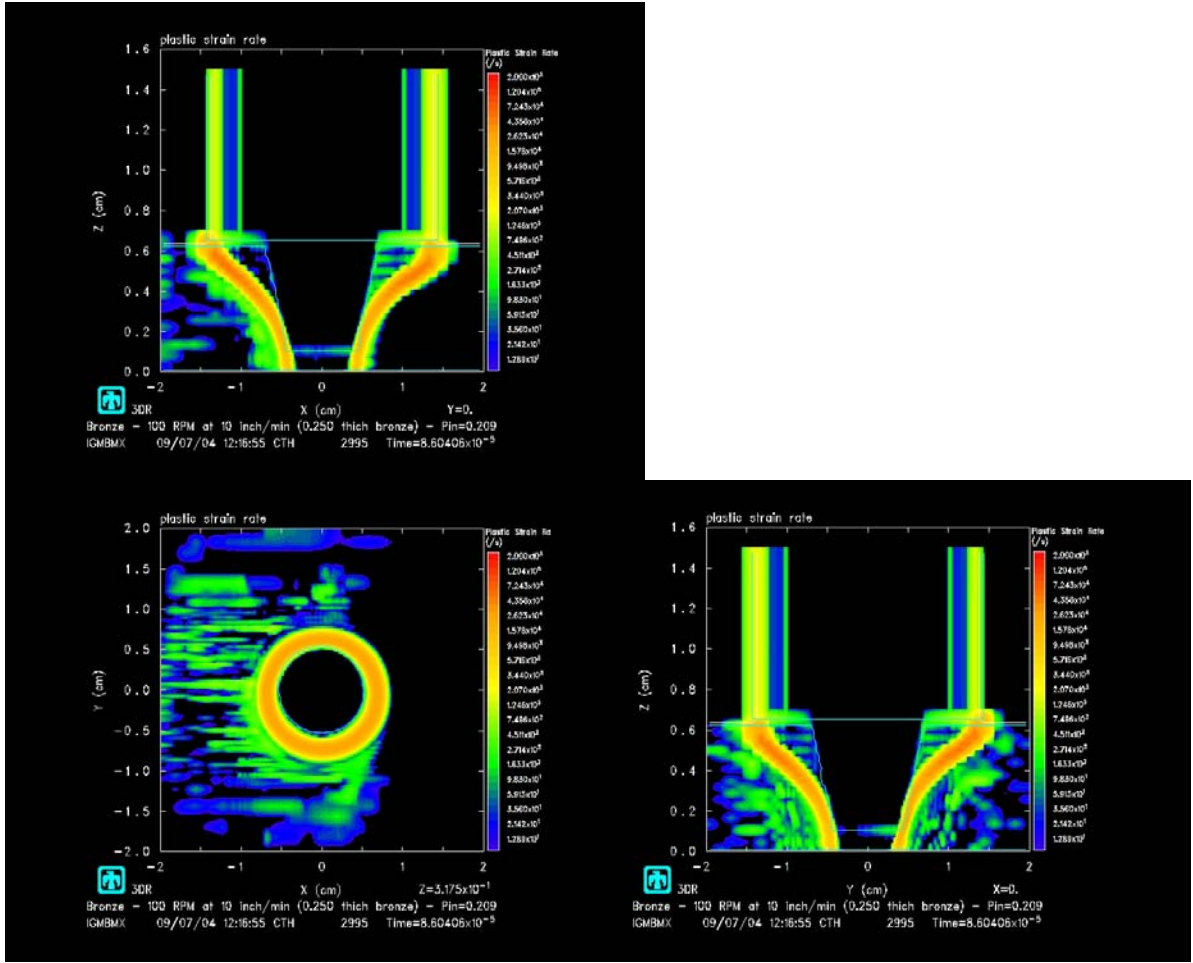


Figure 36. 100 rev/min 10 inch/min – Strain-rate distribution.

It is easy to see that the maximum strain-rates are attained a significant distance away from the tool/material interface. This correlates to the maximum temperature attained further away from the tool. The maximum strain-rates are leading the tool. The large strain-rate field leading and to the sides extends further and with more intensity from the tool than in Figure 32.

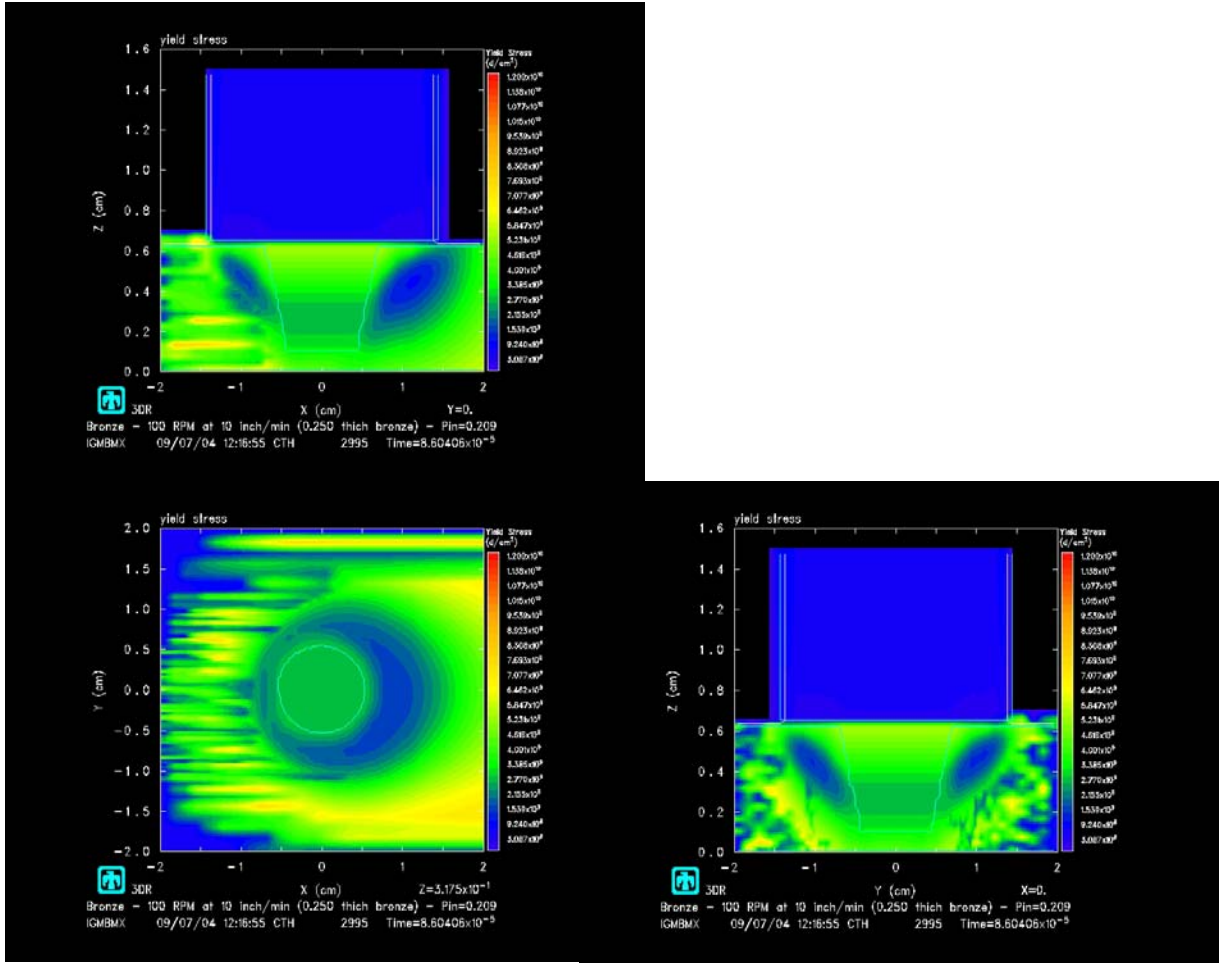


Figure 37. 100 rev/min 10 inch/min – Stress distribution.

It is easy to see that the minimum stress is attained congruent to the higher temperatures, thus correlating with thermal softening. The volume of material at low stress leading the tool has all but disappeared. The flow of material around the pin has almost mitigated the adiabatic heating. The maximum stress occurs further from the tool within the previously viewed strain-rate field of Figure 36. A larger stress is noted on the retreating side vice the advancing side of the tool. It is also noticed that the stress is higher lower on the pin due to the lower temperatures attained. This picture also shows the residual stress field post processing.

D. 100 RPM 20 IPM

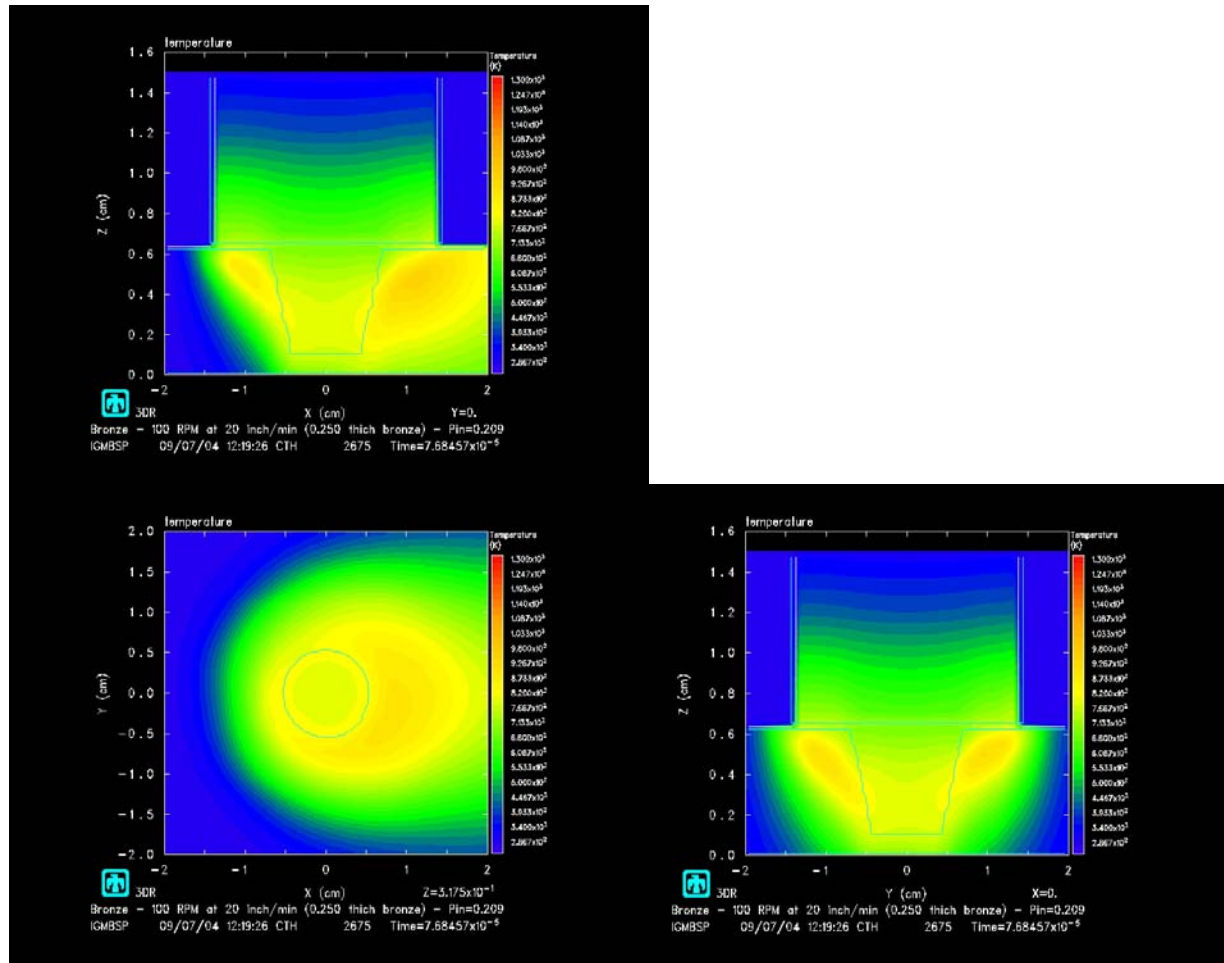


Figure 38. 100 rev/min 20 inch/min – Temperature distribution.

The lower half of the pin is exposed to the lower temperature material flowing around it, therefore the pin is approximately 515 °C. The capacity of the tool to conduct heat away is higher than the flux of the heat transferred into it. Therefore the temperature of the tool is lower than the material in deformation. A relatively large volume of material trailing the tool is maintaining a maximum temperature approximately 700 °C. The shape of the temperature field is elongated with emphasis to the trailing side. The volume of material reaching the higher temperatures is lower on the advancing side vice the retreating side. It is noteworthy that the maximum temperature in the volume leading the tool is only approximately 600 °C.

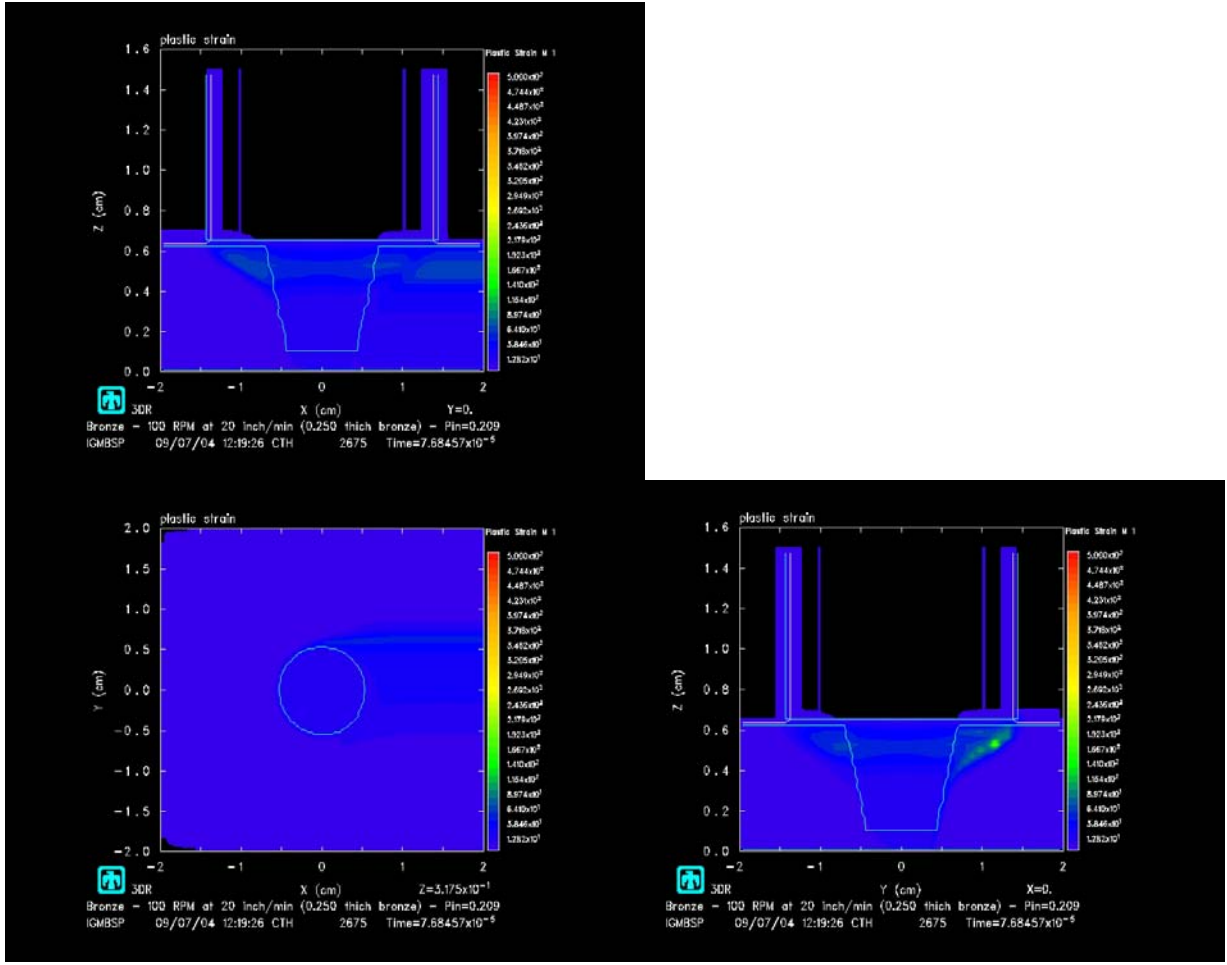


Figure 39. 100 rev/min 20 inch/min – Strain distribution.

The maximum strains are seen on the advancing side of the tool as expected. It is noteworthy to write that all accumulated strain is very low compared to that achieved by lower traversing rates. This strain field extends further from the tool than that seen in figure 35.

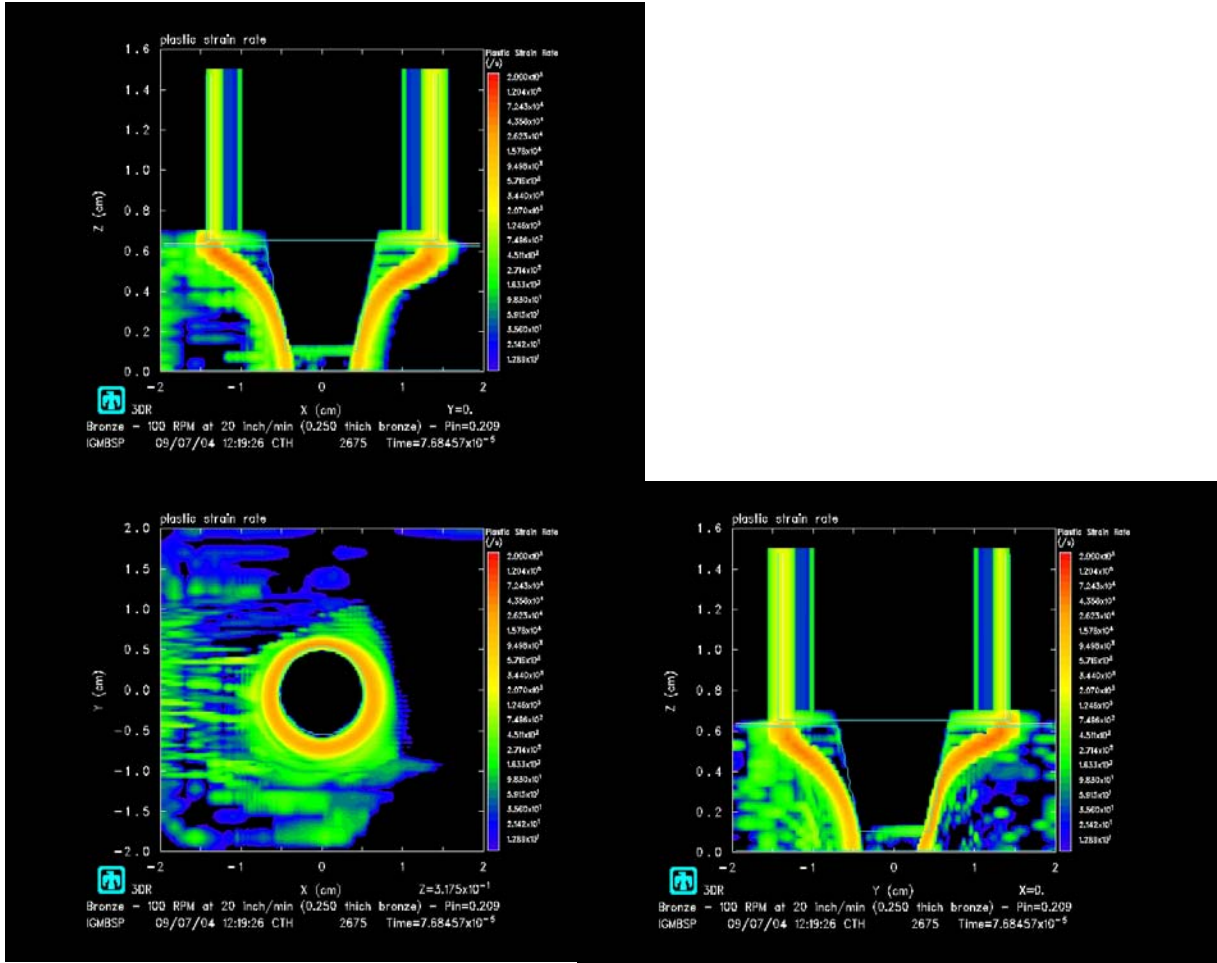


Figure 40. 100 rev/min 20 inch/min – Strain-rate distribution.

It is easy to see that the maximum strain-rates are attained a significant distance away from the tool/material interface. This correlates to the maximum temperature attained further away from the tool. The strain-rate on the advancing side is more compacted toward the pin than the retreating side. The large strain-rate field leading and to the sides extends further and with more intensity from the tool than in Figure 36.

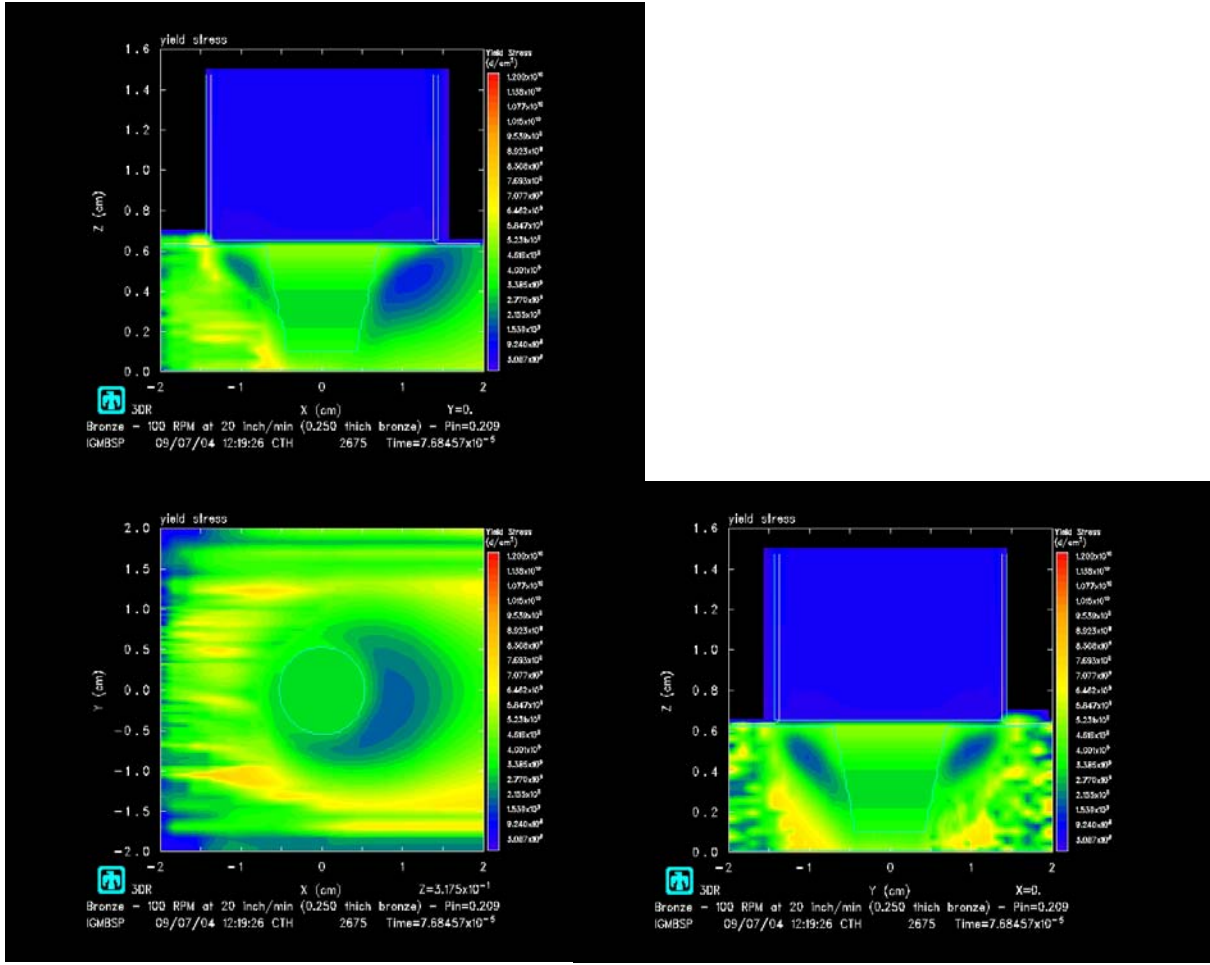


Figure 41. 100 rev/min 20 inch/min – Stress distribution.

It is easy to see that the minimum stress is attained congruent to the higher temperatures, thus correlating with thermal softening. The volume of material at low stress leading the tool has disappeared. The flow of material around the pin has almost mitigated the adiabatic heating. The maximum stress occurs within the lower half of the material and with a significant volume on the retreating side of the tool. It is also noticed that the stress is higher lower on the pin due to the lower temperatures attained.

E. 500 RPM 1 IPM

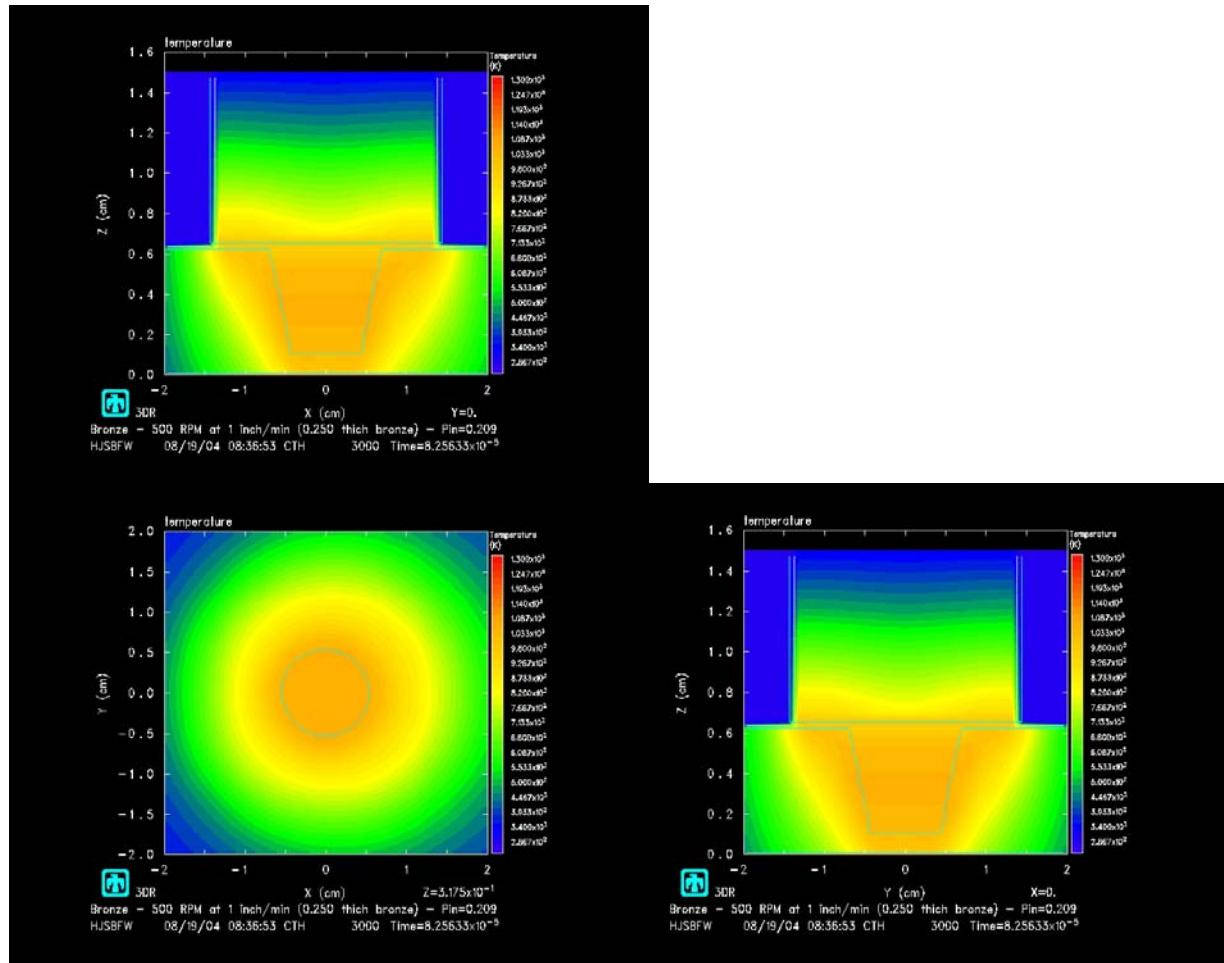


Figure 42. 500 rev/min 1 inch/min – Temperature distribution.

It is easy to see the volume of material around the tool and the pin are nearly the same maximum temperature. The shape of the temperature profile is consistent with what the reader might imagine for a rotating tool with a traversing rate of zero. The maximum temperature attained is approximately 750 °C.

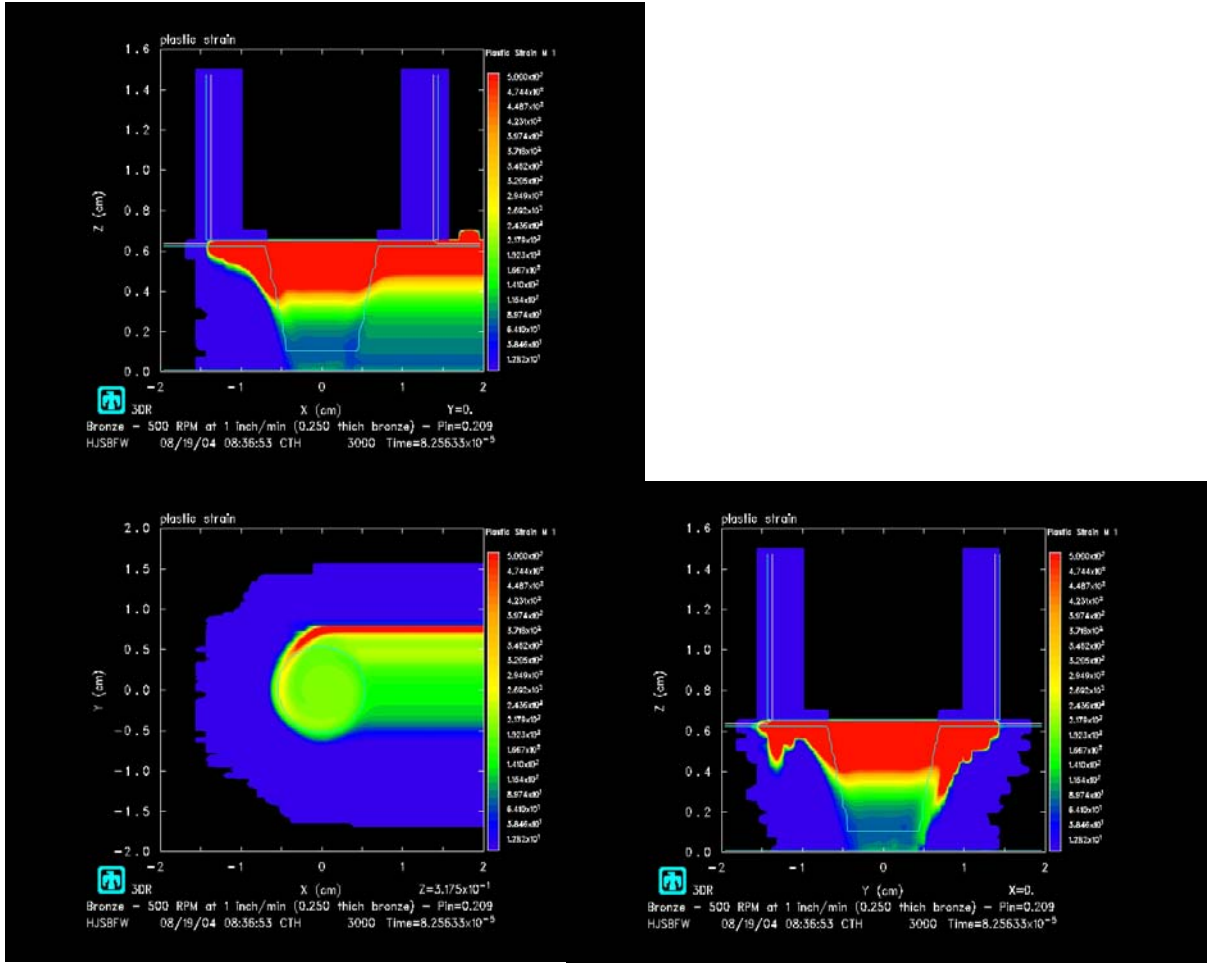


Figure 43. 500 rev/min 1 inch/min – Strain distribution. The maximum accumulated strain occurs on the advancing side as expected. The volume of material experiencing the maximum strain is relatively small compared to the volume experiencing a very low strain. The material in the lower half of the block experiences very little if any strain. It is noteworthy to emphasize the blue strain field leading and to the sides of the tool.

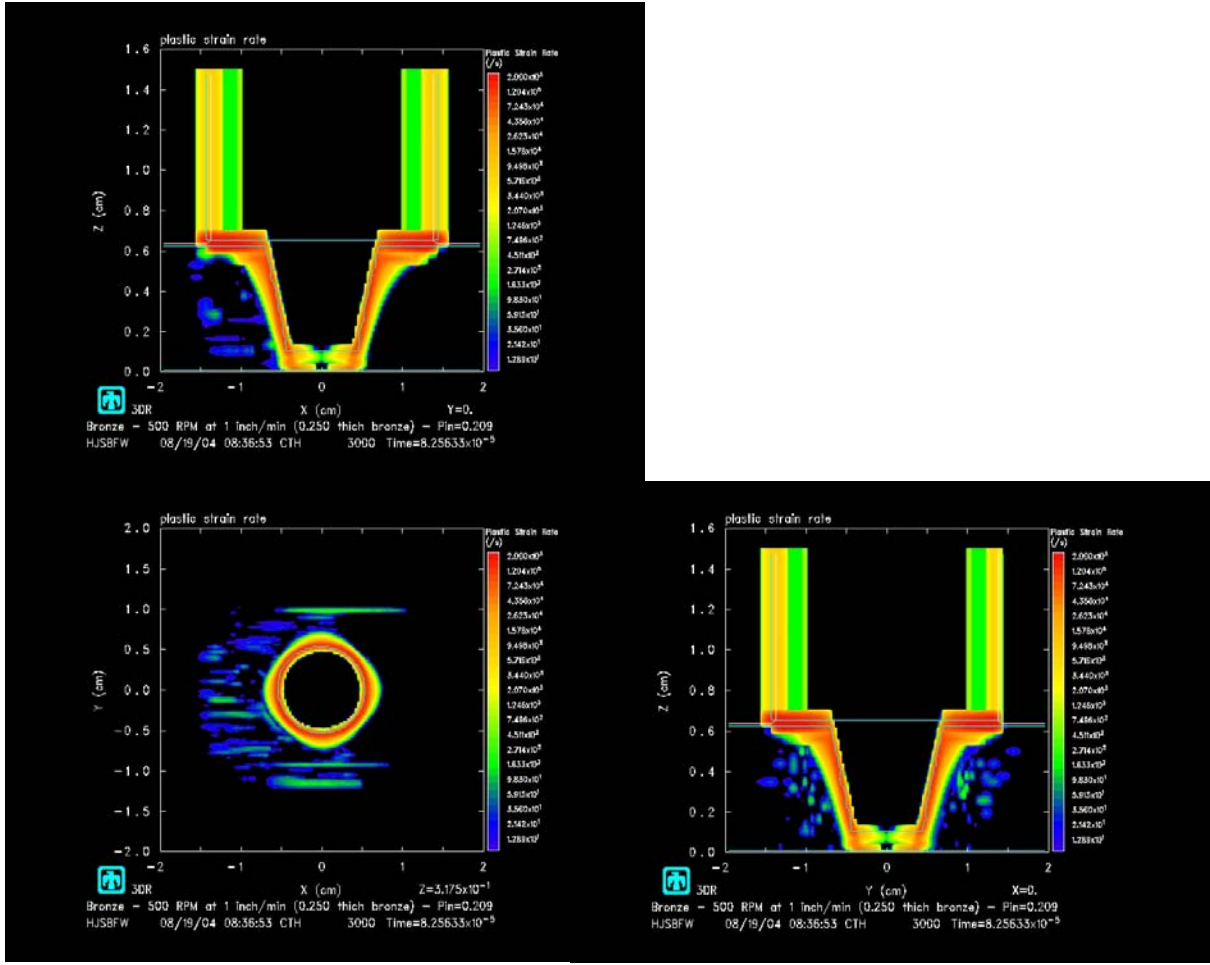


Figure 44. 500 rev/min 1 inch/min – Strain-rate distribution.

It is easy to see that the highest strain-rates are attained very near the tool/material interface with a large fraction near the shoulder. The strain-rate field leading the tool is nearly non-existent. The maximum strain-rate is attained at near the shoulder as expected since the shoulder has the highest velocity.

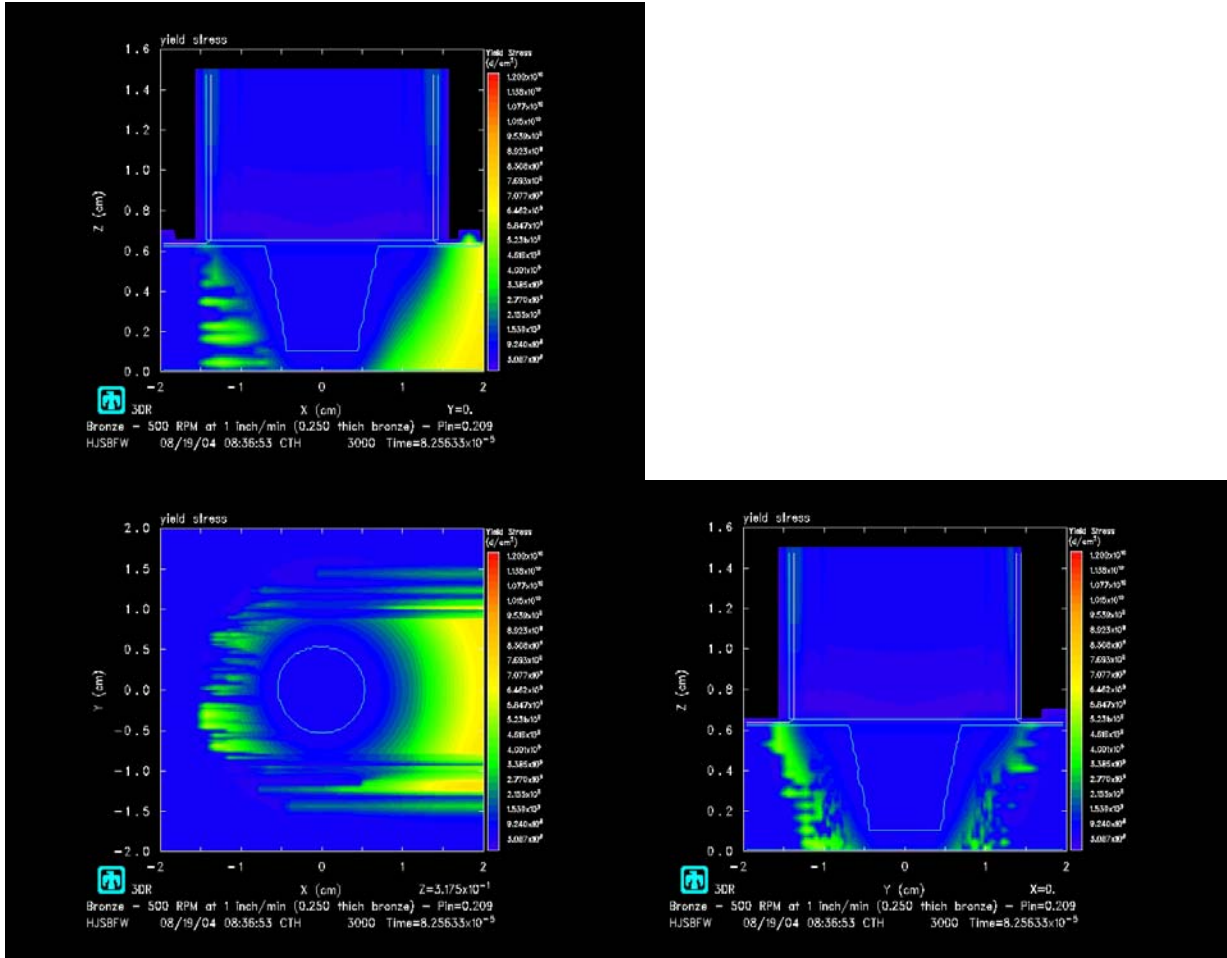


Figure 45. 500 rev/min 1 inch/min – Stress distribution.

The low stress field around the tool correlates with the higher temperatures and the theory of thermal softening. A relatively small volume of material leading the tool is experiencing a low stress. The residual stress of the process can be seen in the xy-plane picture trailing the tool.

F. 500 RPM 5 IPM

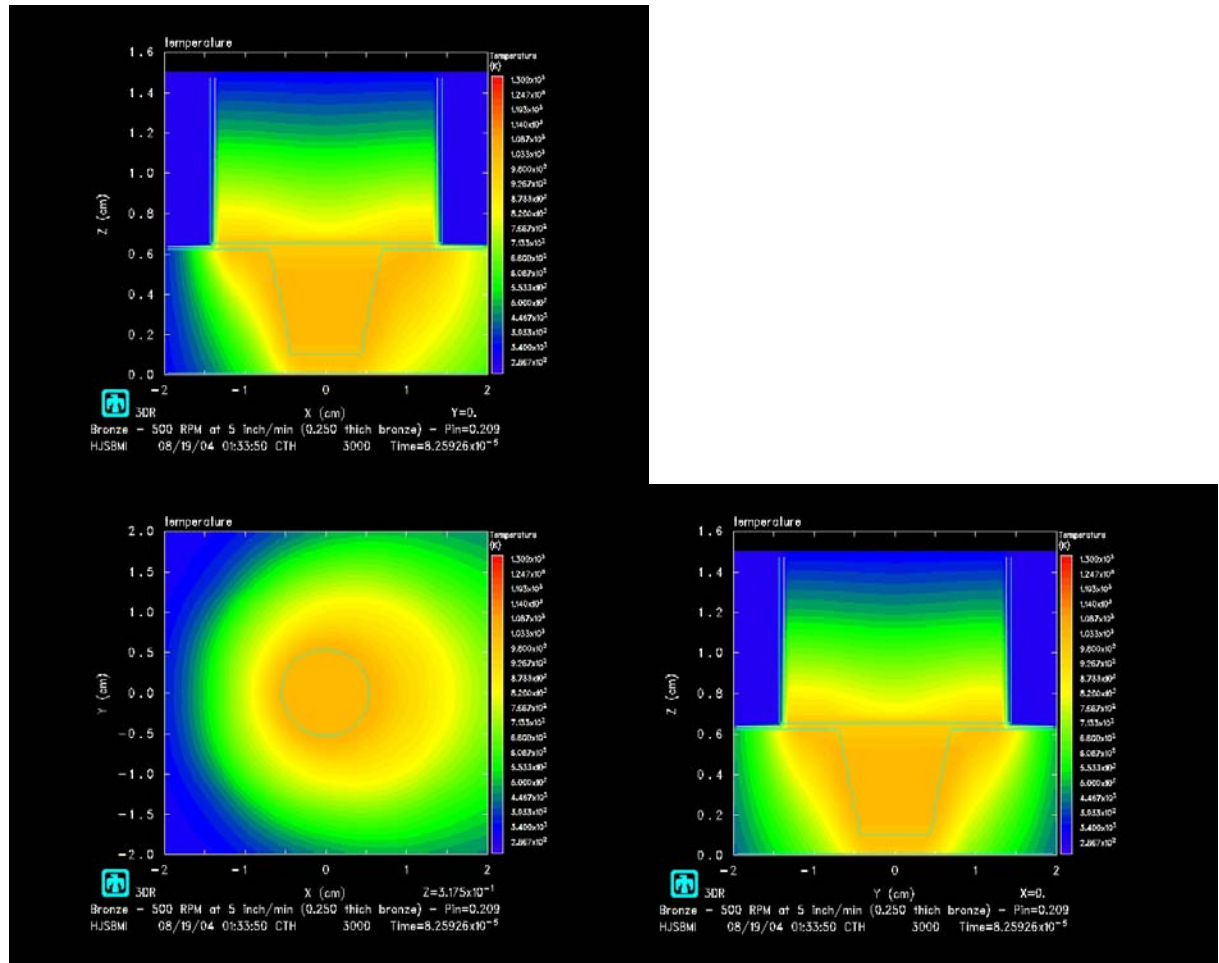


Figure 46. 500 rev/min 5 inch/min – Temperature distribution.

It is easy to see the volume of material around the tool and the pin are nearly the same maximum temperature. The shape of the temperature profile is slightly elongated and skewed toward the trailing side of the tool due to the traversing rate. The maximum temperature attained is approximately 750 °C.

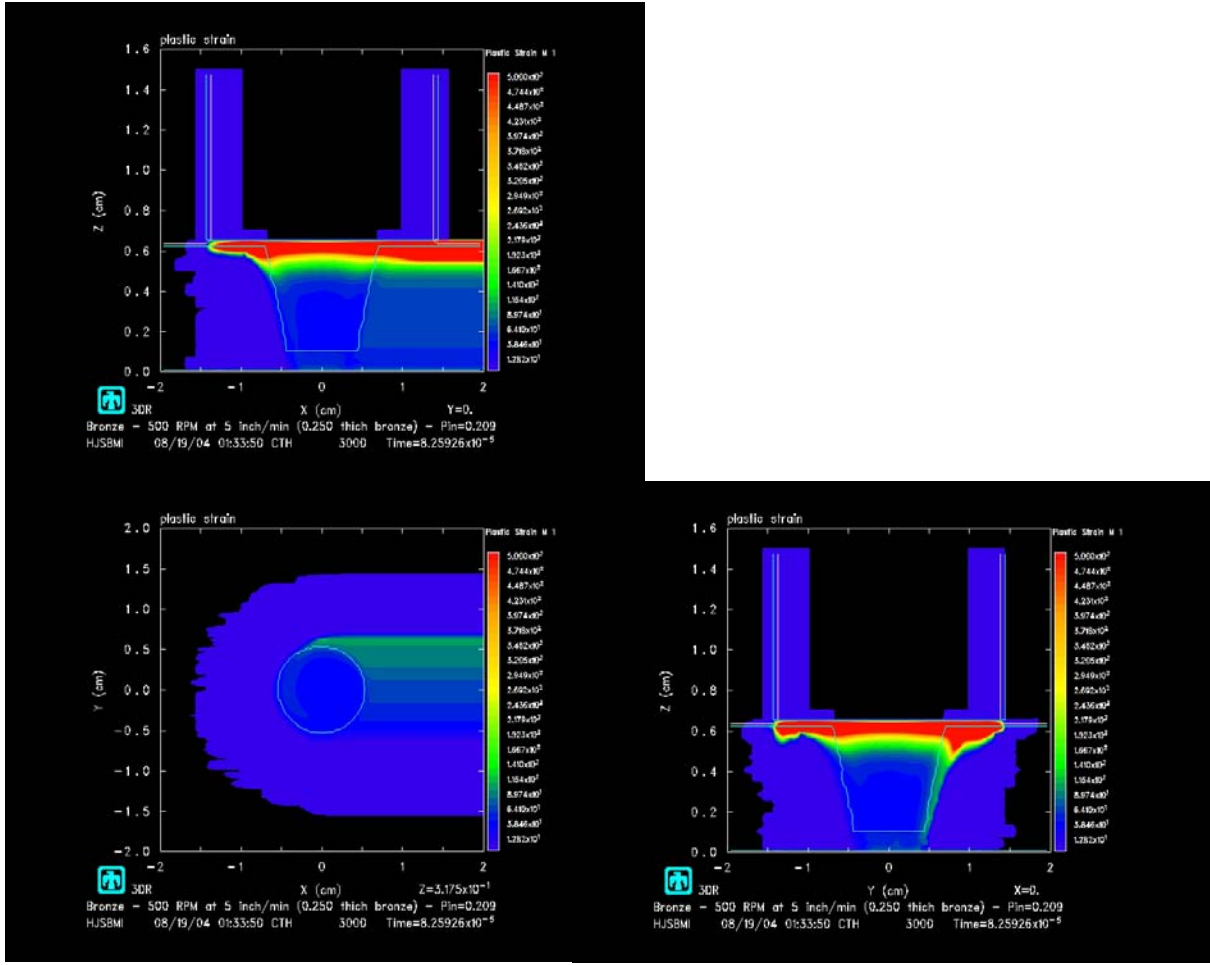


Figure 47. 500 rev/min 5 inch/min – Strain distribution. The maximum strain is occurring near the shoulder. The material below one millimeter is only accumulating a very small amount of strain. The low strain field leading and to the sides of the tool is relatively the same size as that of Figure 43.

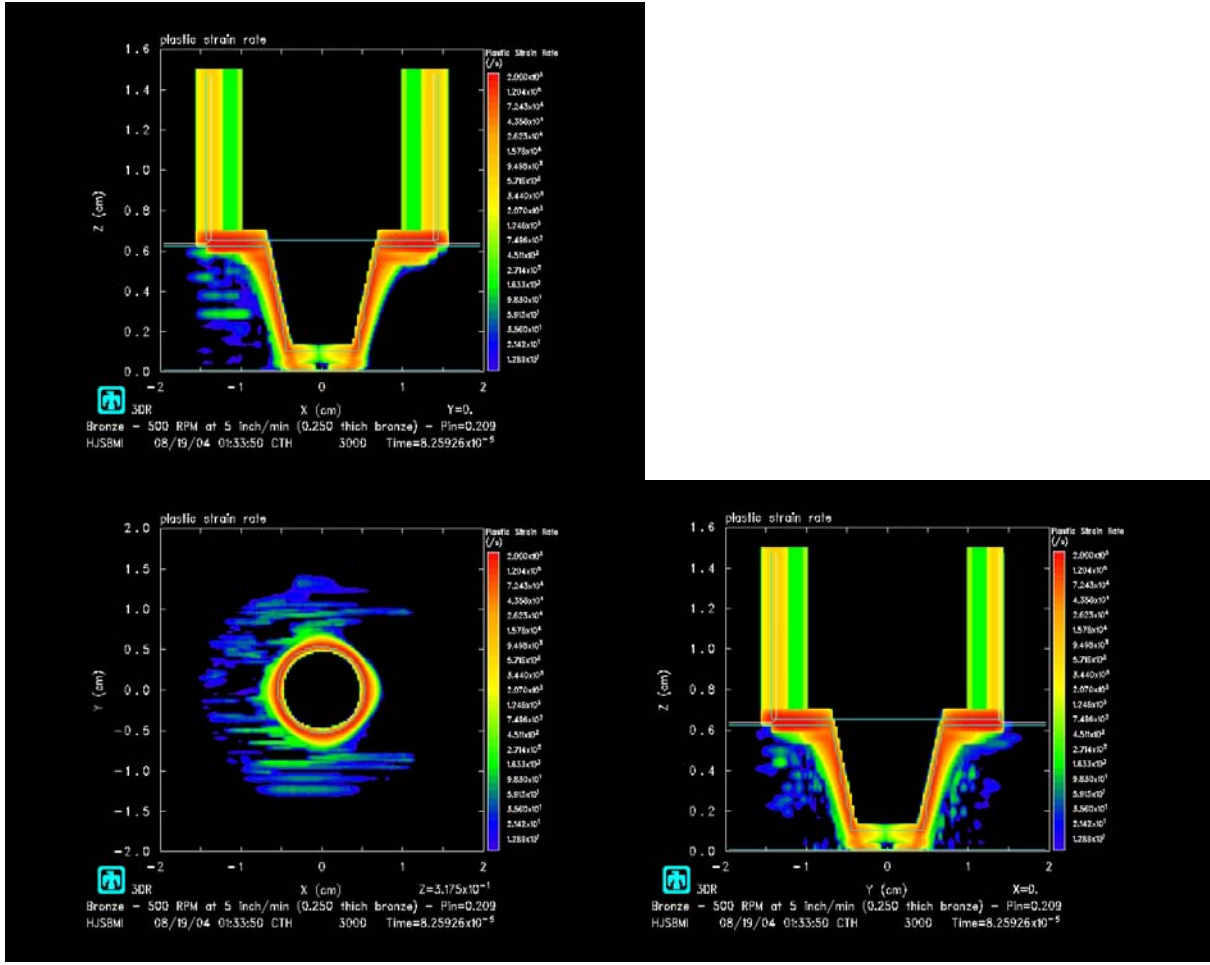


Figure 48. 500 rev/min 5 inch/min – Strain-rate distribution.

It is easy to see that the highest strain-rates are attained very near the tool/material interface with a large fraction near the shoulder. The maximum strain-rate is attained at or near the shoulder as expected since the shoulder has the highest velocity. The strain-rate field leading the tool has grown in magnitude and volume as compared to Figure 44.

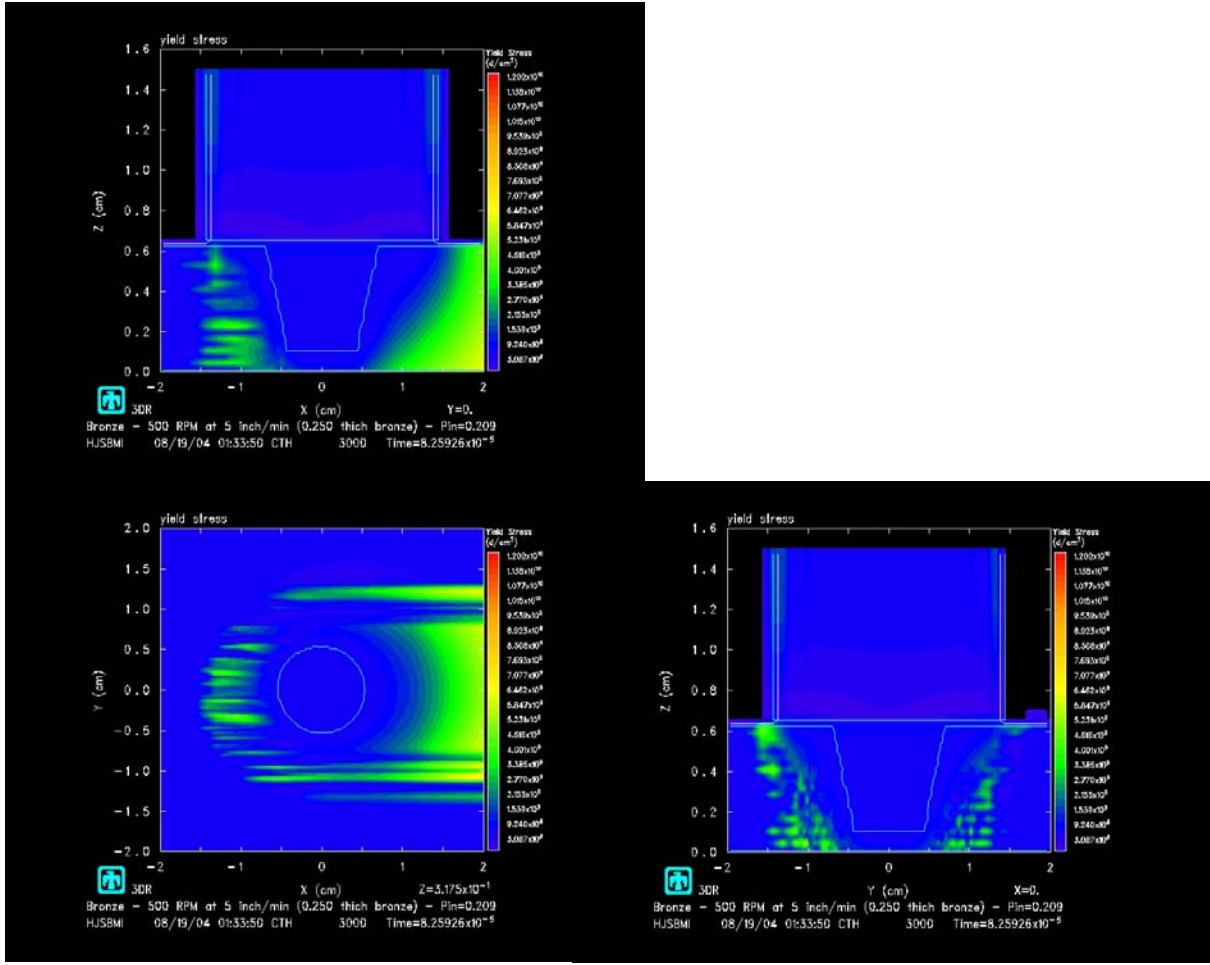


Figure 49. 500 rev/min 5 inch/min – Stress distribution.

The low stress field around the tool correlates with the higher temperatures and the theory of thermal softening. A larger volume of material leading the tool is experiencing a stress compared to Figure 45. The residual stress of the process can be seen in the xy-plane picture trailing the tool.

G. 500 RPM 10 IPM

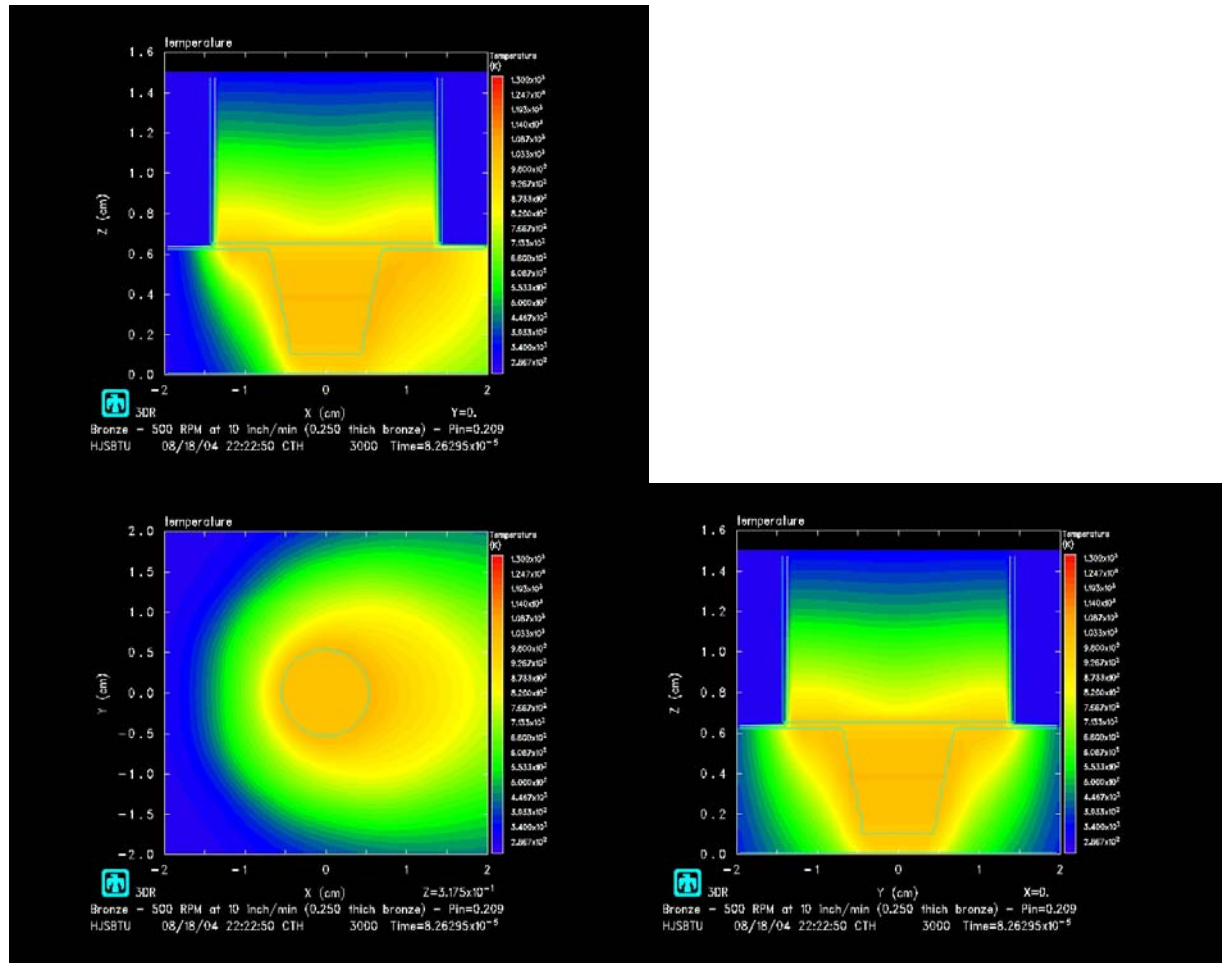


Figure 50. 500 rev/min 10 inch/min – Temperature distribution.

It is easy to see the volume of material around the tool and the pin are nearly the same maximum temperature. The tip of the pin is slightly cooler than the top of the pin. The shape of the temperature profile is elongated and skewed toward the trailing side of the tool due to the traversing rate. The maximum temperature attained is approximately 750 °C.

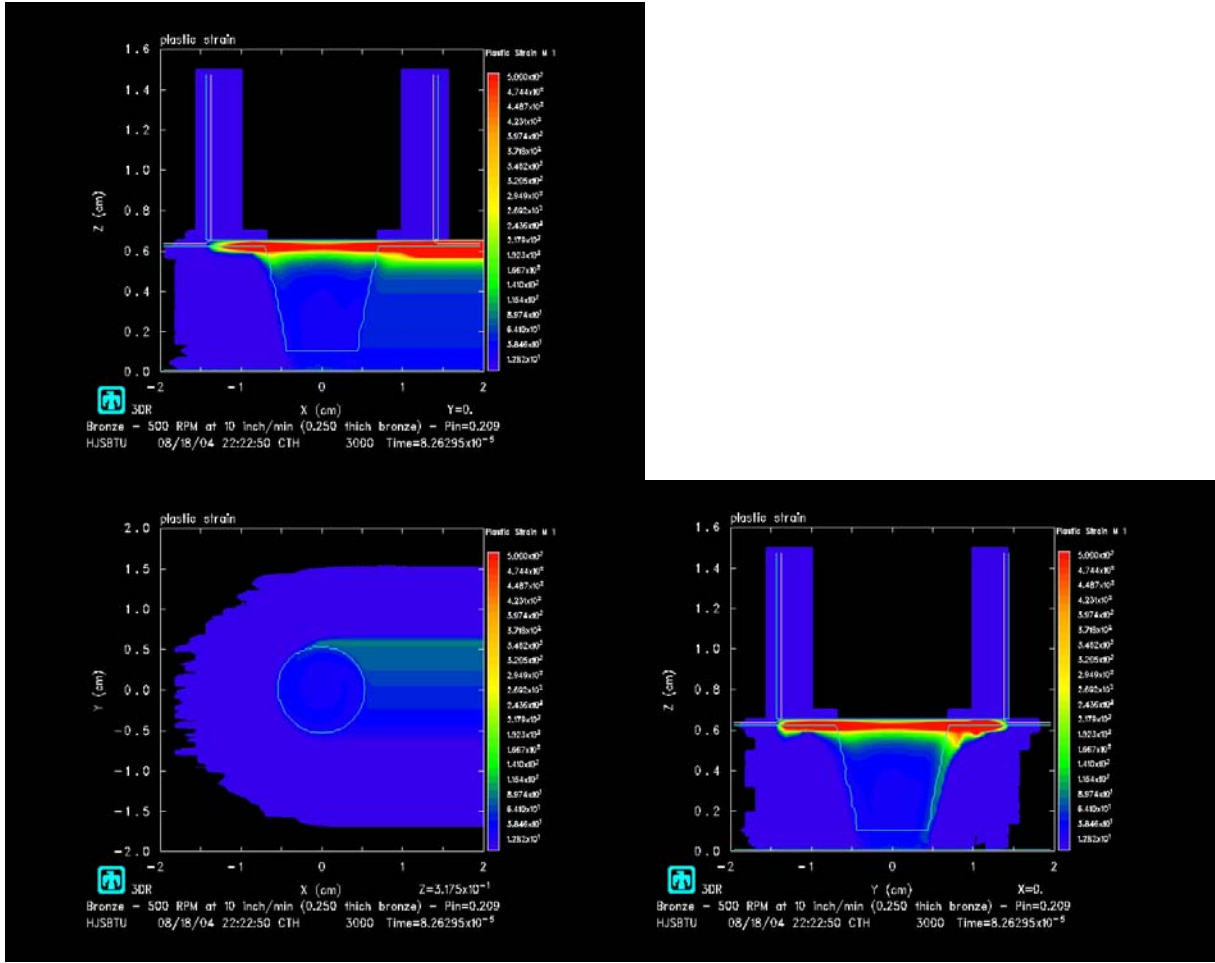


Figure 51. 500 rev/min 10 inch/min – Strain distribution.

The maximum strain is occurring near the shoulder resulting a very small volume undergoing large amounts of strain. The material below one millimeter is only accumulating a very small amount of strain. The low strain field leading and to the sides of the tool is relatively the same size as that of Figure 47.

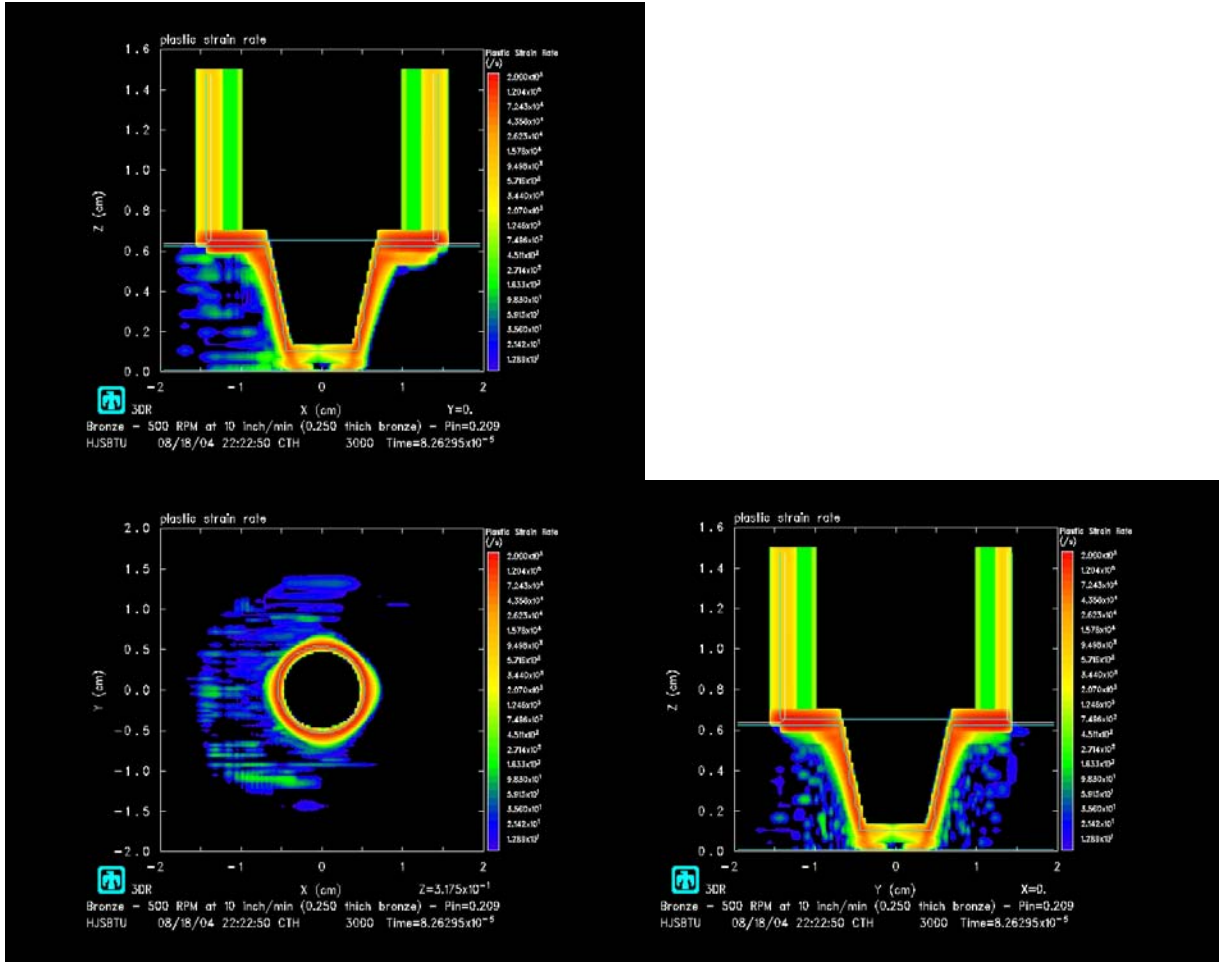


Figure 52. 500 rev/min 10 inch/min – Strain-rate distribution.

It is easy to see that the highest strain-rates are attained very near the tool/material interface with a large fraction near the shoulder. The maximum strain-rate is attained at or near the shoulder as expected since the shoulder has the highest velocity. The strain-rate field leading the tool has grown in magnitude and volume as compared to Figure 48.

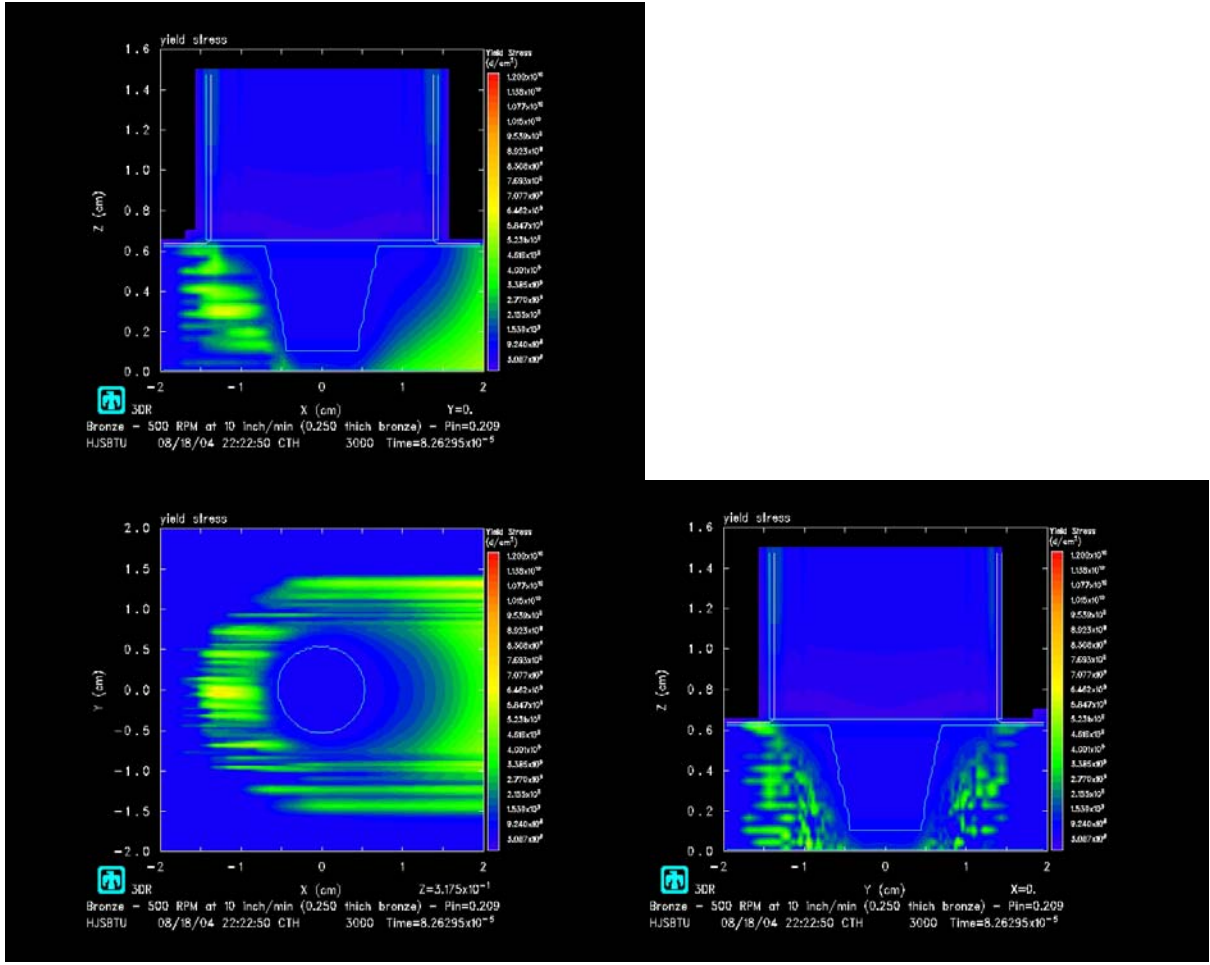


Figure 53. 500 rev/min 10 inch/min – Stress distribution.

The stress field around the tool in the material is consistent with thermal softening. It is noteworthy to point out the large stress field growing leading and to the sides of the tool. The stress field is larger on the retreating side of the tool. The residual stress field upon cooling of the material is evident.

H. 500 RPM 20 IPM

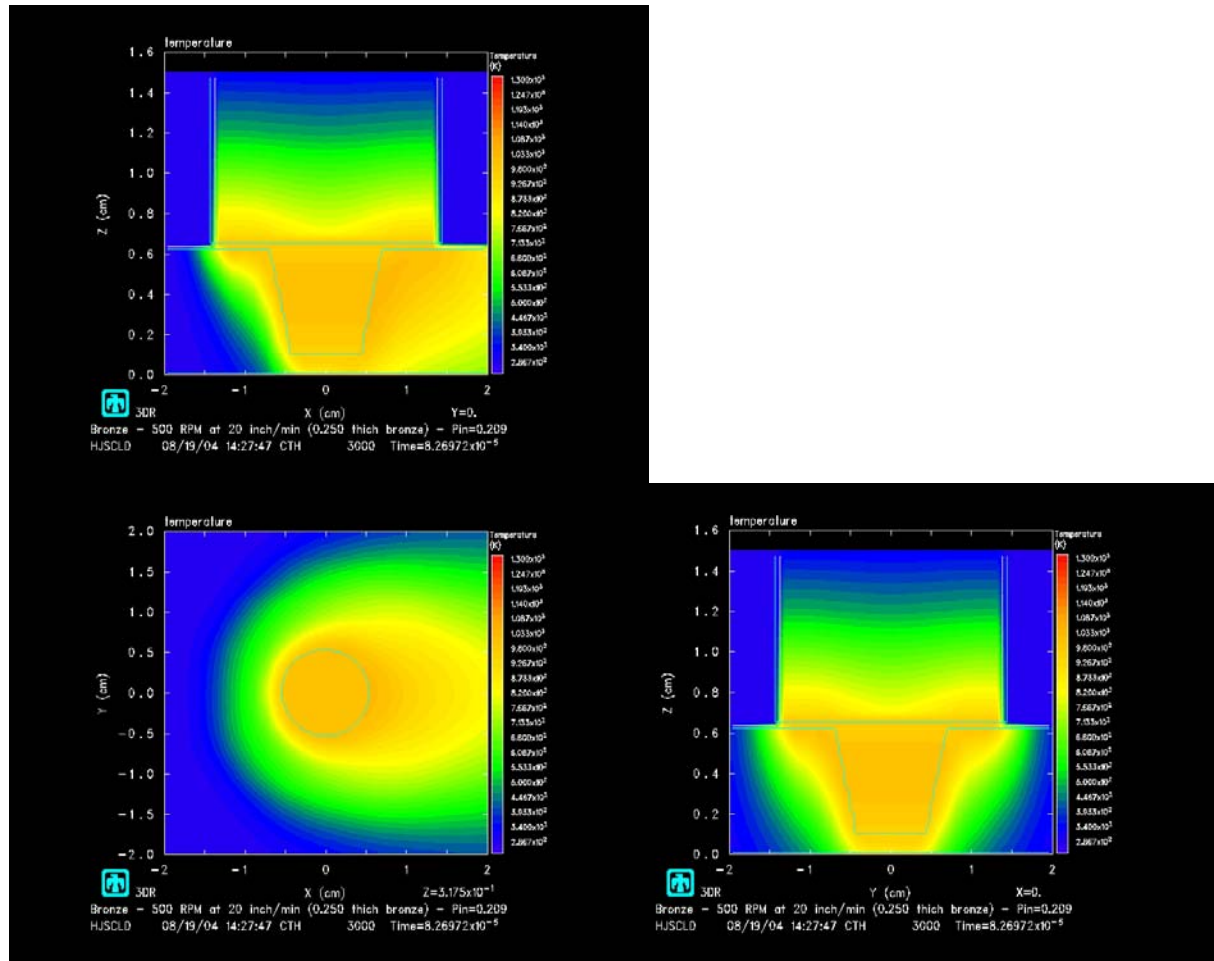


Figure 54. 500 rev/min 20 inch/min – Temperature distribution.

The material immediately leading the tool is just below maximum temperature while a sufficient volume trailing the tool is at or near maximum temperature of 750 °C. The tip of the pin is cooler than observed in Figure 50. The temperature profile is egg shape due to the flow of material around the tool.

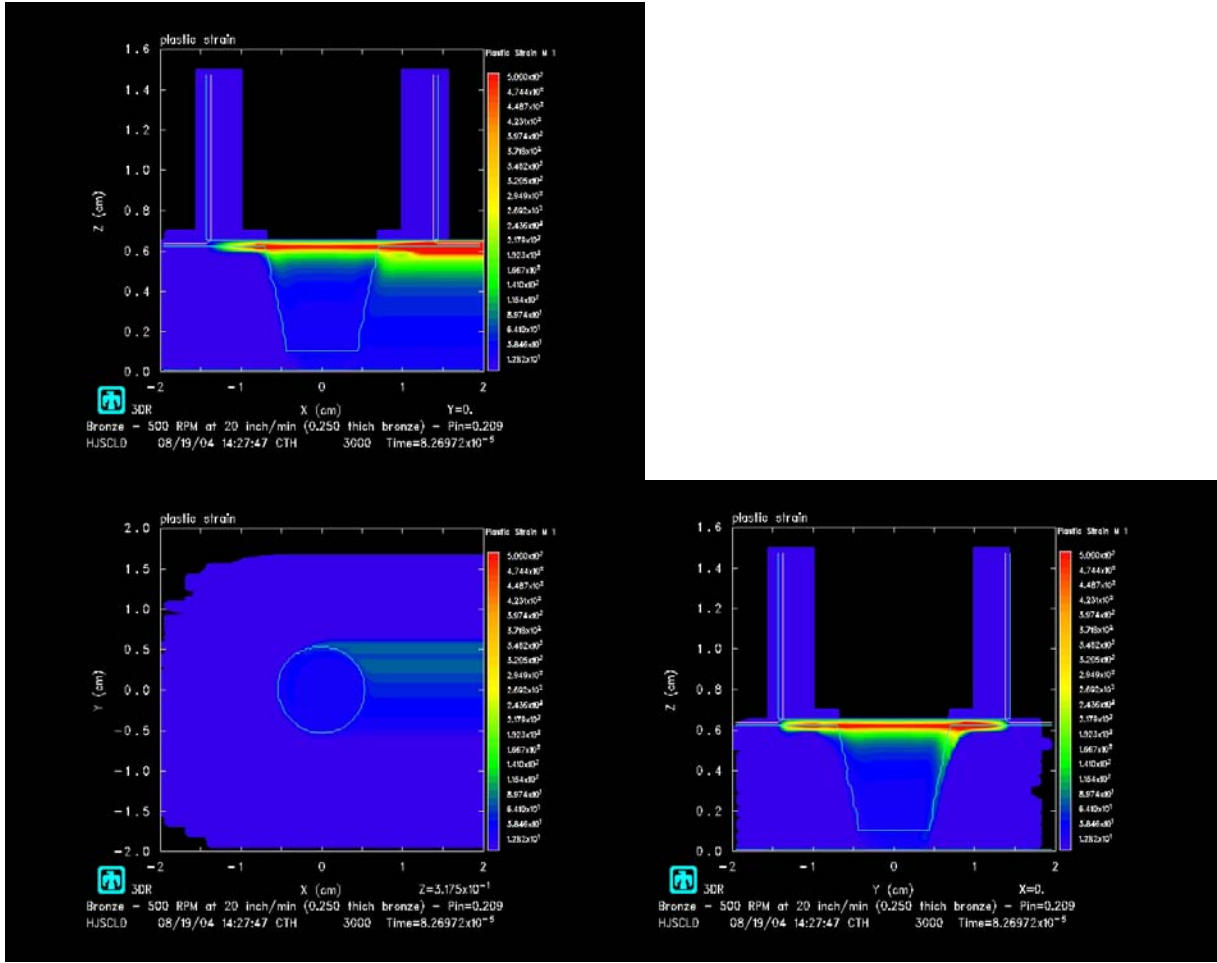


Figure 55. 500 rev/min 20 inch/min – Strain distribution.

The maximum strain is occurring near the shoulder resulting a very small volume undergoing large amounts of strain. The material below one half millimeter is only accumulating a very small amount of strain. The low strain field leading and to the sides of the tool is relatively the larger in size as that of Figure 51.

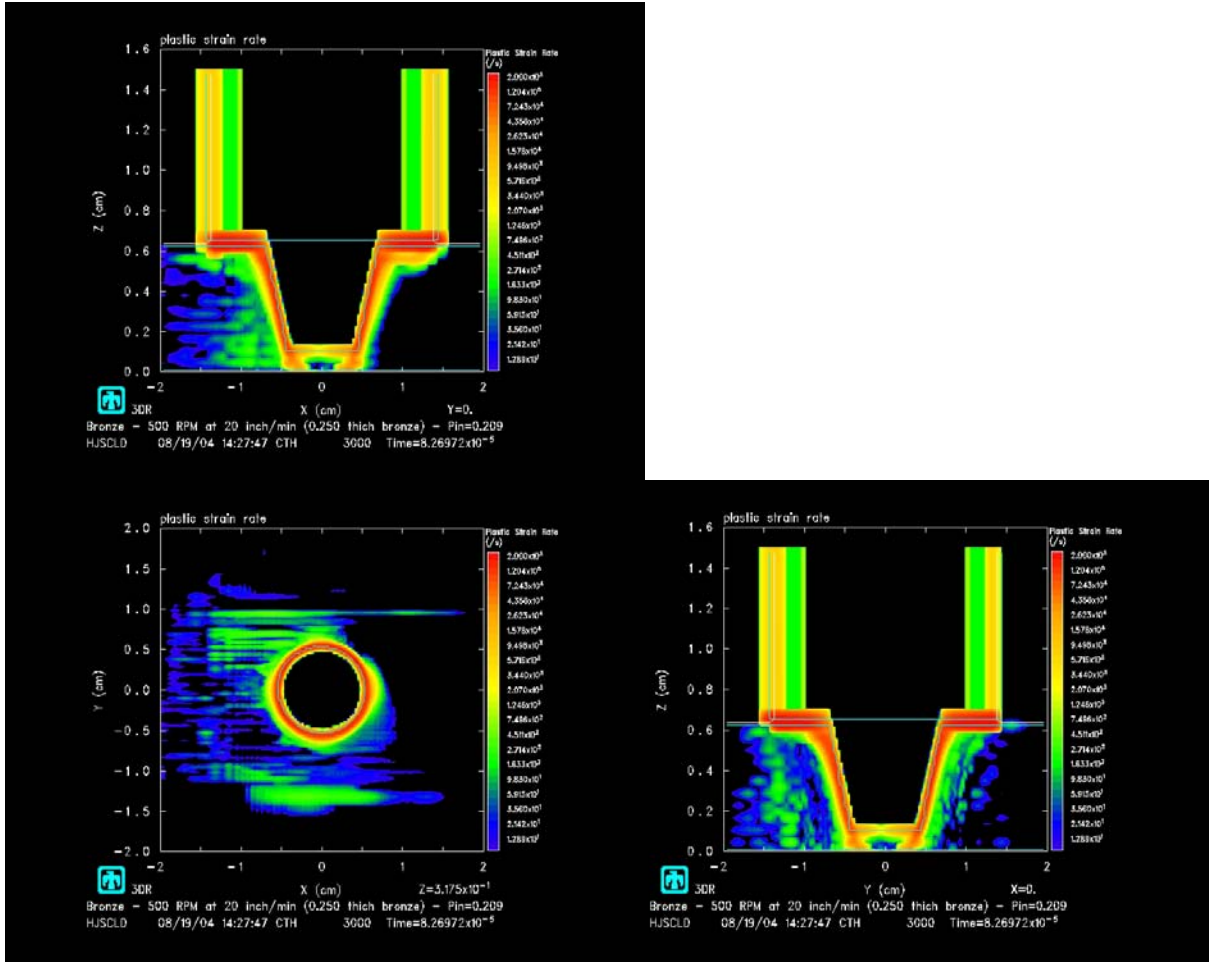


Figure 56. 500 rev/min 20 inch/min – Strain-rate distribution.

It is easy to see that the highest strain-rates are attained very near the tool/material interface with a large fraction near the shoulder. The maximum strain-rate is attained at or near the shoulder as expected since the shoulder has the highest velocity. The strain-rate field leading the tool has grown in magnitude and volume as compared to Figure 52. The strain-rate of the leading and retreating sides have considerably increased in volume.

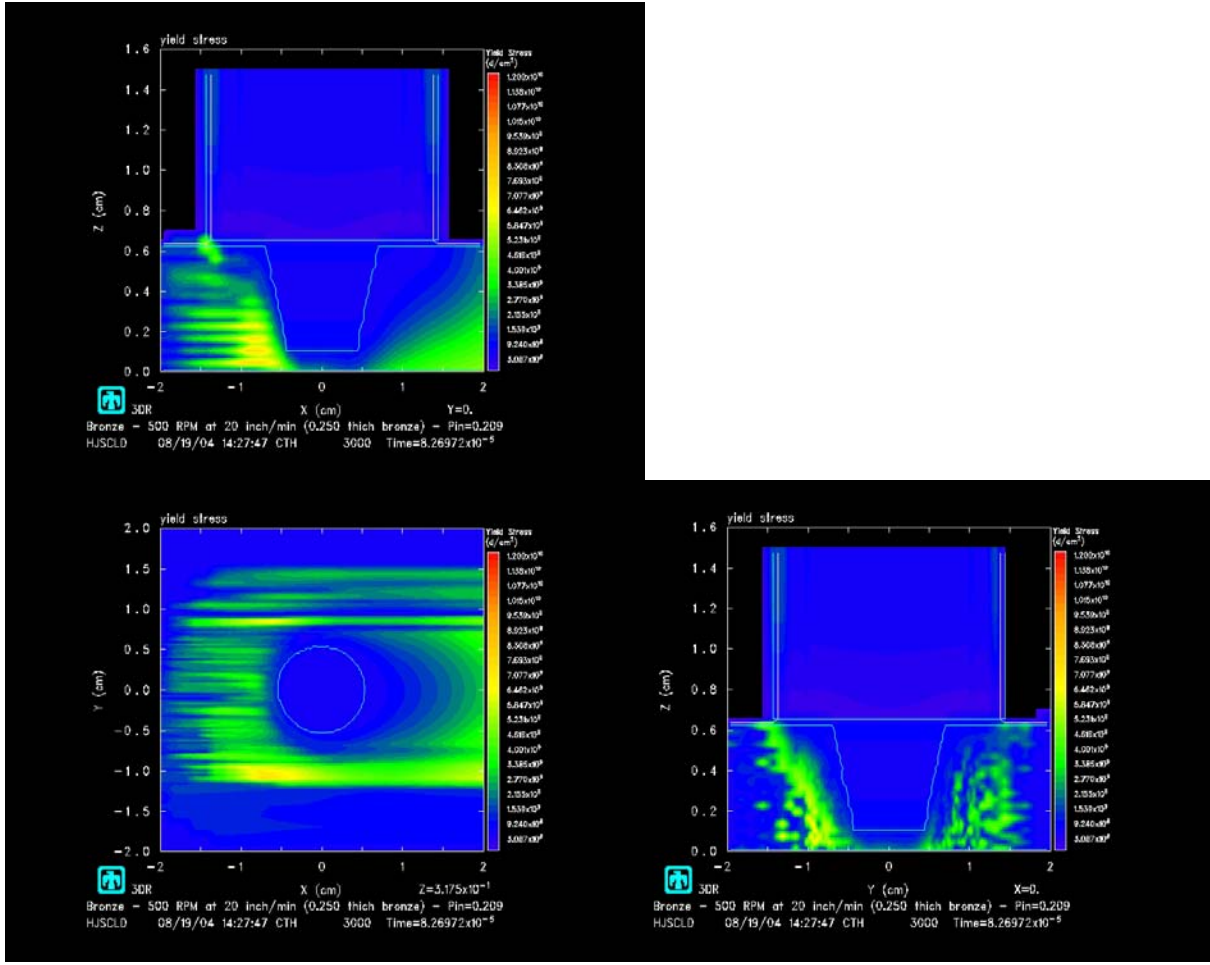


Figure 57. 500 rev/min 20 inch/min – Stress distribution.

It is easy to see that the highest stresses are attained very near the tip of the pin in the leading material. The material leading the pin has not been thermally softened enough and the highly stressed material is in contact with the bottom of the pin. The stress field leading the tool has grown while the residual stresses trailing the tool have declined compared to Figure 53.

I. 1000 RPM 1 IPM

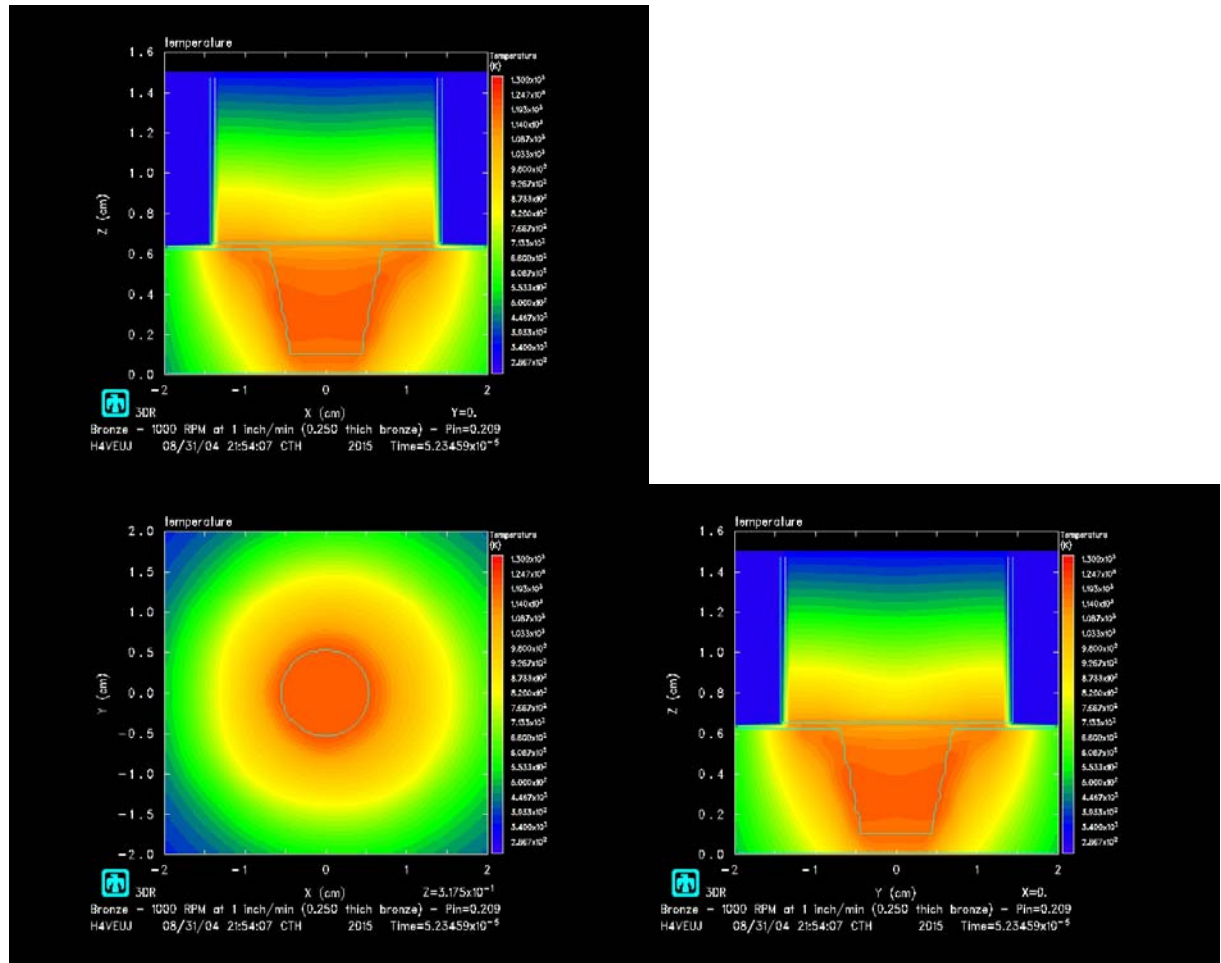


Figure 58. 1000 rev/min 1 inch/min – Temperature distribution.

It is easy to see the volume of material around the tool and the pin are nearly the same maximum temperature. The shape of the temperature profile is consistent with what the reader might imagine for a rotating tool with a traversing rate of zero. The maximum temperature attained is approximately 920 °C.

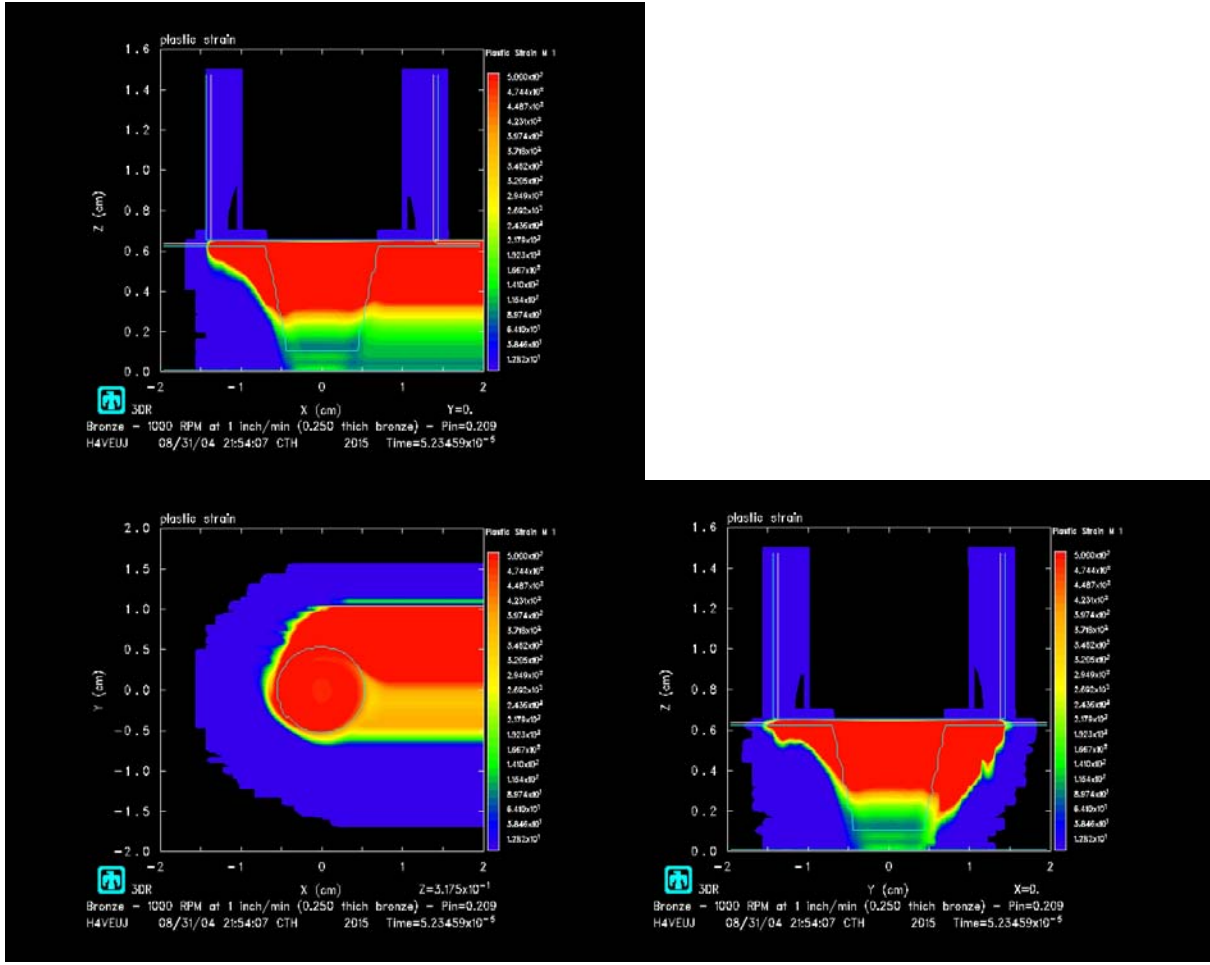


Figure 59. 1000 rev/min 1 inch/min – Strain distribution.

It is easy to see that there is a much larger volume of material which experiences a larger accumulated strain than that for lower rotation rates. The majority of the strained material ends up on the advancing side of the tool. The material in the lower half of the block is experiencing dramatically less strain than the upper half.

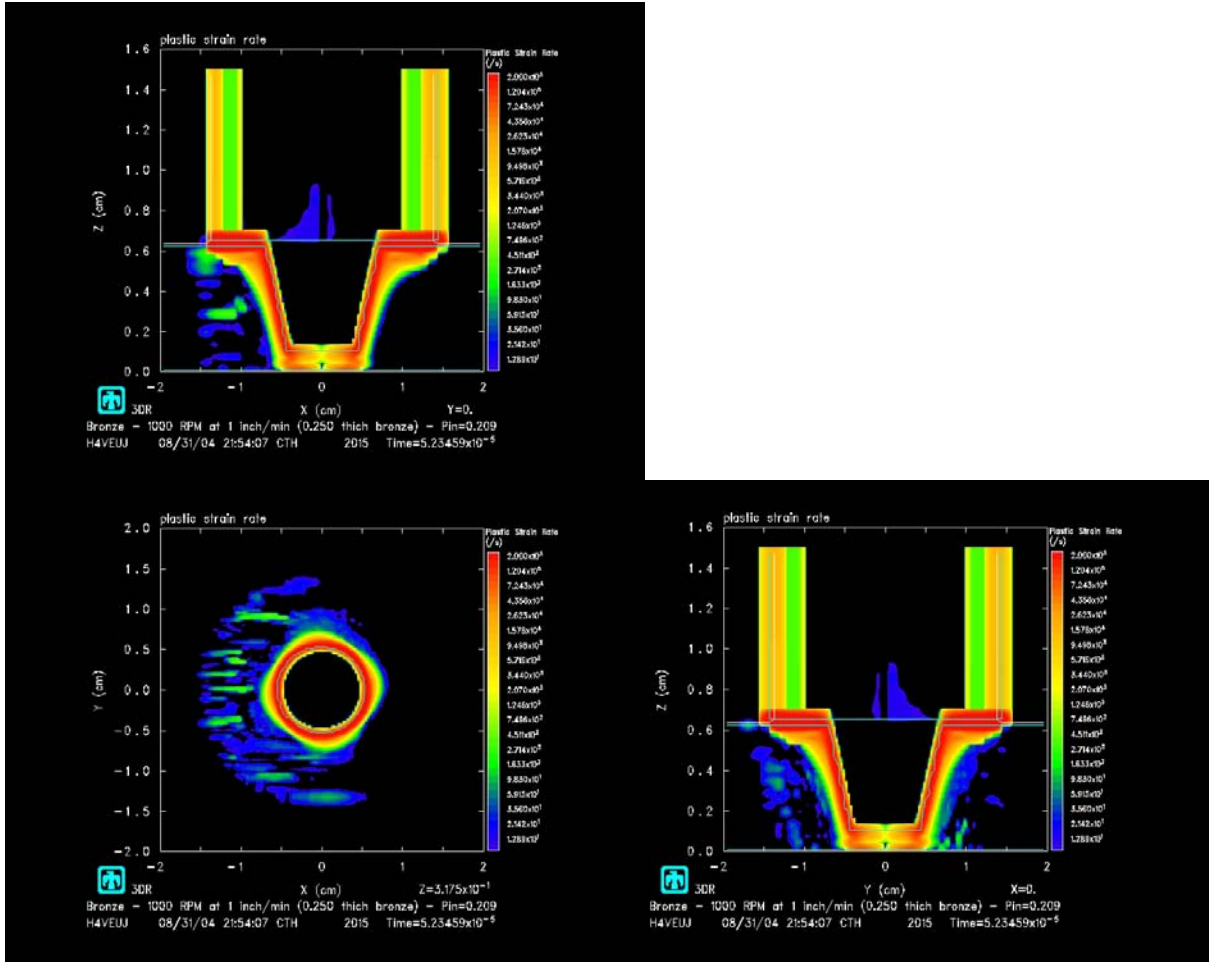


Figure 60. 1000 rev/min 1 inch/min – Strain-rate distribution.

It is easy to see that the highest strain-rates are attained very near the tool/material interface with a large fraction near the shoulder. The maximum strain-rate is attained at or near the shoulder as expected since the shoulder has the highest velocity. There is a strain-rate field leading the tool and on both sides of the tool.

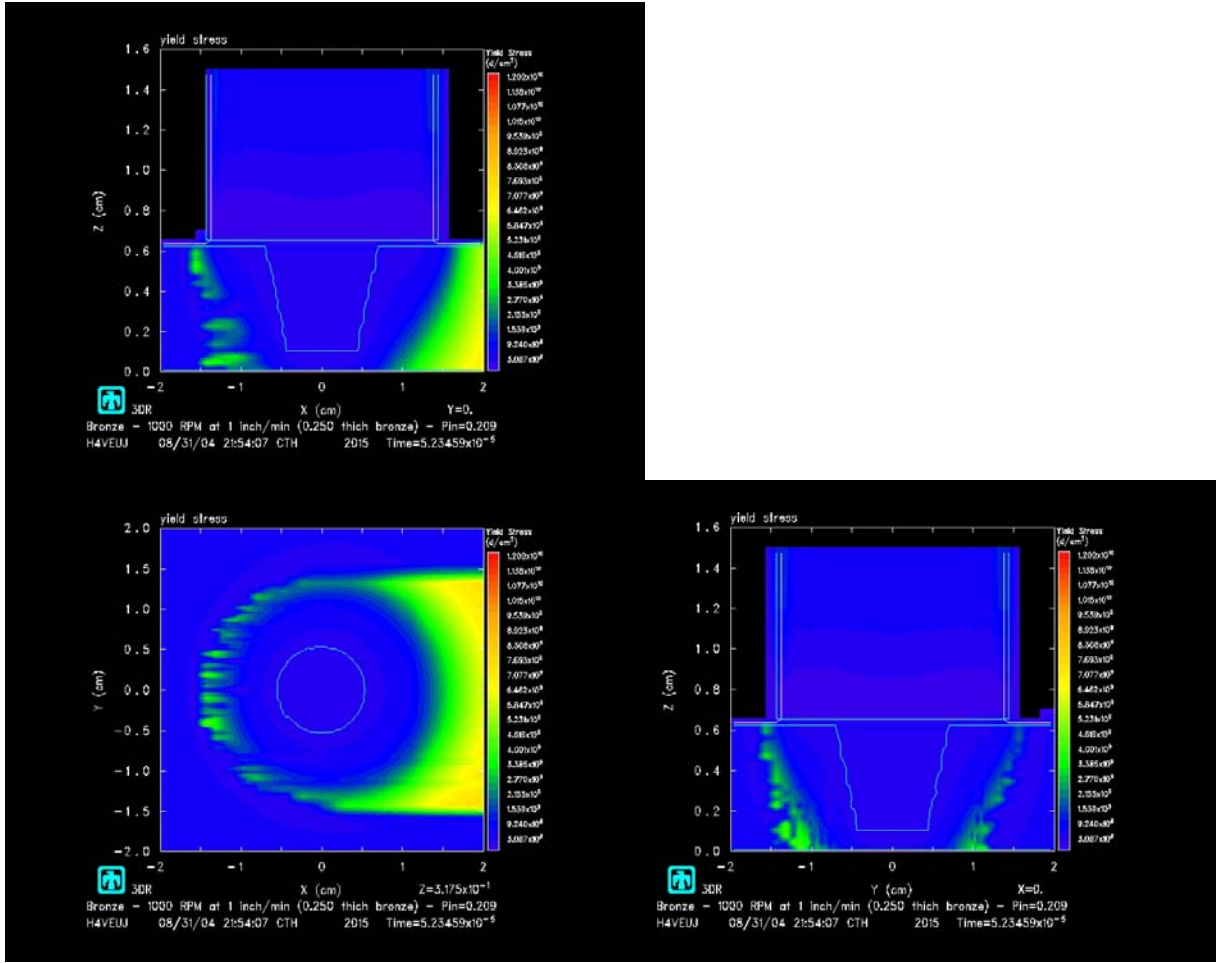


Figure 61. 1000 rev/min 1 inch/min – Stress distribution.

The low stress field around the tool correlates with the higher temperatures and the theory of thermal softening. A relatively small volume of material leading the tool is experiencing a low stress. The residual stress of the process can be seen in the xy-plane picture trailing the tool.

J. 1000 RPM 5 IPM

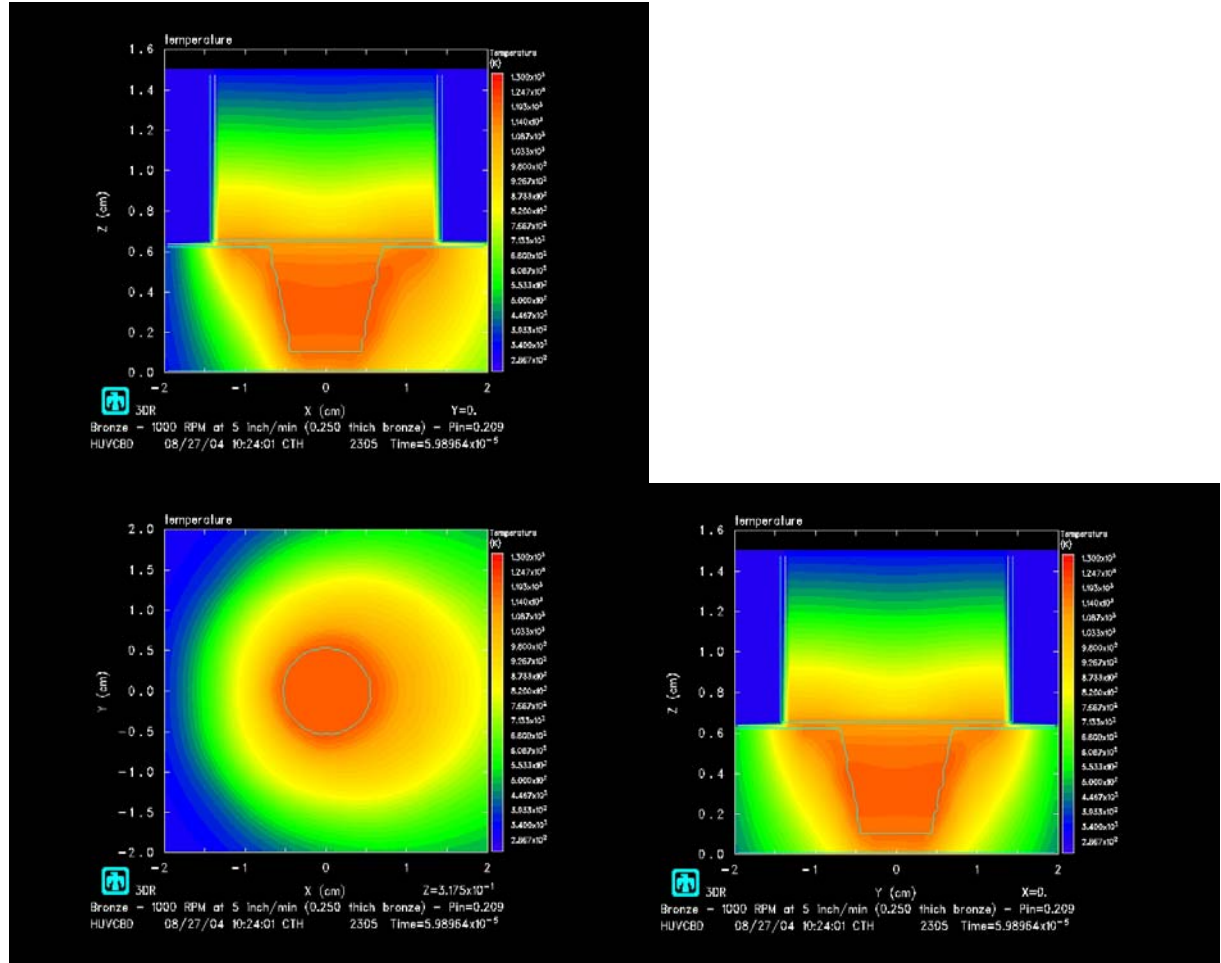


Figure 62. 1000 rev/min 5 inch/min – Temperature distribution.

It is easy to see the volume of material around the tool and the pin are nearly the same maximum temperature. The shape of the temperature profile is slightly elongated with emphasis on the trailing side of the tool. The maximum temperature attained is approximately 920 °C.

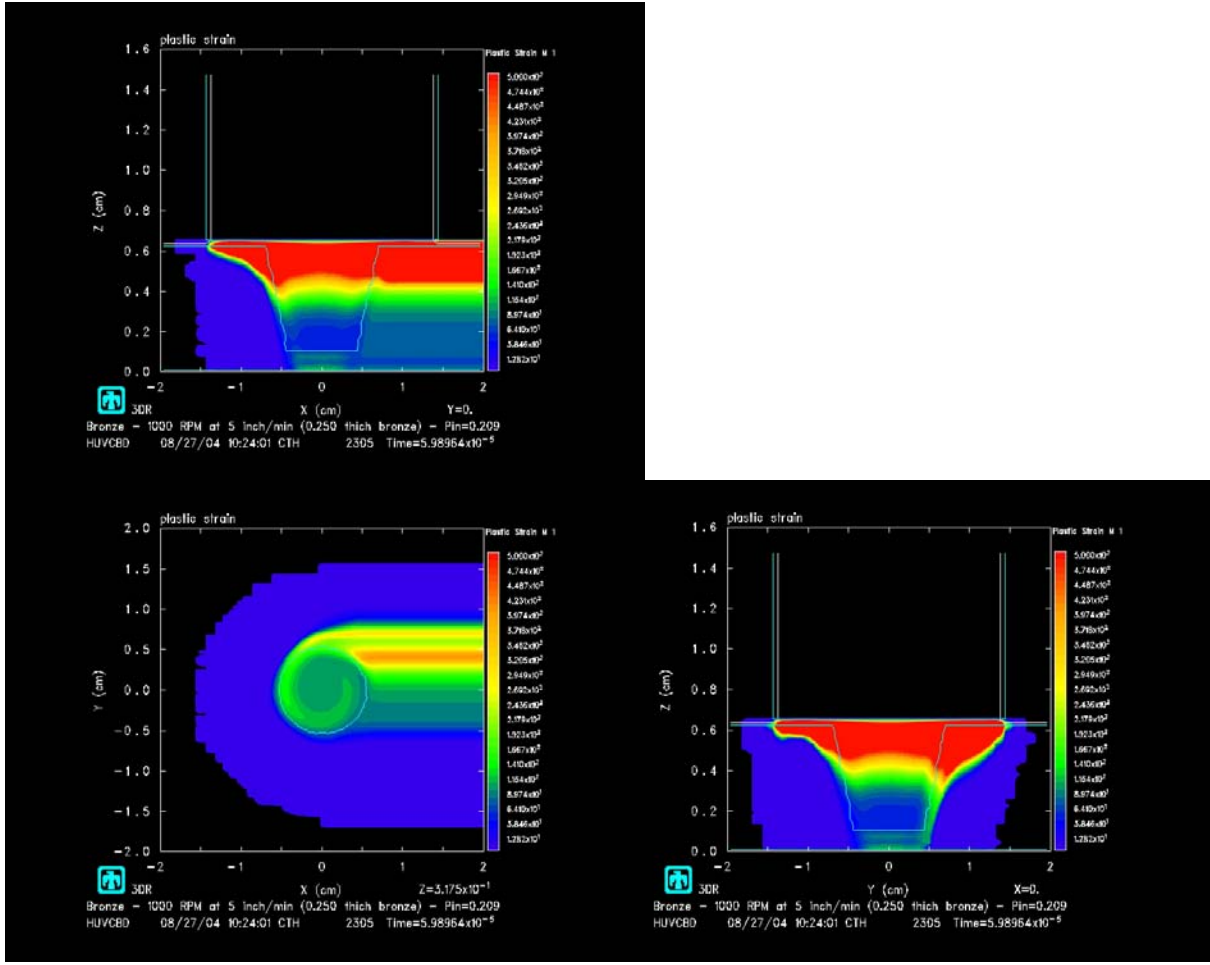


Figure 63. 1000 rev/min 5 inch/min – Strain distribution.

It is easy to see that there is a much larger volume of material which experiences a larger accumulated strain than that for lower rotation rates. The majority of the strained material ends up on the advancing side of the tool. The material in the lower two-thirds of the block is experiencing dramatically less strain than the upper third. There exists the low strain field leading and to the side of the tool with an emphasis on the retreating side.

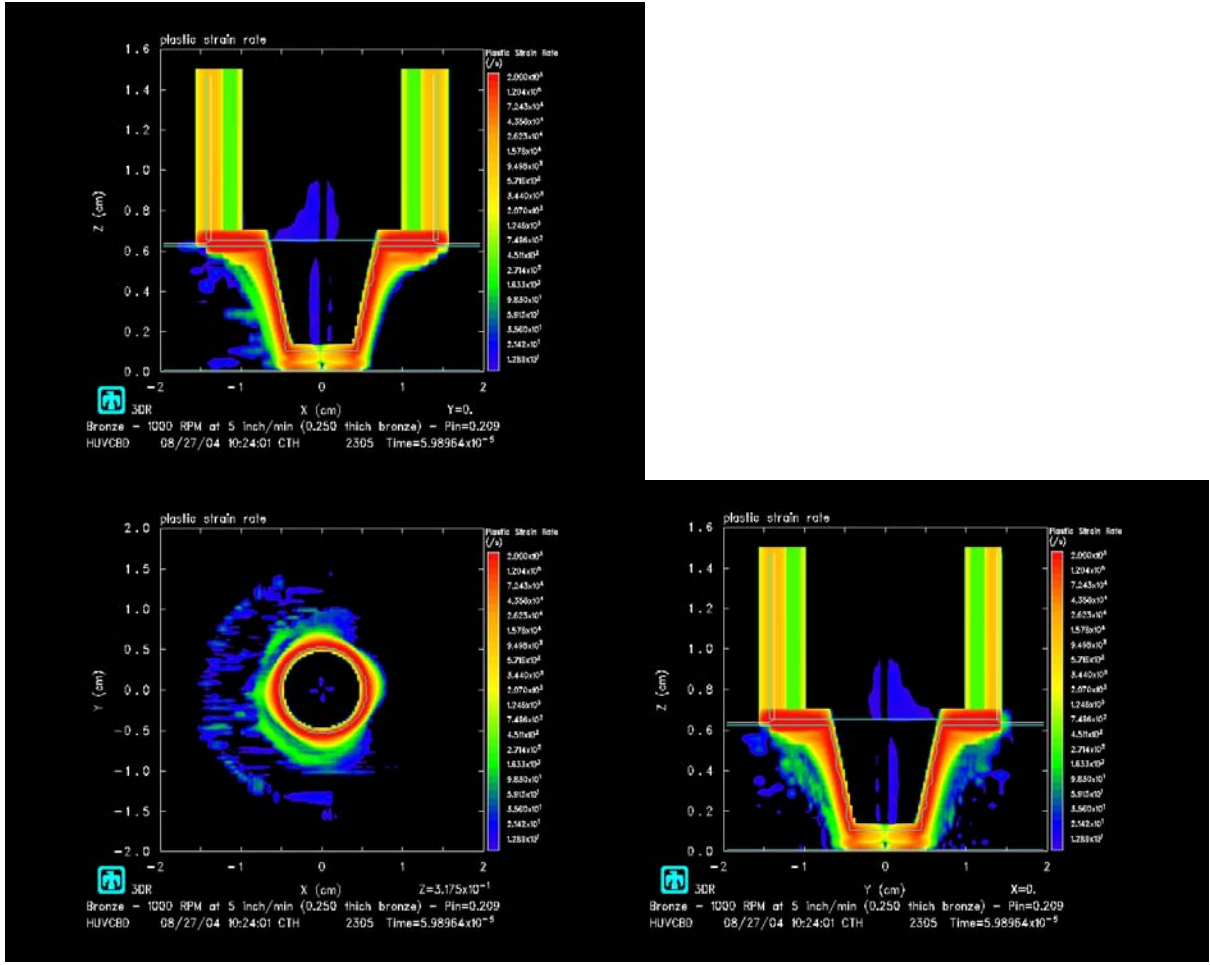


Figure 64. 1000 rev/min 5 inch/min – Strain-rate distribution.

It is easy to see that the highest strain-rates are attained very near the tool/material interface with a large fraction near the shoulder. The maximum strain-rate is attained at or near the shoulder as expected since the shoulder has the highest velocity. There is a smaller strain-rate field leading the tool and on both sides of the tool than seen in the lower traversing rate in Figure 60.

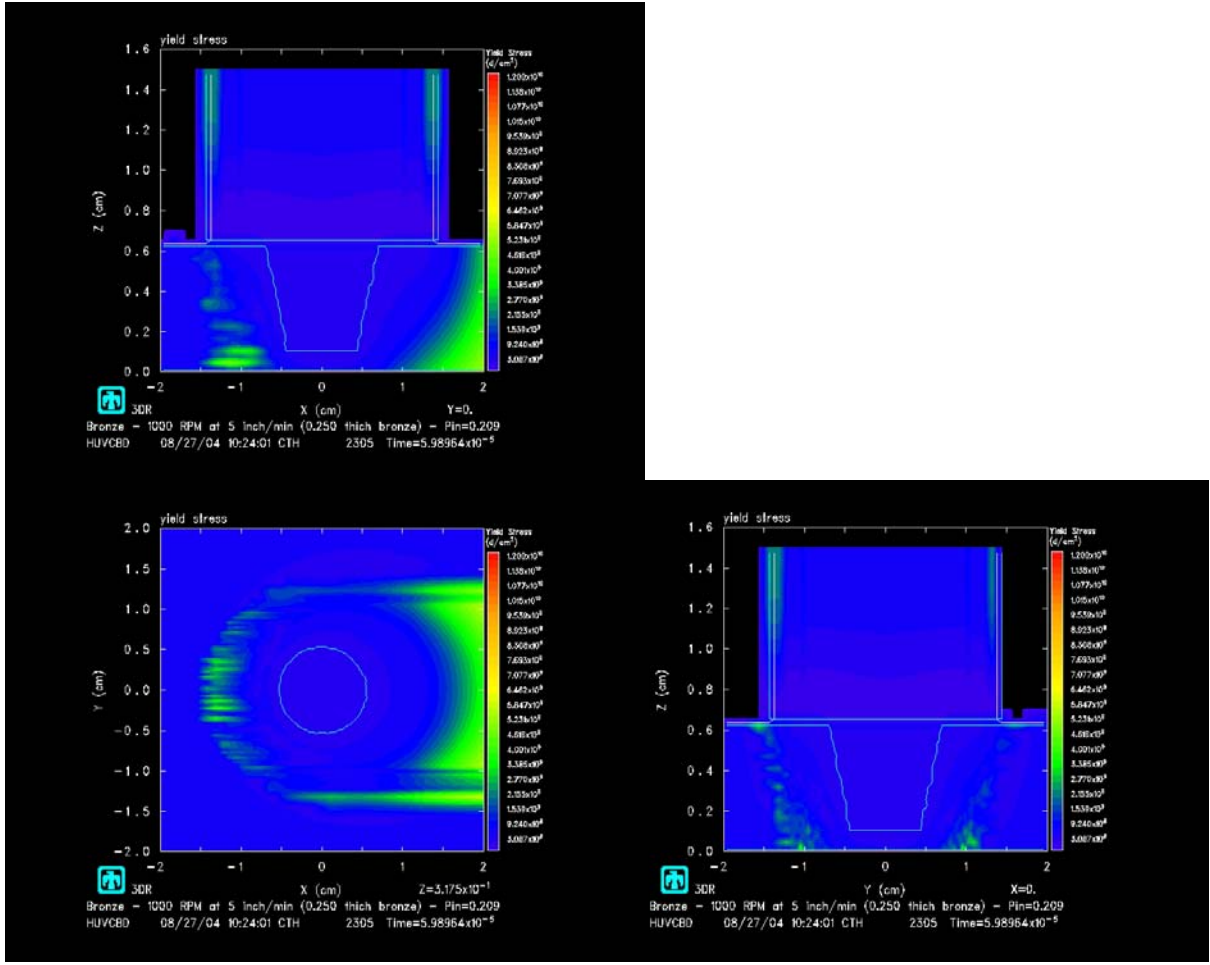


Figure 65. 1000 rev/min 5 inch/min – Stress distribution.

The higher traversing rate has slightly elongated the stress field with emphasis toward the trailing side of the tool. The low stress field around the tool correlates with the higher temperatures and the theory of thermal softening. A relatively small volume of material leading the tool is experiencing a low stress. The residual stress of the process can be seen in the xy-plane picture trailing the tool.

K. 1000 RPM 10 IPM

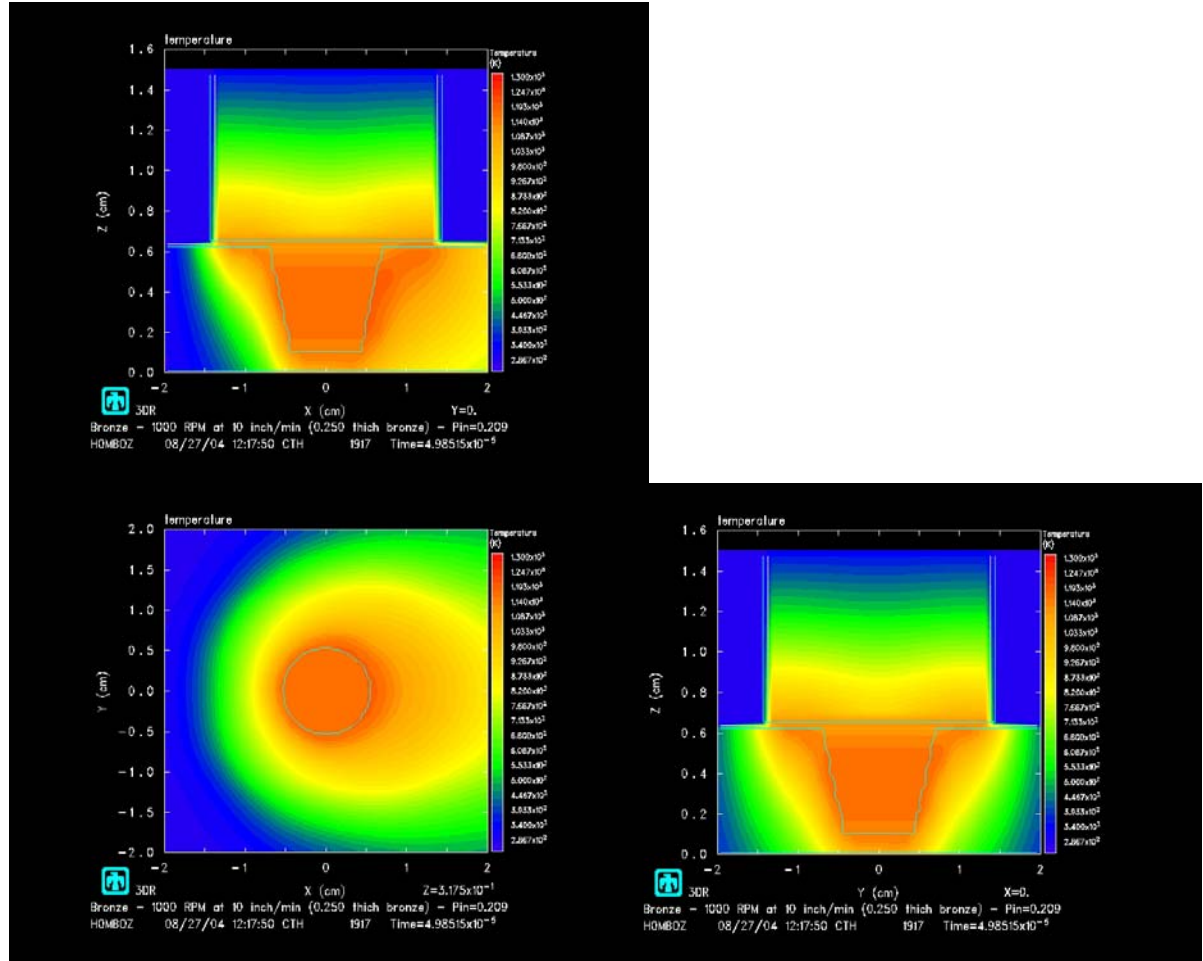


Figure 66. 1000 rev/min 10 inch/min – Temperature distribution.

It is easy to see the volume of material around the tool and the pin are nearly the same maximum temperature. The shape of the temperature profile is egg shaped with emphasis on the trailing side of the tool. The volume of material at the higher temperature on the leading side of the tool is lower than observed in Figure 62. The volume of material trailing the tool is larger. The maximum temperature attained is approximately 920 °C.

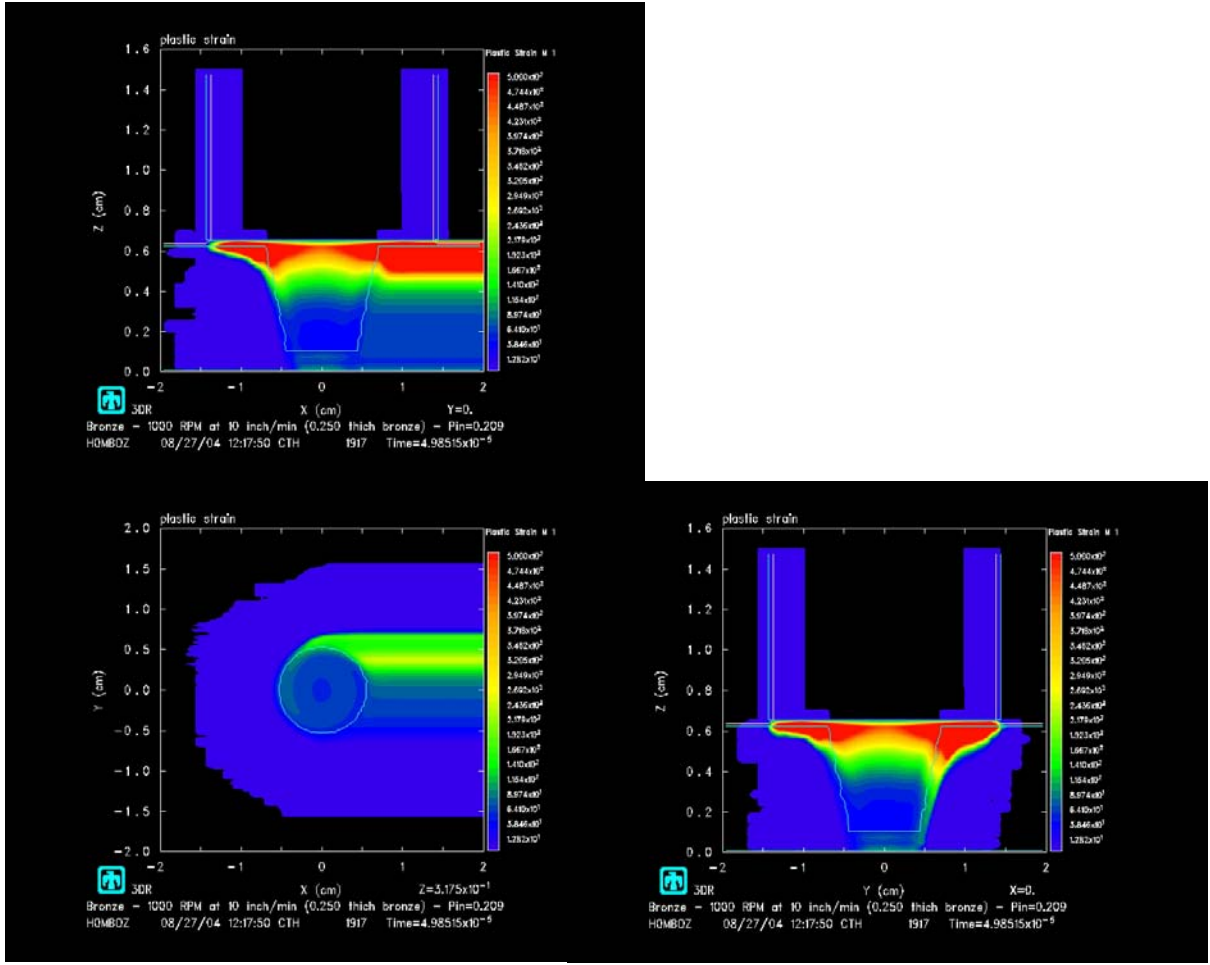


Figure 67. 1000 rev/min 10 inch/min – Strain distribution.

The highly strained material is only by near the shoulder. The material below two millimeters has accumulated very little if any strain. Of the material that is strained, the majority ends up on the advancing side of the tool. There exists the low strain field leading and to the side of the tool with an emphasis on the retreating side.

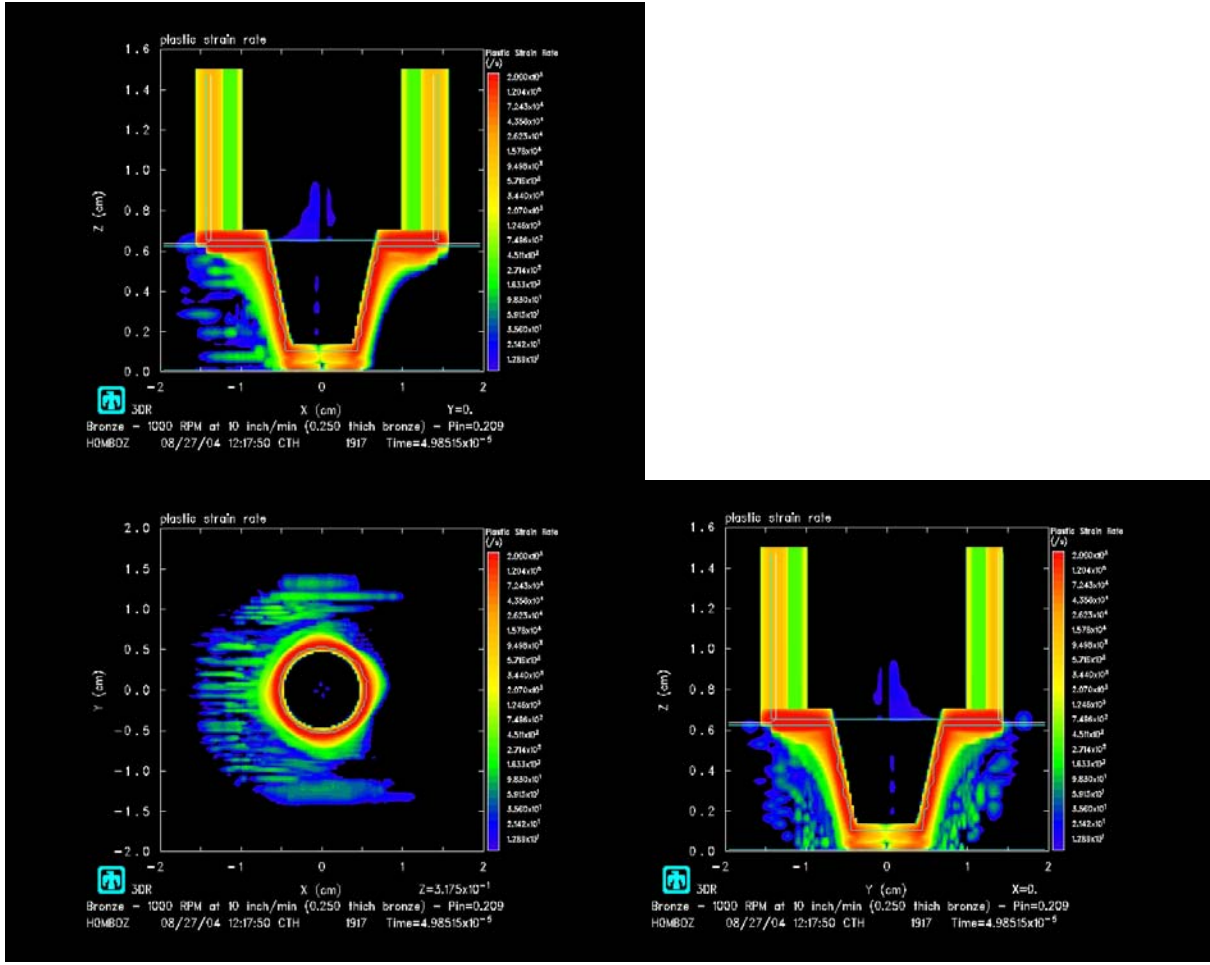


Figure 68. 1000 rev/min 10 inch/min – Strain-rate distribution.

It is easy to see that the highest strain-rates are attained very near the tool/material interface with a large fraction near the shoulder. The maximum strain-rate is attained at or near the shoulder as expected since the shoulder has the highest velocity. The strain-rate field is larger and is more intense than observed in Figure 64. The strain-rate seems to be evenly distributed leading and on the sides of the tool.

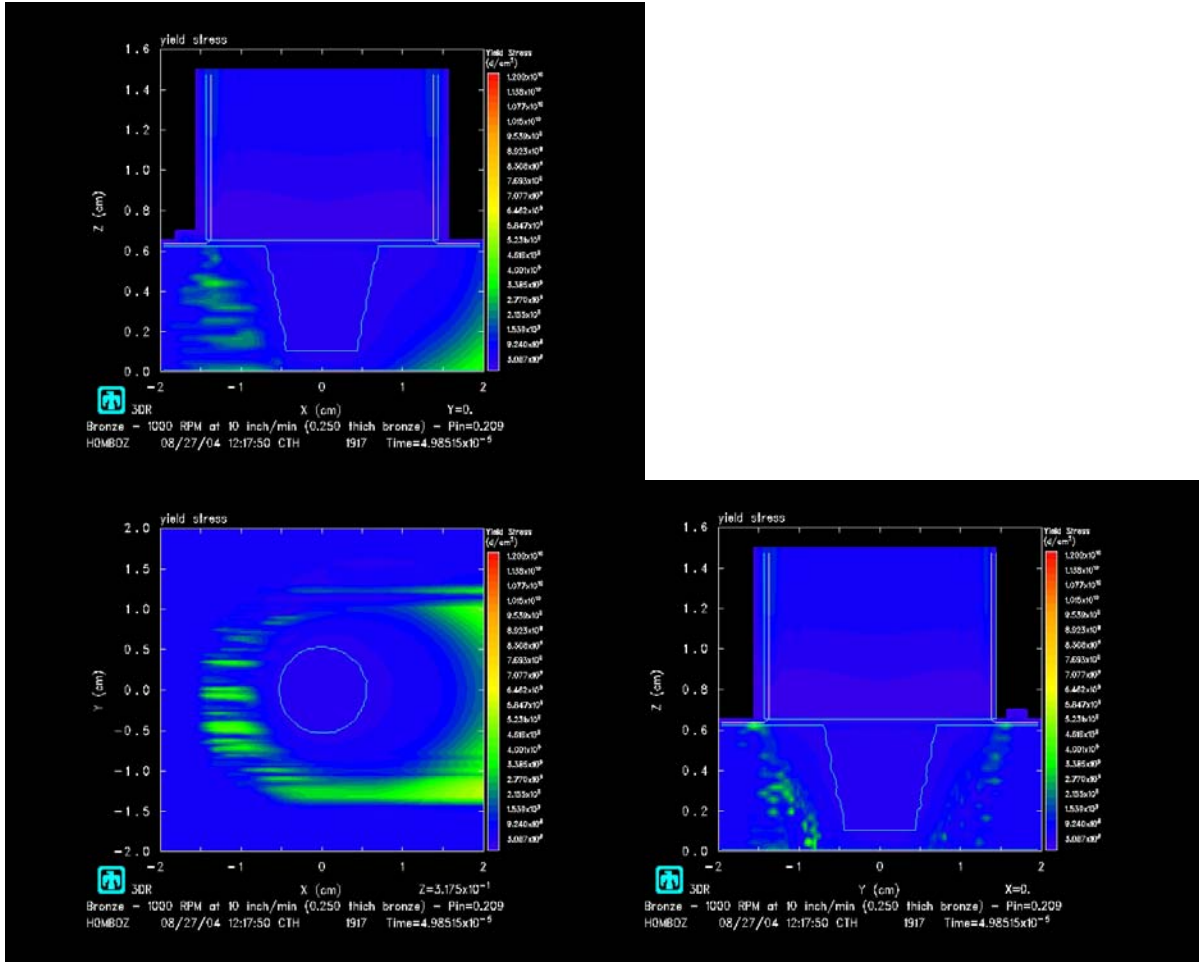


Figure 69. 1000 rev/min 10 inch/min – Stress distribution.

The higher traversing rate has slightly elongated the stress field with emphasis toward the trailing side of the tool. The low stress field around the tool correlates with the higher temperatures and the theory of thermal softening. A relatively small volume of material leading the tool is experiencing a low stress. A larger volume of material is experiencing stress on the leading to retreating side of the tool.

L. 1000 RPM 20 IPM

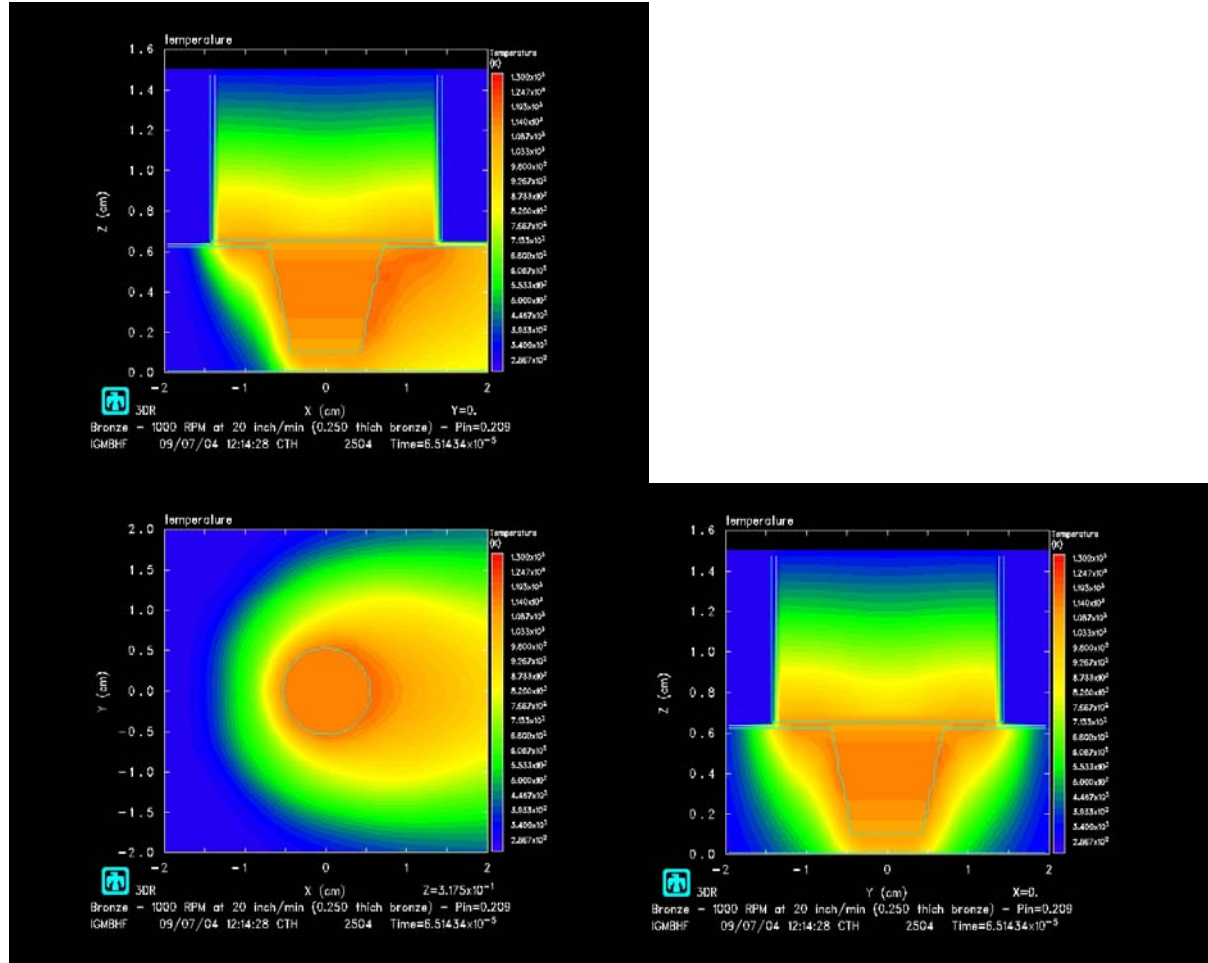


Figure 70. 1000 rev/min 20 inch/min – Temperature distribution.

The volume of material at the higher temperature on the leading side of the tool is lower than observed in Figure 66. The maximum temperature attained is approximately 920 °C. But the volume attaining this maximum temperature is very small. The majority of the higher temperature is near 850 °C. The flow of material around the tool is not allowing the material to store as much energy therefore the lower temperature of the leading material and the pin. The shape of the temperature profile is egg shaped with emphasis on the trailing side of the tool. The volume of material at or above 800 °C which is trailing the tool is larger.

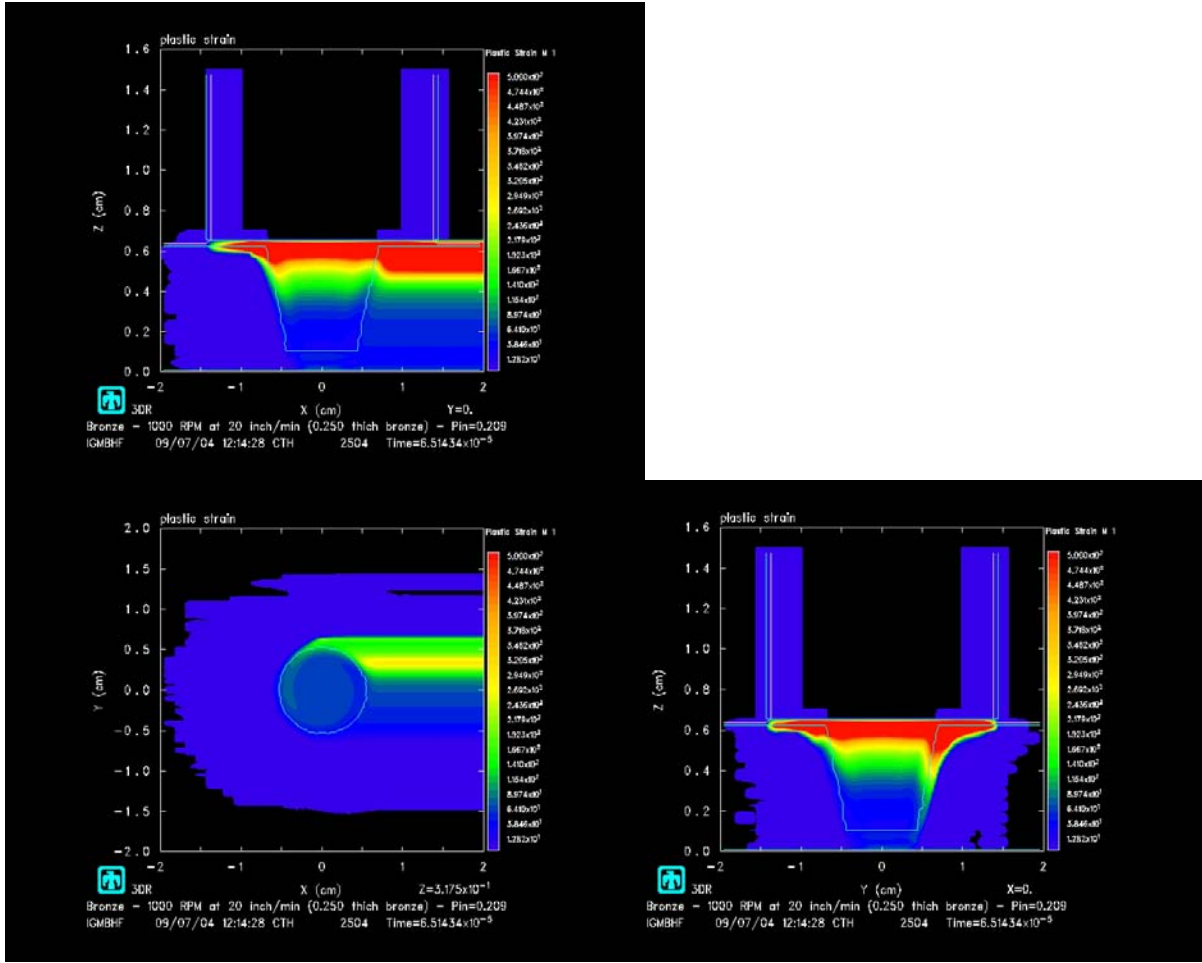


Figure 71. 1000 rev/min 20 inch/min – Strain distribution.

The highly strained material is only by near the shoulder. The material below two millimeters has accumulated very little if any strain. Of the material that is strained, the majority ends up on the advancing side of the tool. There exists the low strain field leading and to the side of the tool with an emphasis on the retreating side.

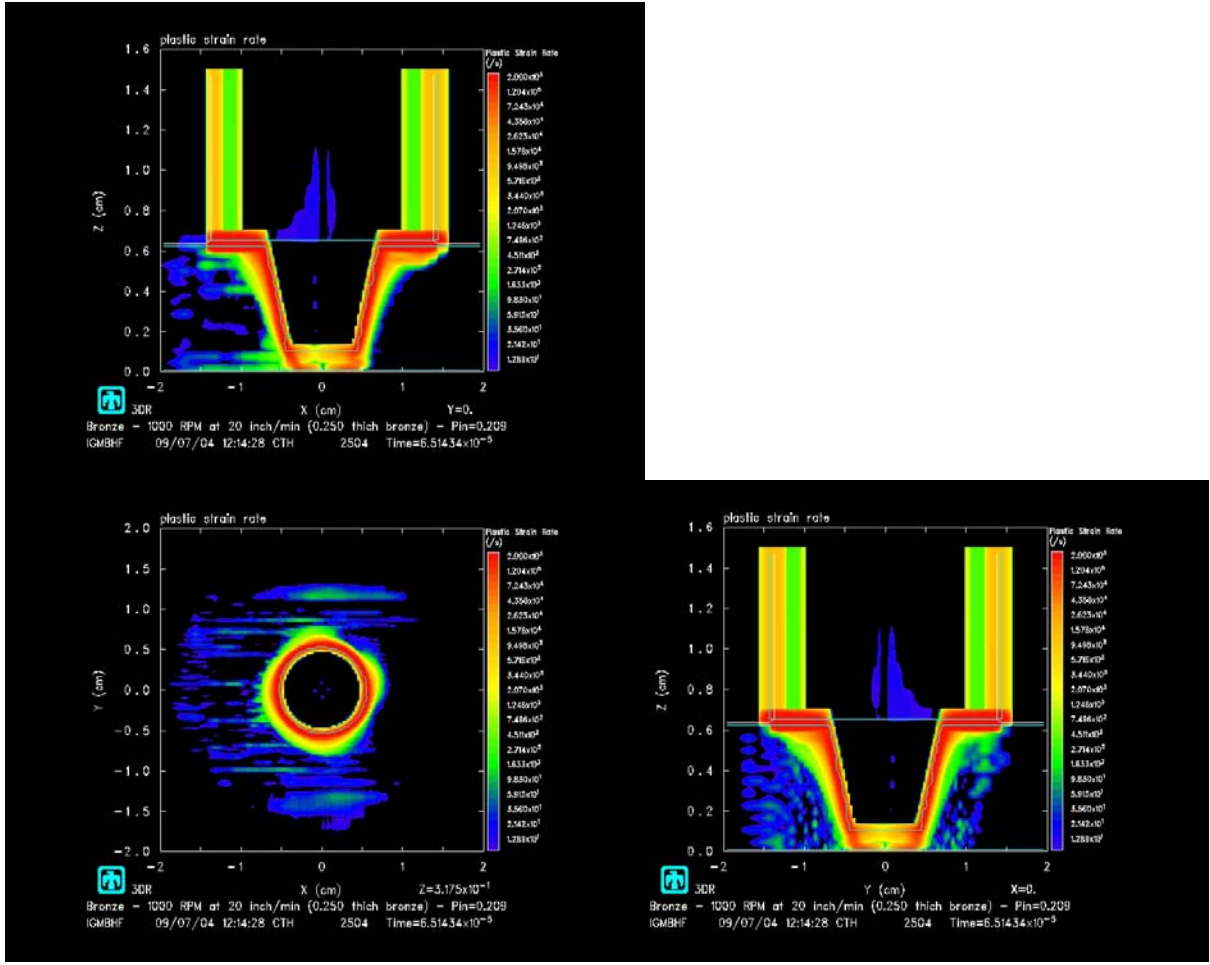


Figure 72. 1000 rev/min 20 inch/min – Strain-rate distribution.

It is easy to see that the highest strain-rates are attained very near the tool/material interface with a large fraction near the shoulder. The maximum strain-rate is attained at or near the shoulder as expected since the shoulder has the highest velocity. The strain-rate field is larger and is more intense than observed in Figure 68. The strain-rate field is larger leading the tool and on the retreating side.

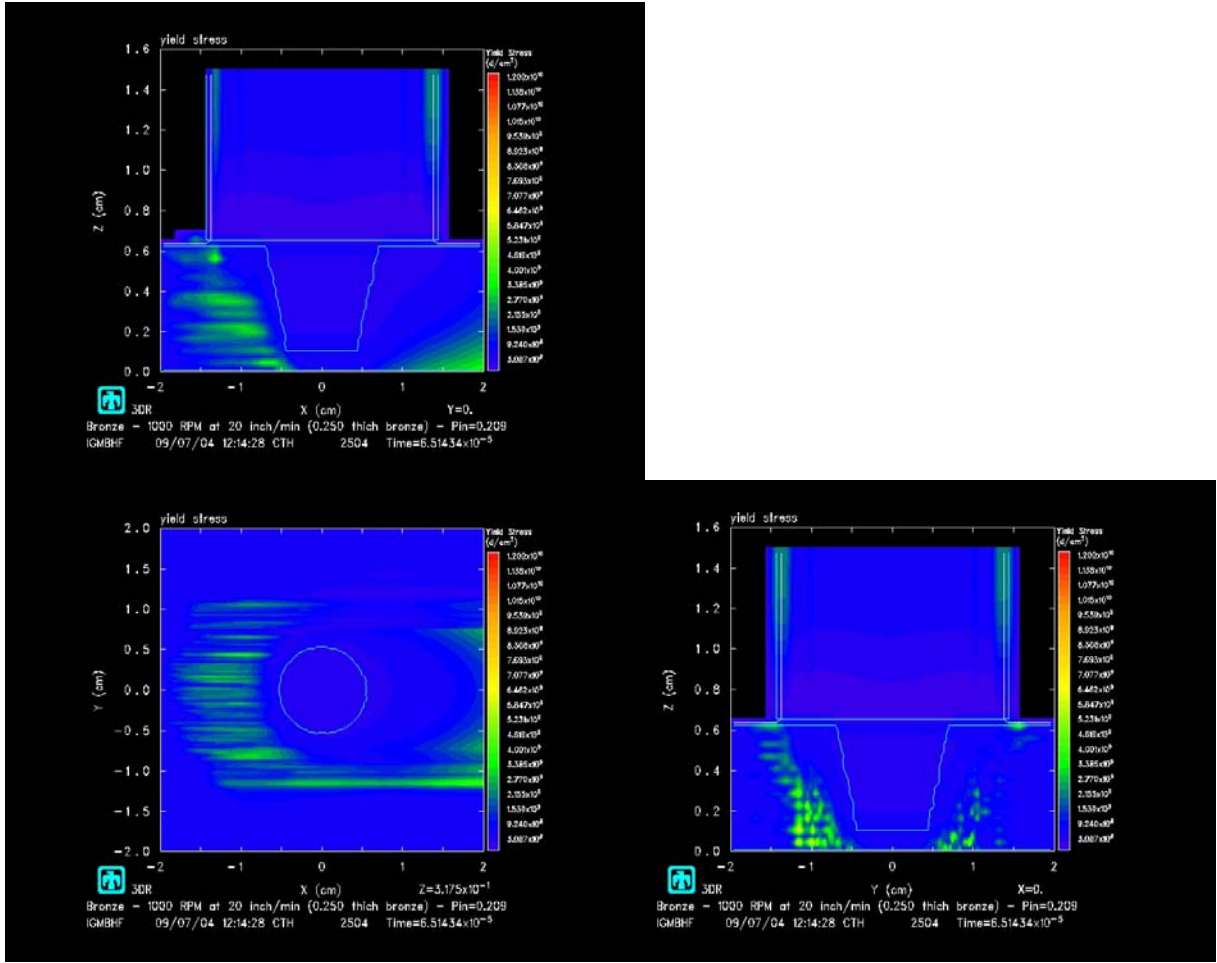


Figure 73. 1000 rev/min 20 inch/min – Stress distribution.

The higher traversing rate has slightly elongated the stress field with emphasis toward the trailing side of the tool. The low stress field around the tool correlates with the higher temperatures and the theory of thermal softening. A relatively small volume of material leading the tool is experiencing a low stress. A larger volume of material is experiencing stress on the leading to retreating side of the tool. It is noteworthy to compare Figure 69 to this. The field for 20 ipm is smaller in volume yet more intense on the retreating side.

M. 2000 RPM 1 IPM

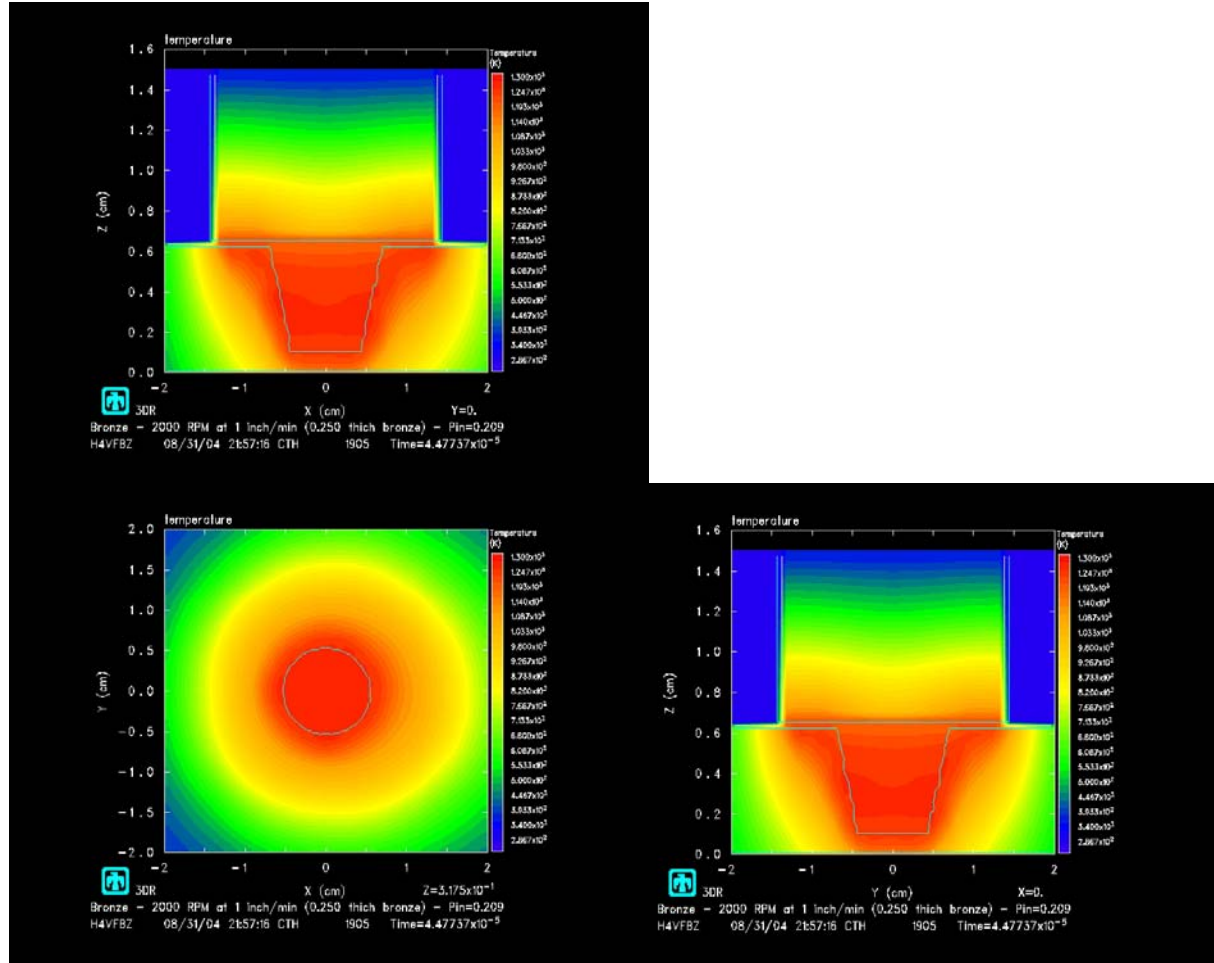


Figure 74. 2000 rev/min 1 inch/min – Temperature distribution.

It is easy to see the volume of material around the tool and the pin are nearly the same maximum temperature. The shape of the temperature profile is consistent with what the reader might imagine for a rotating tool with a traversing rate of zero. The maximum temperature attained is approximately 1000 °C.

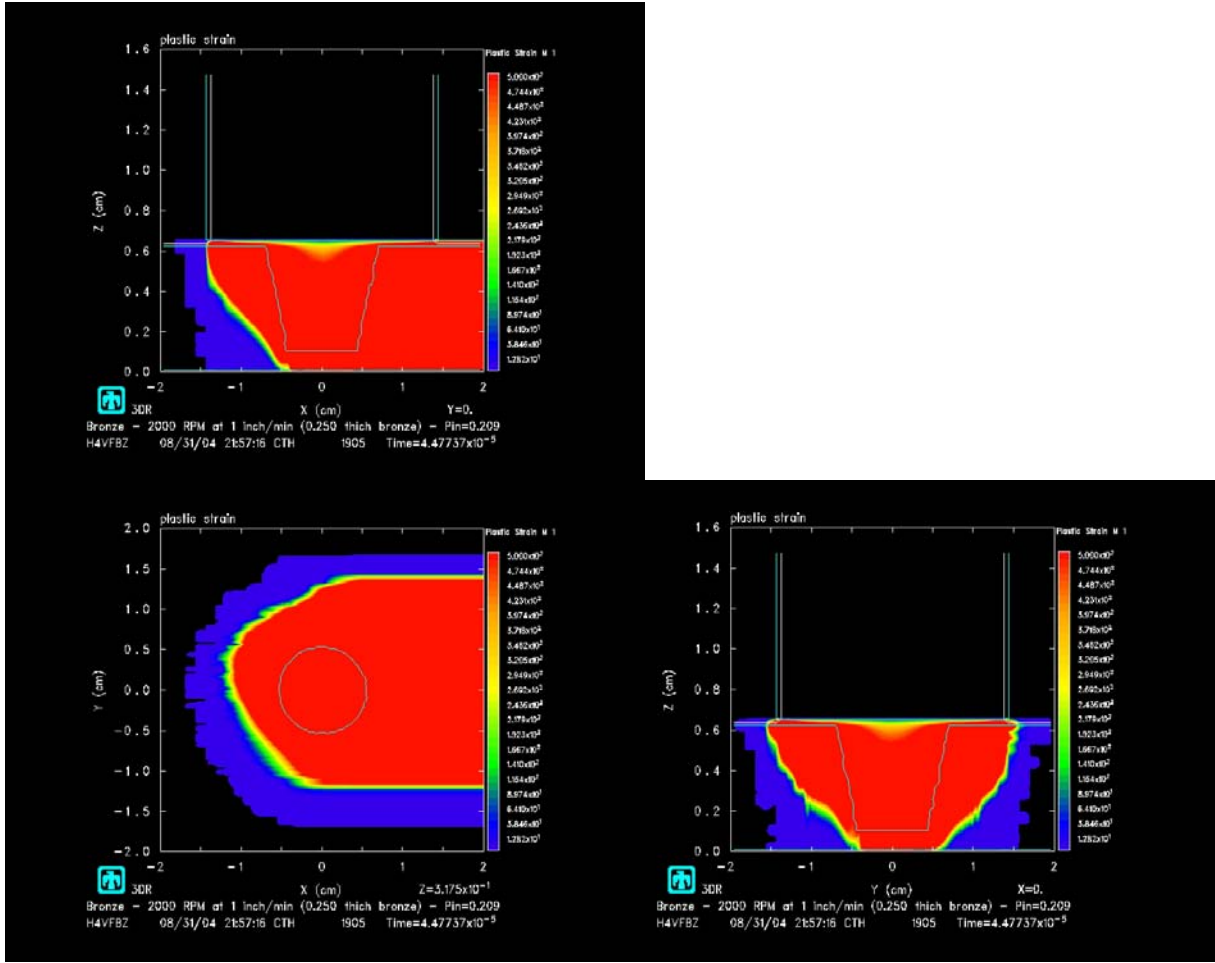


Figure 75. 2000 rev/min 1 inch/min – Strain distribution.

It is easy to see that there is a much larger volume of material which experiences a larger accumulated strain than that for lower rotation rates. The transverse cross-section is very nearly a semicircle. This means that there is very little distinction between the retreating and the advancing sides. There is still an evenly spaced volume around the tool experiencing a low strain.

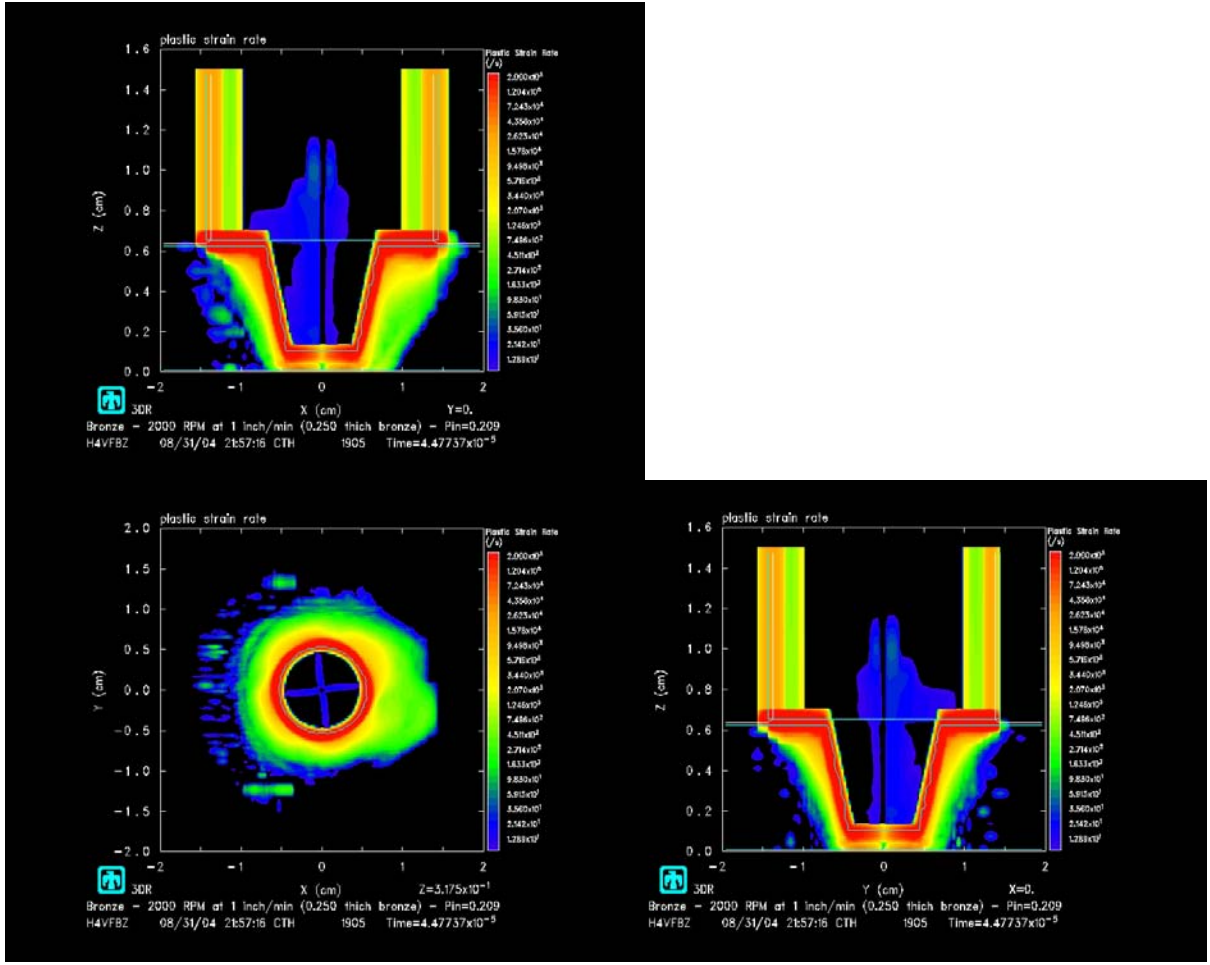


Figure 76. 2000 rev/min 1 inch/min – Strain-rate distribution.

It is easy to see that the highest strain-rates are attained very near the tool/material interface with a large fraction near the shoulder. The maximum strain-rate is attained at or near the shoulder as expected since the shoulder has the highest velocity. There is a strain-rate field leading the tool. A larger volume of material around the tool is experiencing significant strain-rate. The strain-rate profile is elongated with emphasis on the trailing side.

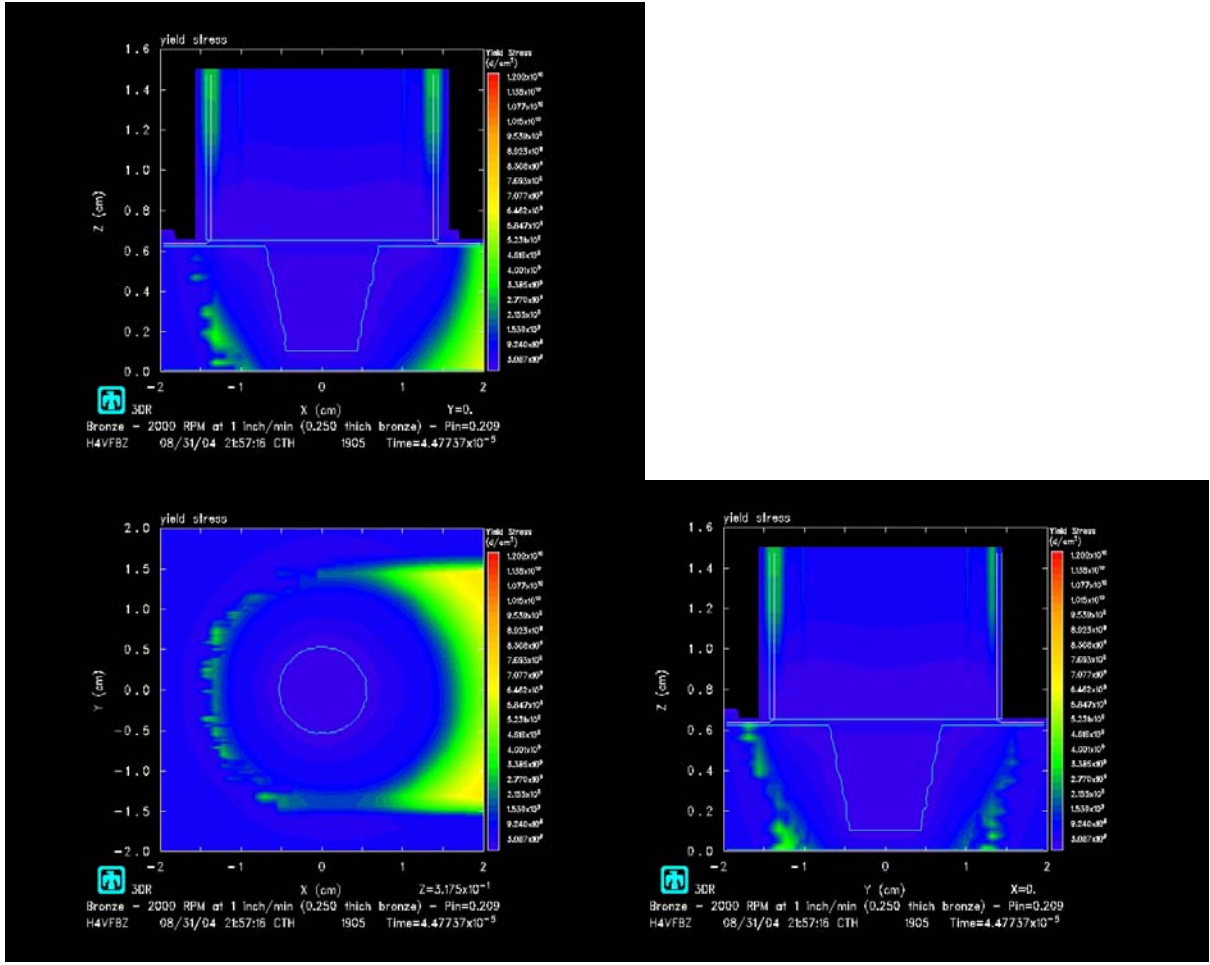


Figure 77. 2000 rev/min 1 inch/min – Stress distribution.

The low stress field around the tool correlates with the higher temperatures and the theory of thermal softening. A relatively small volume of material leading the tool is experiencing a low stress. The residual stress of the process can be seen in the xy-plane picture trailing the tool.

N. 2000 RPM 5 IPM

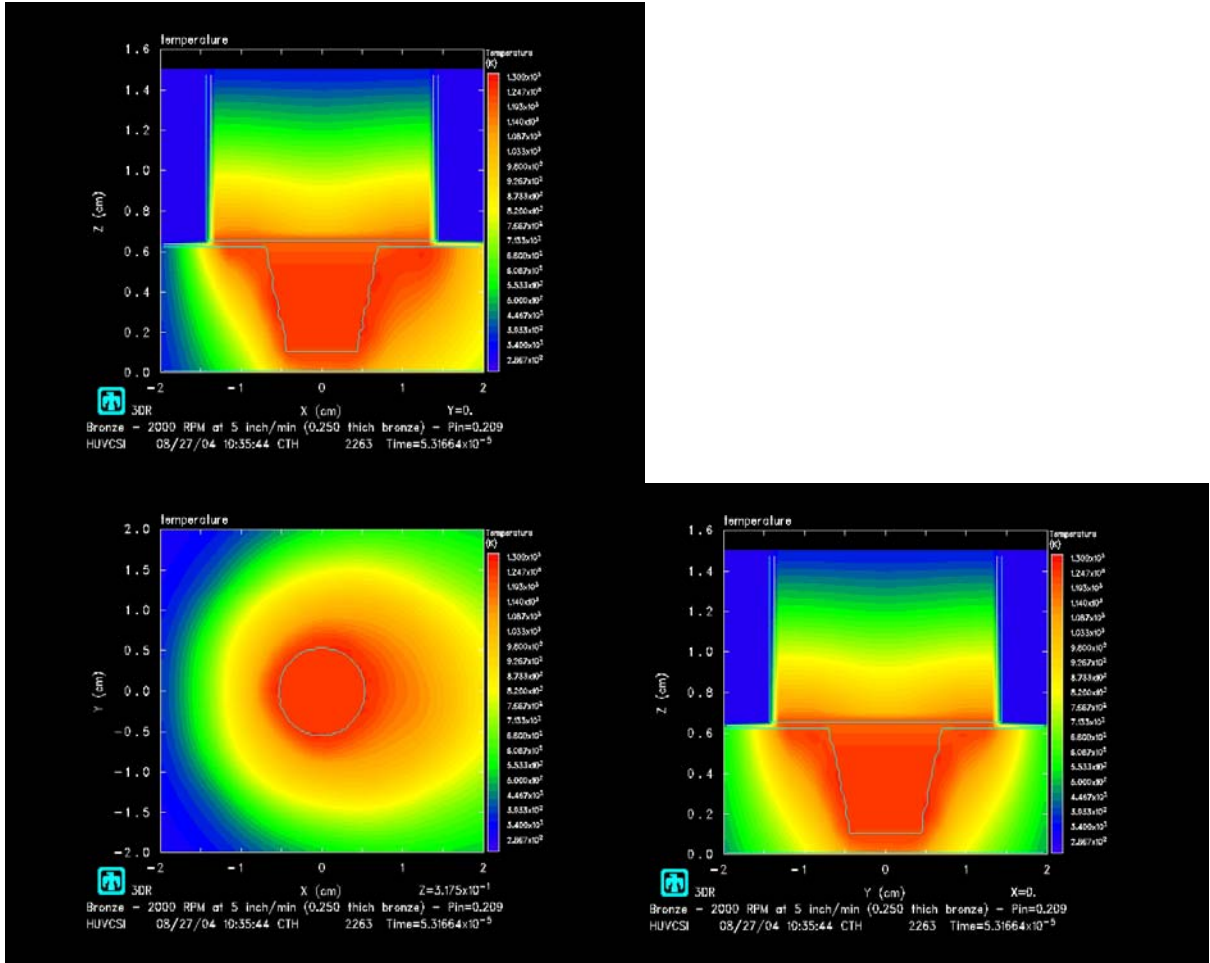


Figure 78. 2000 rev/min 5 inch/min – Temperature distribution.

It is easy to see the volume of material around the tool and the pin are nearly the same maximum temperature. The temperature profile is elongated with emphasis on the trailing side of the tool. The material flowing around the tool has significantly lowered the temperature in the volume leading the tool. The maximum temperature attained is approximately 1000 °C trailing the tool.

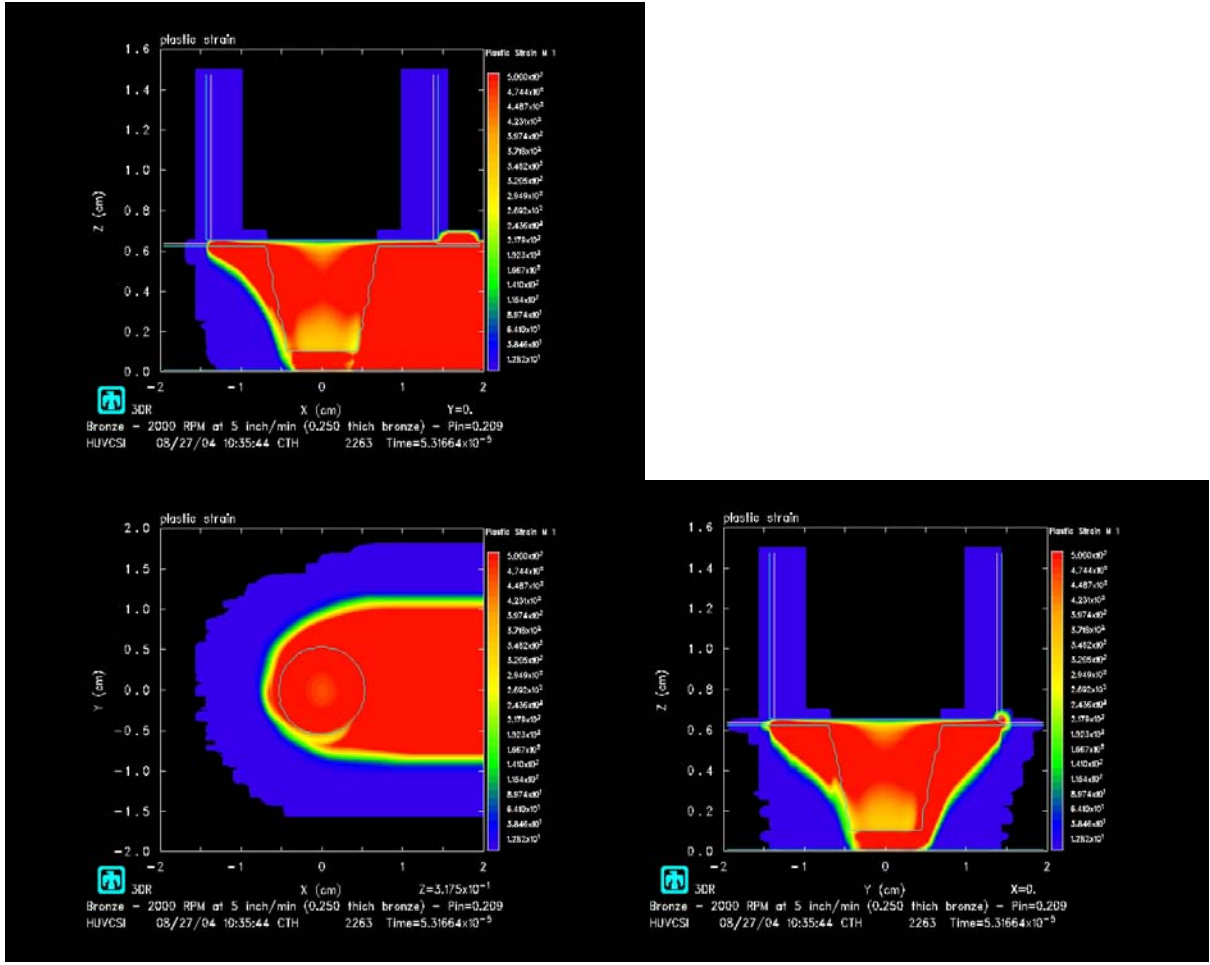


Figure 79. 2000 rev/min 5 inch/min – Strain distribution.

It is easy to see that there is a much larger volume of material which experiences a larger accumulated strain than that for lower rotation rates. The transverse cross-section is very nearly a blunted triangle. There is a slight difference between the retreating and the advancing sides. The advancing side has more volume that is accumulating more strain. There is still an evenly spaced volume around the tool experiencing a low strain.

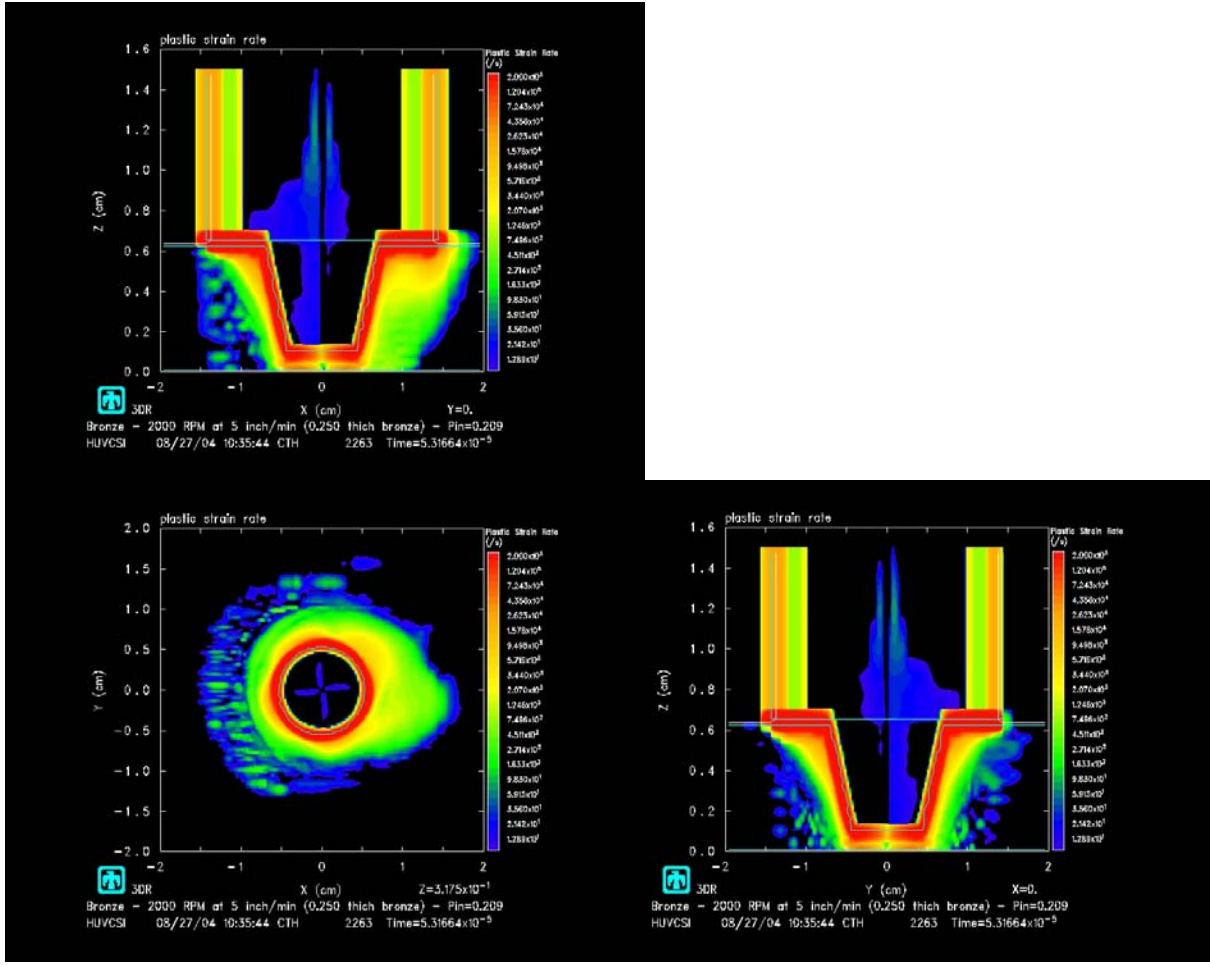


Figure 80. 2000 rev/min 5 inch/min – Strain-rate distribution.

It is easy to see that the highest strain-rates are attained very near the tool/material interface with a large fraction near the shoulder. The maximum strain-rate is attained at or near the shoulder as expected since the shoulder has the highest velocity. There is a strain-rate field leading the tool. A larger volume of material around the tool is experiencing significant strain-rate. The strain-rate profile is elongated with emphasis on the trailing side.

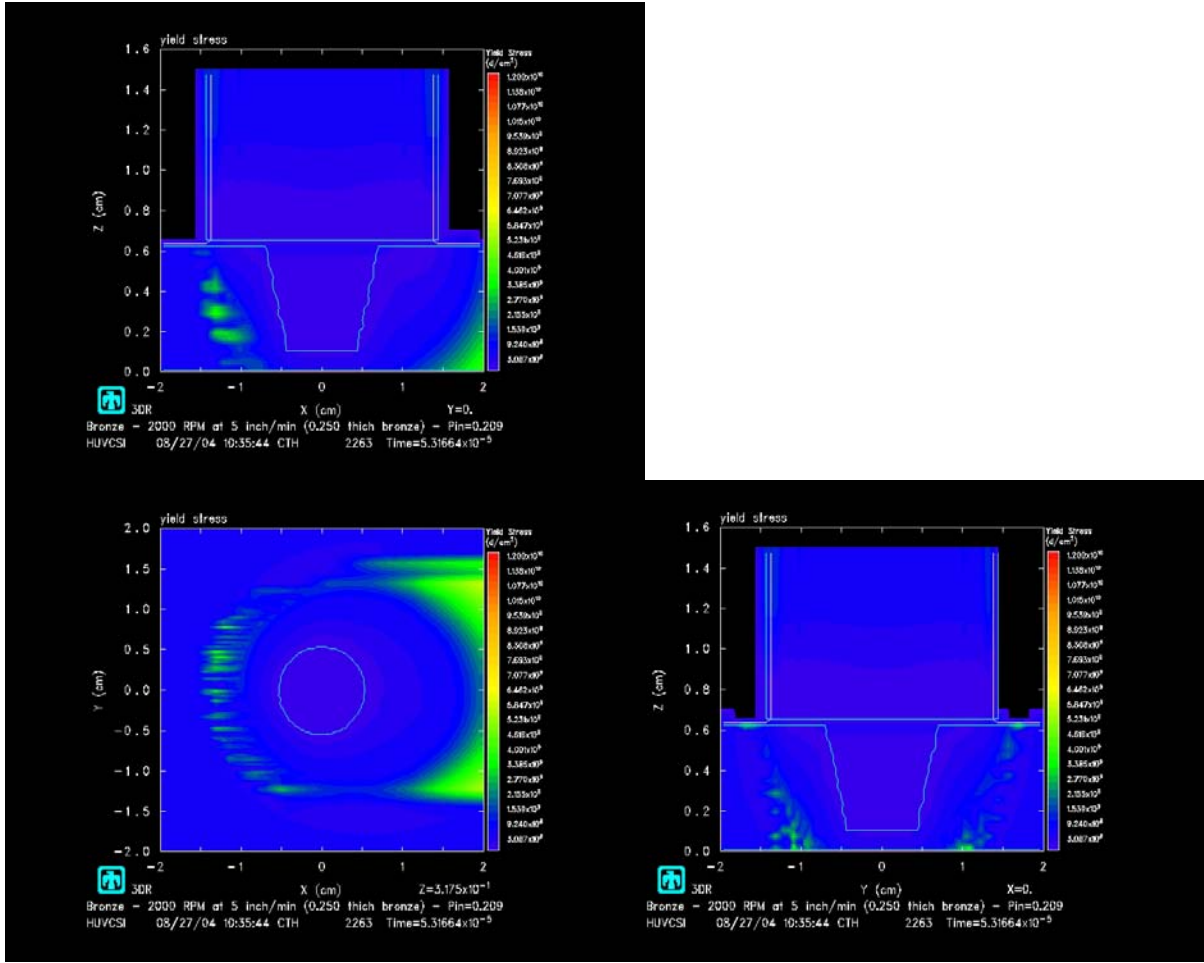


Figure 81. 2000 rev/min 5 inch/min – Stress distribution.

The elongated low stress field around the tool correlates with the higher temperatures and the theory of thermal softening. A relatively small volume of material leading the tool is experiencing a low stress. The residual stress of the process can be seen in the xy-plane picture trailing the tool.

O. 2000 RPM 10 IPM

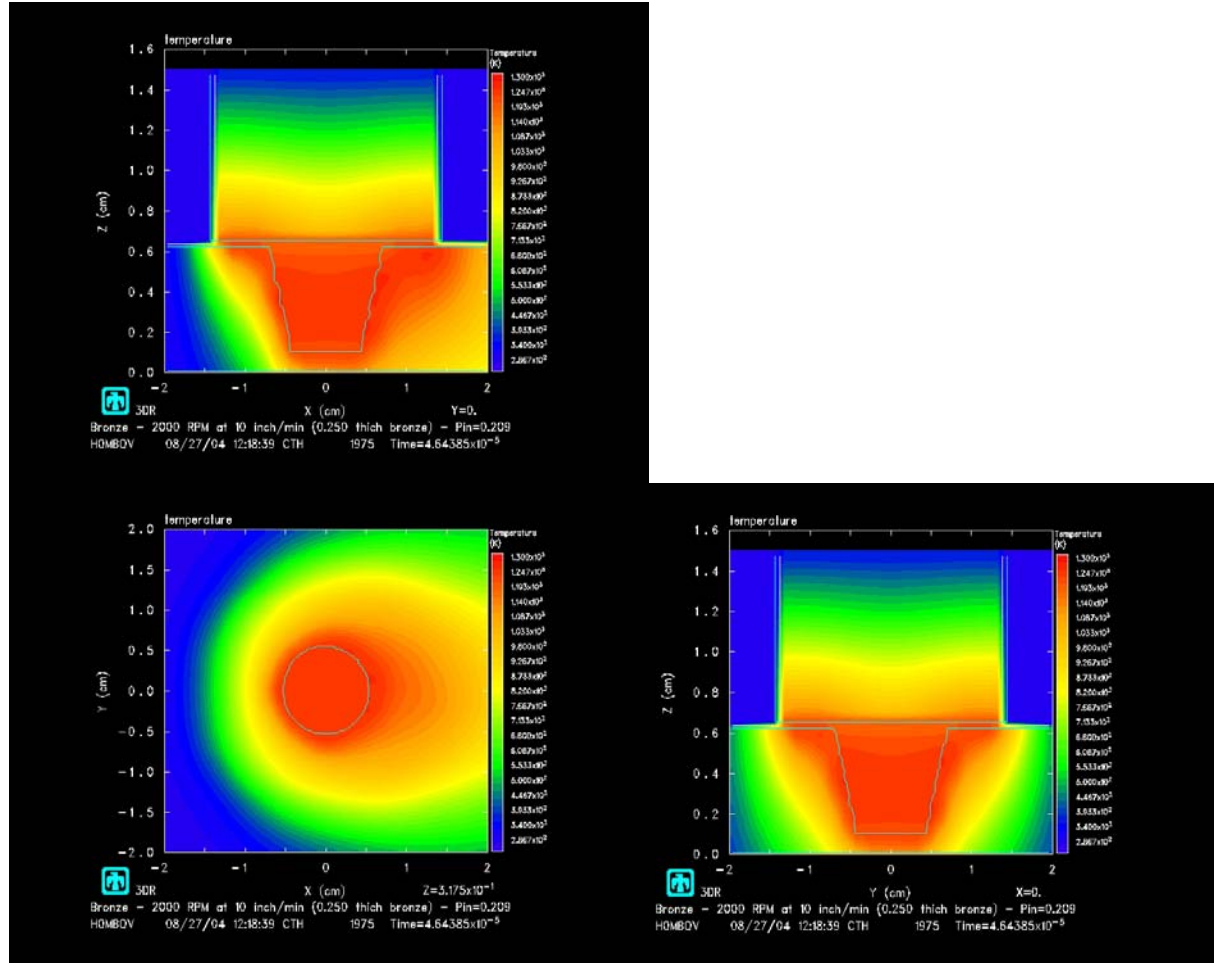


Figure 82. 2000 rev/min 10 inch/min – Temperature distribution.

It is easy to see the volume of material around the tool and the pin are nearly the same maximum temperature. The temperature profile is elongated with emphasis on the trailing side of the tool. The material flowing around the tool has significantly lowered the temperature throughout the volume. The maximum temperature attained is approximately 970 °C trailing the tool.

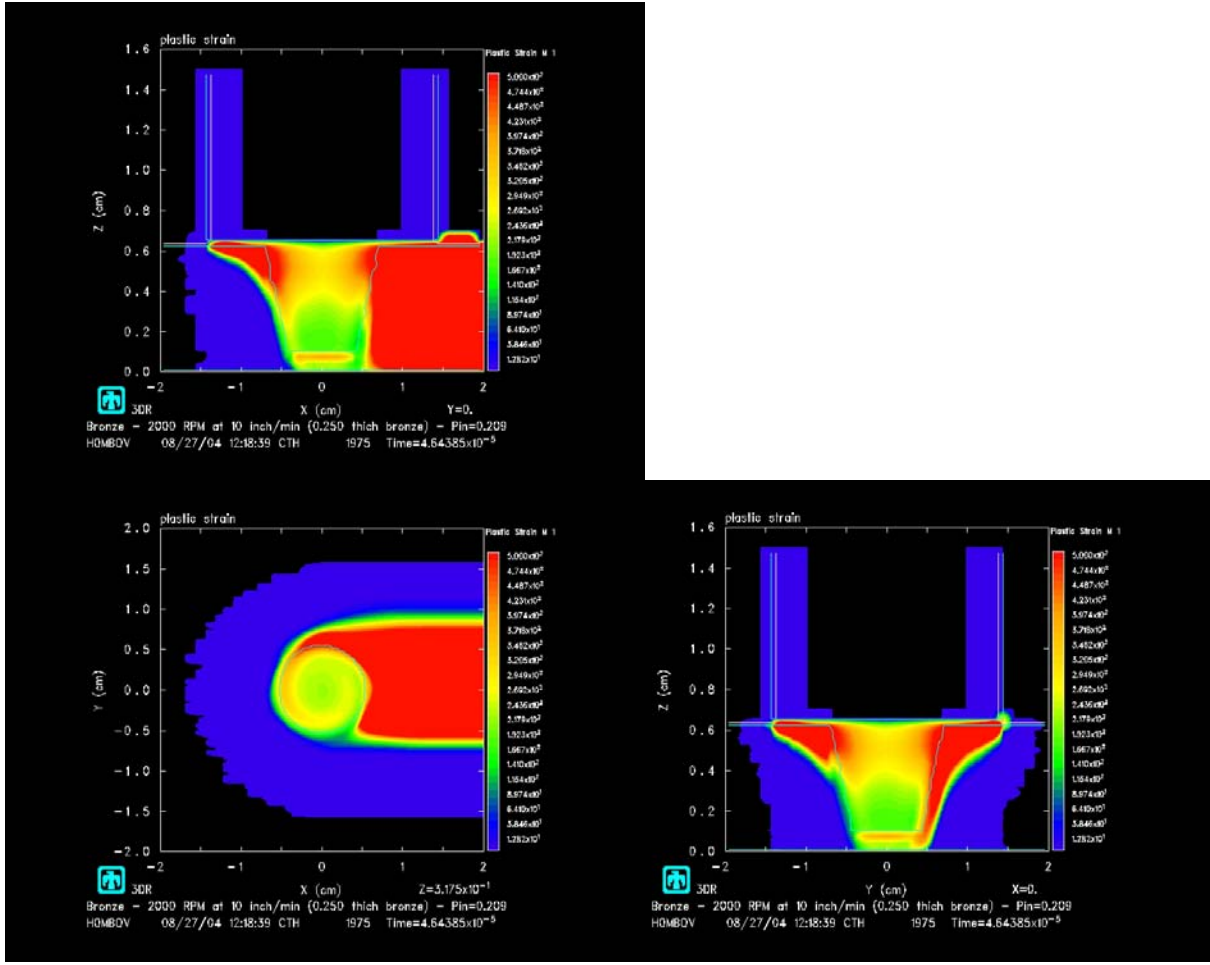


Figure 83. 2000 rev/min 10 inch/min – Strain distribution.

The volume of material that experiences significant strain is greatly reduced from Figure 79. The material under the shoulders accumulates the majority of the strain. The majority of the strained material ends up on the advancing side of the centerline. There is still an evenly spaced volume around the tool experiencing a low strain.

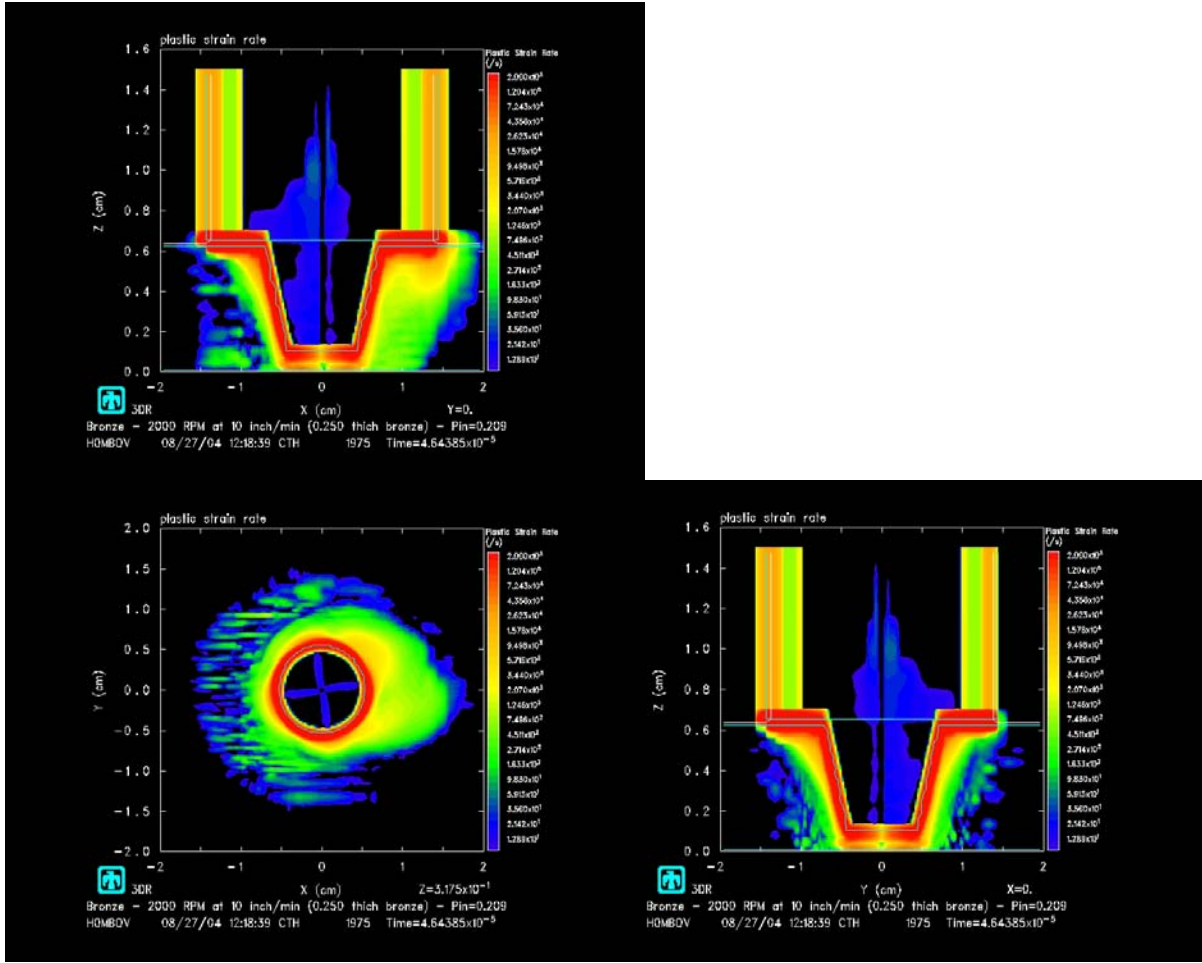


Figure 84. 2000 rev/min 10 inch/min – Strain-rate distribution.

It is easy to see that the highest strain-rates are attained very near the tool/material interface with a large fraction near the shoulder. The maximum strain-rate is attained at or near the shoulder as expected since the shoulder has the highest velocity. There is a larger and more intense strain-rate field leading the tool than observed in Figure 80. A larger volume of material around the tool is experiencing significant strain-rate due to thermal softening. The strain-rate profile is elongated with emphasis on the trailing side.

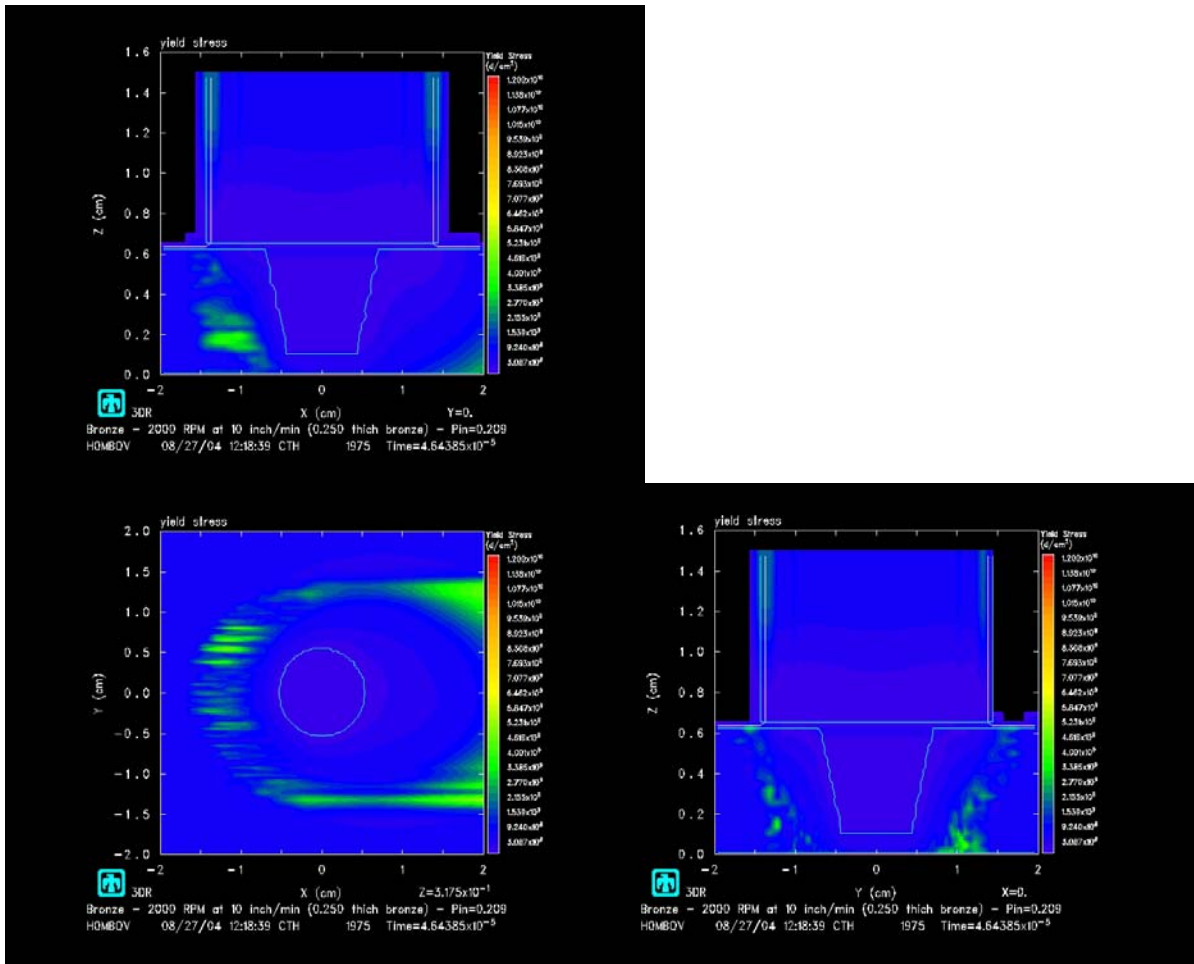


Figure 85. 2000 rev/min 10 inch/min – Stress distribution.

The elongated low stress field around the tool correlates with the higher temperatures and the theory of thermal softening. A relatively small volume of material leading the tool is experiencing a low stress.

P. 2000 RPM 20 IPM

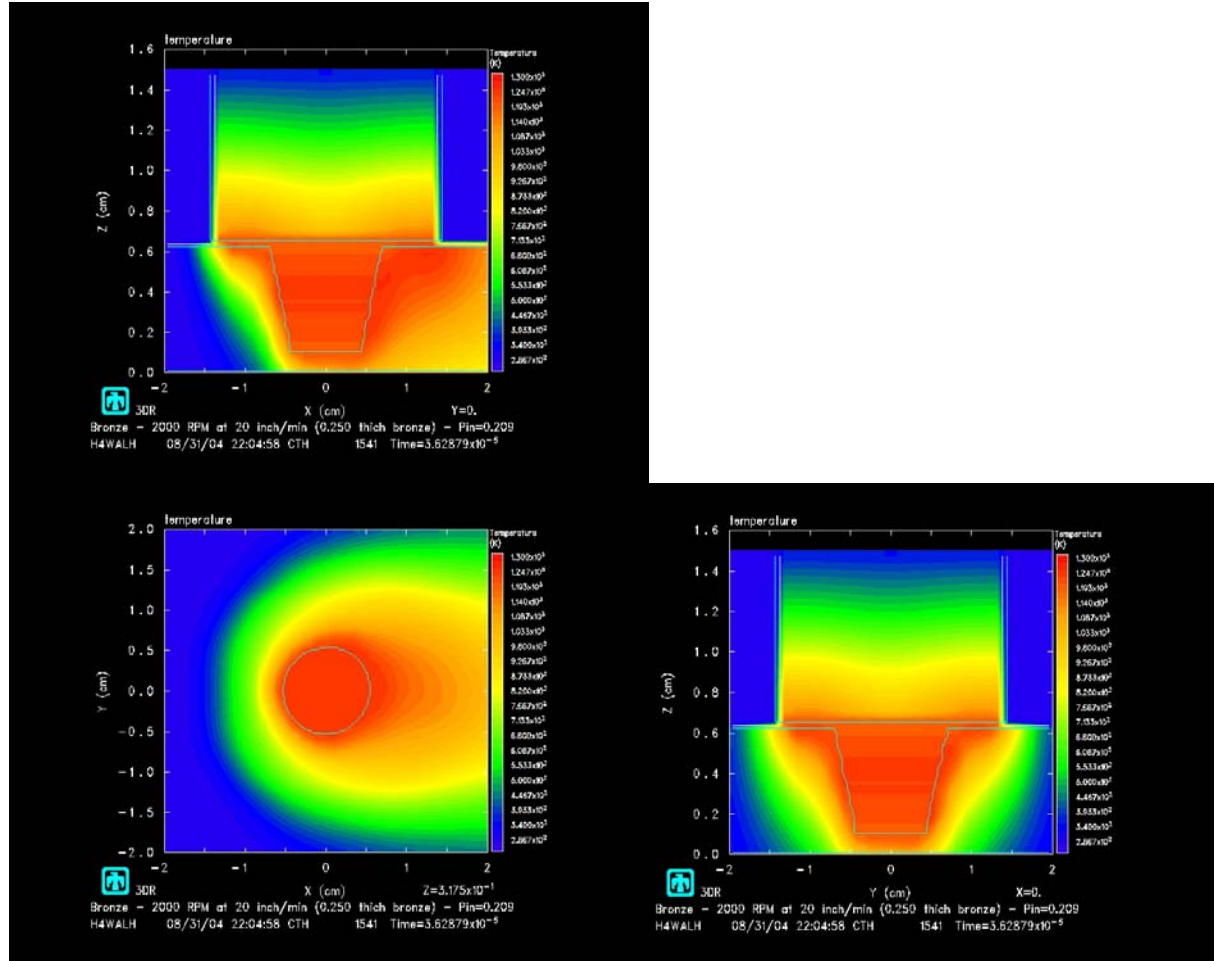


Figure 86. 2000 rev/min 20 inch/min – Temperature distribution.

It is easy to see the volume of material around the tool and the pin are nearly the same maximum temperature. The temperature profile is elongated with emphasis on the trailing side of the tool. The material flowing around the tool has significantly lowered the temperature throughout the volume and the pin. The maximum temperature attained is approximately 970 °C trailing the tool with the majority of the volume only experiencing a temperature near 920 °C.

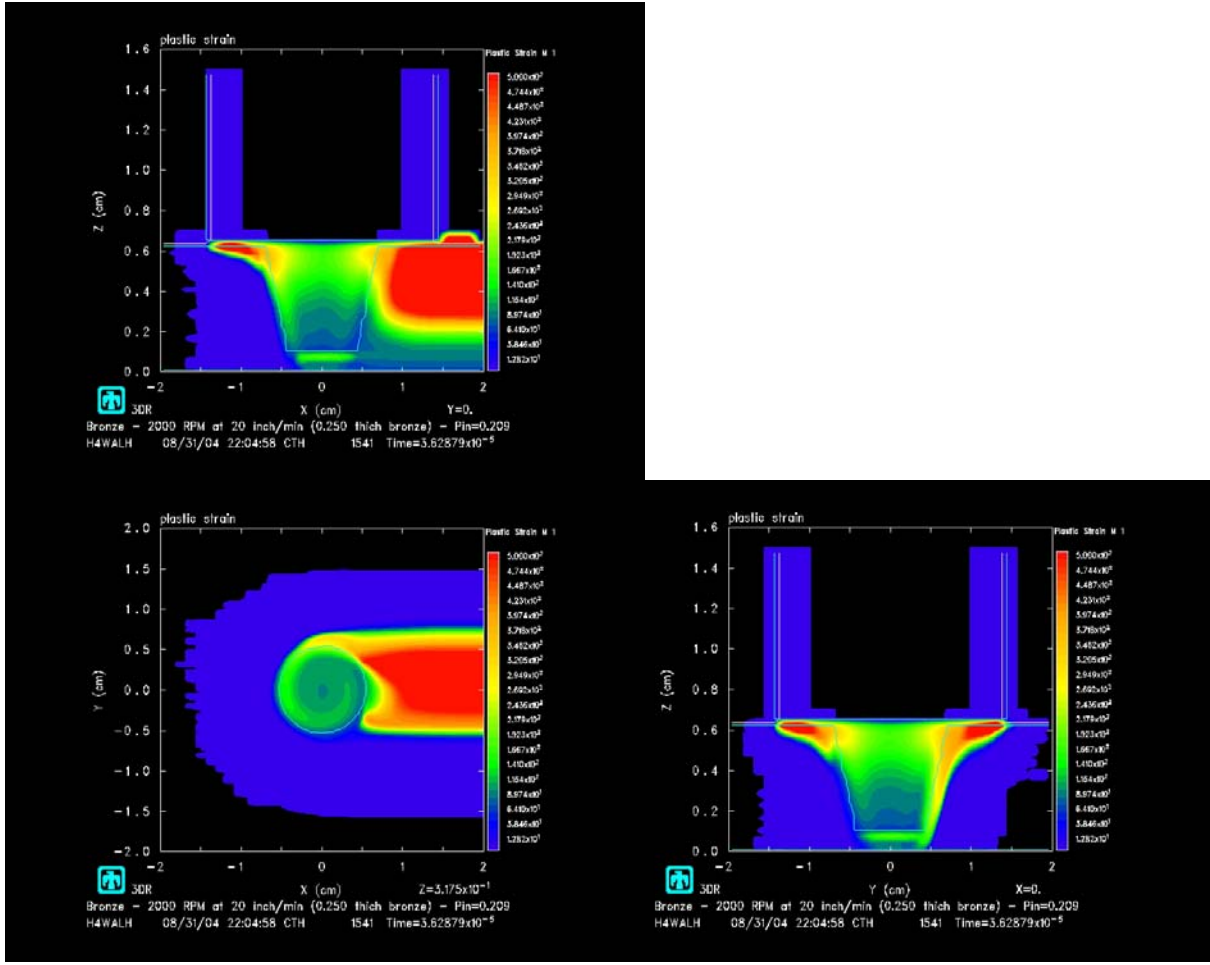


Figure 87. 2000 rev/min 20 inch/min – Strain distribution.

The volume of material that experiences significant strain is greatly reduced from Figure 83. The majority of the strain seems to be accumulating after the pin has traversed through the material and the shoulder is mixing that volume. The majority of the strained material ends up directly trailing the tool. There is still an evenly spaced volume around the tool experiencing a low strain.

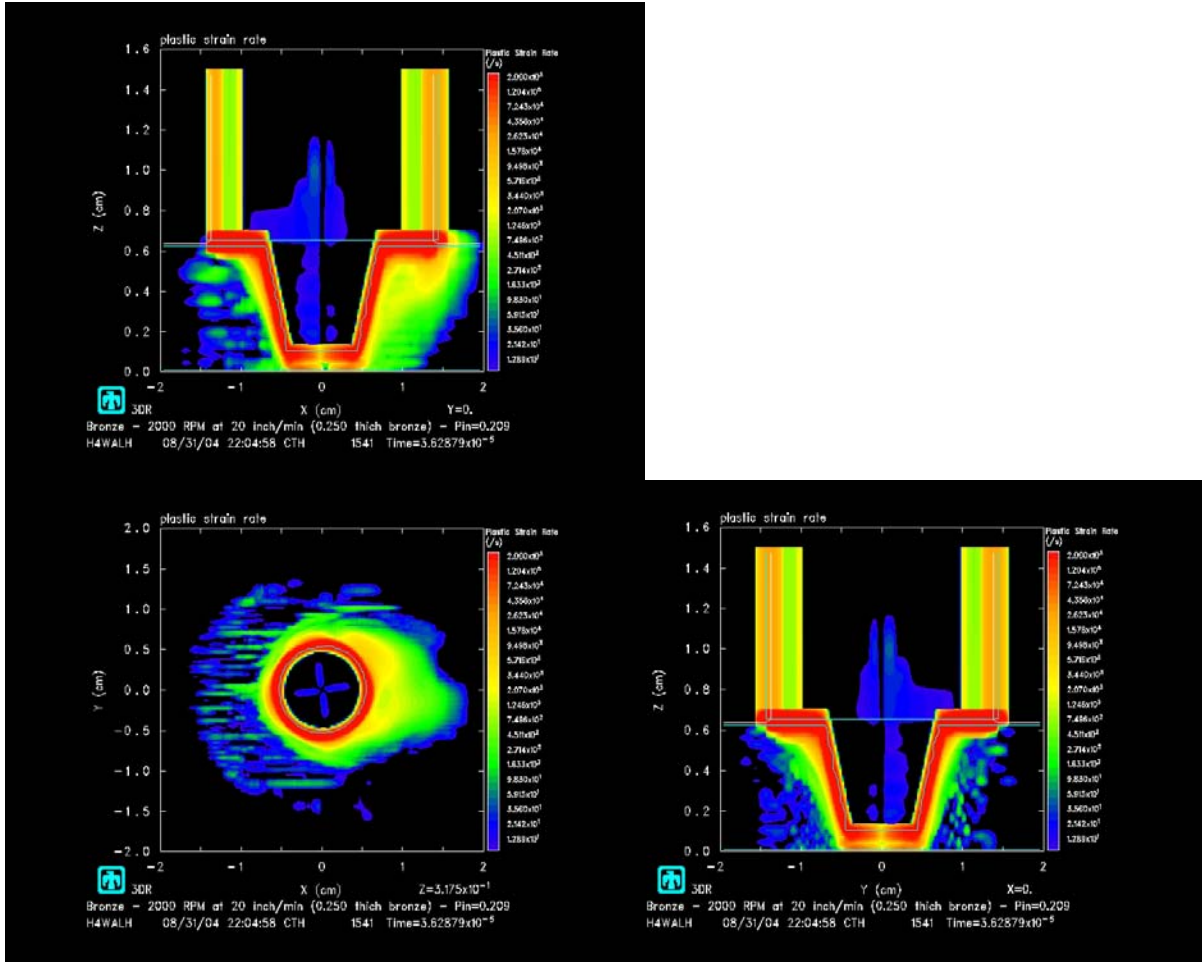


Figure 88. 2000 rev/min 20 inch/min – Strain-rate distribution.

It is easy to see that the highest strain-rates are attained very near the tool/material interface with a large fraction near the shoulder. The maximum strain-rate is attained at or near the shoulder as expected since the shoulder has the highest velocity. There is a strain-rate field leading the tool near to the same size as that observed in Figure 84. A larger volume of material trailing the tool is experiencing significant strain-rate due to thermal softening. This larger strain-rate would account for the large strains trailing the tool in Figure 87. The strain-rate profile is elongated with emphasis on the trailing side.

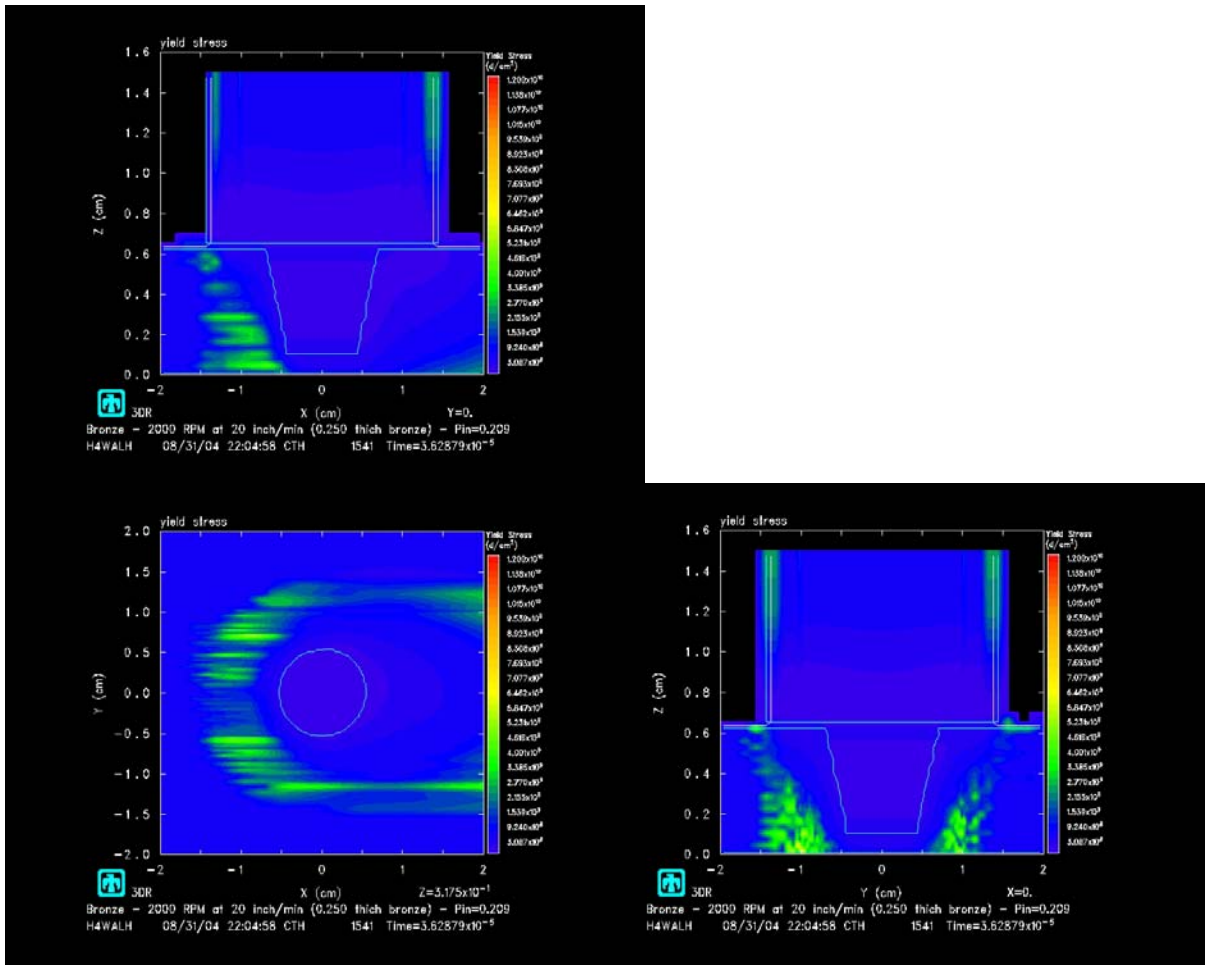


Figure 89. 2000 rev/min 20 inch/min – Stress distribution.

The elongated low stress field around the tool correlates with the higher temperatures and the theory of thermal softening. A relatively small volume of material leading the tool is experiencing a low stress. The intensity of the stress is larger toward the tip of the pin with emphasis on the retreating side.

Q. 5000 RPM 1 IPM

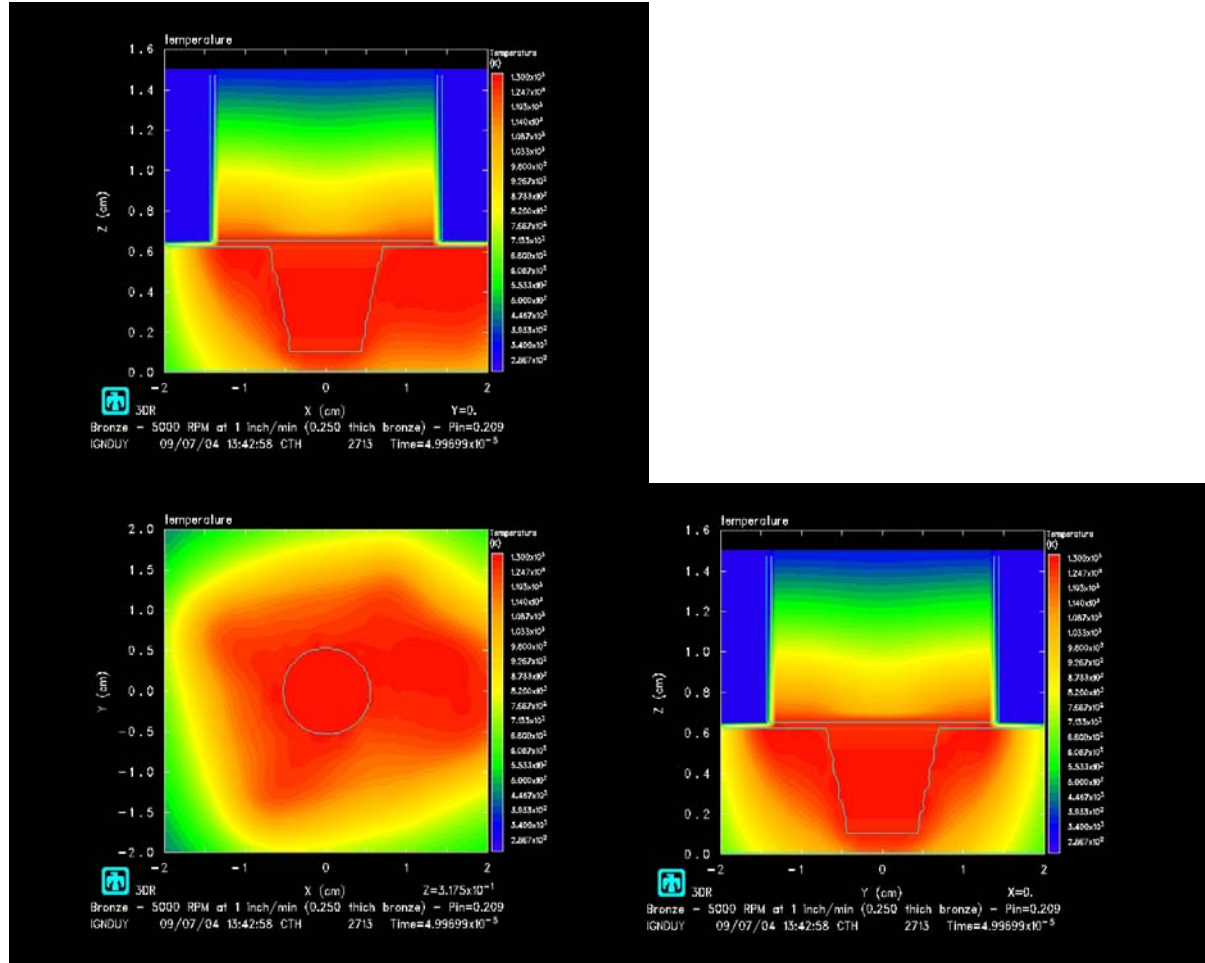


Figure 90. 5000 rev/min 1 inch/min – Temperature distribution.

It is easy to see the volume of material around the tool and the pin are nearly the same maximum temperature. The shape of the temperature profile in the z-direction is consistent with logic. The temperature profile in the xy-plane is elongated in four directions. The maximum temperature attained is approximately 1020 °C.

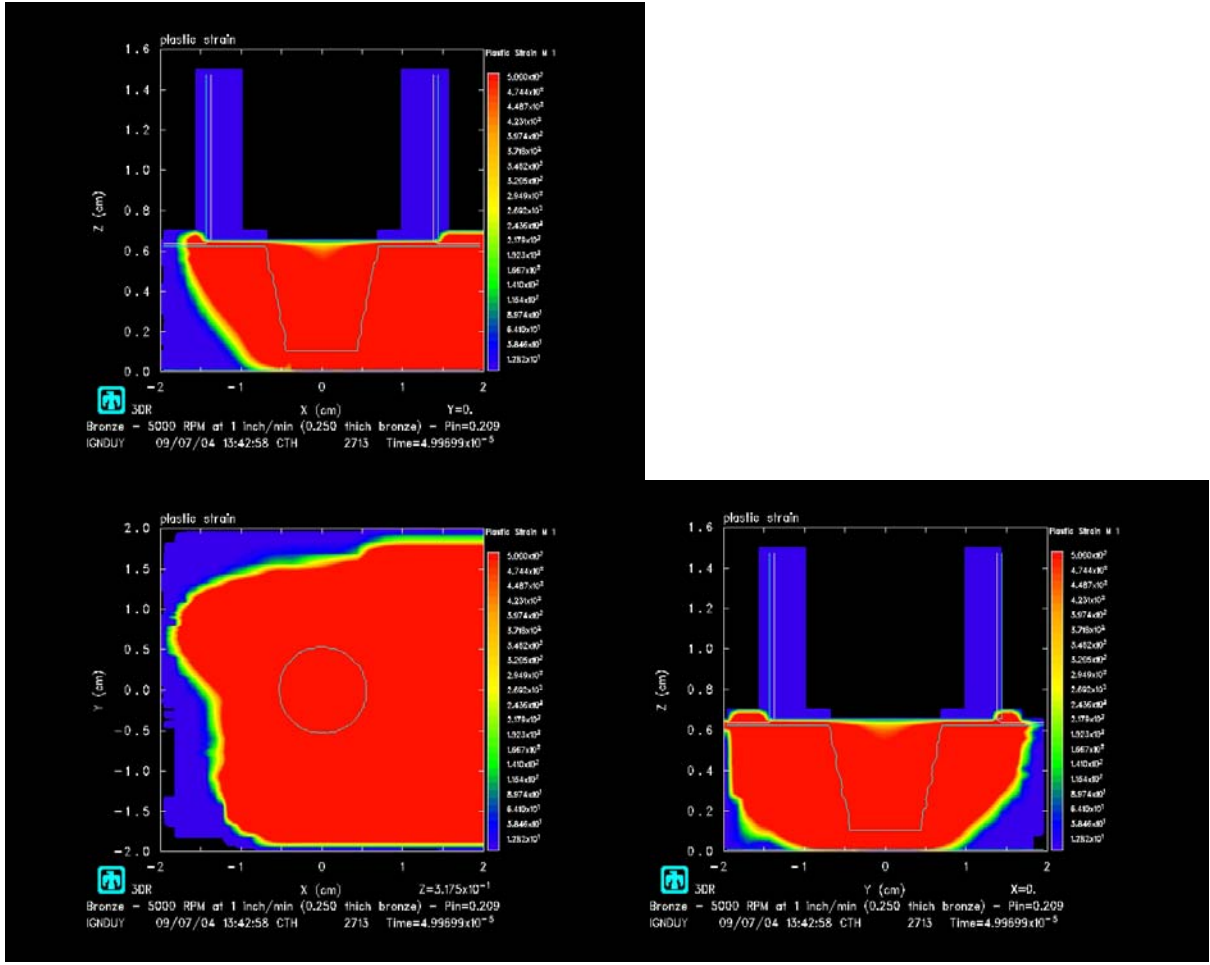


Figure 91. 5000 rev/min 1 inch/min – Strain distribution.

It is easy to see that there is a much larger volume of material which experiences a larger accumulated strain than that for lower rotation rates. The volume experiencing a significant strain is very large. The majority of the material with large strains is on the retreating side of the tool.

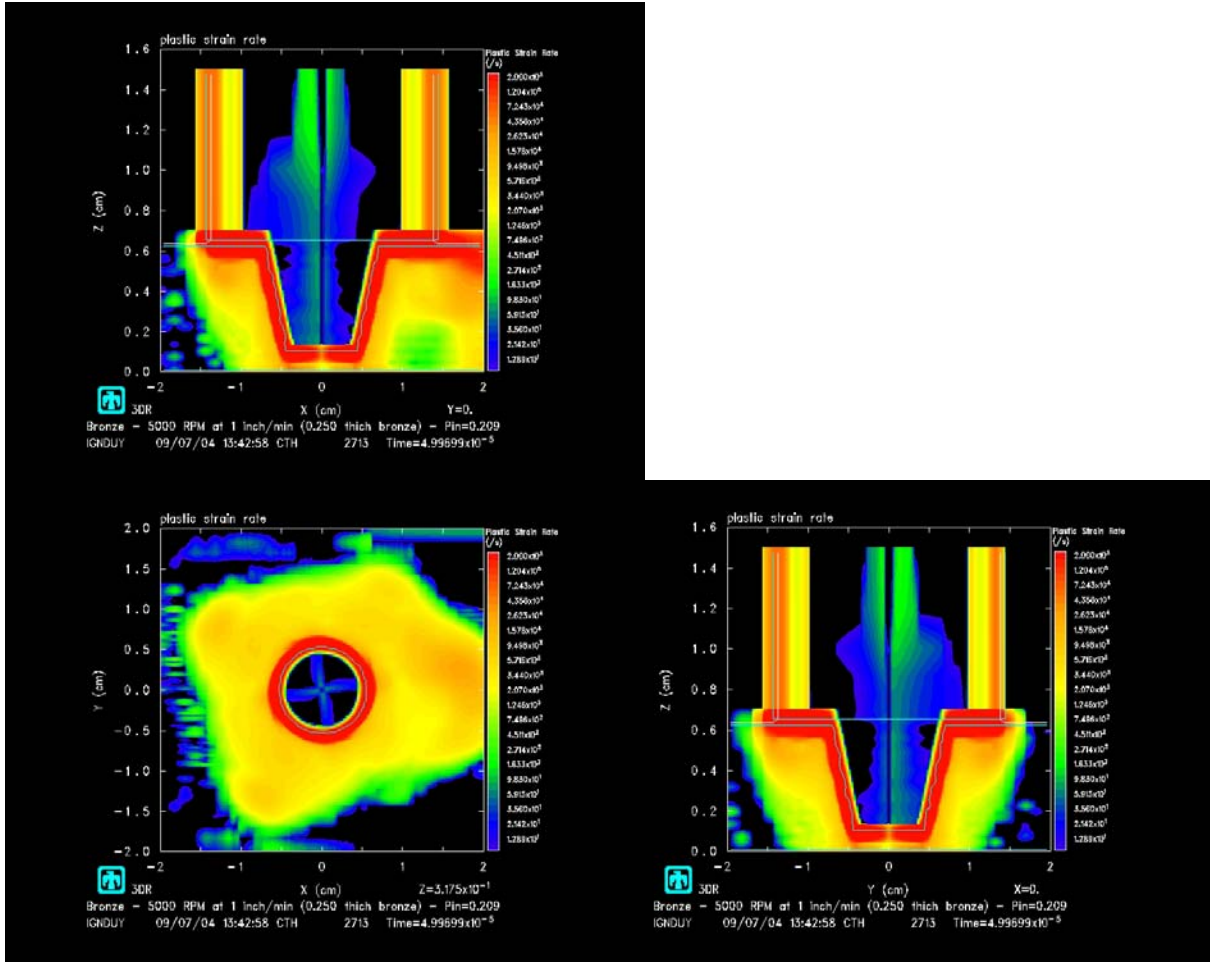


Figure 92. 5000 rev/min 1 inch/min – Strain-rate distribution.

It is easy to see that the highest strain-rates are attained very near the tool/material interface with a large fraction near the shoulder. The maximum strain-rate is attained at or near the shoulder as expected since the shoulder has the highest velocity. There is a strain-rate field completely engulfing the tool. The strain-rate profile is elongated with a profile similar to the temperature profile in Figure 90.

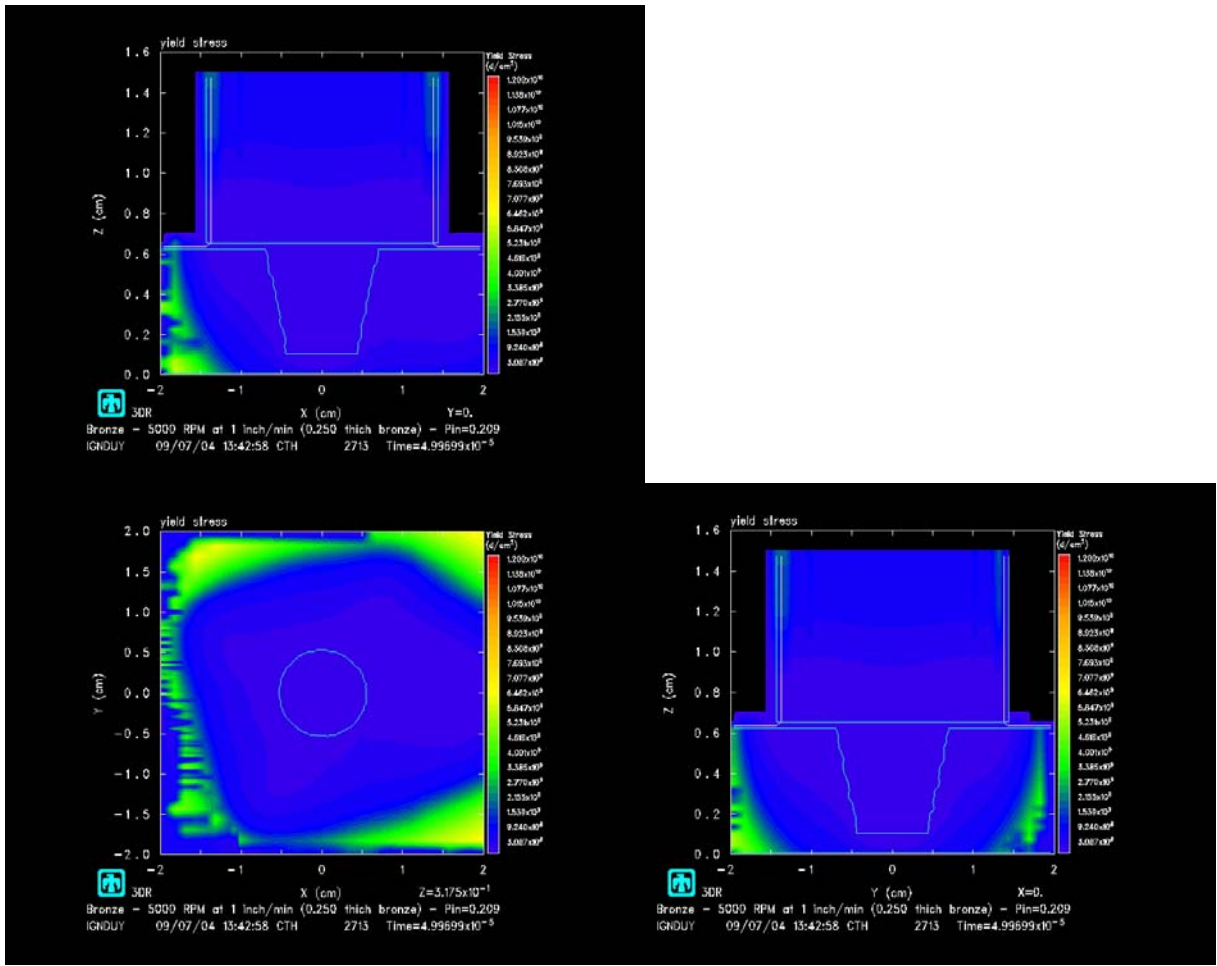


Figure 93. 5000 rev/min 1 inch/min – Stress distribution.

The elongated flow stress field around the tool correlates with the higher temperatures and the theory of thermal softening. A relatively large volume of material around the thermally softened region is experiencing a significant stress.

R. 5000 RPM 5 IPM

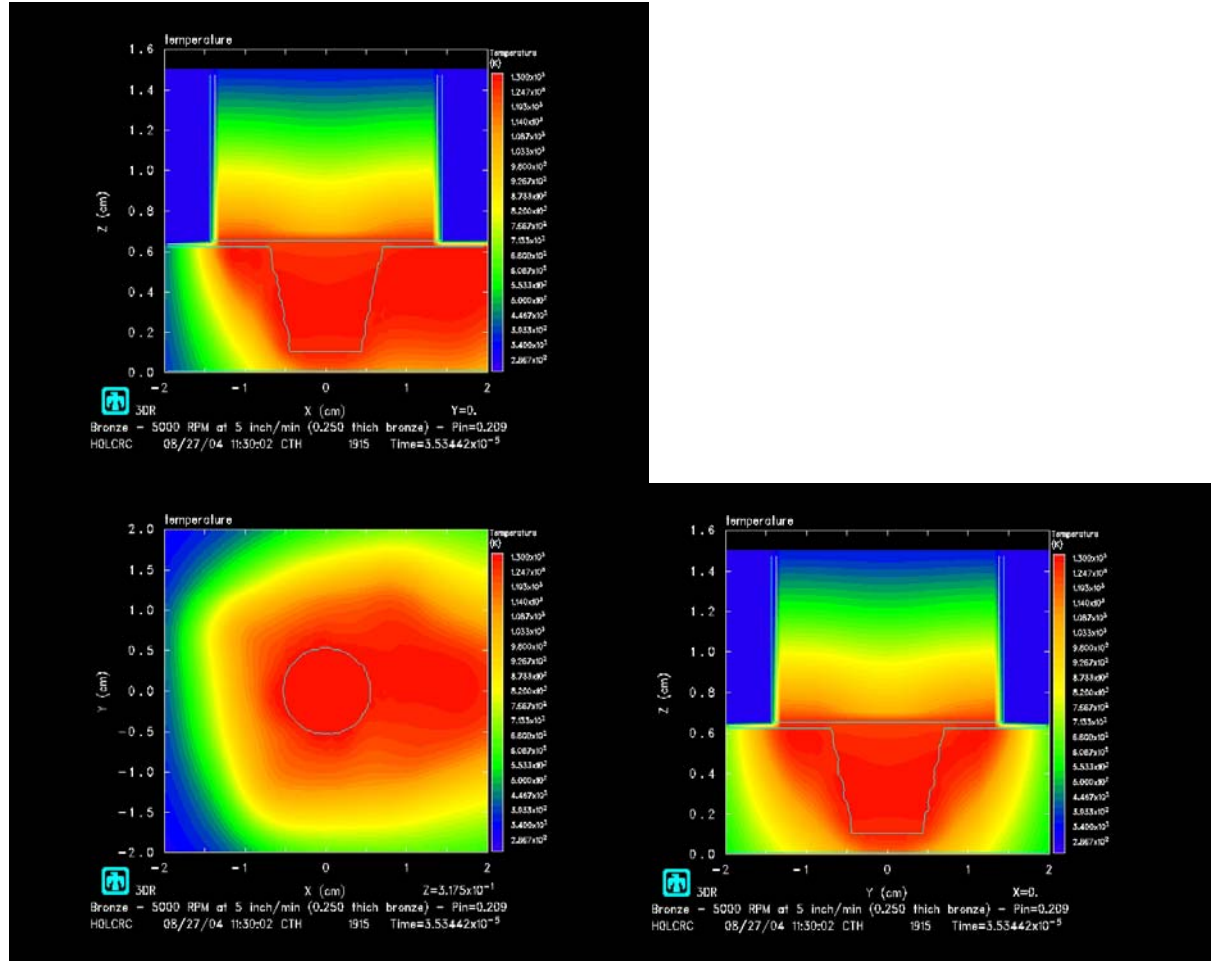


Figure 94. 5000 rev/min 5 inch/min – Temperature distribution.

It is easy to see the volume of material around the tool and the pin are nearly the same maximum temperature. The shape of the temperature profile in the z-direction is consistent with logic. The temperature profile in the xy-plane is elongated in the same four directions observed in Figure 90. The flow of the material around the tool is changing the shape of the temperature field by lowering the overall temperature leading the tool. The maximum temperature attained is approximately 1020 °C seen in a significant volume trailing the tool.

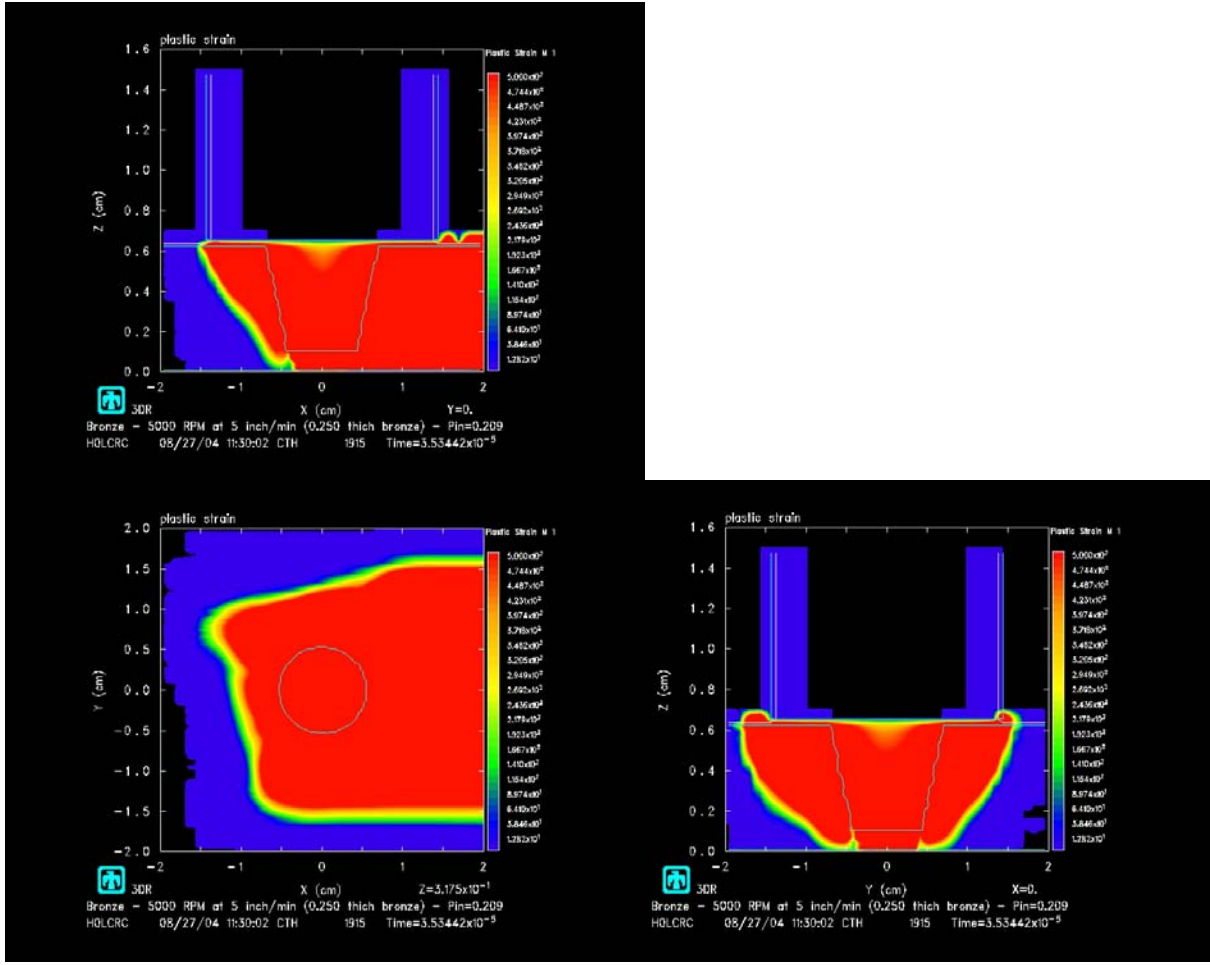


Figure 95. 5000 rev/min 5 inch/min – Strain distribution.

It is easy to see that there is a much larger volume of material which experiences a larger accumulated strain than that for lower rotation rates. The volume experiencing a significant strain is very large. The transverse cross-section is nearly semi-circular in shape.

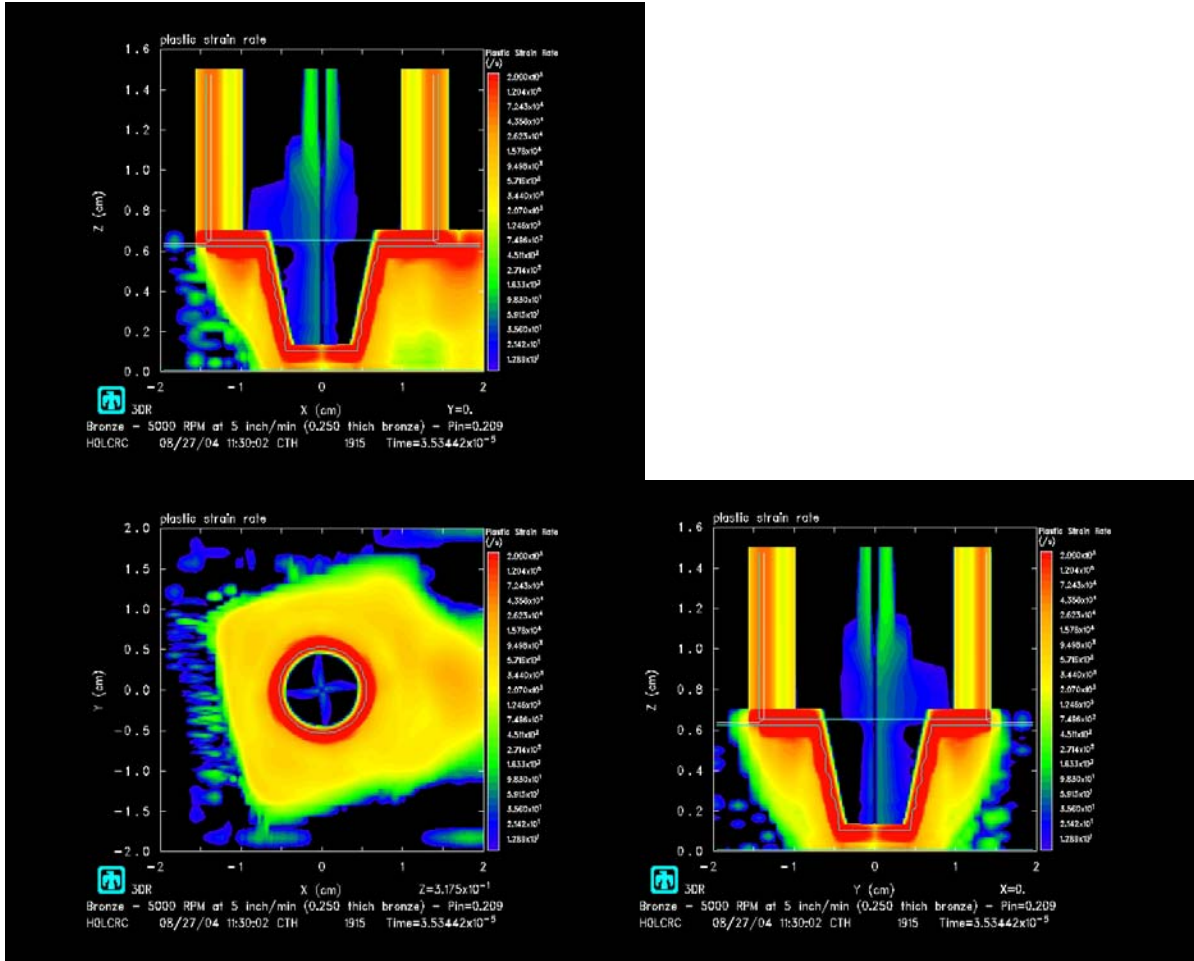


Figure 96. 5000 rev/min 5 inch/min – Strain-rate distribution.

It is easy to see that the highest strain-rates are attained very near the tool/material interface with a large fraction near the shoulder. The maximum strain-rate is attained at or near the shoulder as expected since the shoulder has the highest velocity. There is a strain-rate field completely engulfing the tool. The strain-rate profile is elongated with a profile similar to the temperature profile in Figure 94.

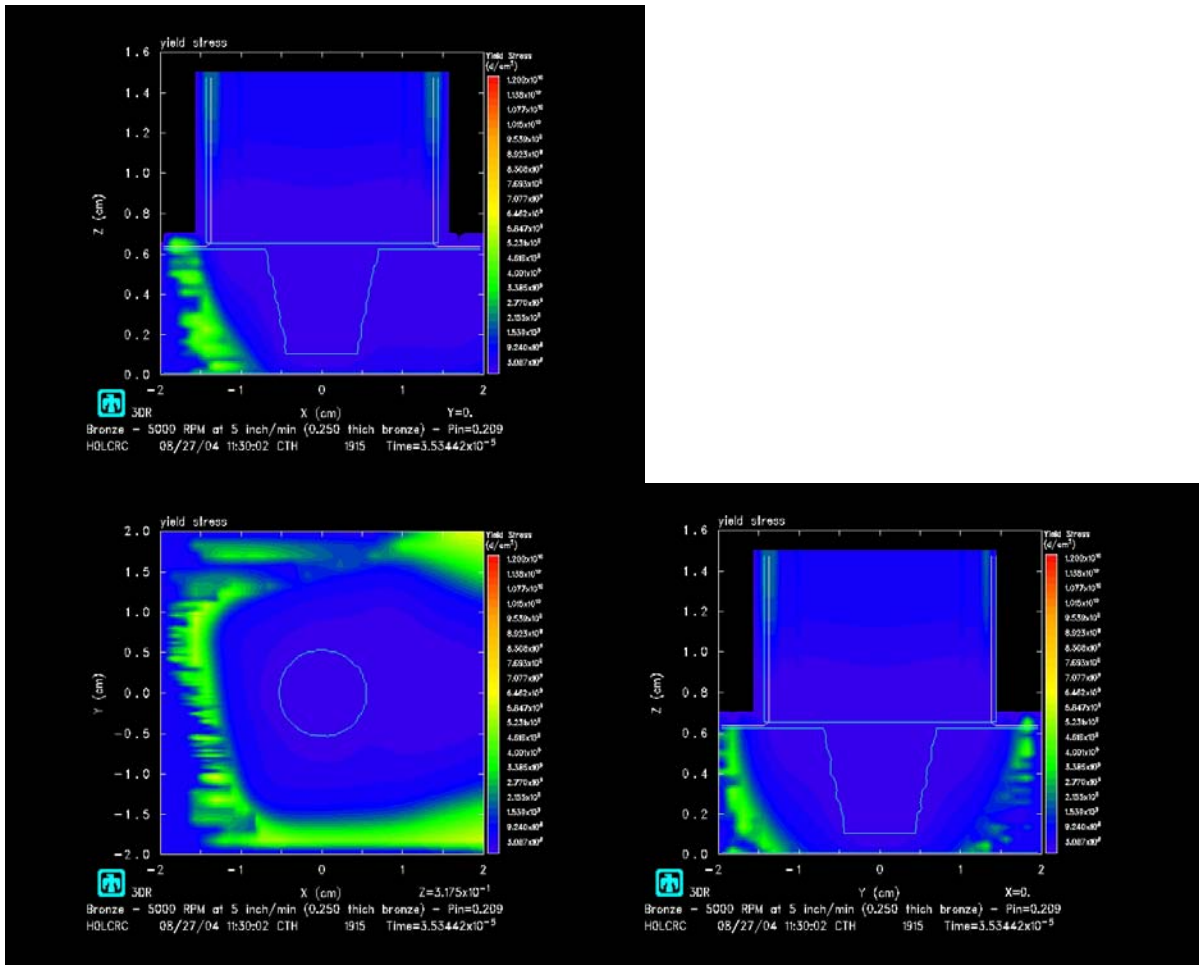


Figure 97. 5000 rev/min 5 inch/min – Stress distribution.

The elongated flow stress field around the tool correlates with the higher temperatures and the theory of thermal softening. A relatively large volume of material around the thermally softened region is experiencing a significant stress.

S. 5000 RPM 10 IPM

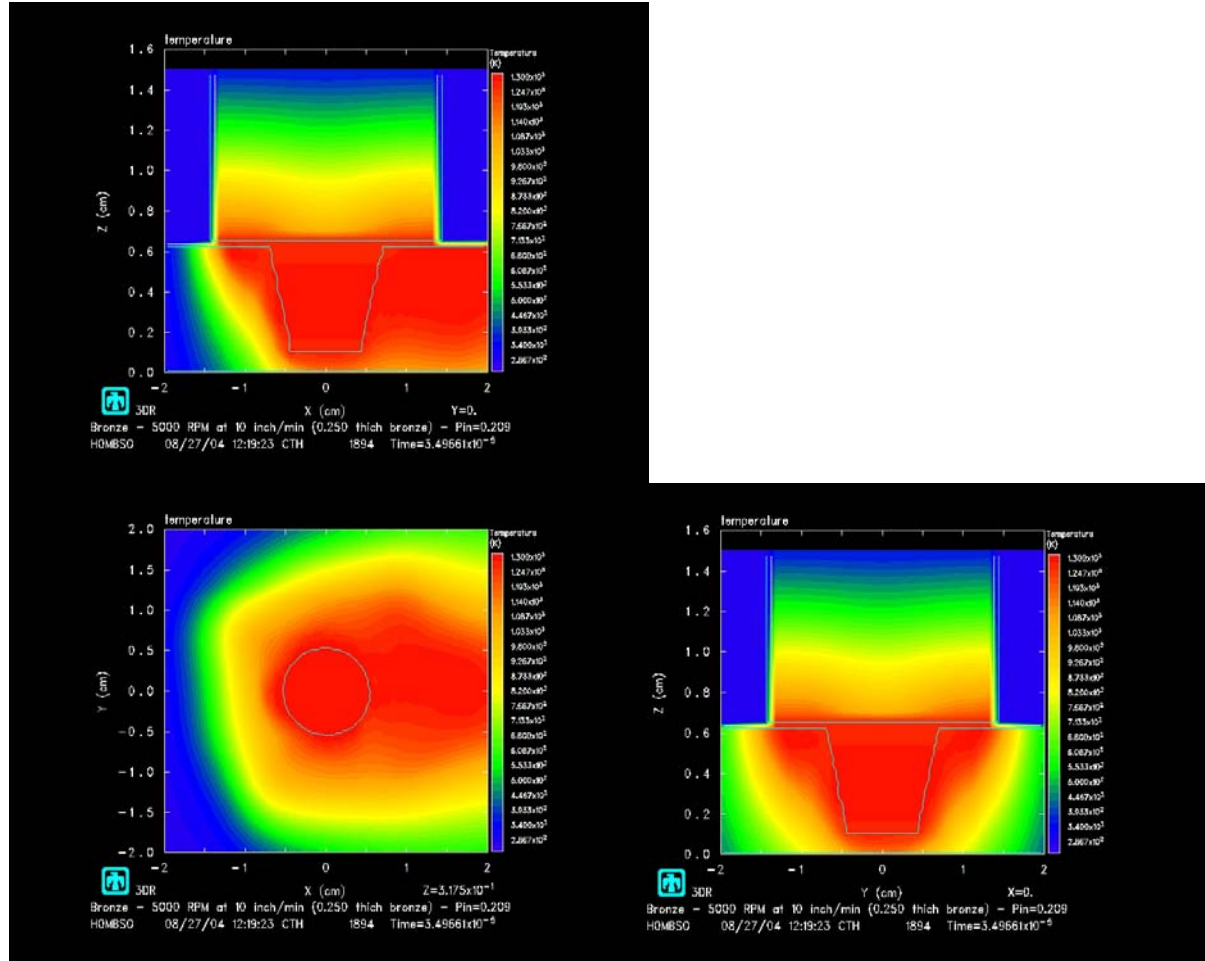


Figure 98. 5000 rev/min 10 inch/min – Temperature distribution.

It is easy to see the volume of material around the tool and the pin are nearly the same maximum temperature. The shape of the temperature profile in the z -direction is similar to the shapes observed for the lower traversing rates. The temperature profile in the xy -plane is elongated due to the flow of material around the tool. The flow of the material around the tool is changing the shape of the temperature field by lowering the overall temperature leading the tool. The maximum temperature attained is approximately 1020 °C seen in a significant volume trailing the tool.

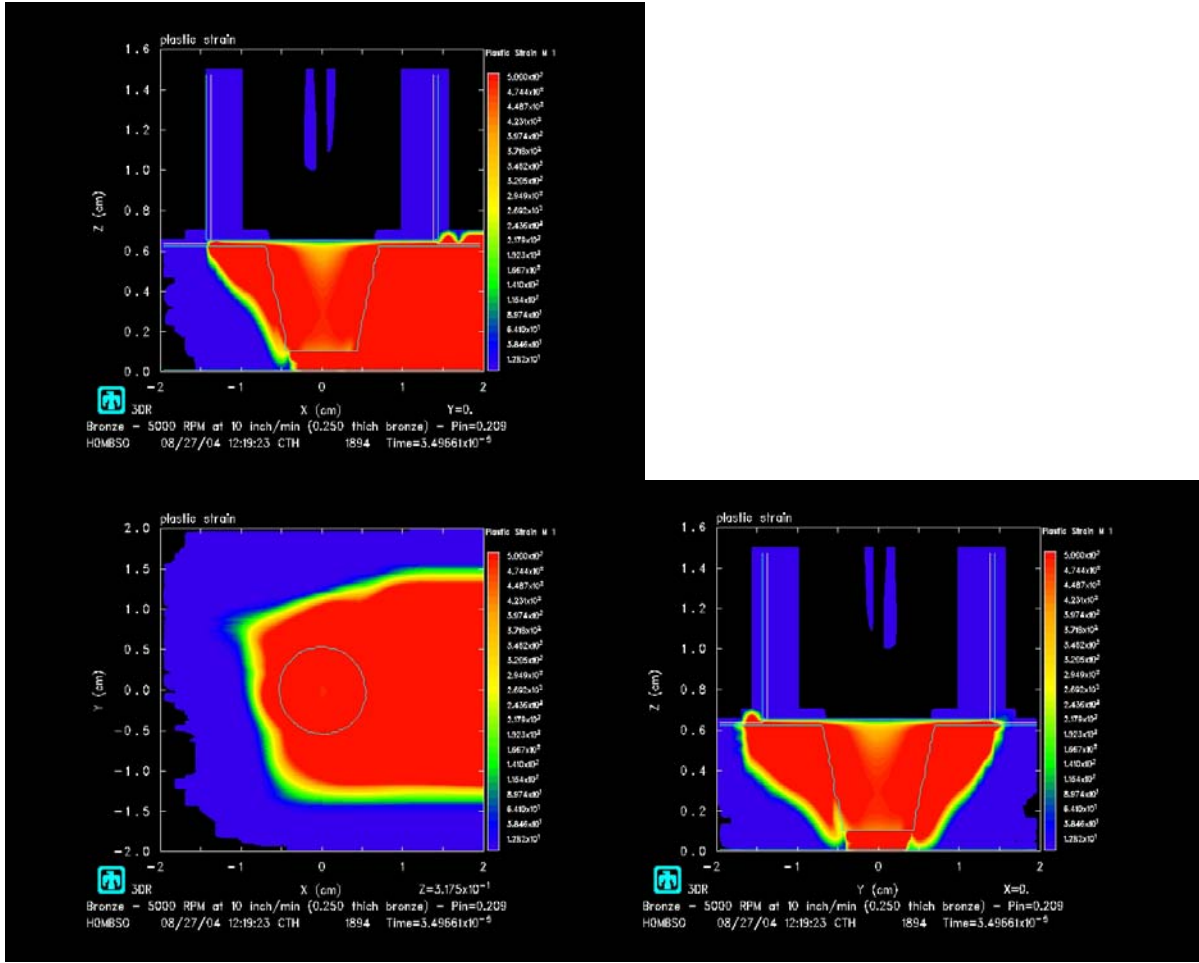


Figure 99. 5000 rev/min 10 inch/min – Strain distribution.

It is easy to see that there is a much larger volume of material which experiences a larger accumulated strain than that for lower rotation rates. The volume experiencing a significant strain is very large. The material flowing past the tool is lowering the average accumulated strain.

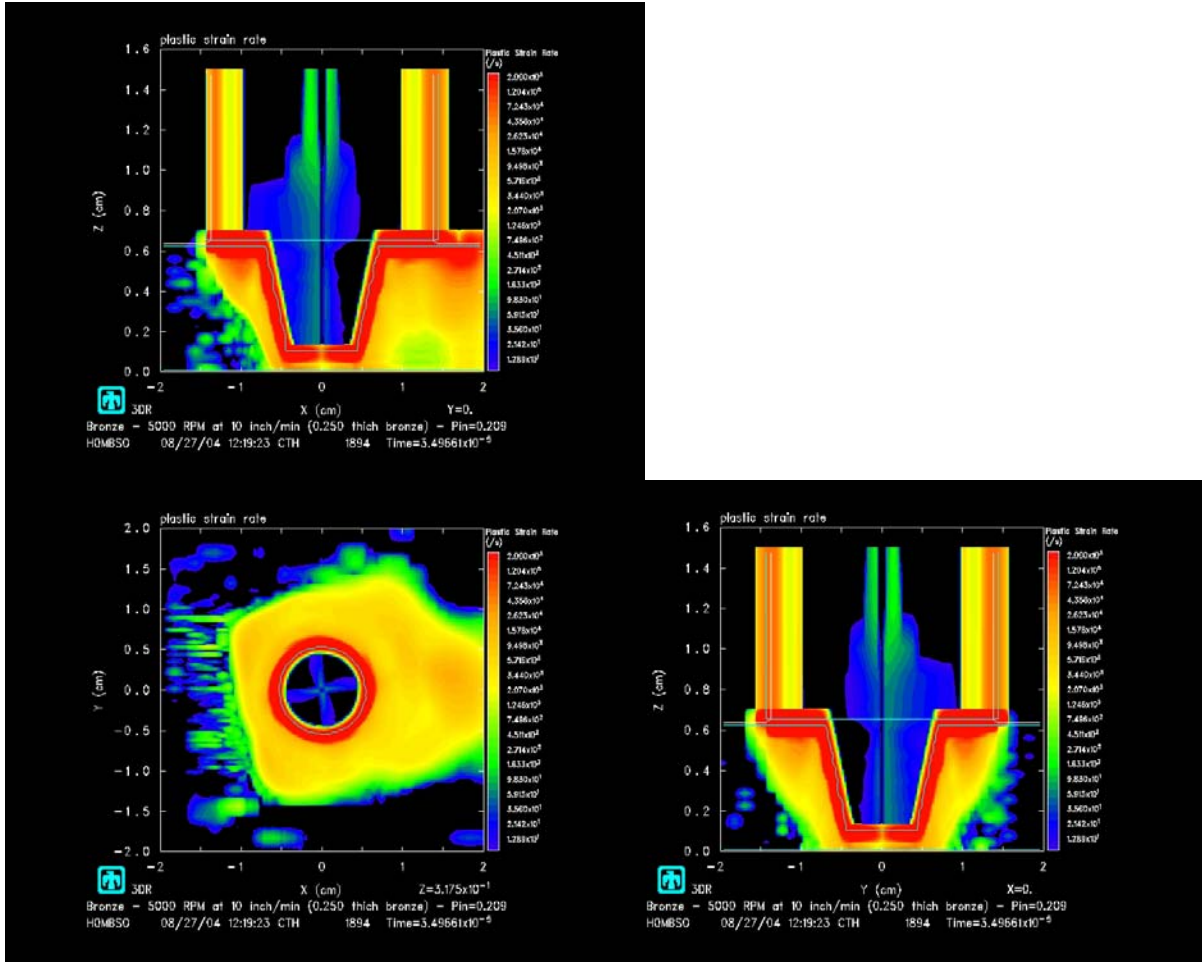


Figure 100. 5000 rev/min 10 inch/min – Strain-rate distribution.

It is easy to see that the highest strain-rates are attained very near the tool/material interface with a large fraction near the shoulder. The maximum strain-rate is attained at or near the shoulder as expected since the shoulder has the highest velocity. There is a strain-rate field completely engulfing the tool. The strain-rate profile is similar to, but slightly smaller than, the profile seen in Figure 96. The low intensity strain-rate field is approximately the same size.

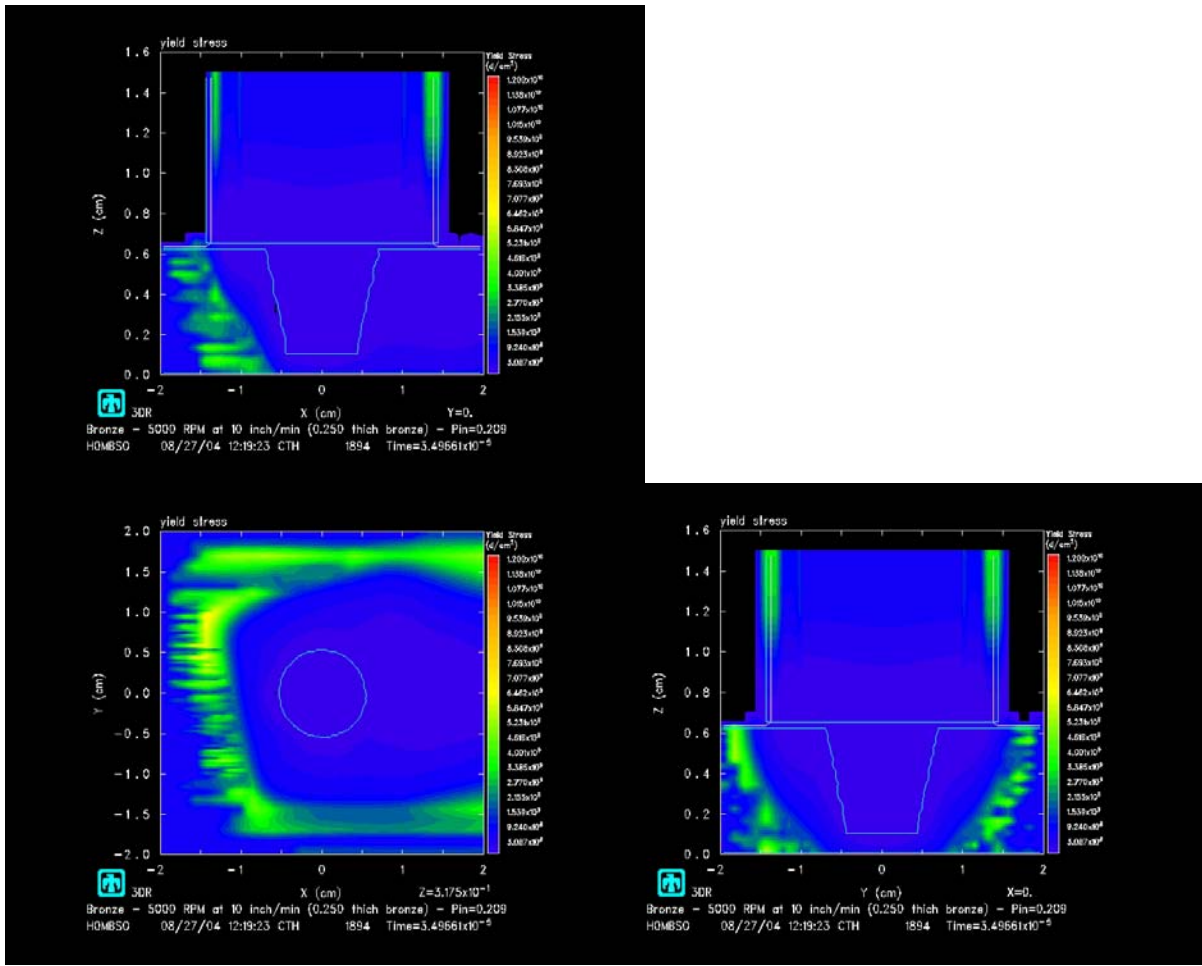


Figure 101. 5000 rev/min 10 inch/min – Stress distribution.

The elongated flow stress field around the tool correlates with the higher temperatures and the theory of thermal softening. A relatively large volume of material around the thermally softened region is experiencing a significant stress.

T. 5000 RPM 20 IPM

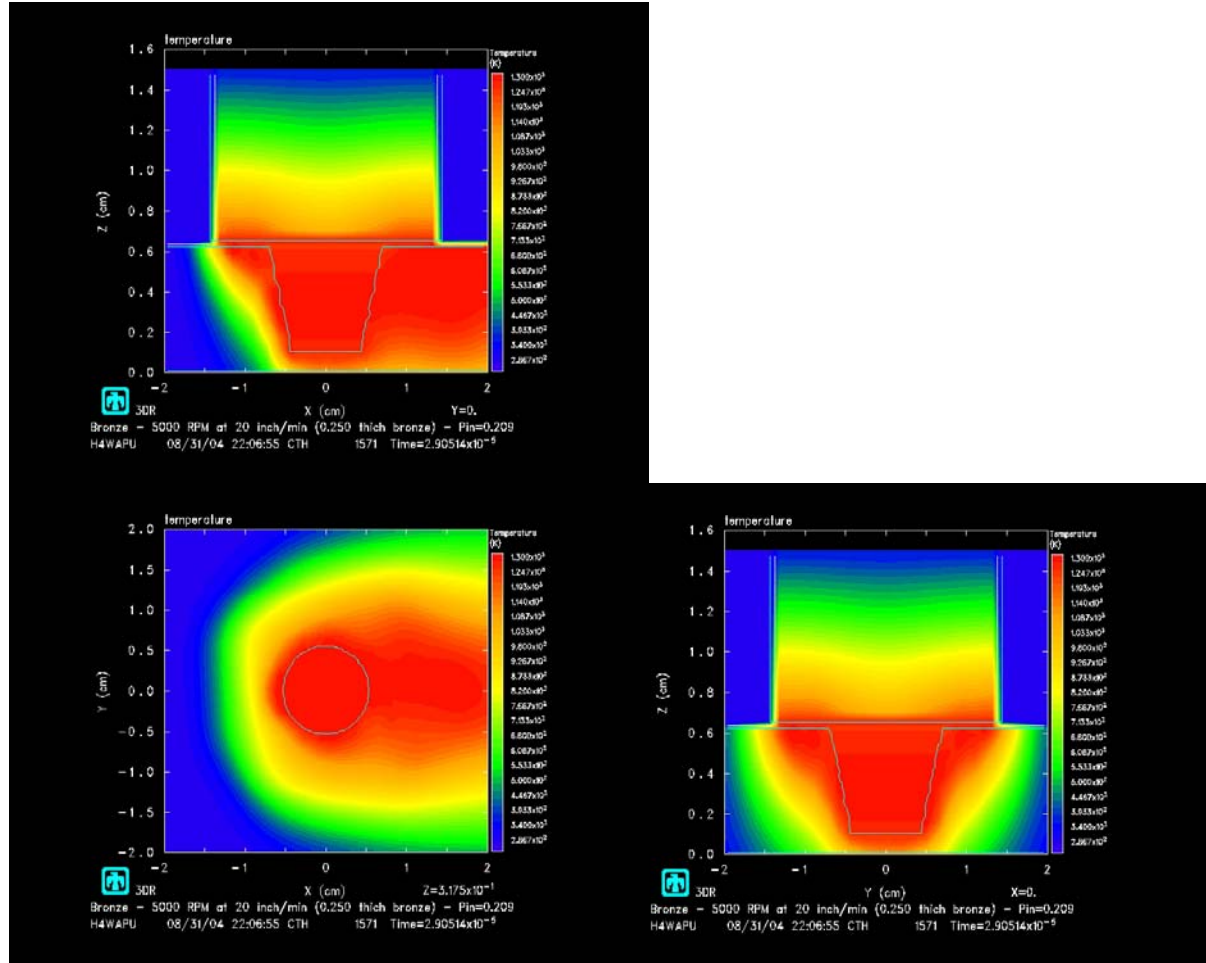


Figure 102. 5000 rev/min 20 inch/min – Temperature distribution.

It is easy to see the volume of material around the tool and the pin are nearly the same maximum temperature. The shape of the temperature profile in the z-direction is similar to the shapes observed for the lower traversing rates. The temperature profile in the xy-plane is elongated due to the flow of material around the tool. The flow of the material around the tool is changing the shape of the temperature field by lowering the overall temperature leading the tool. The maximum temperature attained is approximately 1020 °C seen by the material directly around the pin and in a significant volume trailing the tool.

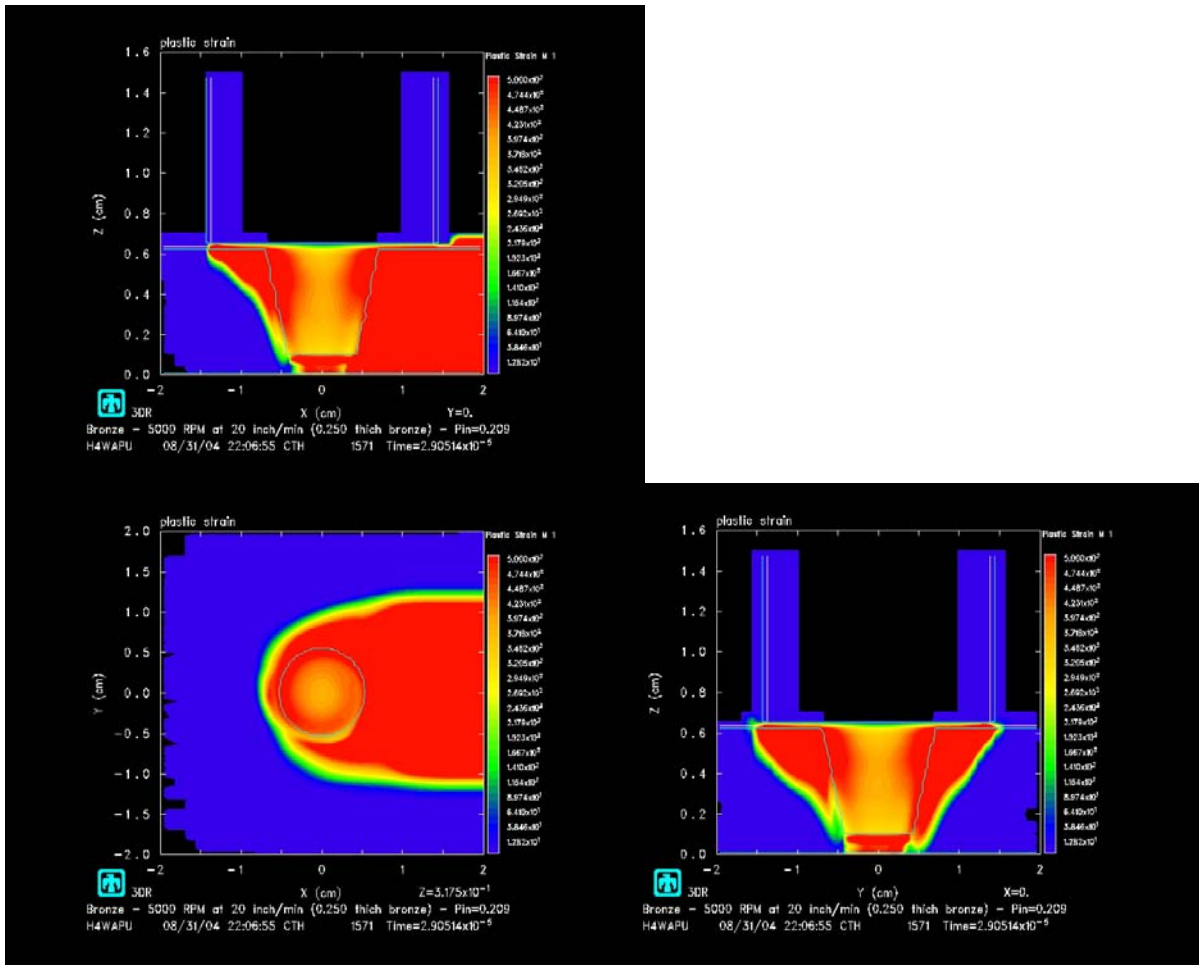


Figure 103. 5000 rev/min 20 inch/min – Strain distribution.

The material flowing past the tool is greatly lowering the average accumulated strain. The majority of the strained material ends up on the advancing side of the centerline. The lower strain field is similar to that seen in the lower traversing rates.

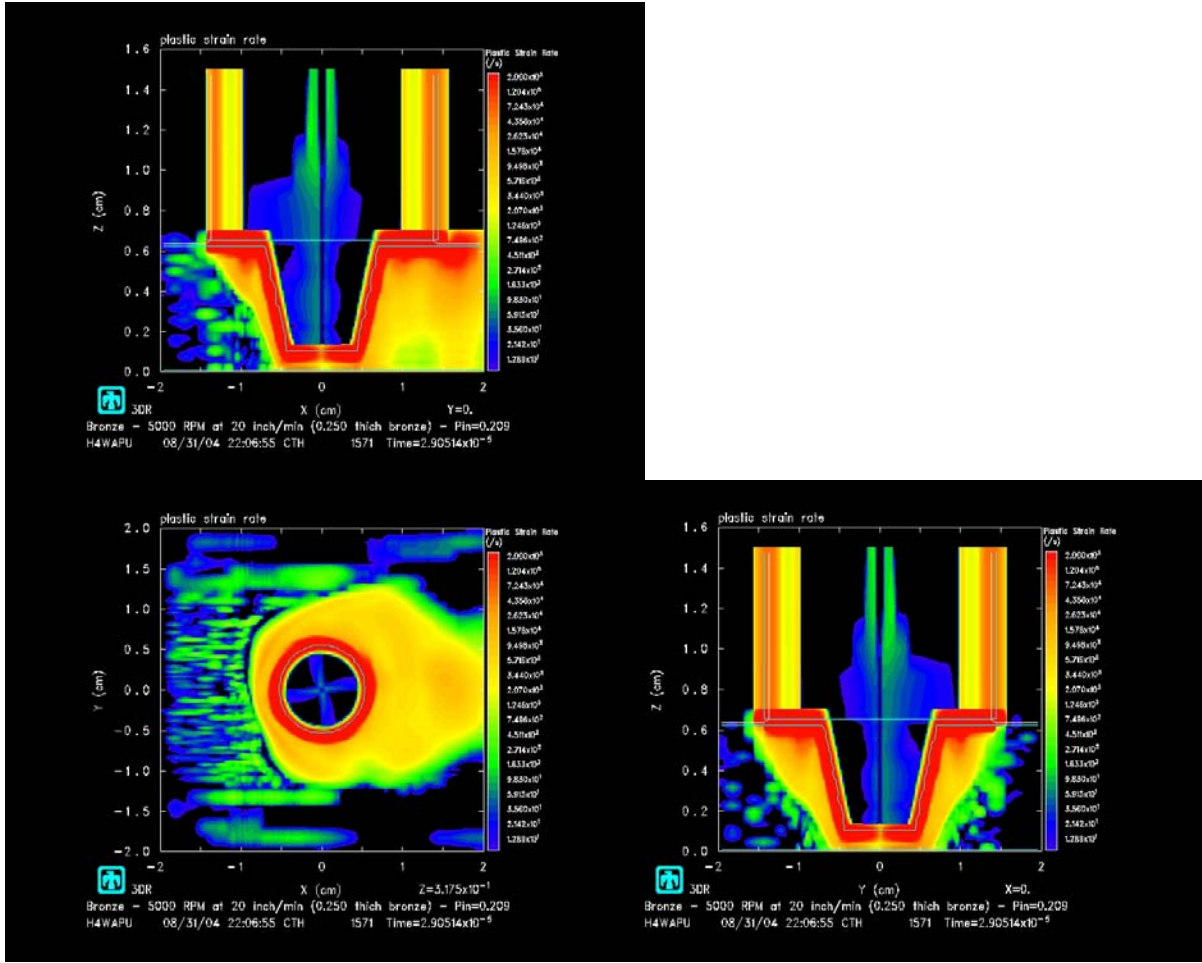


Figure 104. 5000 rev/min 20 inch/min – Strain-rate distribution.

It is easy to see that the highest strain-rates are attained very near the tool/material interface with a large fraction near the shoulder. The maximum strain-rate is attained at or near the shoulder as expected since the shoulder has the highest velocity. The flow of the material around the tool has lowered the strain-rate of the volume leading the tool. The lower intensity strain-rate field is larger and more intense than that observed in Figure 100. There is a slightly larger volume of deforming material on retreating side vice the advancing side.

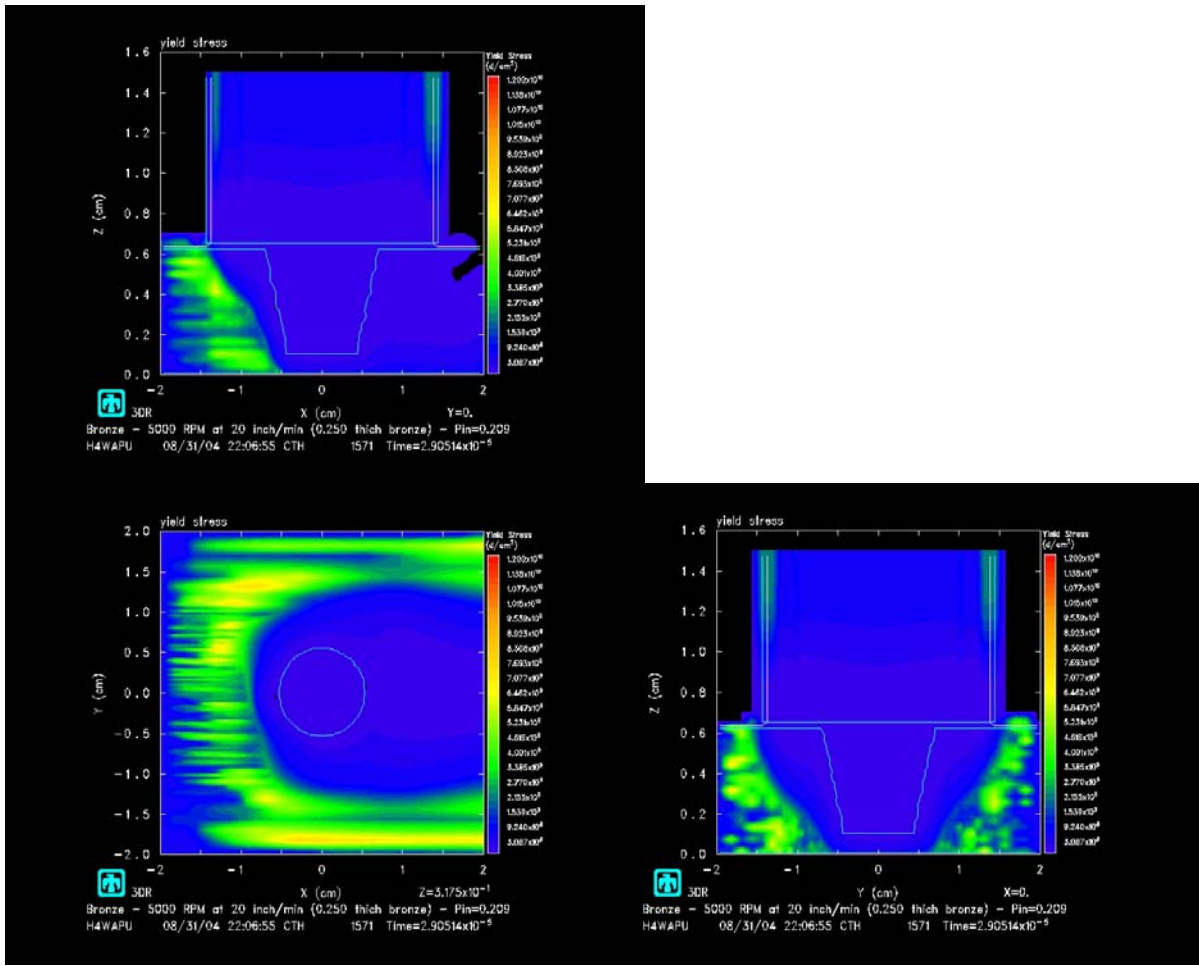


Figure 105. 5000 rev/min 20 inch/min – Stress distribution.

The elongated flow stress field around the tool correlates with the higher temperatures and the theory of thermal softening. A relatively large volume of material around the thermally softened region is experiencing a significant stress with emphasis on the leading and retreating sides.

THIS PAGE INTENTIONALLY LEFT BLANK

APPENDIX B – MATLAB ANALYSIS PLOTS

A. VOLUME PLOTS BASED ON TEMPERATURE

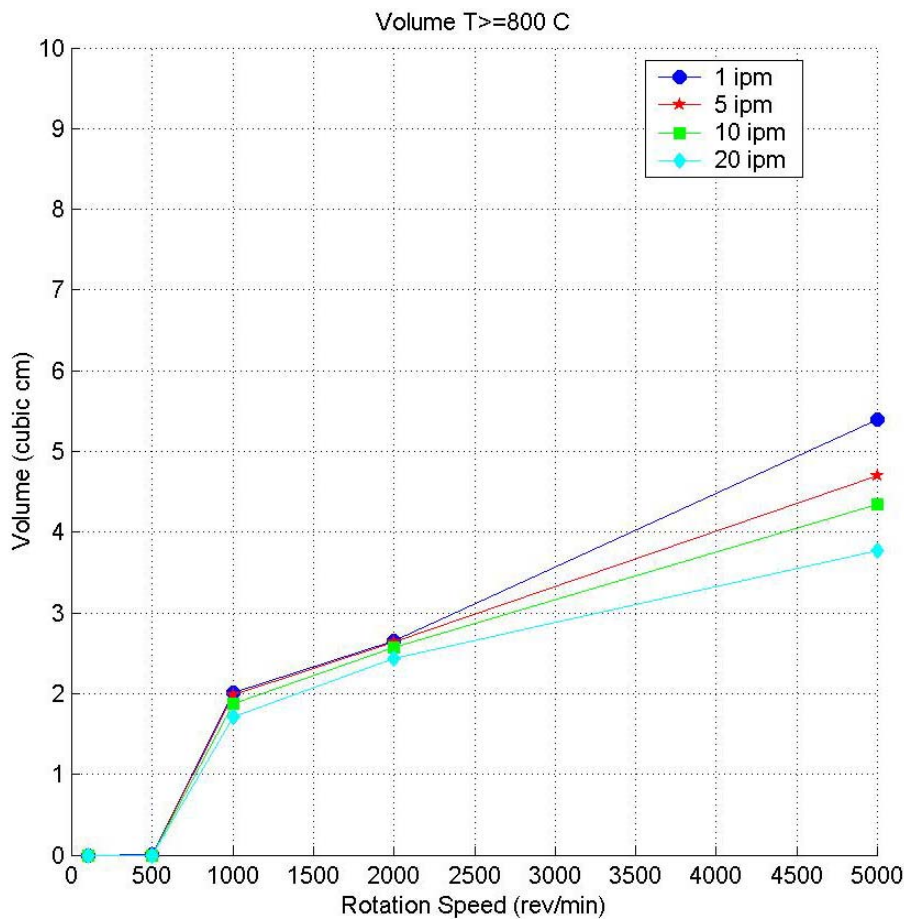


Figure 106. SZ Volume based on $T > 800^{\circ}\text{C}$ wrt Rotation Speed.

The lack of SZ volume that attains 800°C below 1000 rpm is consistent with the observations of the temperature profiles in Appendix A. The increasing volume above 1000 rpm is consistent with the strain-rate and temperature distributions observed also in Appendix A. It is noteworthy that the SZ volume that achieves 800°C has little dependence on traversing rate until near 5000 rpm.

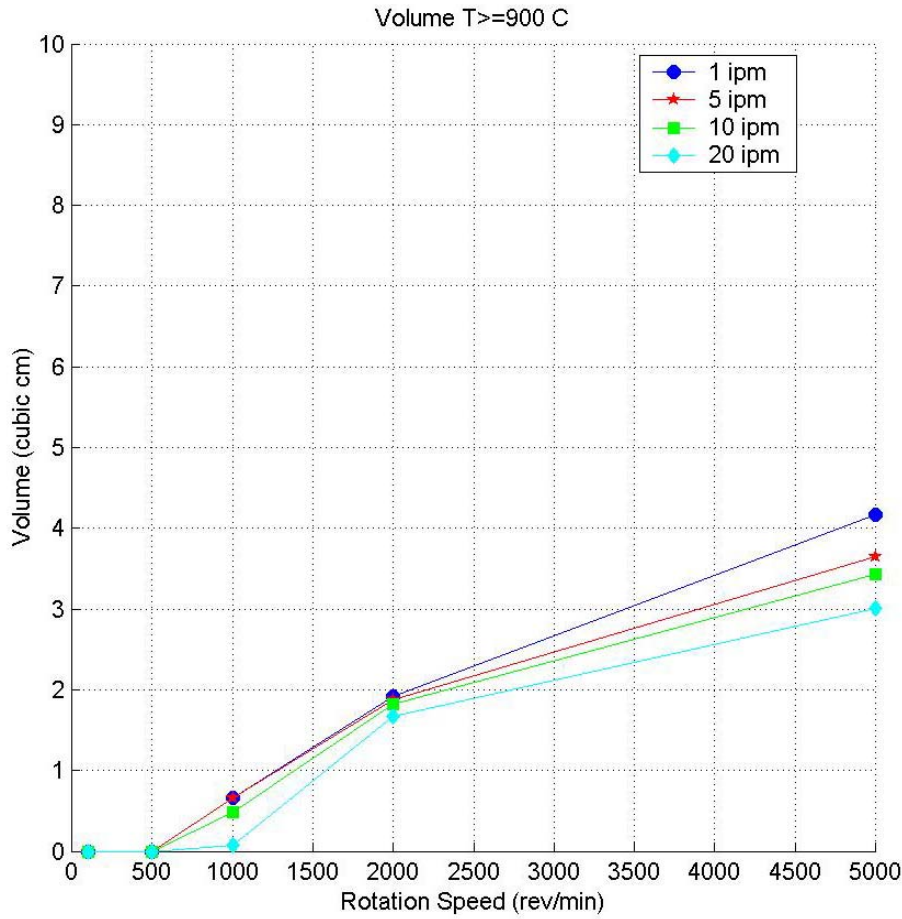


Figure 107. SZ Volume based on $T > 900$ °C wrt Rotation Speed.

The lack of SZ volume that attains 900 °C below 1000 rpm is consistent with the observations of the temperature profiles in Appendix A. The increasing volume above 1000 rpm is consistent with the strain-rate and temperature distributions seen also in Appendix A. The volume of material achieving 900 °C has a stronger dependence at 20 ipm. This is due to the flux of material around the tool being able to remove the heat faster than necessary to maintain 900 °C. The small volume that did exceed 900 °C, was seen directly trailing the pin. It is also noteworthy that the volume attaining 900 °C is approximately 80% of the volume attaining 800 °C for all cases at or above 2000 rpm.

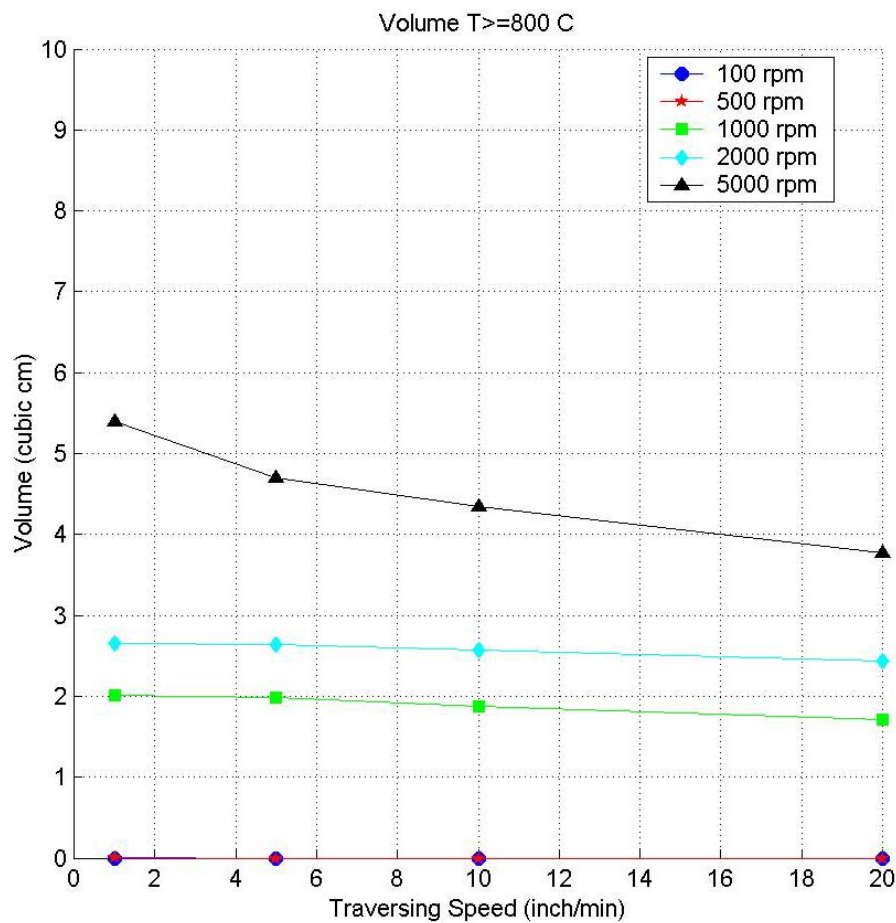


Figure 108. SZ Volume based on $T > 800$ °C wrt Traversing Speed.

This graph verifies the previous finding in Figure 106, namely that, for the temperature attained, there is little dependence upon the traversing rate, with the exception of 5000 rpm.

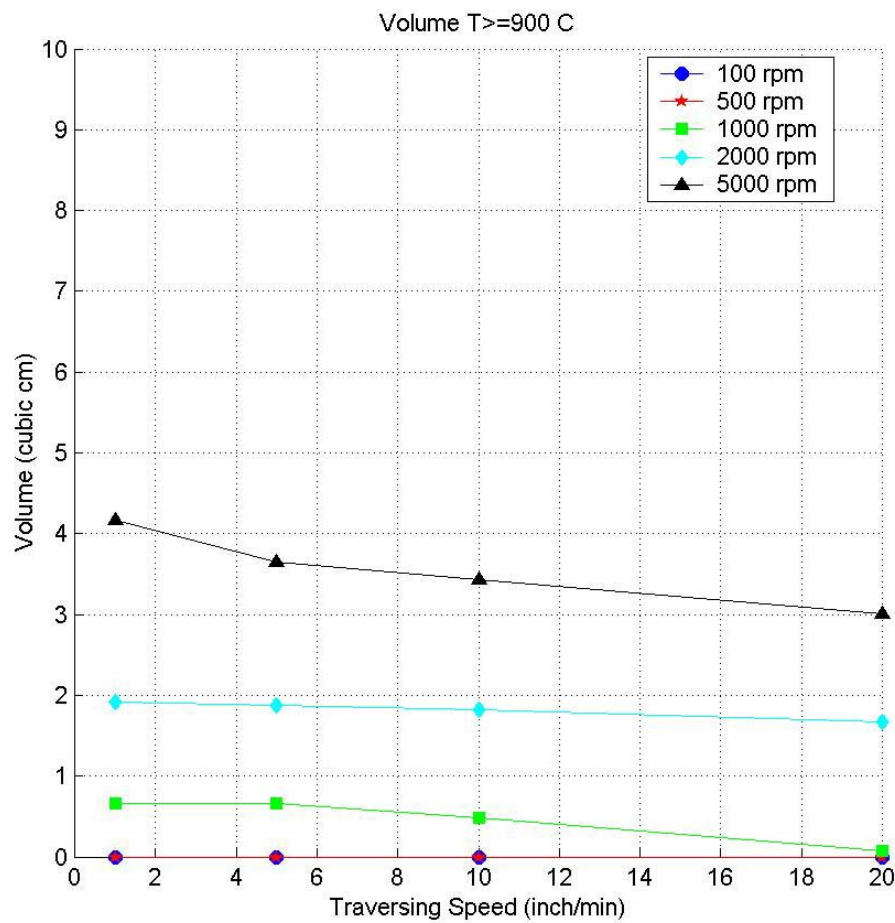


Figure 109. SZ Volume based on $T \geq 900$ °C wrt Traversing Speed.

It can be seen that the volume attaining 900 °C follows the same trends as the volume attaining 800 °C, with the exception of the 100 rpm 20 ipm volume. This is due to the flux of material around the tool being able to remove the heat faster than necessary to maintain 900 °C. The small volume that did exceed 900 °C, was seen directly trailing the pin.

B. VOLUME PLOTS BASED ON STRAIN-RATE

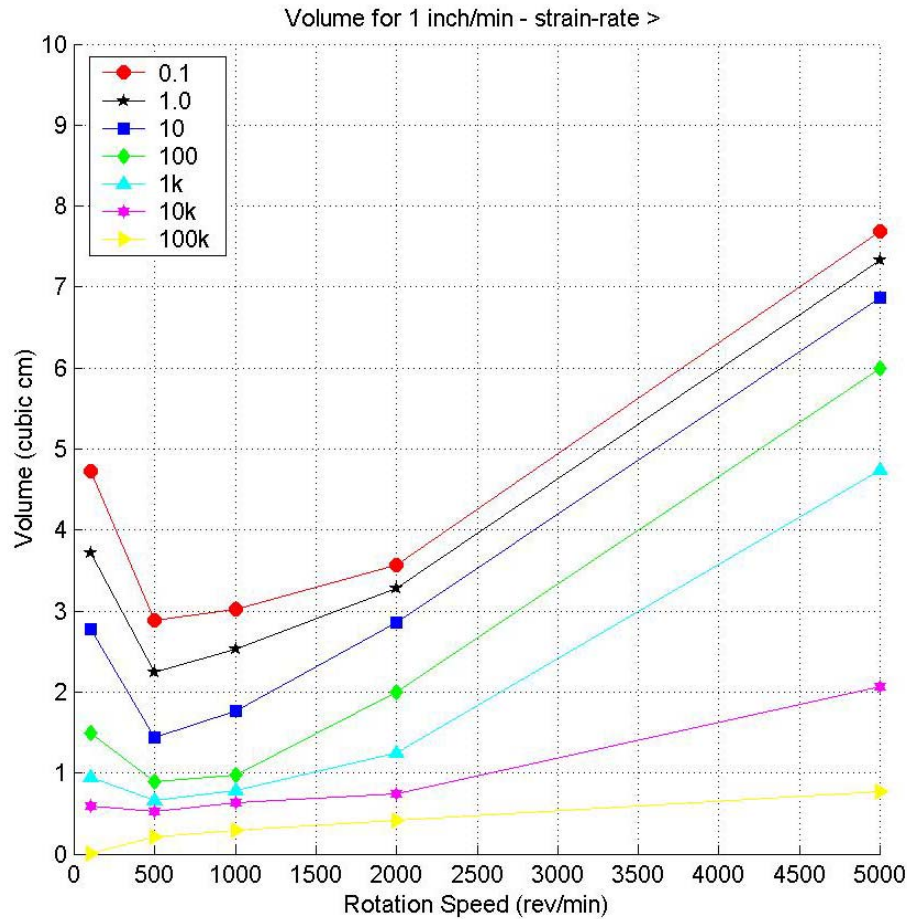


Figure 110. SZ Volume based on $\dot{\epsilon}$ wrt Rotation Speed for Traversing Rate of 1 ipm. The trough seen between 500 to 1000 rpm, is the combination of the plowing regime (below 500 rpm) and the heat generation regime (above 1000 rpm). As expected the plowing regime is dominated by the lower magnitude strain-rates. The higher magnitude strain-rates for 5000 rpm are consistent with the pictures of temperature and strain-rate from Appendix A. It is noteworthy that the highest strain-rate stays relatively constant throughout the variation of rotation rates.

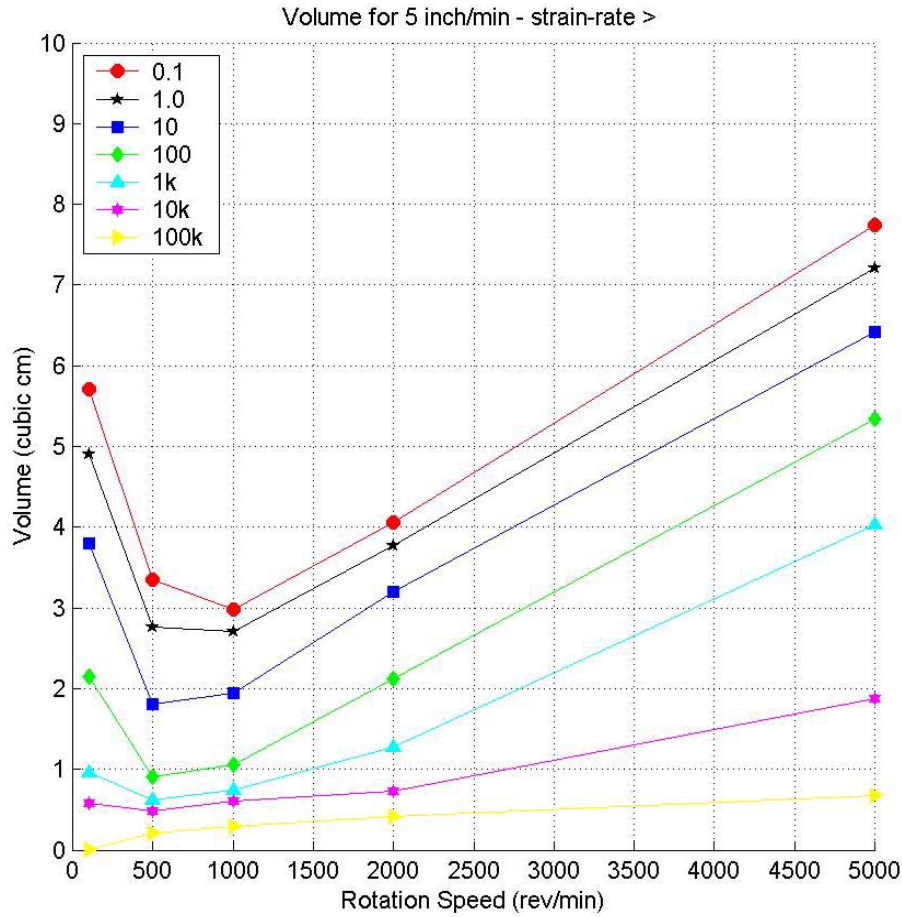


Figure 111. SZ Volume based on $\dot{\epsilon}$ wrt Rotation Speed for Traversing Rate of 5 ipm.

The trough seen at 1000 rpm, is the combination of the plowing regime (below 1000 rpm) and the heat generation regime (above 1000 rpm). As expected the plowing regime is dominated by the lower magnitude strain-rates. The higher magnitude strain-rates for 5000 rpm are consistent with the pictures of temperature and strain-rate from Appendix A. It is noteworthy that the highest strain-rate stays relatively constant throughout the variation of rotation rates and is nearly identical to 1 ipm. The volume at the trough is nearly identical to that of 1 ipm.

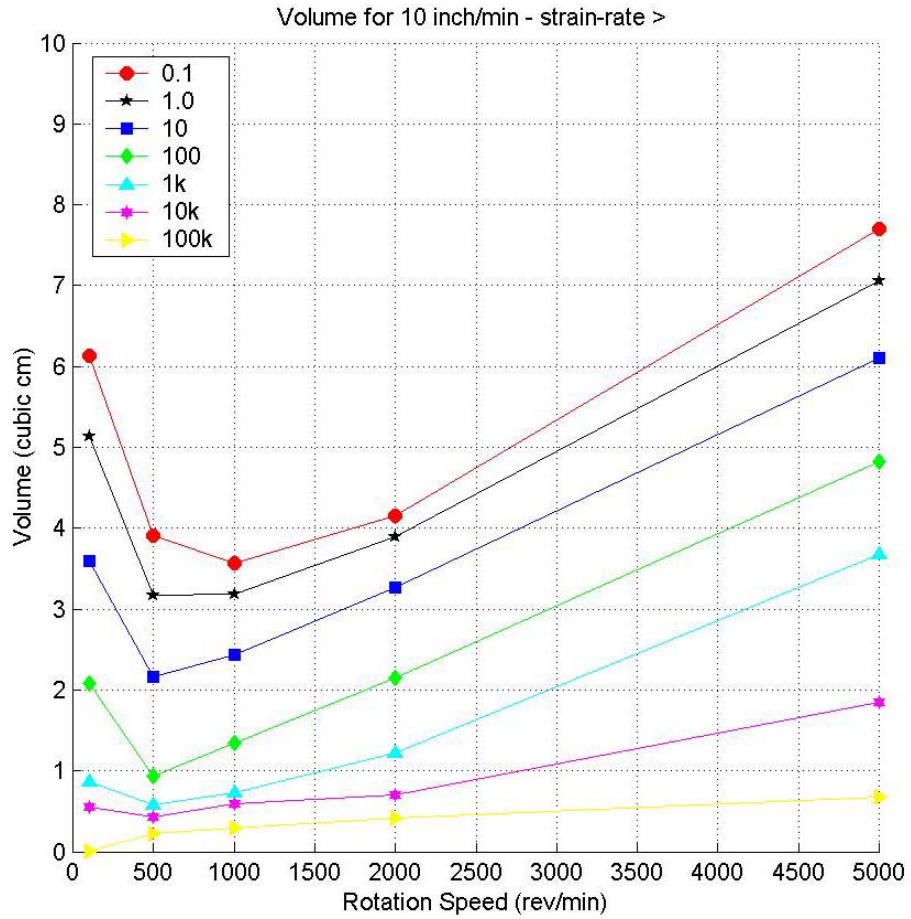


Figure 112. SZ Volume based on $\dot{\varepsilon}$ wrt Rotation Speed for Traversing Rate of 10 ipm. The trough seen at 1000 rpm, is the combination of the plowing regime (below 1000 rpm) and the heat generation regime (above 1000 rpm). As expected the plowing regime is dominated by the lower magnitude strain-rates. The higher magnitude strain-rates for 5000 rpm are consistent with the pictures of temperature and strain-rate from Appendix A. It is noteworthy that the highest strain-rate stays relatively constant throughout the variation of rotation rates and is nearly identical to lower traversing rates. The trough at 1000 rpm is slightly larger than that of the lower traversing rates.

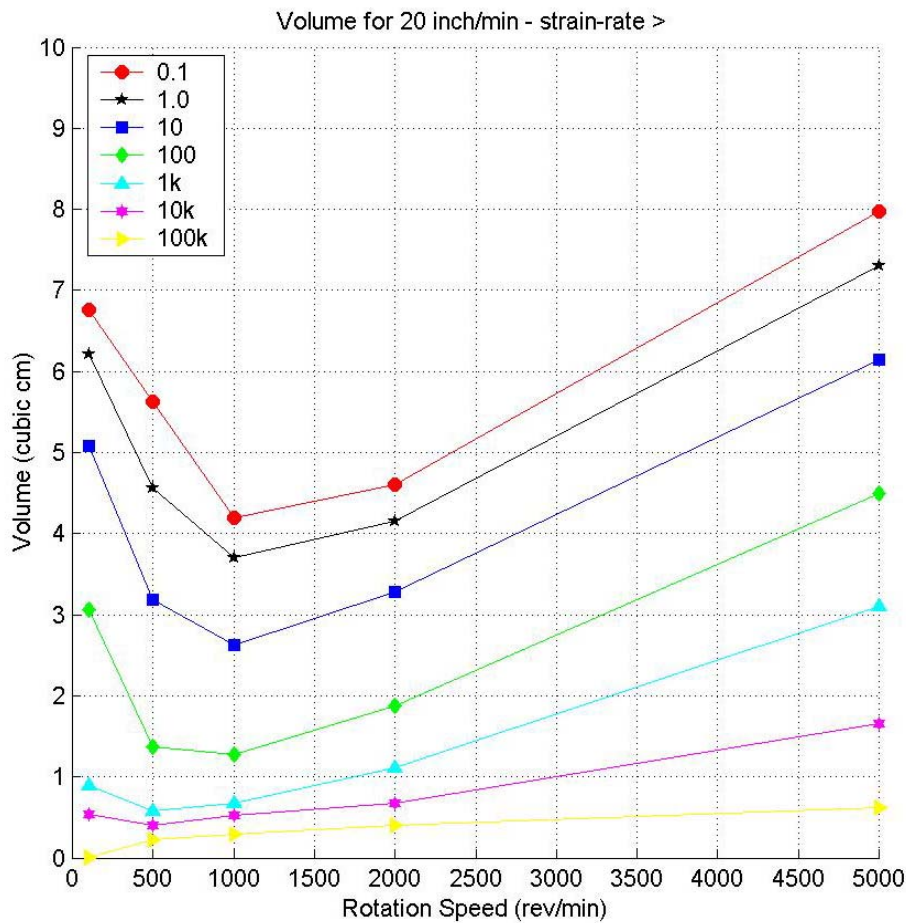


Figure 113. SZ Volume based on $\dot{\epsilon}$ wrt Rotation Speed for Traversing Rate of 20 ipm.

The trough seen at 1000 rpm, is the combination of the plowing regime (below 1000 rpm) and the heat generation regime (above 1000 rpm). As expected the plowing regime is dominated by the lower magnitude strain-rates. The higher magnitude strain-rates for 5000 rpm are consistent with the pictures of temperature and strain-rate from Appendix A. It is noteworthy that the highest strain-rate stays relatively constant throughout the variation of rotation rates and is nearly identical to lower traversing rates. The trough at 1000 rpm is slightly larger than that of 10 ipm.

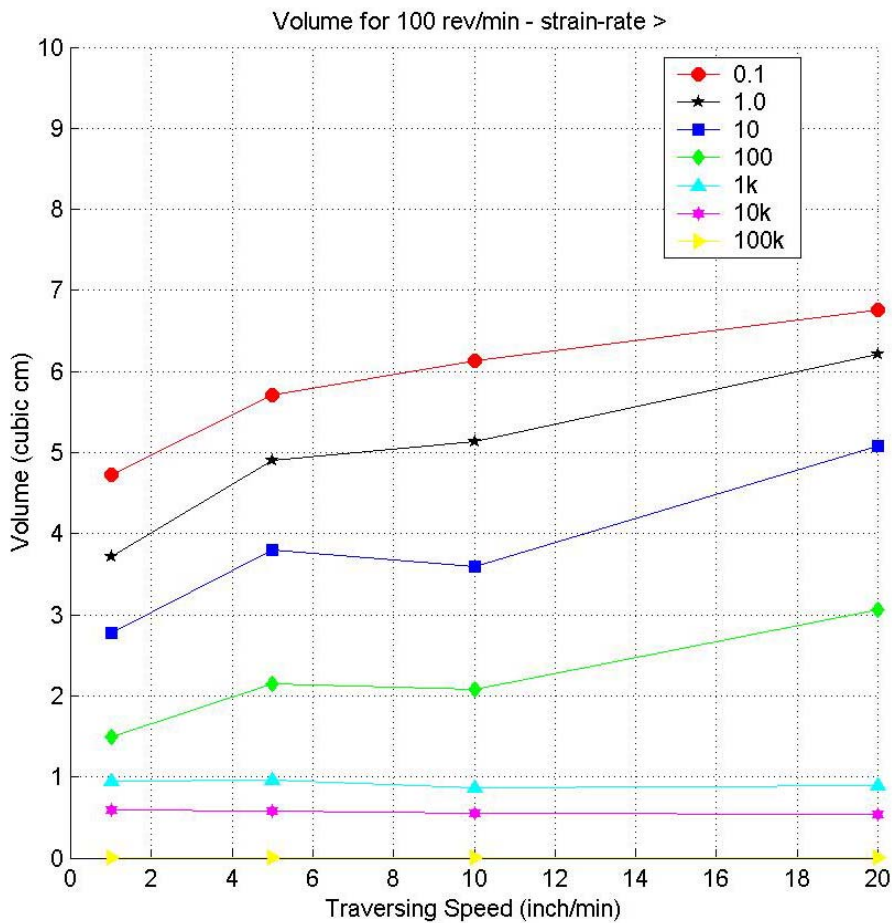


Figure 114. SZ Volume based on $\dot{\varepsilon}$ wrt Rotation Speed for Rotation Rate of 100 rpm.

The strain-rate field is dominated by the lower magnitude strain-rates.

As the traversing rate increases, the lower magnitude strain-rate volumes increase showing that more ‘plowing’ is occurring. The larger strain-rate volumes are staying relatively constant. These volumes are very small and correlate with the volume of material directly around the effective pin diameter as discussed in Appendix A Section A.

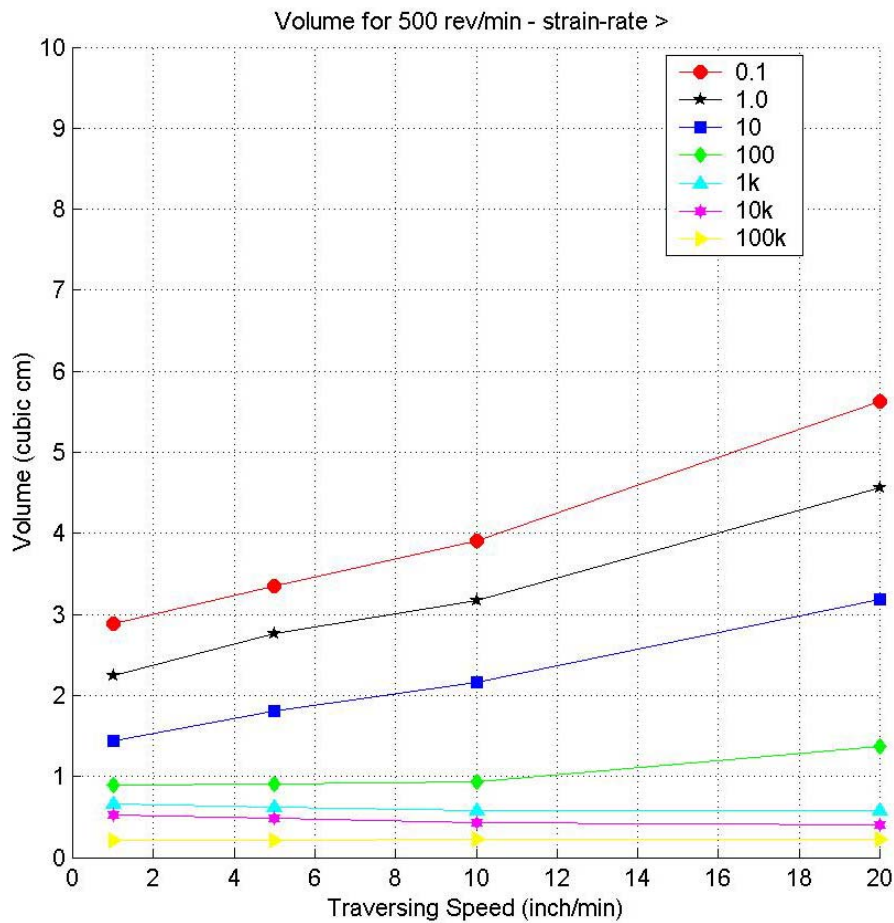


Figure 115. SZ Volume based on $\dot{\varepsilon}$ wrt Rotation Speed for Rotation Rate of 500 rpm. The strain-rate field is dominated by the lower magnitude strain-rates. As the traversing rate increases, the lower magnitude strain-rate volumes increase showing that more ‘plowing’ is occurring. The larger strain-rate volumes are staying relatively constant. These volumes are very small and correlate with the volume of material directly around the tool.

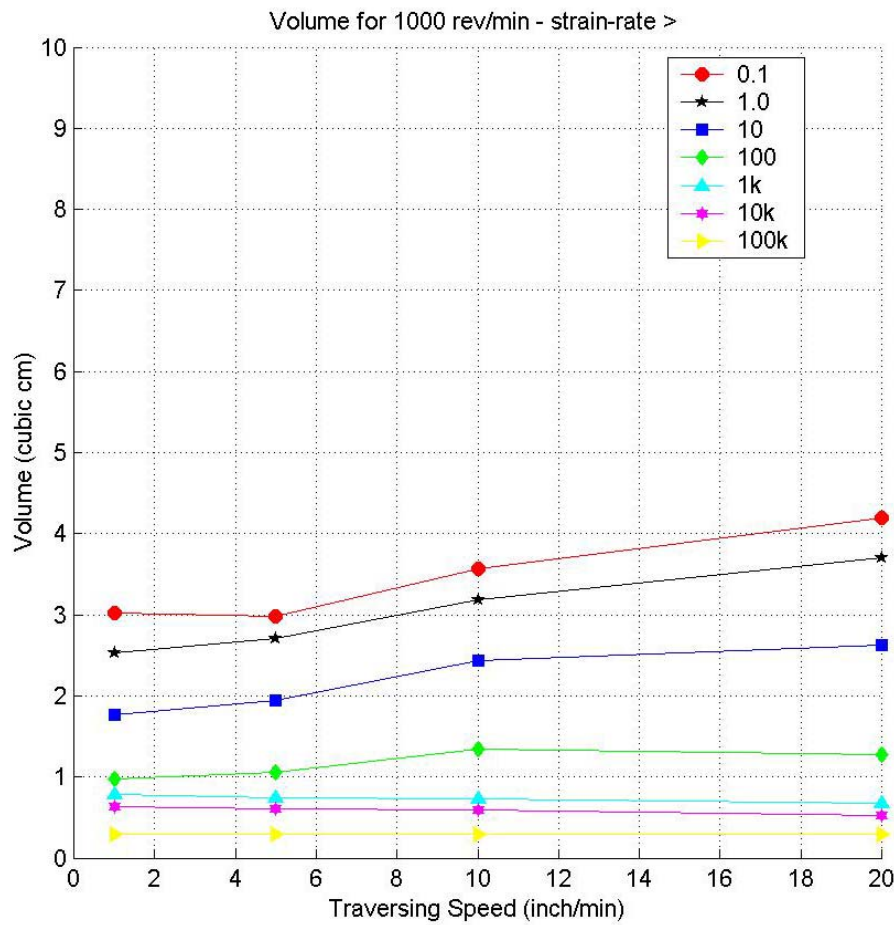


Figure 116. SZ Volume based on $\dot{\epsilon}$ wrt Rotation Speed for Rotation Rate of 1000 rpm.

The strain-rate volumes are staying relatively constant throughout the variation of traversing rates. The slight increase in volume of the lower magnitude strain-rates with increasing traversing rate is due to the temperature field being elongated and distorted with emphasis to trailing the tool. The lower temperature leads to higher stresses and therefore lower strain-rates further away from the tool.

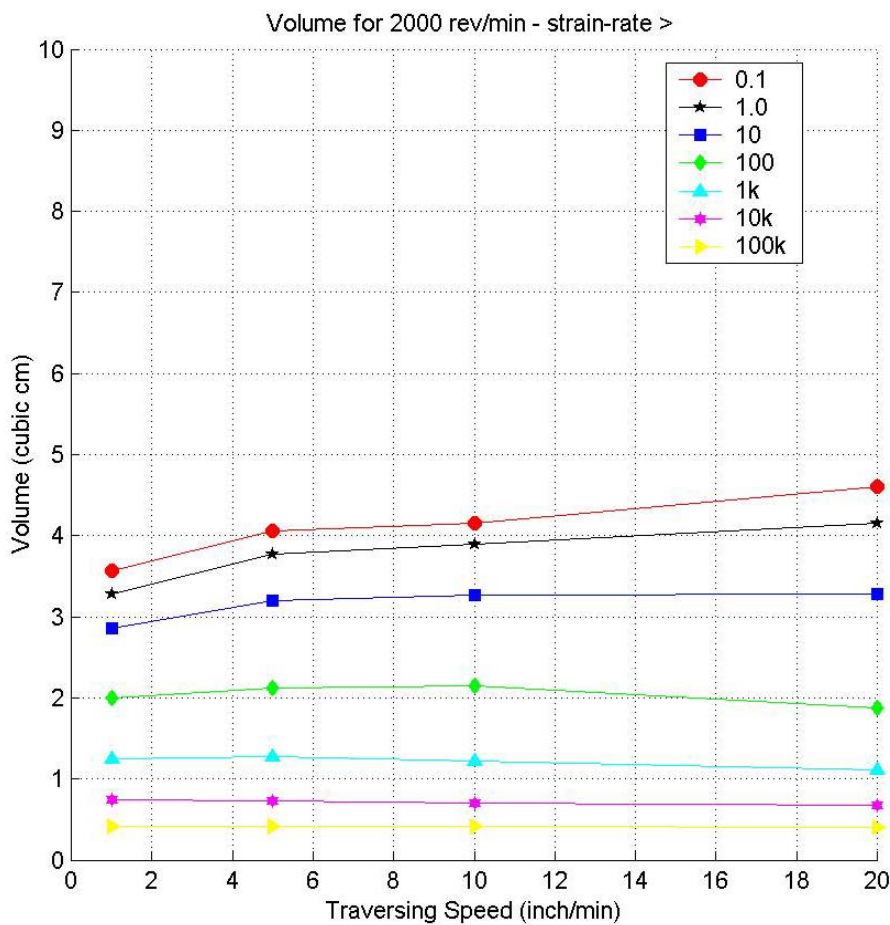


Figure 117. SZ Volume based on $\dot{\epsilon}$ wrt Rotation Speed for Rotation Rate of 2000 rpm.

The strain-rate volumes are staying relatively constant throughout the variation of traversing rates. The slight increase in volume of the lower magnitude strain-rates with increasing traversing rate is due to the temperature field being elongated and distorted with emphasis to trailing the tool. The lower temperature leads to higher stresses and therefore lower strain-rates further away from the tool.

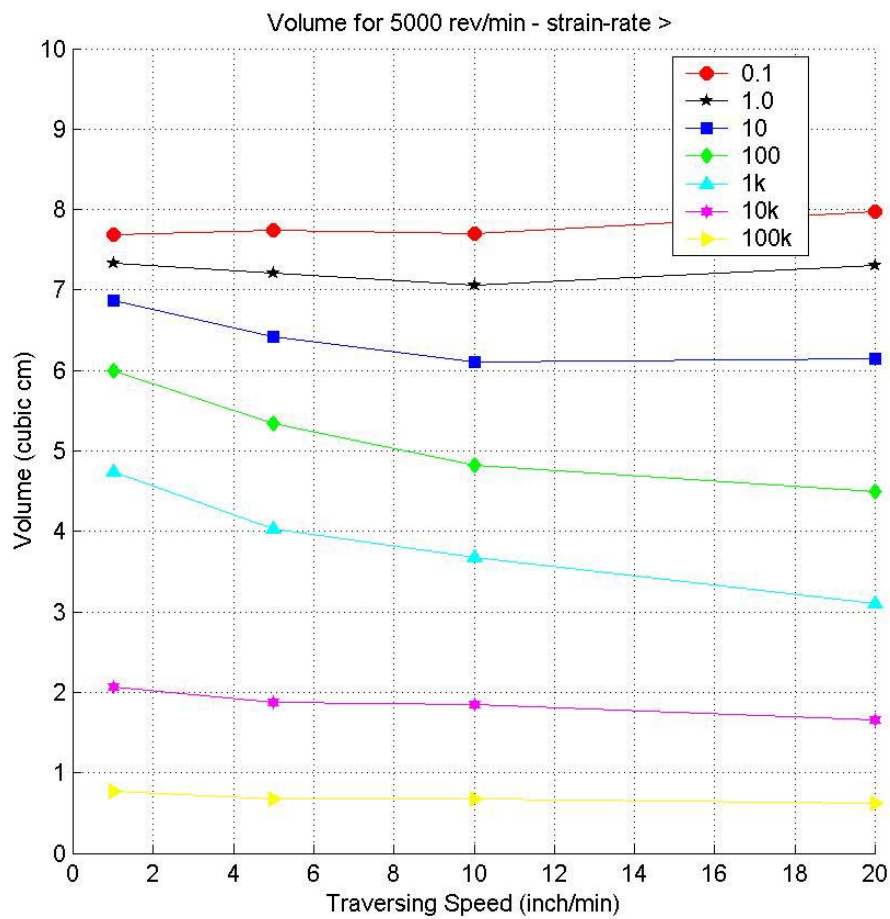


Figure 118. SZ Volume based on $\dot{\varepsilon}$ wrt Rotation Speed for Rotation Rate of 5000 rpm.

The higher and lower magnitude strain-rate volumes are staying relatively constant throughout the variation of traversing rates. The middle magnitude strain-rates are lowering with increasing traversing rate. This effect is due to the flux of material around the tool shaping the strain-rate, temperature and stress fields. All of these fields are being elongated with emphasis trailing the tool as discussed in Figure 102 (Appendix A).

C. POWER GENERATION FRACTIONS

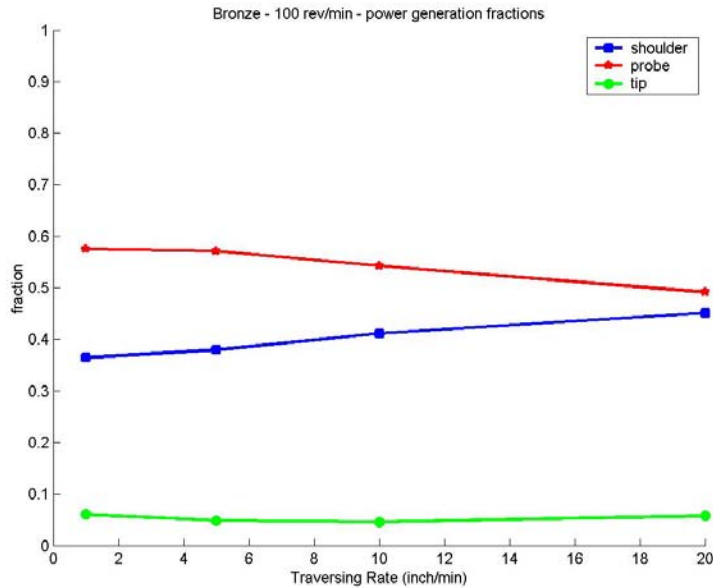


Figure 119. Power Generation Fractions wrt Traversing Rate for Rotation Speed of 100 rpm.

The relative fractions are showing that the shoulder and the pin are equally important in generating the adiabatic heat with the pin having a slightly larger importance. This is opposite compared to the rest of the rotation rates tested.

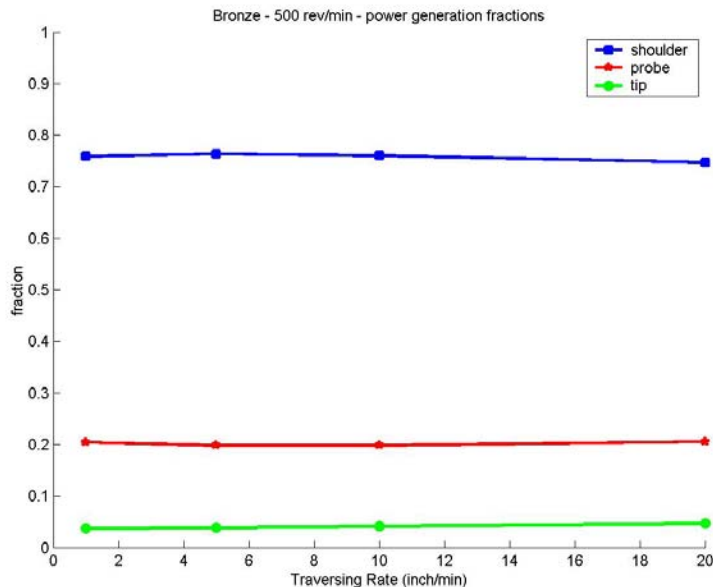


Figure 120. Power Generation Fractions wrt Traversing Rate for Rotation Speed of 500 rpm.

Nearly 75% of the generated power is produced at or near the shoulder.
The relative fractions are nearly independent of the traversing rate.

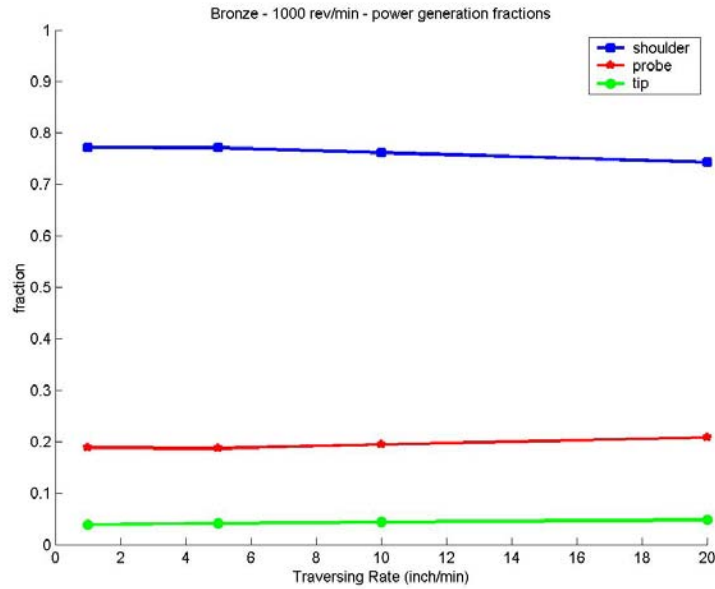


Figure 121. Power Generation Fractions wrt Traversing Rate for Rotation Speed of 1000 rpm.

Nearly 75% of the generated power is produced at or near the shoulder.
The relative fractions are nearly independent of the traversing rate.

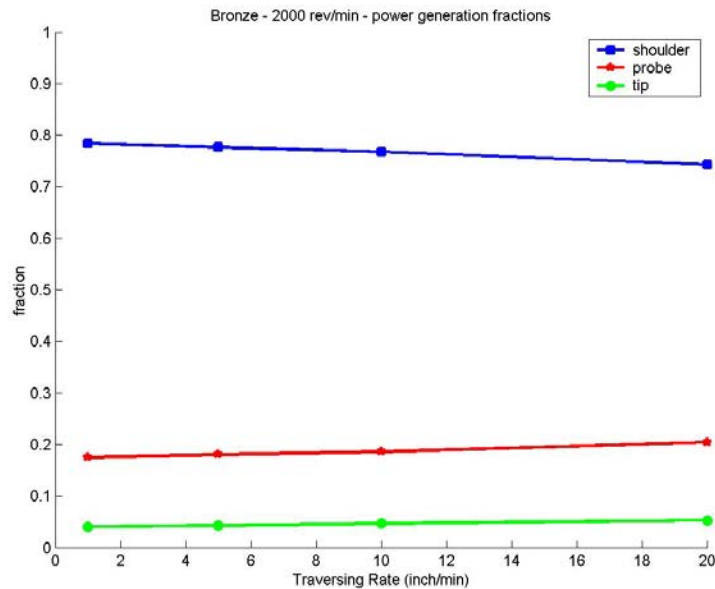


Figure 122. Power Generation Fractions wrt Traversing Rate for Rotation Speed of 2000 rpm.

Nearly 75 - 80% of the generated power is produced at or near the shoulder. The relative fractions change slightly as the traversing rate increases.

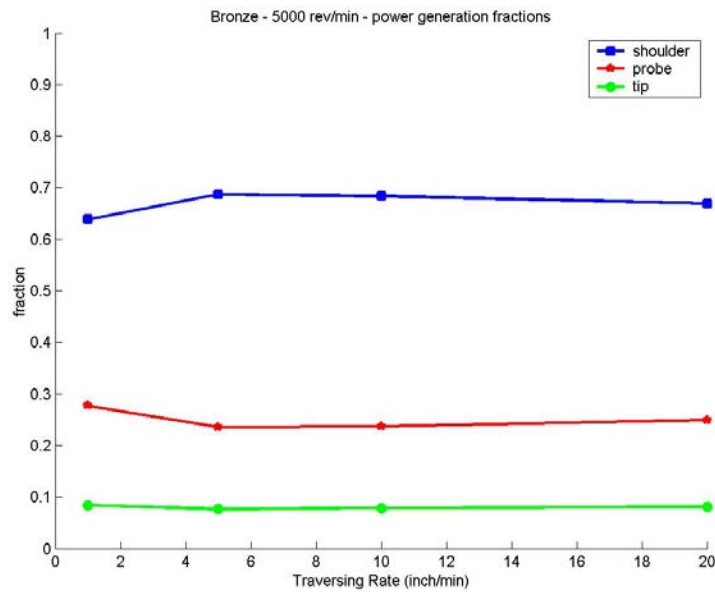


Figure 123. Power Generation Fractions wrt Traversing Rate for Rotation Speed of 5000 rpm.

Nearly 65 - 70% of the generated power is produced at or near the shoulder. At relative fractions for 1ipm and 20 ipm are near equal.

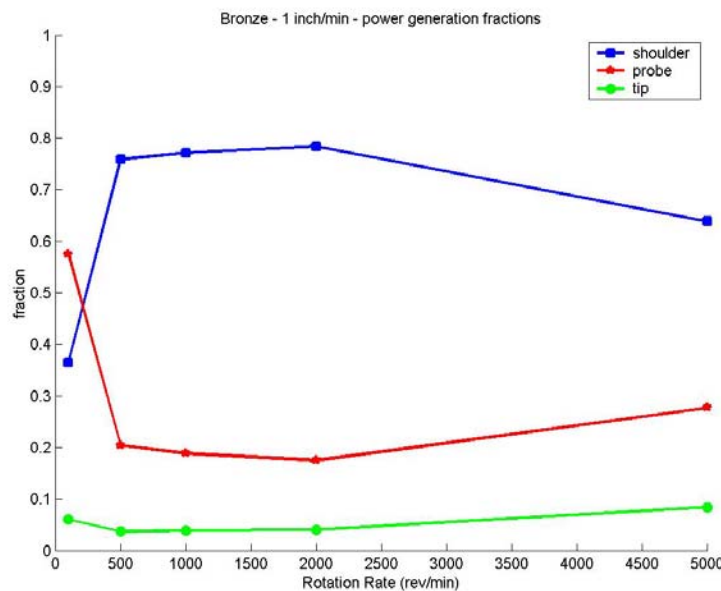


Figure 124. Power Generation Fractions wrt Rotation Speed for Traversing Rate of 1 ipm.

At 100 rpm, the pin is showing it's importance. The plateau at 500 to 2000 rpm is nearly 80%.

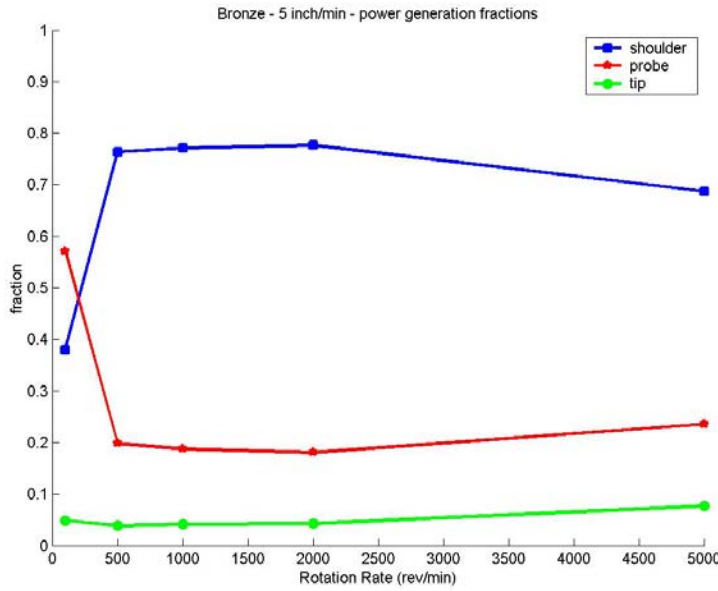


Figure 125. Power Generation Fractions wrt Rotation Speed for Traversing Rate of 5 ipm.

At 100 rpm, the pin is showing it's importance. The plateau at 500 to 2000 rpm is nearly 80%. The shape is staying similar to 1 ipm.

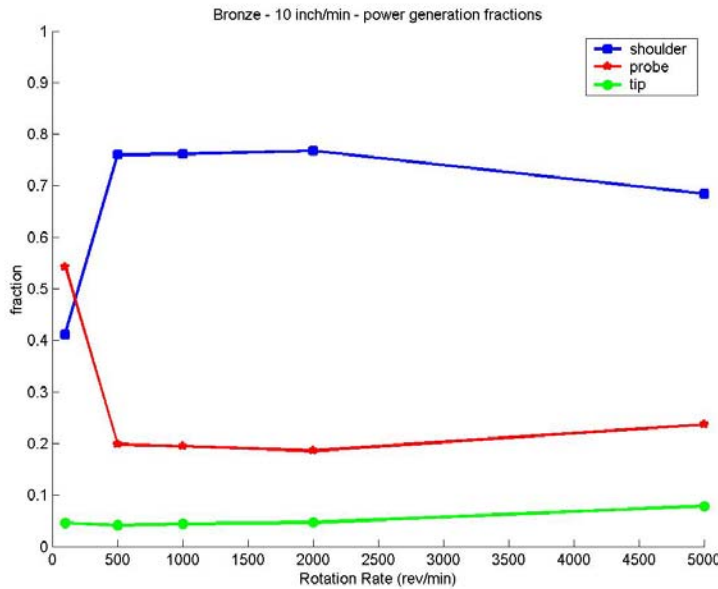


Figure 126. Power Generation Fractions wrt Rotation Speed for Traversing Rate of 10 ipm.

At 100 rpm, the pin is showing it's importance. The plateau at 500 to 2000 rpm is nearly 75%. The shape is staying similar to the lower traversing rates.

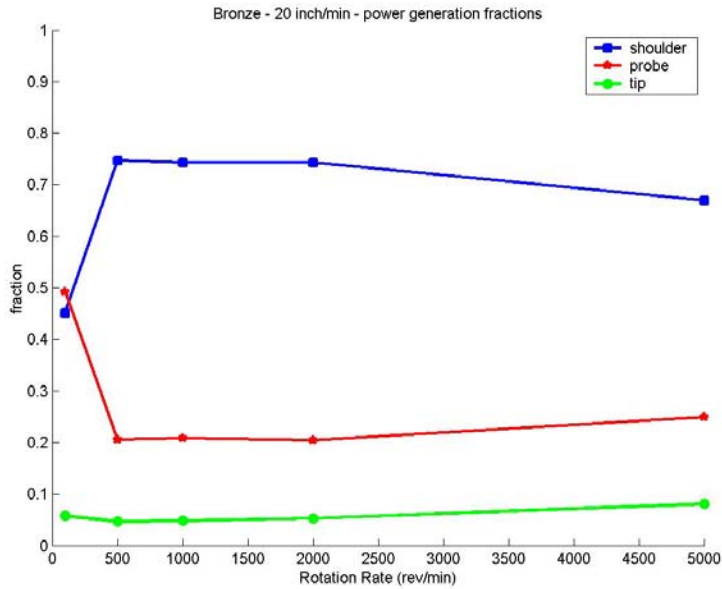


Figure 127. Power Generation Fractions wrt Rotation Speed for Traversing Rate of 20 ipm.

At 100 rpm, the pin is showing it's importance. The plateau at 500 to 2000 rpm is nearly 75%. The shape is staying similar to the lower traversing rates.

D. DERIVATION OF THE POWER LAW RELATIONSHIP

$$\begin{aligned}
 \log(H) &= 0.969 \log(TC) - 0.75 \log(RPM) - 0.8 \\
 \Rightarrow H &= TC^{0.969} RPM^{-0.75} 10^{-0.8} \\
 \Rightarrow \frac{Q}{IPM} &= \left(\frac{RPM}{IPM} \right)^{0.969} RPM^{-0.75} 10^{-0.8} \\
 \Rightarrow Q &= RPM^{(0.969-0.75)} IPM^{(1-0.969)} 10^{-0.8}
 \end{aligned}$$

converting units and scaling the appropriate variables

$$\Rightarrow Q(\text{kW}) = 9.3595 RPM^{0.219} IPM^{0.031}$$

E. ROSENTHAL'S 3-DIMENSIONAL APPROXIMATION

For the discussion of thermal cycles, the z-direction will be measured from the bottom of the NAB, therefore the surface will be at 0.635 cm.

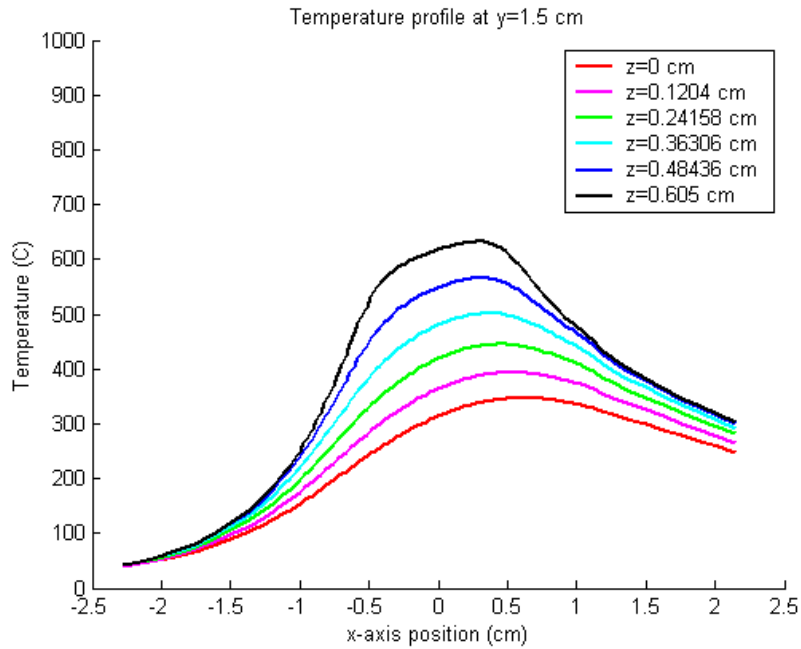


Figure 128. Temperature profiles of 1000 rpm 5 ipm simulation at $y=1.5$ cm

The temperature profiles were created with $y=1.5$ cm, due to this parameter being just outside of the shoulder. Even yet, the top of the material is flattened due to the influence of the larger distributed power source of the shoulder. The measurement of the z-direction is within a cell with dimensions of 0.03 cm, therefore, the $z=0.605$ cm represents the surface of the material. For the 1000 rpm 5 ipm simulation, the generated thermal power was calculated to be 1902 W.

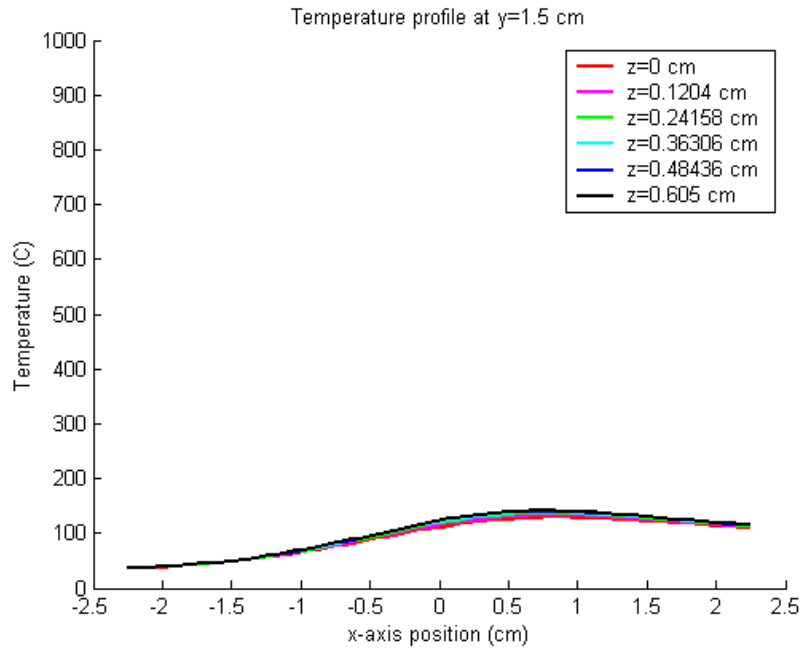


Figure 129. Rosenthal's 3D approximation for $Q=1.902$ kW at $y=1.5$ cm

The Rosenthal's 3D solution is based on several assumptions. The source is a point source moving on the surface of the material. The Rosenthal's approximation is only valid outside of the fusion zone. The power used in the approximation was 1902 W, correlating to the generated thermal power from Figure 128. The material properties used were from Ref. 11 for NAB.

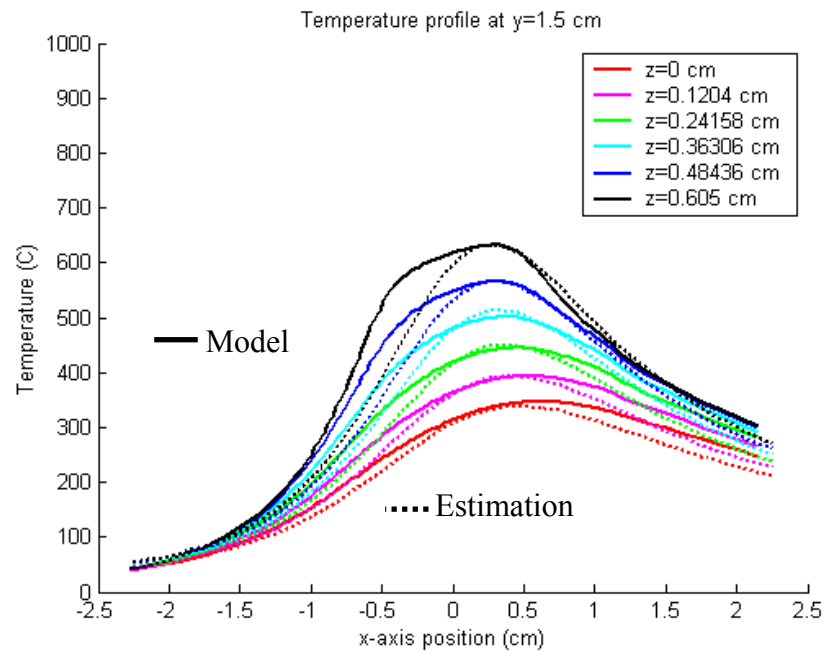


Figure 130. Comparison of modified Rosenthal's 3D solution

The modified Rosenthal's solution used the same information as previously, only the radial distance to the source was modified. A constantly varying correction was subtracted from the radial distance to correlate to the distance to the edge of the stir zone. Further work will need to be done on this problem. This will prove to be a difficult challenge due to the ever-changing shape of the SZ.

THIS PAGE INTENTIONALLY LEFT BLANK

LIST OF REFERENCES

1. W. M. Thomas et. al.: ‘Friction Stir Butt Welding,’ International Patent Appl. No. PCT/GB92/02203 and GB Patent Appl. No. 9125978.8, Dec 1991, U.S. Patent No. 5,460,317 – from [Ref. 2] in support of information by Stephan Kallee and Dave Nicholas TWI.
2. Rhodes, C. G. et al., “Effects of Friction Stir Welding on Microstructure of 7075 Aluminum,” *Scripta Materialia*, v. 36, No. 1, p. 69-75, 1997.
3. Mishra, R.S. and Mahoney, M.W., “Friction Stir Processing: A New Grain Refinement Technique to Achieve High Strain Rate Superplasticity in Commercial Alloys,” *Materials Science Forum*, v. 357-359, p. 507-514, 2001.
4. K.V. Jata and S.L. Semiatin, “Continuous Dynamic Recrystallization During Friction Stir Welding of High Strength Aluminum Alloys,” *Scripta Materialia*, v. 43, p. 743-749, 2000.
5. O. T. Midling and G. Rorvik, “Effect of Tool Shoulder Material on Heat Input during Friction Stir Welding,” 1st International Symposium on Friction Stir Welding, p. 1-9, Jun 1999.
6. P. A. Colegrove and P. L. Threadgill, “Modelling and Development of the Trivex™ Friction Stir Welding Tool,” 4th International Symposium on Friction Stir Welding, p. 1-16, MAY 2003.
7. A. Askari, S. Silling, B. London and M. Mahoney, “Modeling and Analysis of Friction Stir Welding Processes,” The Minerals, Metals & Materials Society, 2001.
8. Sahoo, M., “Structure and Mechanical Properties of Slow-Cooled Nickel-Aluminum Bronze Alloy C95800,” *AFS Trans*, v. 90, p. 913-926, 1982.
9. Culpan, E.A. and Rose, G., “Corrosion Behaviour of Cast Nickel Aluminium Bronze in Sea Water,” *British Corrosion Journal*, v. 14, p. 160-166, 1979.
10. American Society for Testing and Materials (ASTM) B148 – 93a, Standard Specification for Aluminum-Bronze Sand Castings.
11. Metals Handbook, 9th Ed., v. 2, Properties & Selections: Nonferrous Alloys and Pure Metals.
12. Wenschot, P., “The Properties of Ni-Al Bronze Sand Cast Ship Propellers in Relation to Section Thickness,” *International Shipbuilding Progress*, v. 34, p.112-123,1987.

13. Sahoo, M., "Weldability of Nickel-Aluminum Bronze Alloy C95800," *AFS Trans*, v. 112, p. 893-911, 1982.
14. A. Jahanafrooz, F. Hasan, G.W. Lorimer and N. Ridley, "Microstructural Development in Complex Nickel-Aluminum Bronze," *Met. Trans A*, v. 14a, p. 1951-1956, 1983.
15. Culpan, E.A. and Rose, G., "Microstructural Characterization Of Cast Nickel Aluminium Bronze," *Journal of Materials Science*, v. 13, p. 1647-1657, 1978.
16. Weston, G.M., "Survey of Nickel-Aluminium-Bronze Casting Alloys on Marine Applications," Australia Dept. of Defence Report, DSTO MRL, Melbourne, Victoria, MRL-R-807, 1981.
17. F. Hasan, A. Jahanafrooz, G.W. Lorimer and N. Ridley, "The Morphology, Crystallography, and Chemistry of Phases in As-Cast Nickel-Aluminum Bronze," *Met. Trans A*, v. 13a, p.1337-1345, 1982.
18. D.M. Lloyd, G.W. Lorimer and N. Ridley, "Characterization of Phases in a Nickel-Aluminium Bronze," *Metals Technology*, v. 7, p. 114-119,
19. Ø. Frigaard, Ø. Grong, B. Bjørneklett and O. T. Midling, "Modelling of the thermal and microstructure fields during friction stir welding of aluminum alloys," 1st International Symposium on Friction Stir Welding, p. 1-10, Jun 1999.
20. Y. Li, L. E. Murr and J. C. McClure, "Solid-State Flow Visualization in the Friction-Stir Welding of 2024 Al to 6061 Al," *Scripta Materialia*, v. 40, n. 9, p. 1041-1046, 1999.
21. A. P. Reynolds, "Visualisation of material flow in autogenous friction stir welds," *Metallurgical and Materials Transactions A*, v. 32A, p. 2878-2884, Nov 2001.
22. J. H. Ouyang and R. Kovacevic, "Material flow and microstructure in the friction stir butt welds of the same and dissimilar aluminum alloys," *Journal of Materials Engineering and Performance*, v. 11, n. 1, p. 51-70, Feb 2002.
23. T. Dickerson, H. R. Shercliff and H. Schmidt, "A Weld Marker Technique for Flow Visualization in Friction Stir Welding," 4th International Symposium on Friction Stir Welding, p. 1-12, MAY 2003.
24. B. London, M. Mahoney, W. Bingel, M. Calabrese, R. Bossi and D. Waldron, "Material Flow in Friction Stir Welding Monitored with Al-Si and Al-W Composite Markers," The Minerals, Metals & Materials Society, 2003.

25. Y. L. Chao and X. Qi, "Thermal and Thermo-Mechanical Modeling of Friction Stir Welding of Aluminum Alloy 6061-T6," *Journal of Materials Processing & Manufacturing Science*, v. 7, n. 2, p. 215-233, 1998.
26. Y. J. Chao, X. Qi and W. Tang, "Heat Transfer in Friction Stir Welding – Experimental and Numerical Studies," *Transactions of ASME*, v. 125, p. 138-145, FEB 2003.
27. M. J. Russell and H. R. Shercliff, "Analytical Modelling of Microstructure Development in Friction Stir Welding," First International Symposium on Friction Stir Welding, p. 1-11, JUN 1999.
28. Ø. Frigaard, Ø. Grong and O. T. Midling, "A Process Model for Friction Stir Welding of Age Hardening Aluminum Alloys," *Metalurgical and Materials Transactions A*, v. 32A, p. 1189-1200, MAY 2001.
29. M. Z. H. Khandkar, J. A. Khan and A. P. Reynolds, "Prediction of temperature distribution and thermal history during friction stir welding: input torque based model," *Science and Technology of Welding and Joining*, v. 8, n. 3, p. 165-174, 2003.
30. P. Colgrove, "3 Dimensional Flow and Thermal Modelling of the Friction Stir Welding Process," The 2nd International Symposium on Friction Stir Welding, p. 1-11, Jun 2000.
31. G. J. Bendzsak, T. H. North and C. B. Smith, "An Experimentally Validated 3D Model for Friction Stir Welding," The 2nd International Symposium on Friction Stir Welding, p. 1-12, Jun 2000.
32. P. A. Colgrove and H. R. Shercliff, "Experimental and numerical analysis of aluminium alloy 7075-T7351 friction stir welds," *Science and Technology of Welding and Joining*, v. 8, n. 5, p. 360-368, 2003.
33. T. Dickerson, Q. Y. Shi and H. R. Shercliff, "Heat flow into friction stir welding tools," 4th International Symposium on Friction Stir Welding, p. 1-11, MAY 2003.
34. C. Chen and R. Kovacevic, "Finite Element Modeling of Thermomechanical Performance of Friction Stir Welding," 4th International Symposium on Friction Stir Welding, p. 1-15, MAY 2003.
35. L. D'Alvise, "Using ASTER (EDF-GDF) to model the Friction Stir Welding process," www.cenaero.be, User's Meeting, 14/10/2003.

36. Q. Y. Shi, T. Dickerson and H. R. Shercliff, "Thermo-Mechanical FE Modelling of Friction Stir Welding of AL-2024 Including Tool Loads," 4th International Symposium on Friction Stir Welding, p. 1-12, MAY 2003.
37. J. E. Gould, Z. Feng and P Ditzel, "Preliminary Modeling of the Friction Stir Welding Process," North American Welding Research Conference, p. 1-16, 1996.
38. H. Schmidt, J. Hattel and J. Wert, "An Analytical model for the heat generation in friction stir welding," *Modelling Simul. Mater. Sci. Eng.*, v. 12, p. 143-157, NOV 2003.
39. K. Oh-Ishi and T. McNelley, "Microstructural Modification of As-Cast NiAl Bronze by Friction Stir Processing," *Metallurgical and Materials Transactions A*, v. 35A, in publication 2004.
40. B. K. Vasquez, MS Thesis, "The Effects of Isothermal Deformation and Annealing on the Microstructure of Nickel-Aluminum Bronze in Relation to the Friction Stir Process," Naval Postgraduate School, Monterey, CA, DEC 2002.
41. F. A. Pierce, MS Thesis, "The Isothermal Deformation on Nickel Aluminum Bronze in Relation to Friction Stir Processing," Naval Postgraduate School, Monterey, CA, JUN 2004.

INITIAL DISTRIBUTION LIST

1. Defense Technical Information Center
Ft. Belvoir, Virginia
2. Dudley Knox Library
Naval Postgraduate School
Monterey, California
3. Professor Terry McNelley
Naval Postgraduate School
Dept. of Mechanical Engineering
Monterey, California
4. Professor A. J. Healey
Naval Postgraduate School
Dept. of Mechanical Engineering
Monterey, California
5. CDR S. Cunningham
Naval Postgraduate School
Dept. of Mechanical Engineering
Monterey, California
6. Abe Askari
Boeing Corporation
Bellevue, Washington
7. Murray W. Mahoney
Rockwell Science Center
Thousand Oaks, California
8. William Palko
Naval Surface Warfare Center
Caderock Division
West Bethesda, Maryland
9. Dr. Leo Christodoulou
DARPA/DSO
Arlington, Virginia